7-12-2014

Nanoparticle Cerium oxide and Mixed Cerium Oxides for Improved Fuel Cell Lifetime

Stephen Stewart

Stephen Michael Stewart
Candidate

Chemical and Nuclear Engineering
Department

This dissertation is approved, and it is acceptable in quality and form for publication:

Approved by the Dissertation Committee:

Dr. Abhaya Datye, Chairperson

Dr. Fernando Garzon

Dr. Kateryna Artyushkova

Dr. Plamen Atanassov

NANOPARTICLE CERIUM OXIDE AND MIXED CERIUM OXIDES FOR IMPROVED FUEL CELL LIFETIME

by

STEPHEN MICHAEL STEWART
B.S., Chemical Engineering, NC State University, 2007
B.S., Chemistry, NC State University, 2007

DISSERTATION

Submitted in Partial Fulfillment of the
Requirements for the Degree of

Doctorate of Philosophy

Engineering

The University of New Mexico
Albuquerque, New Mexico

May, 2014

ACKNOWLEDGMENTS

I would like to acknowledge both Dr. Abhaya Datye and Dr. Fernando Garzon, my advisers and dissertation chairs, for their help in writing this thesis and the associated manuscripts. I would also like to thank Dr. Plamen Antanassov and Dr. Kateryna Kateryna Artyushkova for serving as my committee members, and an additional thanks to Kateryna for her assistance in acquiring x-ray photoelectron spectra of my samples over the past two years.

I would also like to thank Dr. Andrew DeLaRiva for his help in acquiring high resolution transmission electron microscopy data, Dr. Barr Halevi for his help in processing XPS data, and Dr. Mukundan Ranganchary and Dr. Courtney Kreller for their help in understanding and interpreting impedance spectra.

Finally, I would like to thank my future wife, Lauren Sittel, for her support through my last years of graduate school.

Nanoparticle Cerium oxide and Mixed Cerium Oxides for Improved Fuel Cell Lifetime

By

Stephen Michael Stewart

B.S., Chemical Engineering, NC State University, 2007

B.S., Chemistry, NC State University, 2007

ABSTRACT

While there is a rich body of literature concerning of properties of bulk cerium oxide and cerium cations in solution, the discussion has been inappropriately applied to nanoscale cerium oxide resulting in many unexpected or unexplained results. In particular, there is very limited understanding about the properties of cerium oxide and its potential use as a radical scavenger, and how the catalytic properties of cerium oxide change as the particle size approaches the nanoscale. For example, the involvement of Ce^{+4} and Ce^{+3} cations in reactions such as hydrogen peroxide decomposition have been investigated for both cerium cations and bulk cerium oxide. However, while both are assumed to decompose hydrogen peroxide through the same mechanism, whereby Ce^{+4} is involved in peroxide decomposition while Ce^{+3} is involved in radical scavenging, there has been very little done to address how the selectivity and activity of these reactions are affected by changing the majority cation population, as cerium cations in solution are predominantly in the +3 oxidation state while cerium cations are predominantly in the +4

oxidation state in cerium oxide. This matter is further complicated in cerium oxide nanoparticles where the surface concentration of Ce^{+3} cations is increased due to particle curvature effects.

Due to the potential of controlling the surface cerium oxidation state using particle size and using this control to change the catalytic properties, this project investigated the effect of particle size and composition and the activity and selectivity of cerium oxide nanoparticles, and has served to expand the understanding of the properties of pure and mixed nanoparticle cerium oxide. This work explains the metric developed for measuring the catalytic properties of pure and mixed cerium oxide nanoparticles, which is also good at predicting the immediate and long-term behavior of nanoparticles in hydrogen fuel cells. This work also directly demonstrates praseodymium enrichment of cerium-praseodymium oxide nanoparticles and how both size and composition affected the catalytic properties. Finally, this project has given new direction for doped cerium oxide nanoparticles in hydrogen fuel cells. Both gadolinium and praseodymium doped cerium oxide nanoparticles have been shown to be poor choices for improving fuel cell lifetime, while zirconium doped cerium oxide nanoparticles show the greatest promise for improving fuel cell lifetime as the doped oxides give both better catalytic behavior than pure cerium, and unlike pure cerium oxide, does not ultimately dissolve to give a destructive nanoparticle.

TABLE OF CONTENTS

LIST OF FIGURES

LIST OF TABLES

Chapter 1: Literature Review

1.1 Introduction

Cerium oxide (CeO_2) has found widespread use in the field of catalysis as a catalytically active oxide[1-3] and doped oxide,[4,5] as well as an excellent support for other catalysts,[6-9] due to its ability to easily change its oxidation state through either water, free oxygen,[10] or the use of bulk oxygen.[11] However, despite its utility and the wealth of knowledge about cerium oxide, there remain several conflicting reports on the physical properties of cerium oxide. Like many other materials, the properties of cerium oxide have a strong dependence on particle size,[12,13] which can create confusion when different length scales are compared, such as bulk material versus nanoparticles. This review will provide an overview of what is currently understood about pure cerium oxides, as well as doped oxides, and will seek to illustrate where there are gaps in the understanding of this ubiquitous material.

1.2 Physical Properties

The two most common varieties of cerium oxide are cerium (IV) oxide, CeO_2, which consists primarily of Ce in a +4 oxidation state, and cerium (III) oxide, Ce_2O_3, which consists primarily of Ce in a +3 oxidation state. While it is possible to obtain Ce_2O_3 which contains no detectable Ce^{+4} cations,[14] CeO_2 contains a mixture of Ce^{+3} and Ce^{+4} cations, regardless of method of synthesis.[15] In reality, CeO_2 exists as a sub-stoichiometric oxide, CeO_{2-x},[16] and appears light yellow for $x<0.004$, becoming grey then dark blue for increasing sub-stoichiometry, and eventually turning blue-black for $x=0.283$.[17] However, in terms of catalytic activity, CeO_2 is the oxide of interest for most catalytic reactions, with Ce_2O_3 being used as an intermediate oxide in reactions catalyzed

by CeO_2 such as in catalytic converters as an intermediate oxide form in the conversion of CO to CO_2[18] or NO to N_2.[19,20] Ce_2O_3 can be obtained from CeO_2 when it is heated to 623 K under a hydrogen atmosphere, but beneath this temperature, reduction of cerium is limited to the surface.[20] CeO_2 and Ce_2O_3 are easily resolved from one another using x-ray diffraction, given sufficiently large crystal domains. CeO_2 is a cubic lattice with the F_{m-3m} space group, which is stable from room temperature until its melting point at circa 2750 K,[16] while Ce_2O_3 is a hexagonal lattice with a P_{-3m1} space group.[21] The XRD pattern of CeO_2 is shown in Figure 1.1; for the CeO_2 lattice, the observed reflections are limited to only reflections where the sum of {h,k,l} must either (1) sum to (4n+2), or (2) {h,k,l} must all be even or odd. As CeO_2 is the most commonly used polymorph of cerium oxide, it will be the focus of the rest of this review, and any reference to cerium oxide will refer to the CeO_2 polymorph.

The preferred method of synthesis for CeO_2 is by precipitation due to good particle size control, and the surface area of bulk cerium oxide prepared by precipitation from solution is generally reported to be around 100-120 m^2/g for most studies and shows low porosity,[2,22-28] but low surface area circa 10-20 m^2/g,[29] can be obtained using higher calcination temperatures exceeding 800 K.[30,31] While there have been reports of high surface area cerium oxide synthesis with high mesoporosity, with the surface area being reported as 194 m^2/g even at temperatures as high as 723 K, these studies have been complicated by the presence of a large, unidentified hexagonal crystal phase,[32,33] which is consistent with a Ce_2O_3 phase. Nitrogen absorption studies of cerium oxide nanoparticles reveal that the material is generally non-porous, with pore volumes less than 1 cm^3/g,[34] so

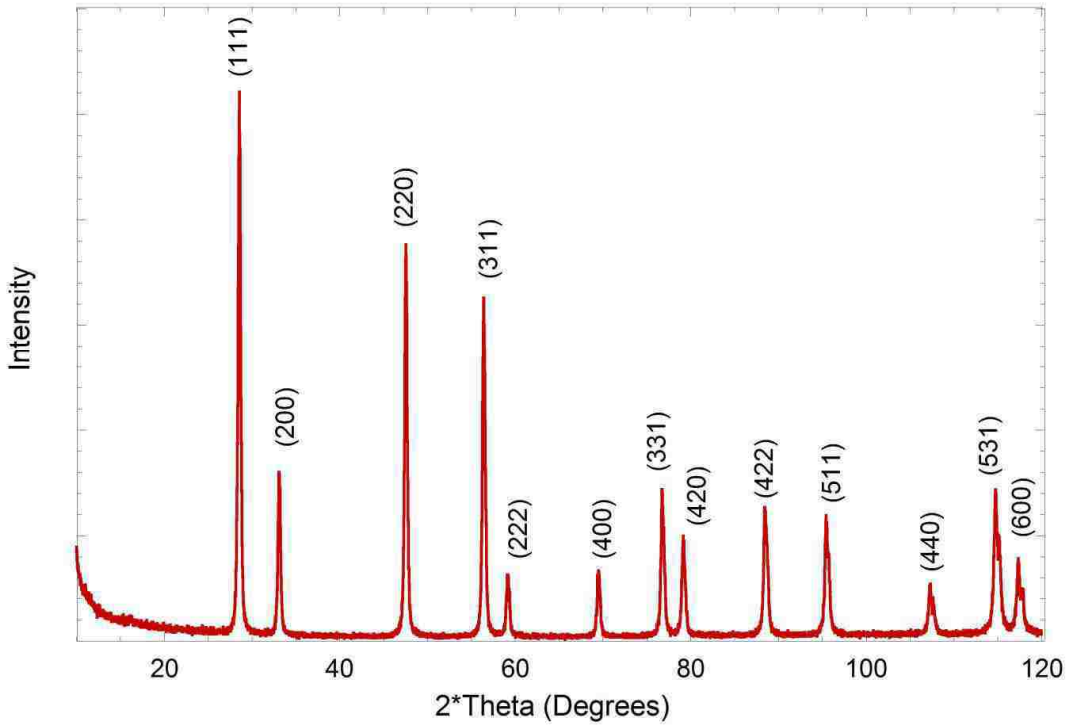

Figure 1.1 X-ray diffraction pattern of 40 nm CeO_2 particles, with the index of each reflection listed above the peak. Splitting of the higher reflection peaks is due the presence of both Cu $K_{\alpha 1}$ and $K_{\alpha 2}$ diffraction peaks.

the nanoparticles are generally solid cerium oxide. The bulk density of cerium oxide is 7.22 g/cm^3, and the specific heat and thermal conductivity are 460 J/kg*K and 12 W/m*K, respectively.[16]

The UV-vis spectrum of cerium oxide contains multiple absorption bands; between 250 and 265 nm absorption is attributed to charge transfer from $O^{-2} \rightarrow Ce^{+3}$, between 275 and 295 nm absorption is attributed to charge transfer from $O^{-2} \rightarrow Ce^{+4}$, between 320-350 nm absorption is attributed to inter-band transitions of cerium oxide, and between 588 and 650 nm absorption is attributed to charge transfer from $Ce^{+3} \rightarrow Ce^{+4}$ transitions.[35-37] To the best of the authors' knowledge, there has been little done in quantifying Ce^{+3}/Ce^{+4} concentration using UV-vis, though this may be due to need to use diffuse reflection techniques, which are complicated by large bandwidths and specular reflectance.[36] Excellent work by Ivanov, et al.,[38] investigated the effects of temperature and synthesis conditions on the physical and electrical properties of cerium oxide nanoparticles, and was able to gather some data relating particle size and band gap. Summarized briefly, when cerium oxide is synthesized using isopropanol added to an aqueous solution of cerium (III) nitrate and the solution is precipitated with fivefold excess 3M ammonia solution, most physical parameters such as band gap, measured by diffuse UV-vis, and particle size, measured by XRD, remain comparable for similar treatment, but the degree of agglomeration increases and the surface area subsequently decreases. For increased synthesis time, the band gap of cerium oxide falls off slowly from 3.35 eV for the first thirty minutes, then rapidly down to 3.15 eV until 50 minutes, at which point the band gap remains stable at 3.15 eV for up to 100 minutes, regardless of the amount of alcohol used, though solutions of 1:1 and 1:3 water to alcohol (by volume)

show a slower fall off. While in principle it is possible to measure the average particle size from the UV-vis spectrum using the relationship $\lambda_g = 1240/E_g$, where E_g is the band gap energy (eV), which is a function of particle size, and λ_g (nm) is the absorption of cerium oxide at the band gap energy,[39] a good understanding of the relationship between E_g and particle size is necessary first. While the work by Ivanov and coworkers has come the closest to developing a quantitative relationship between band gap and particle size, these results remain only qualitative in that no analytical relationship was developed, and it can only be said that generally λ_g will decrease with decreasing particle size. Instead, most groups simply rely on X-ray diffraction and use Scherrer broadening to determine the average particle size. As expected, increased annealing temperature results in larger crystal domains, and as determined by Scherer broadening, particles annealed beneath 300 °C are circa 5 nm large, but crystallite size increase in an exponential fashion between 300 °C and 700 °C from 5 nm to 20 nm, regardless of the alcohol content of the precursor solution. As particle size increases, the fractal dimensional exponent of the cerium oxide decreases falling slowly from 2.56 to 2.52 between 100 °C to 400 °C then increasingly faster from 2.52 to 2.35 between 400 °C and 700 °C, similar to size of the crystal domains, as determined by nitrogen absorption experiments and analyzed by the Neimark-Kiselev method.

The infrared spectrum of CeO_2 is similar to that of most metal oxides, and is shown in Figure 1.2 for CeO_2 octahedron, wires, and cubes. Hydroxyl modes are found between 4000 and 3500 cm^{-1}, with the peak at 3610 cm^{-1} attributed to hydroxyl groups associated with three cerium cations which are easily lost under hydrogen reduction

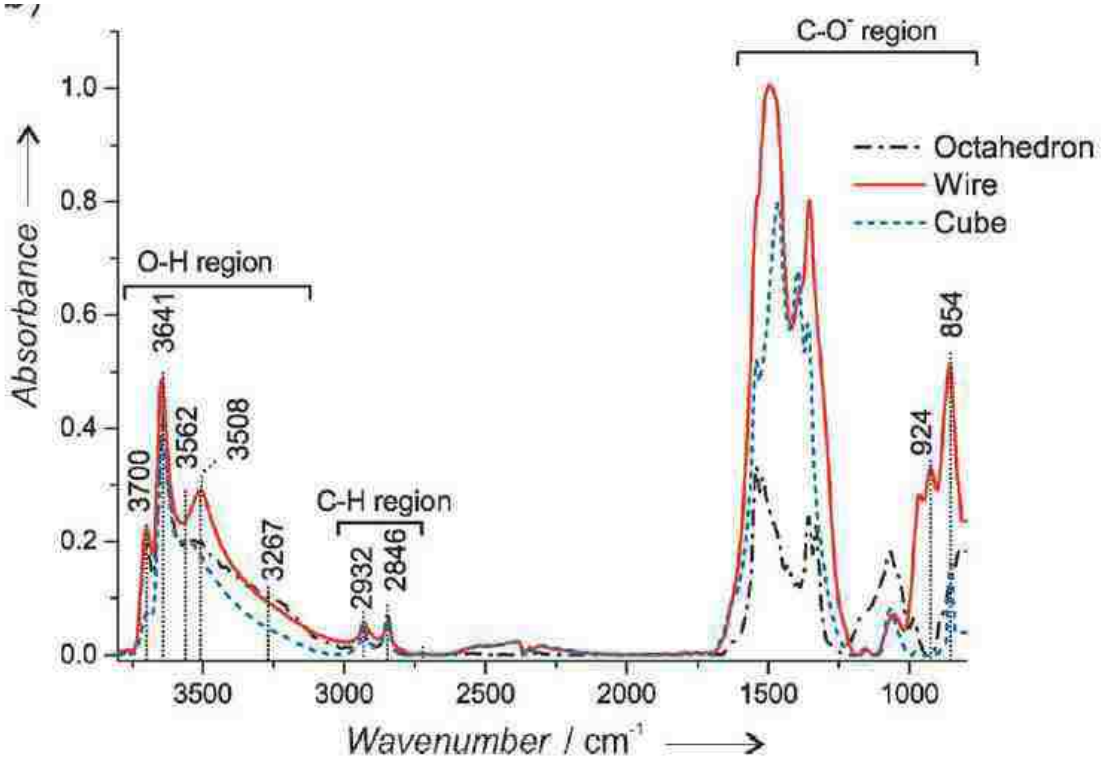

Figure 1.2 FTIR spectrum of pure CeO_2 octahedron, wires, and cubes.[40]

(OH-III), a peak at 3650 cm^{-1} (OH-IIA) and the associated shoulder at 3675 cm^{-1} (OH-IIB) assigned to geminal hydroxyl groups which can be lost on reaction with CO, a well-defined peak at 3710 cm^{-1} assigned to a unidentate hydroxyl groups (OH-I), and a broad peak centered at 3500 cm^{-1} attributed to oxyhydroxide impurities in pores.[22,30,41-44] Exposure to deuterium, D_2, does not cause H-D exchange with surface hydroxyl groups at or below 423 K, though above this temperature substitution with all but the oxyhydroxide impurities, whereby υ(OD) peaks appear at 2740 cm^{-1} (OD-I), 2696 cm^{-1} (OD-IIA), 2655 cm^{-1} (OD-III), and the OH-IIB hydroxyls are lost altogether due to their instability at these high temperatures.[44] Carbonate peaks appear as a series of 8 peaks, assigned as 1045, 1085, 1295, 1390, 1475, and 1585 cm^{-1}, with two shoulders at 1330 and 1560 cm^{-1}.[22] It is possible, either through the use of CO or reduction with H_2 at temperature greater than 623 K, to generate a well-defined absorption peak at circa 2120 cm^{-1} which cannot be produced on oxidized cerium oxide, and this peak has been attributed to ${}^2F_{5/2} \rightarrow {}^2F_{7/2}$ electronic transition, which is classically forbidden for an isolated Ce^{+3} cation but may be allowed via crystal field effects.[45]

The complementary technique of Raman spectroscopy has other information to offer as well. The Raman spectrum of CeO_2 has been used to quantify oxygen vacancies and the relationship between oxygen sub-stoichiometry and particle size has even been used to estimate particle size from the number oxygen vacancies.[15] A characteristic peak at 465 cm^{-1} is attributed to the F_{2g} lattice bending mode, which is consistent with a cubic phase.[20] The high frequency tail of the 465 cm^{-1} mode at 598 cm^{-1} is associated with oxygen vacancies.[40,46,47] A typical Raman spectrum for pure CeO_2 is shown in Figure 1.3. Raman has also been used to determine the relative concentration of cerium relative to

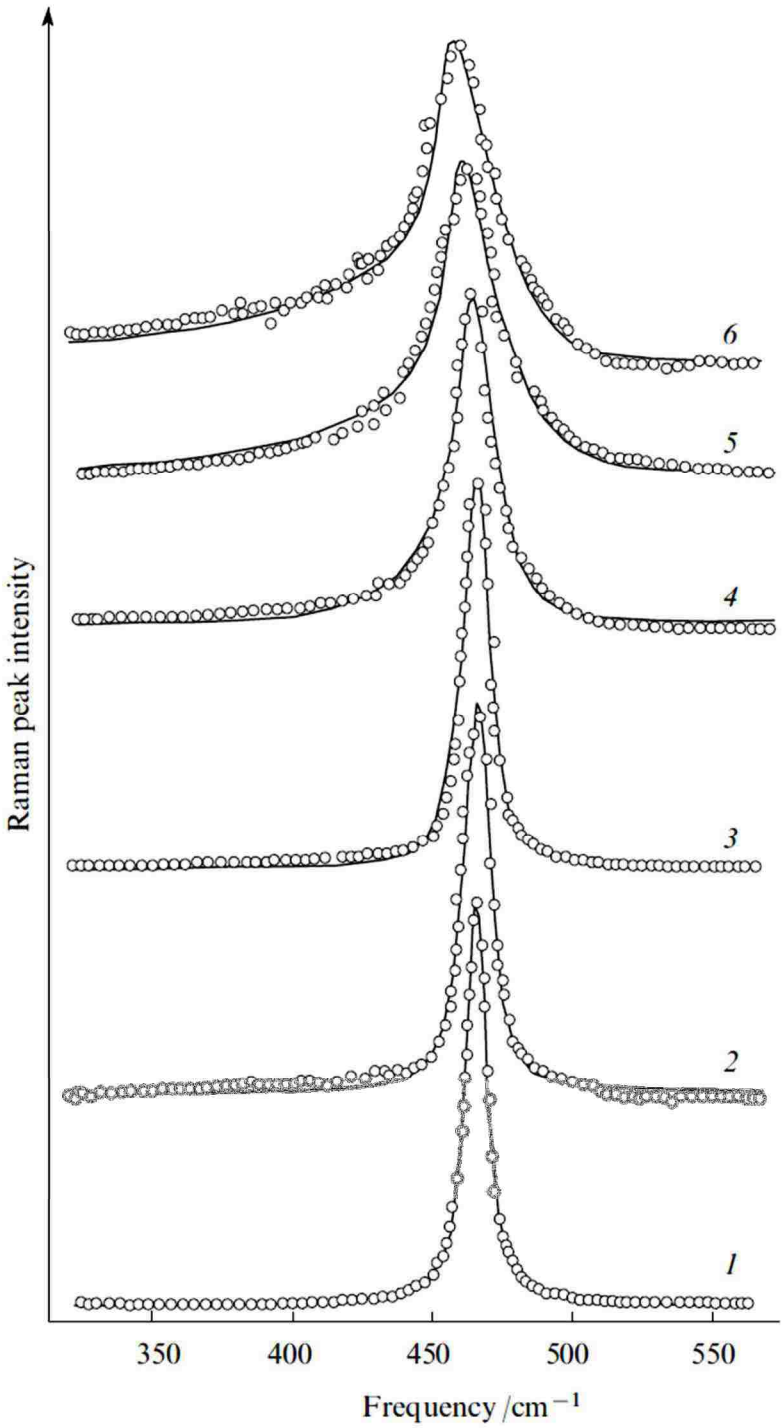

Figure 1.3 Raman spectrum of pure CeO_2 for different particle sizes; (1) single crystalline, (2) 150 nm, (3) 64 nm, (4) 20 nm, (5) 9 nm, and (6) 4 nm.[15]

dopants as a function of laser penetration.[48] When tetravalent dopants, such as samarium and gadolinium, are incorporated into cerium oxide, a peak emerges at 550 cm^{-1} which is attributed to the O^{-2} vacancies formed by these dopants.[49] Oxygen vacancies are believed to predominantly be responsible for the electrical conductivity of cerium oxide due to oxygen reduction during voltage biasing of the bulk metal oxide[50] as well as the linear dependence of conductivity on temperature, which is consistent with small polarons.[51] These vacancies may be increased through the use of trivalent cations and decreased through the use of higher valence cations such as vanadium.[16,52]

The generation and loss of vacancies by auto-reduction and the incorporation of dopants is described below using the Kröger-Vink notation, where Ce'_{Ce} refers to Ce^{+3}, Ce_{Ce} refers to Ce^{+4}, O_O refers to lattice oxygen, X_{Ce} refers to a metal cation neighboring a cerium atom, and $V_{\ddot{O}}$ refers to oxygen vacancies;

$$O_O + 2Ce_{Ce} \leftrightharpoons \frac{1}{2}O_{2(g)} + V_{\ddot{O}} + 2Ce'_{Ce} \quad (reduction\ of\ ceria)$$

$$Gd_2O_3 \leftrightharpoons 2Gd'_{Ce} + V_{\ddot{O}} + 3O_O\ (vacancies\ due\ to\ doping)$$

$$Nb_2O_5 \leftrightharpoons 2Nb_{Ce}^{\cdot} + 2e^-\ (free\ electron\ generation\ due\ to\ doping)$$

1.3 Sub-stoichiometry, Bulk Electrical and Ionic Conductivity

When platinum is deposited on CeO_2, it is possible to exchange $^{18}O_2$ with surface oxygen to isotopically enrich the surface,[31] and while the above reaction implies this should be possible without platinum, to the authors' knowledge this has never been verified experimentally except at high temperatures. Theoretical calculations have shown that the spontaneous evolution of oxygen from the (100) surface of cerium requires 6.58 eV for the bulk material, while the (111) and (110) surfaces require 2.71 eV and -0.47 eV, respectively, showing evolution from the (110) is spontaneous;[53] the authors go

further to state that the high barrier oxygen evolution discounts the possibility of CO oxidation being favorable without a catalyst, which would bolster the likelihood that without a supported metal catalyst or a dopant to increase surface oxygen lability, exchange of $^{18}O_2$ with surface oxygen cannot occur at an appreciable rate. It has, however, been verified using secondary ion mass spectrometry (SIMS) with ion etching that for yttrium doped cerium oxide that not only is the surface exchanged, but the dissociated oxygen diffuses into the bulk as well.[54] A survey of the literature reveals that while cerium oxide can promote redox reactions on its own and can gain or lose oxygen, this is only accomplished quickly at high temperatures or in the presence of a metal capable of dissociating oxygen. Moreover, while cerium oxide exhibits ionic conductivity, the lack of electronic conductivity can severely limit its catalytic capabilities in fuel cells.[55]

Much of the seminal work in understanding oxygen vacancy has stemmed from work by Blumenthal and coworkers, and has relied on relating the number of oxygen vacancies, x, for CeO_{2-x} to a power law of the partial pressure of oxygen, specifically $x \propto P_{O_2}^{-\frac{1}{n}}$.[56] For bulk cerium oxide, CeO_{2-x}, where x is less than 0.006 then n=5,[56] whereby only the value of the constant changes for doping.[16] For increasing oxygen vacancies, the value of n ranges between 5 to 2 for $0.006<x<0.1$,[16,57] and for very high oxygen vacancy density, where $0.1<x<0.3$, this power grows rapidly smaller to $P_{O_2}^{-\frac{1}{30}}$.[56] With regards for the effects of vacancies on lattice structure, for $x<0.1$ little effect is seen on the metal sub-lattice,[52] but for higher sub-stoichiometry, viz., $0.1<x<0.5$, deviation away from the traditional $F_{m\text{-}3m}$ crystal structure has been observed. For example, for low temperature $CeO_{1.804}$ to $CeO_{1.812}$,[17] rhombohedral symmetry was found, and for $CeO_{1.77}$,

it has been reported that a mixture of phases with composition $Ce_{11}O_{20}$ and Ce_7O_{12} dominate.[17] Using neutron scattering, it was determined that in this region, there is local defect ordering or clustering,[58] which is reasonable as the formation of a mixed CeO_2/Ce_2O_3 phase is more thermodynamically favorable than a sub-stoichiometric CeO_2 phase and the clustering of defects to attempt to generate the separate Ce_2O_3 phase is to be expected.[21] Moreover, oxygen vacancies cause cerium oxide to act an n-type semiconductor, with the extra lattice electron localized on cerium cations neighboring the oxygen vacancies,[53] explaining the affinity of CO and CO_2 for CeO_2, especially when it has been highly reduced, as both gases are electron acceptors.[43] In XRD studies by Tuller and Norwick,[46] it was shown that between $0<x<0.2$ and above 600 °C only the traditional FCC phase is found, but beneath this temperature a mixture of FCC and rhombohedral is possible. Extending to even higher numbers of oxygen vacancies, the phase diagram provided by Bevan[17] and Sørensen[59] shows that at $0.2<x<0.4$, pure phases are not observed, and generally a mixture of FCC is found with rhombohedral and BCC phases, until $0.4<x$, at which point the onset of a mixed phase containing hexagonal, and the BCC phases is seen.

The bulk electrical conductivity of cerium oxide has been known for some time,[16] and in general depends on the partial pressure of oxygen as $P_{O_2}^{\frac{1}{5.7}}$. However, there remains much confusion in the literature due to lack of distinction being drawn between electronic and ionic conductivities. Unless specified, conductivities and mobilities herein refer to bulk properties. Since the bulk electrical conductivity, σ, depends both on the number of vacancies as well as the actual mobility of the vacancies, the product of these two dependences can be characterized by an Arrhenius type relationship, as shown next,

$$\sigma = \sigma_0 e^{-\frac{Q}{RT}}$$

Limiting current experiments as a function of oxygen partial pressure have shown that the limiting current is a function the oxygen partial pressure,[60] so the observed electrical and ionic conductivities are a convolution of both the bulk lattice properties, as well as the availability of gas phase oxygen to create and recombine with these vacancies. Therefore electrical conductivity decreases with increasing temperature and decreasing oxygen partial pressure,[61,62] and above 1300 K is roughly the same for $0.00424<x<0.178$, with no hysteresis seen when heating or cooling the sample; however, beneath 1300 K, Q depends strongly on the oxygen vacancies and is generally larger for higher vacancy cerium oxide.[46,63] Moreover, the change in behavior at 1300 K splits the conductivity of cerium oxide into two regions – high temperature and low temperature – resulting in two separate values of Q and σ_0. For x=0.00424 to x=0.178, values for σ_0 and Q range from 1400 to 462 $ohm^{-1}*cm^{-1}$ and 0.59 eV to 0.47 eV for low temperature measurements, respectively, while for high temperature measurements these values range from 2.4 to 96.6 $ohm^{-1}*cm^{-1}$ and 0.22 to 0.37 eV, respectively.

Between 200 °C and 1300 °C cerium oxide acts like an n-type semiconductor via small polaron transport.[50,51] Pure cerium oxide is itself a poor ionic conductor, but on the addition of divalent and trivalent cations, this ionic conductivity increases greatly.[16] One mechanism for this increase is better conductivity at grain boundaries,[62] as well as increased ionic conductivity[64,65] and oxygen vacancy transport in the bulk.[66] Improvement in the ionic conductivity of cerium oxide follows a volcano plot based on the radius of the dopant cation, with ytterbium and lanthanum showing the least

improvement, and samarium being the best cation for improving the ionic conductivity of cerium oxide, with a dopant cation radius of 0.11 nm.[16]

Density functional theory (DFT) studies of cerium oxide have been carried out to better understanding the binding energy of the different faces, and how oxygen vacancies play a role both in ionic conductivity and the actual structure of the material.[67] Investigating the fully oxidized CeO_2 (111) face, Chen and coworkers found four possible adsorption configurations for diatomic oxygen – end-on, side-on, planar bridging, and non-planar bridging – shown in Figure 1.4. All structures showed only slight affinity for the surface, if any. However, when oxygen vacancies were introduced into the surface to mimic sub-stoichiometric cerium oxide, diatomic oxygen showed the strongest affinity for the oxygen vacancies, both for side-on and end-on attachment, as well as for the side-on binding with the Ce^{+3} sites; however, while all sites showed a favorable electronic energy change for binding diatomic energy, attachment to the cerium oxide cations showed the most electronically favorable change of all possible binding sites. From their studies, the authors were able to conclude that when oxygen absorbs to the surface of sub-stoichiometric cerium oxide, there are two pathways for oxygen dissociation. Either oxygen will participate in an absorption equilibrium (no dissociation), or will become incorporated into the surface. In the latter pathway, oxygen reduces to form the superoxo species, O_2^{-2}, before dissociating into $2O^-$. The O^- species can then combine with an oxygen vacancy and reduce to an O^{-2} species. The different configurations for oxygen incorporation into the lattice, as well as the associated transition states, were calculated and were shown to be close to those seen

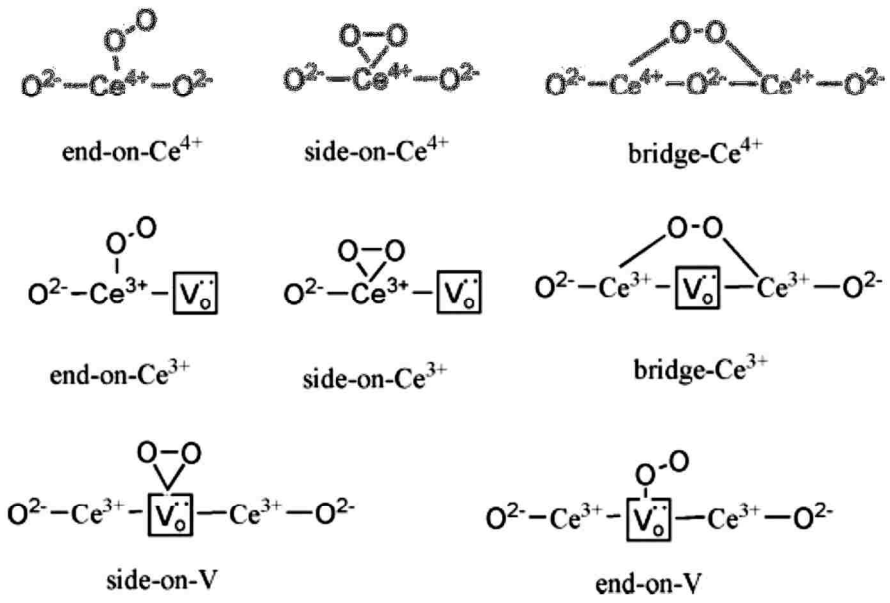

Figure 1.4 Different binding configurations for oxygen onto a sub-stoichiometric cerium oxide surface[67]

experimentally. Also, migration of oxygen vacancies were shown to have an activation barrier of 1.60 eV, which was close to the value of 1.54 eV seen experimentally.

1.4 Synthesis

There exist a myriad of methods for making pure and doped CeO_2, such as hydrothermal synthesis,[68,69] microemulsions,[70,71] surfactant-assisted precipitation,[32,33,72-77] and variations of spray pyrolysis,[78-81] which generally produce average particle sizes above 10 nm, or in the case of microemulsion, form only amorphous particles with a particle range between 2 and 11 nm. However, most groups follow the basic procedure of dissolving a Ce(III) precursor into water, then adding a base to precipitate out the metal oxide,[15,82] as precipitation is one of the few techniques with a unimodal particle size distribution under 10 nm. Figure 1.5 shows some of the different polymorphs of cerium oxide that can be obtained by the different synthetic routes.

To understand the mechanism of cerium oxide precipitation from solution, the behavior of cerium cations in solution must be understood. A Pourbaix diagram of cerium is provided in Figure 1.6,[83] which used the $HOCl_4/OCl_4^-$ to control pH; due to the lack of interaction of perchlorate and cerium, this system behaves much as the Ce-H_2O system. For cerium(IV) conversion to $Ce(OH)_n^{+(4-n)}$ is believed to be able to proceed through a stepwise procession of hydroxides from n=0 to n=4 (CeO_2 precipitation); equimolar concentrations of $Ce(OH)_n^{+(4-n)}$ and $Ce(OH)_{n+1}^{+(3-n)}$ are found for n=0 at pH=-0.7818, n=1 at pH=0.103, n=2 at pH=0.735, n=3 of pH=1.115, n=4 at a pH of 1.679, and a mixture of n=4 and CeO_2 at pH greater than 1.679. A similar trend is seen for cerium(III) conversion to $Ce(OH)_n^{+(3-n)}$; equimolar concentrations of $Ce(OH)_n^{+(3-n)}$ and $Ce(OH)_{n+1}^{+(2-n)}$ are found for n=0 at pH=8.4, n=1 at pH=9.2, and n=2 at pH=9.6, with the

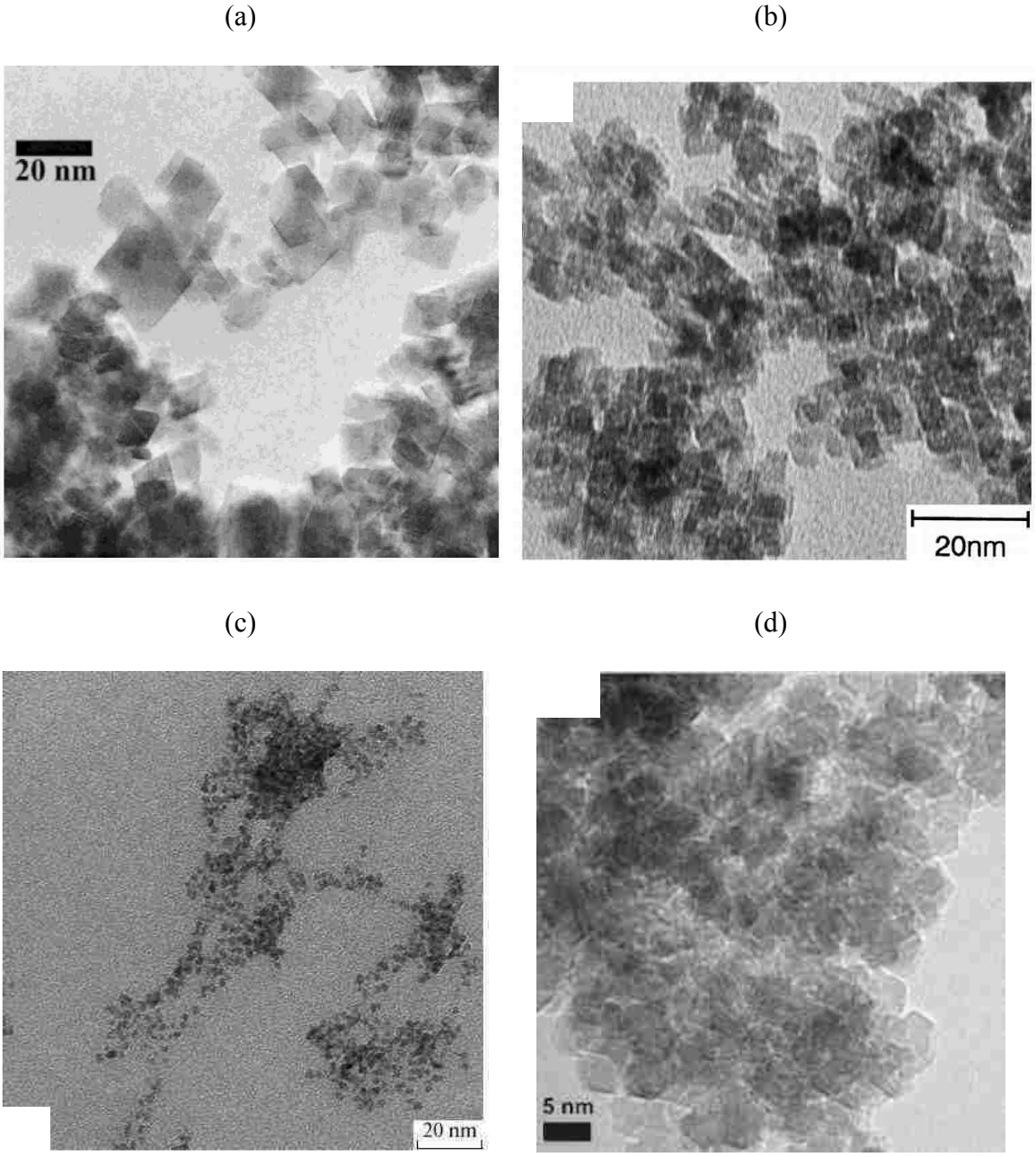

Figure 1.5 Examples of cerium oxide nanoparticles made by (a) flame-spray pyrolysis,[78] (b) hydrothermal synthesis,[69] (c) citrate sol-gel,[84] (d) and precipitation.[85]

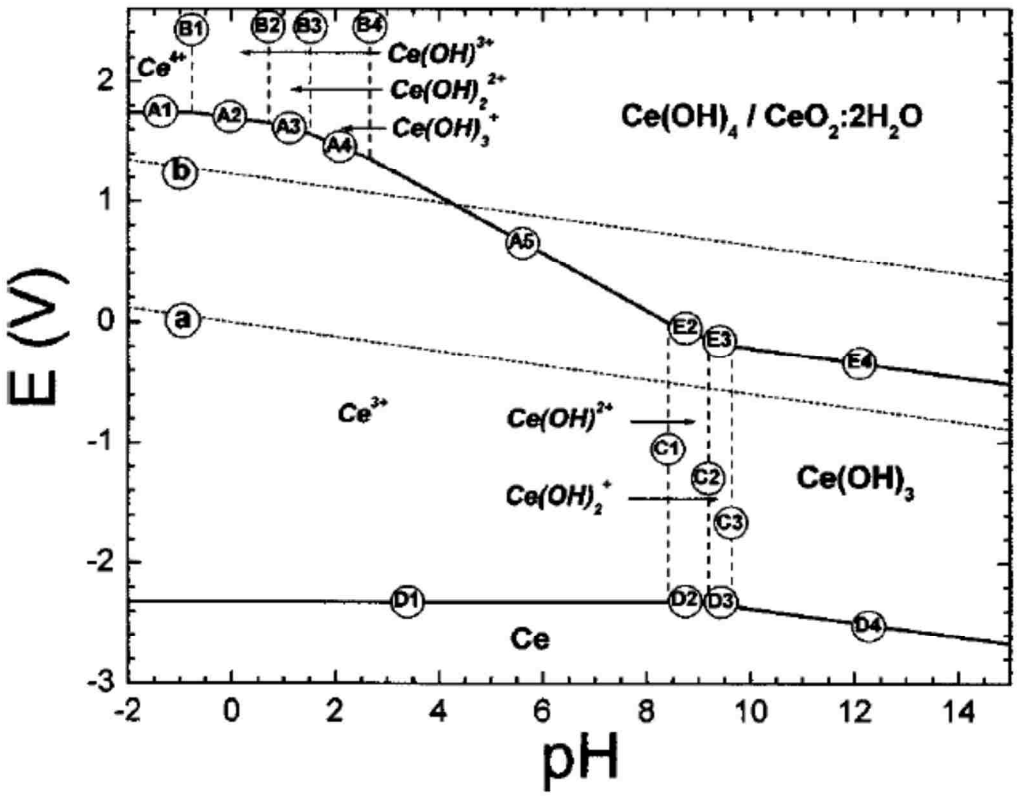

Figure 1.6 Pourbaix diagram for cerium.[83]

actual pH for the precipitation of $Ce(OH)_3$ not well defined. It is possible for Ce^{+3} to convert to Ce^{+4} at pH less than two, but this reaction requires a large external driving force, such as an electric potential, to drive the conversion.[86] Instead, between pH of 2.67 and 8.4, the conversion of Ce^{+3} to Ce^{+4} at proceeds by the following reaction (line (a), Figure 1.6)

$$Ce^{+3} + 4H_2O \rightarrow Ce(OH)_{4,aq} + 4H^+ + e^-$$

This potential for this reaction starts from 1.356 V at pH=2.67 and dropping to a potential of -0.003 V at pH=8.4. Above line (b), Figure 1.6, the concentration of Ce^{+3} is vanishingly small. At high pH, the reaction changes to an interaction of the cerium hydroxides with water to liberate H^+ and electrons, but as with the cation, the potential for this reaction becomes more and more negative as the pH is increased. This would imply that if an oxidizing agent, such as oxygen, is available to interact with the free electron, oxidation of cerium would be possible. This conclusion was supported by work by Hayes and coworkers who reported that the equilibrium between Ce^{+3} and Ce^{+4} obey the following relationship for pH<1,

$$\log\left(\frac{[Ce^{+3}]}{[Ce^{+4}]}\right) = pH + 8.69 - \frac{1}{4}\log p_{O_2}$$

At higher pH, this relationship is complicated by the onset of higher hydroxides of Ce^{+4}. However, even under argon, an equilibrium exists between Ce^{+3} and CeO_2 in solution, with the equilibrium shifted toward CeO_2 at higher oxygen partial pressure; the relationship is given as[87]

$$\log\left(\frac{[CeO_{2,(s)}]}{[Ce^{+3}]}\right) = -\log([Ce^{+3}]) = 3 * pH - 7.288 + \frac{1}{4}\log p_{O_2}$$

This shows that the onset of CeO_2 formation would be faster under more oxygen rich or basic conditions, and was indeed seen by Hayes and workers[83] as the onset of cerium oxide formation was seen earlier with solutions exposed to air versus those sparged with argon, though ultimately precipitation of a solid was seen at pH above 6, and the argon free precipitate was consistent with a highly oxygen deficient cerium oxide.

The addition of base drives the conversion of Ce(III) to Ce(IV) and subsequently drives the precipitation of Ce(IV) by conversion to the hydroxide form. Changes in the method of synthesis can be used to control the proportion of Ce(III) and Ce(IV), as well as the average crystallite size. For example, Scholes and coworkers investigated the effects of hydrogen peroxide on the crystal size and structure for cerium oxide nanoparticles made with cerium (III) chloride. From their studies, with the TEM results shown in Figure 1.7, a high peroxide concentration – 1:10 molar ratio of $CeCl_3$:H_2O_2 – creates the smallest nanoparticles, generating 1 nm particles versus the 5.4 nm nanoparticles made without any peroxide, but this is at the cost of increasing the amount of amorphous cerium oxide. A range of intermediate sizes was also produced by using intermediate concentrations of peroxide.[88] Because of the importance of the phase diagram of cerium in controlling the deposition of cerium, both as a film and nanoparticle, there are Pourbaix diagrams of cerium including the effects of H_2O_2,[83] which are complicated by reactions of cerium with hydrogen peroxide.

Niesz and Morse[89] reports the use of cerium (III) isopropoxide dissolved in 1-butanol, which generates a nanoparticle containing gel when sonicated in a double flask with 38 % $HCl_{(aq)}$ in the second flask; when dried, the gel produced ten times more nanoparticles than the standard precipitation method, and while the average particle size

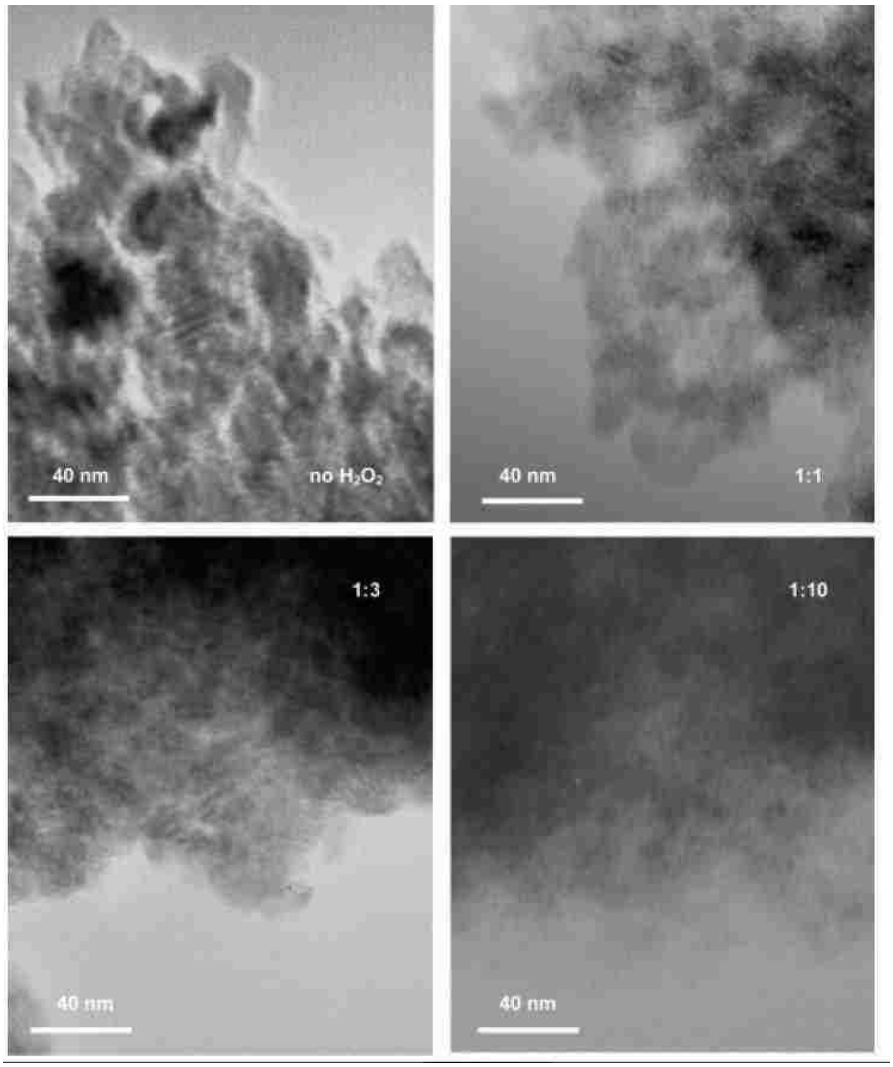

Figure 1.7 CeO_2 nanoparticles made with $CeCl_3$ and H_2O_2; the ratio of $CeCl_3$to H_2O_2 is shown in each figure.[88]

was 4.0 nm with particles as small as 3.4 nm and as large as 4.8 nm, the XRD pattern shows a large amorphous profile suggesting that the synthesis is not entirely clean. The final product had an increased Ce^{+3} concentration with a formula of $CeO_{1.89}$, which became stoichiometric when heated to 700 °C. When this process is modified to use cerium (III) nitrate and water, and aqueous ammonia is used in the second flask, controlled growth of cerium oxide nanocrystals can be obtained giving insight into the progress of crystal faces as the cerium oxide grows from amorphous small seeds to 10 nm particles.[85] Starting from the amorphous seeds, 1.8 nm spherical particles are transformed into truncated octahedral crystals between 2 nm and 10 nm, until ultimately the crystals become cubic. The progression of crystal growth over time is shown in Figure 1.8. As with most reports involving cerium oxide nanoparticle formed under strongly oxidizing conditions, the lattice parameter generally decreased for increasing particle size, eventually attaining a bulk lattice parameter of 0.541 nm. Additionally, diffuse UV-vis spectroscopy was used to measure the band gap of the material, and it was revealed that the band gap increased from 2.58 eV to 3.51 eV until the particles approached 10 nm, at which point the band gap decreased back to 3.34 eV, with the increase in bad gap at intermediate size explained by quantum confinement. The authors state that, although Sayle[90] and Conessa[21] cite the {100} face as being the least thermodynamically stable face, the low temperature synthesis essentially creates a kinetic product as opposed to the thermodynamic product. Torrente-Murciano, et al.,[91] attempted to map out a morphological phase diagram of cerium oxide as a function of temperature and of pH of synthesis using $Ce(NO_3)_3$ and NaOH in air, shown in Figure 1.9. Three poorly defined regions were found – agglomerated spherical particles,

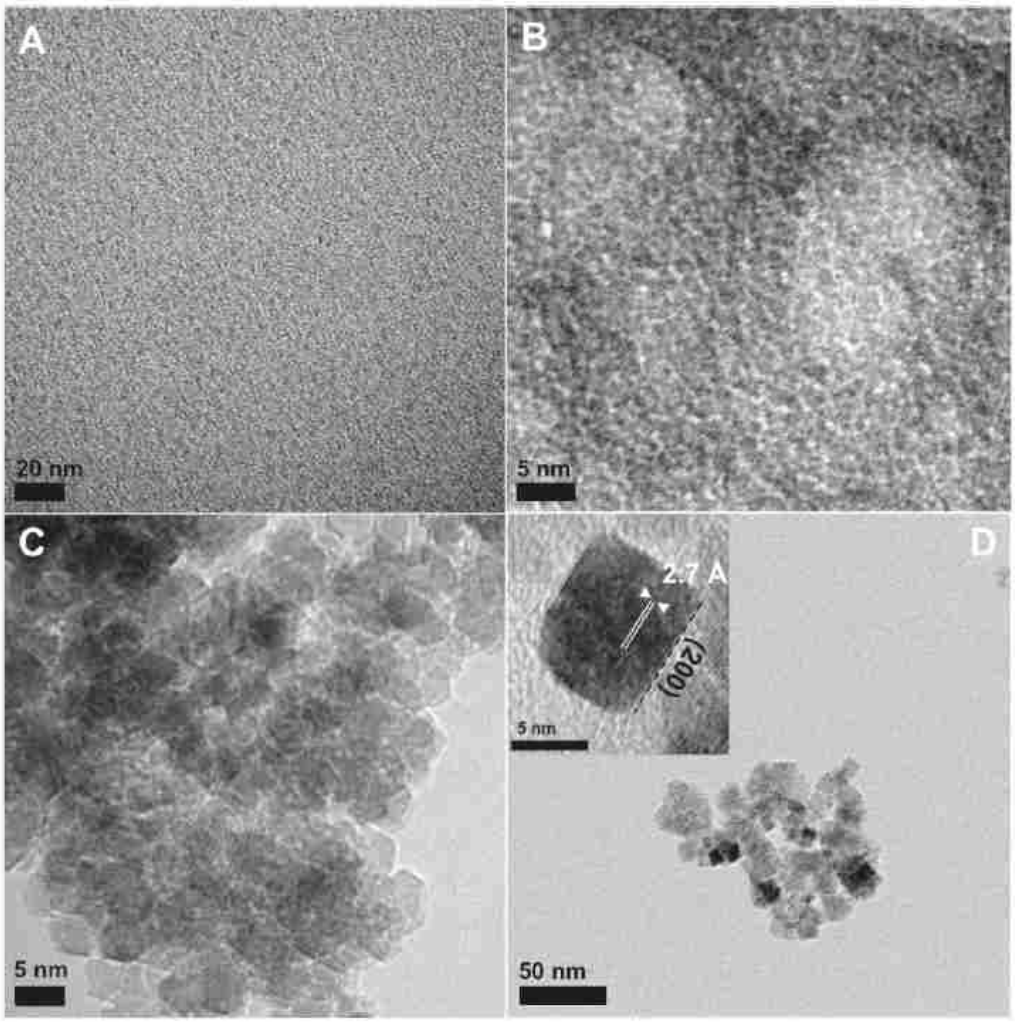

Figure 1.8 Evolution of cerium oxide nanoparticle growth from precipitation after (a) 3 min, (b) 6 min, (c) 20 min, and (d) 5 hours.[85]

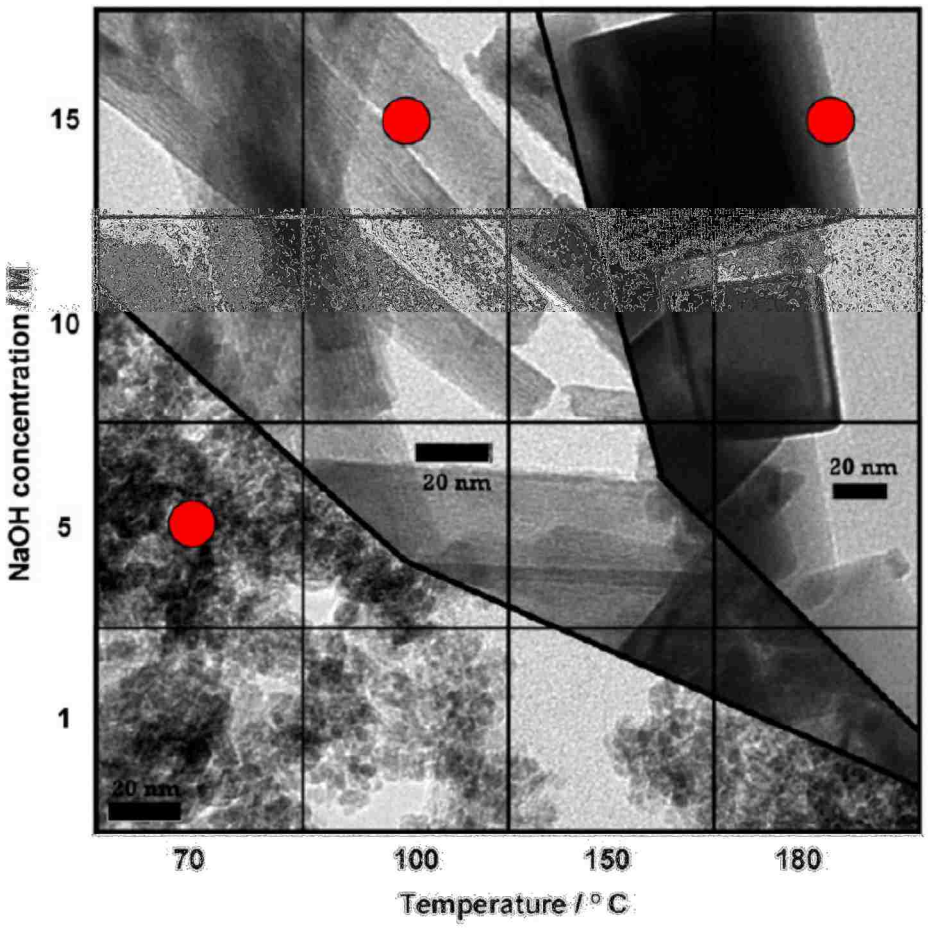

Figure 1.9 Morphology diagram for cerium oxide synthesis using $Ce(NO_3)_3$ and NaOH in air.[91] Red dots indicate the representative samples used in the catalytic testing of these materials by Torrente-Murciano and coworkers.

nanorods, and nanocubes. At the intersection of two different morphologies, a mixture of the two phases is found; however, the nanotubes phase separates the cubic and spherical particle phase, so that a mixture of spherical nanoparticles and cubes was never found.

Dutiful choice of synthesis has been used to create tetrahedral and octahedral particles,[92] nanorods,[93-96] nanoplates,[2] sunflower-like microspheres,[97,98] nanospheres,[99,100] and nanocubes,[40,101] and while some methods of preparation rely on precipitation,[102-104] more complicated structures such as cubes, nanorods, and nanotubes require more sophisticated procedures to obtain morphologically pure products, though delineation between spheres and very small tetrahedra and octahedra is not clear except for particles larger than 10 nm as spheres are thought to be formed from the agglomeration of cubes.[100] Images of these reported structures are shown in Figure 1.10. Most synthesis has focused on increasing the proportion of {100} faces, since this is the most catalytically active face.[105] From simulations, the {111} facet is the most stable, followed by {110}, and finally {100}, the least stable facet; the {211} face is expected to restructure to the {111} facet at room temperature, and the {210} and {310} facets are expected to be too unstable to exist for long times.[21,90]

Formation of spheres, cubes, and nanowires require only the use of soft templating agents such as surfactants or solvents with affinities for particular cerium oxide facets. The mechanism of sphere formation from cerium(III) nitrate using polyvinylpyrrolidone (PVP) was investigated by Zhang, et al.,[100] who determined that the onset of spheres occurs only in the presence of a capping or surfactant agent, which prevents particle agglomeration during nanoparticle growth but also serves as a template for sphere formation. Furthermore, the choice of solvent is critical in determining what

(a) (b)

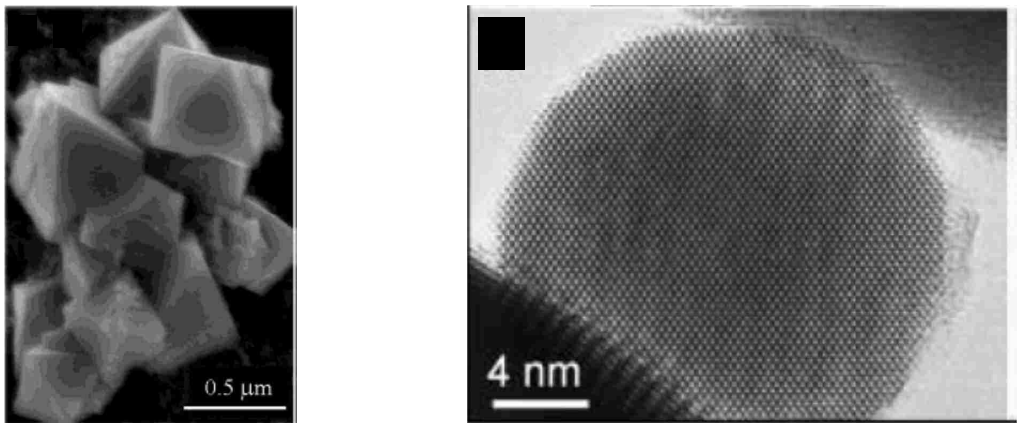

(c) (d)

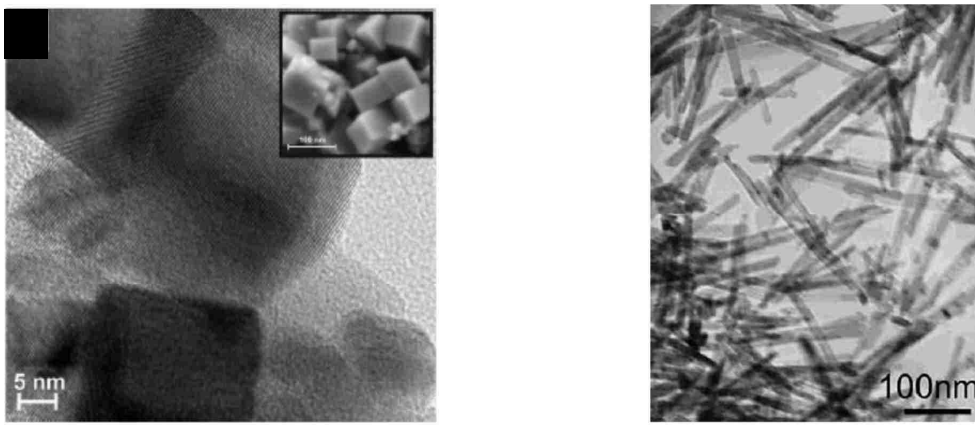

Figure 1.10 Different cerium oxide shapes as reported in the literature. (a) Octahedral,[92] (b) sphere,[99] (c) cube,[40] and (d) rod.[93]

final morphology is recovered; pure water gave both spheres and cubes, whereas pure diethylene glycol gives nanowires formed from bridging nanospheres. In fact, the effect of solvent in the formation of different morphologies has been widely reported. In general, formation of cubes occurs as an initial phase of cerium oxide growth from aqueous solution, and solvents which form reverse micelles around cerium oxide result in cubes if interparticle interactions are blocked, or spheres if the particles are allowed to agglomerate within the reverse micelle. Surfactants and solvents which slow particle growth but allow selective interaction of only certain planes cause agglomeration of particles to form nanorods, by allowing individual cubes or spheres to fuse end to end.[96,104,106-110]

For example, synthesis of cerium oxide nanorods shows an increased exposure of {100} and {111} planes for the higher oxygen vacancy nanorods, whereas the lower oxygen vacancy nanorods predominantly expose the {100} and {110} planes.[18] Octahedrals can be formed by sintering of tetrahedral particles, with the tetrahedrals exposing both the {100} and {111} planes while the subsequently formed octahedral particles lose their {100} facets, which are joined at the {111} and {200} faces.[92] However, it is questionable if TEM is actually capable of imaging vacancies and it is possible and more likely that the observed vacancies are really voids in the nanorods. CrystalMaker© models of the catalytically relevant faces are shown in Figure 1.11; the {100} face exposes only cerium cations forming a polar surface so that the opposing face exposes oxygen atoms, whereas the {111} face exposes both cerium and oxygen ions.

Ligands can also serve as oxidizers converting the Ce^{+3} precursor to a Ce^{+4} cation.[86] Oleic acid (OLA) has been used to control the morphology of the growing

{100} {111}

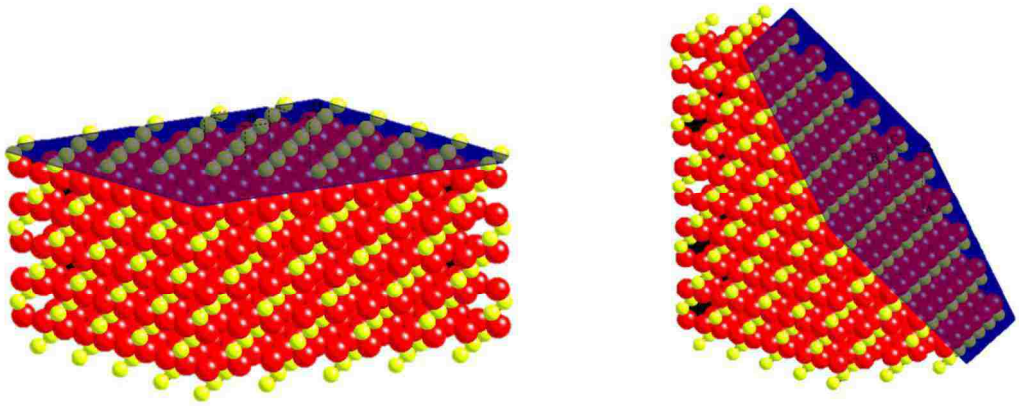

Figure 1.11 Images of the cerium oxide {100} and {111} faces.

cerium oxide nanoparticles because it preferentially absorbs to the {200} and thus favors {111} plane growth.[105,111-113] From earlier studies by Dang and workers, the band gap of the cubes is 3.15 eV, versus 3.35 eV for the polyhedral nanoparticles, even though both sets of nanoparticles had an average particle size of circa 4.2 nm.[105] Additionally, from the same study Dang was able to show that for increasing OLA, more cubic nanoparticles, the concentration of Ce^{+3} also increased on the surface. In the 2011 study by the same group,[112] the OLA ligand was further investigated to show that increasing the temperature of synthesis from 160 °C to 220 °C narrowed the particle size distribution at the cost of increasing the average particle size. Moreover, complicated monolayers and bilayers of CeO_2 nanocubes were made by adding OLA to the nanocube dispersions after nucleation and using the evaporation of solvent to cast a thin membrane of the particles. Orientation of the particles in the film was dictated by the facets with the largest surface area. The effect of time on crystal size and morphology is shown in Figure 1.12.

In their study, Cordeiro found that an OLA:Ce^{+3} molar precursor ratio of 4:1 produced octahedral nanoparticles, while an 8:1 ratio produced cubes, even though both types of nanoparticles had an average particle size of 5.2-5.2 nm. When nanoparticles were removed from solution during the early steps of nucleation and observed using HRTEM, cubes with high degrees of concavity on the {200} faces, which were not observed when the reaction was allowed proceed for long times. The reaction was allowed to proceed for longer and when observed using HRTEM, the cubes were shown not to be perfect cubes, but cubes whose edges had been replaced with {220} faces and corners replaced by {111} faces, and the faces of the cube were concave, not flat. The octahedral particles, when observed under HRTEM, showed only {200} and {111} faces.

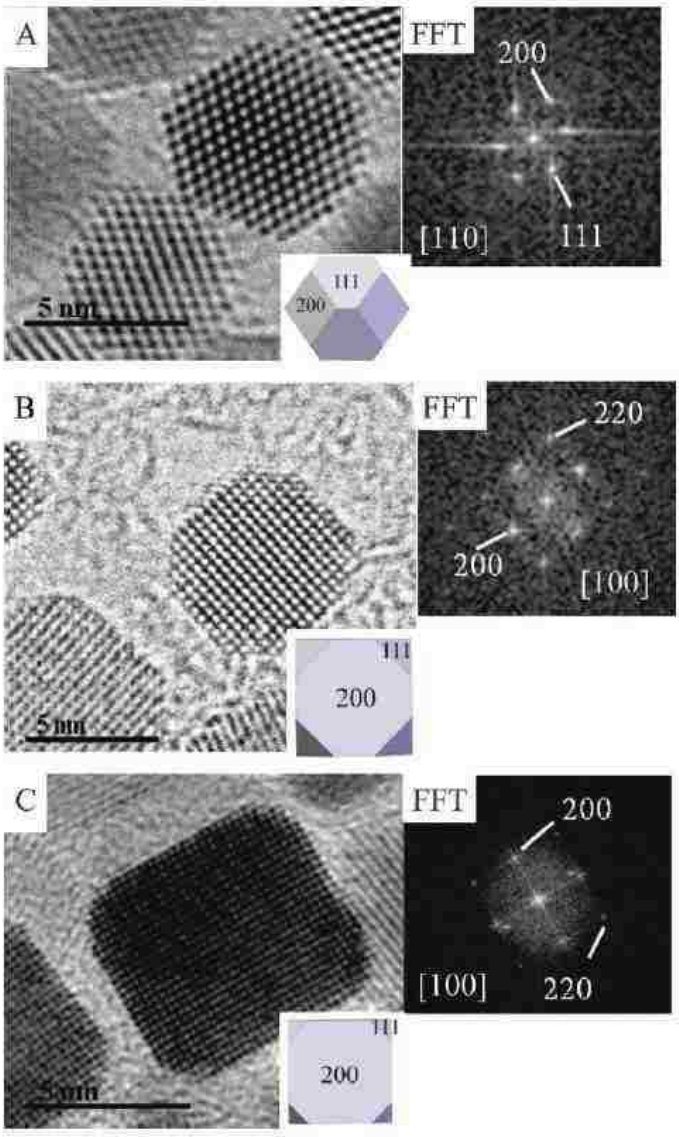

Figure 1.12 Effects of time for synthesizing cerium oxide using and OLA:Ce ratio of 8:1 at 180 °C: (a) 24 hours, (b) 36 hours, and (c) 48 hours.[105]

Cordeiro and coworkers have suggested two models for the growth of Cerium oxide cubes using OLA; growth of individual cubes, and the growth of larger cubes from the agglomeration of smaller cubes, since initial nucleation products that were investigated with HRTEM also saw small nanocubes. This view was supported by Yang and Gao,[113] who has attributed the growth as proceeding from the enlargement of individual cubes and agglomeration due to the presence of small, unbound cubes during the initial onset of nucleation, as well as the presence of grain defects in the final cubes, consistent with particle agglomeration.

In order to form cerium oxide nanotubes hard templating agents are required, which must be removed after synthesis. Wang, et al.,[114] have synthesized mesoporous cerium oxide nanotubes using ZnO nanorods as the starting template; $Ce(NO_3)_3$ solution was used to precipitate CeO_2 onto the surface of NaOH-treated ZnO nanorods, then was washed and

annealed at 500 °C before washing in 5 % HNO_3 solution, which removed the ZnO core. X-ray diffraction of the nanotubes showed a pure fluorite diffraction pattern, and HRTEM images show that the thickness of the cerium oxide walls of the nanotubes is circa 5-10 nm. Nitrogen absorption on these nanorods show that the nanotubes have an inner diameter range between 2 and 30 nm, with most tubes having an inner diameter of less than 20 nm. Deconvolution of the Ce 3d XPS spectrum of the nanorods showed that the synthesized nanorods were 34 % Ce^{+3}, though no work on the catalytic activity of these materials was reported. Templating with the triblock copolymer, poly(ethylene oxide)-b-poly(propylene oxide)-b-poly(ethylene oxide) (PEO-PPO-PEO) with the surfactant P123 has been used, with the effects of synthesis conditions worked out by Lu

and coworkers;[94] from their study, it was determined that P123 is necessary for the onset of nanotubes as only spherical particles are obtained without it, with higher temperatures increasing the length of the synthesized nanotubes, though little is reported on the physical characteristics of these nanorods. Hydrothermal synthesis can also be used to synthesize cerium oxide nanorods using a precipitation method, and much like the P123 synthesis, forms nanorods through agglomeration of the individual spherical particles; nanoparticles dispersed in a water-ethanol mixture were heated to 180 °C in an autoclave for 24 hours, then heat treated at 80 °C in air for 6 hours to obtain a mixture of both nanoparticles and nanorods.[95] Zhang, et al.,[115,116] synthesized CeO_2 nanotubes over carbon nanotubes using $(NH_4)_2Ce(NO_3)_6$, $Ce(NO_3)_6$, ethylene glycol, ethanol, and dimethylformamide (DMF). By XRD, it was verified that the final product was both a cubic CeO_2 phase and a carbon nanotube phase. From HRTEM images of the final product, it was concluded that the growth mechanism of the nanotubes was the same as for nanorods when using ethylene glycol, assembly of cerium oxide spheres. Furthermore, when ethylene glycol was omitted from the synthesis, the final product changed from a nanotube to agglomerations of nanospheres, in agreement with their proposed mechanism of nanotube formation.[117] When the agglomerates were allowed to encircle the nanotube and were subsequently calcined, donut shaped cerium oxide nanoparticles were recovered.[118] While there exist other examples of hard templating, the examples provided illustrate both the advantages and disadvantages of this technique, specifically the difficulty of removing the templating compound and the complexity of the synthesis required.

1.5 Lattice Parameter

There has been considerable debate on the lattice parameter of cerium oxide, specifically the expansion or contraction of the lattice as cerium oxide particles approach the nanoparticle regime. For bulk cerium, the lattice constant is 5.41134 Å with a thermal expansion coefficient of $11.0*10^{-6}$ K^{-1} are room temperature, $11.5*10^{-6}$ from room temperature to 773 K, and $12.1*10^{-6}$ K^{-1} from room temperature to 1273 K.[16] A much more detailed discussion of the effect of temperature and lattice vacancy is given by Mogensen, et al.[16] However, for cerium oxide nanoparticles it has been demonstrated that an expansion for particle sizes less than 10 nm is commonly observed,[119-122] whereby the decrease in the number of Ce^{+4} surface sites and the subsequent increase in Ce^{+3} surface sites for decreasing particle size[12,13] acts as an impetus for decreased surface tension and therefore larger lattice constants.[123] Another proposal for these contractions has included the formation of surface hydrogen peroxide species on the inner surfaces of the Cerium oxides.[124] However, there are other reports which have shown that only contraction is observed, and that only through nanoparticle stabilization, viz., through the use of micelles, can the observed lattice expansion be seen,[125,126] similar to lattice expansion for PVP-capped palladium nanoparticles[127] or palladium nanoparticles deposited *in vacuo*.[128,129] For smaller and smaller nanoparticles, the increased surface tension is expected to drive contraction of the nanoparticle lattice constant,[130,131] as has been seen with silver,[132,133] palladium,[134] platinum,[135] and gold nanoparticles,[136,137] as well as a contraction in the unit cell volume for anatase nanoparticles.[138] This trend, however, is not universal for all nanoparticles, as copper has been shown to have little to

no lattice contraction for smaller nanoparticle sizes due to the low surface tension,[135] and MgO, TiC, and α-Fe_2O_3 have been shown to have lattice expansion.[139]

Authors citing a lattice contraction have generally run their syntheses under strongly reducing conditions, that is to say, under conditions with large amounts of carbon but with a very low oxygen partial pressure. This may seem counter intuitive, as very few syntheses are run under an inert atmosphere as argon or helium, but as these syntheses are generally carried out in water and the partial pressure of dissolved oxygen in water is very low, the syntheses are essentially run in an environment with a very low partial pressure of oxygen and the high concentration of carbon compounds in solution can interfere with cerium interaction with oxidizing agents such as nitrates. Since cerium oxide can act as a combustion catalyst,[126] it is also conceivable that during calcination the conversion of organic side products into CO_2 is associated with the conversion of Ce(III) sites to Ce(IV) sites from the heat of combustion under an oxygen containing atmosphere, thereby generating smaller surface cations and therefore causing lattice contraction. Syntheses reporting lattice expansion[140] have all relied on strongly reducing conditions, such as the use of large concentrations of nitrate anions, facilitating the formation of Ce(III) sites and thus reducing the surface tension due to the surface cation. This is true regardless if cubes, nanoparticles, or nanorods are made.[18,93] This is alluded to in the work by Karakoti, et al., who observed that their organic ligands contributed to the conversion of Ce^{+3} cations to Ce^{+4} cations in solution.[86] Therefore, while the literature consensus has been towards lattice expansion of cerium oxide,[15] there exist reports of lattice contraction under low oxygen reaction conditions from multiple groups as well.

It should be emphasized the of all the papers discussing the effect of synthesis on lattice parameter and surface oxidation state suffer from a poverty in acknowledging the complexity of the local environment on cerium oxidation. While the Pourbaix diagram of cerium has been well established through carefully controlled experimental conditions, the same care has not been taken in reports of cerium oxide synthesis; very little effort has been made to control the partial pressure of oxygen in solution, or maintaining the oxygen and water content during particle firing. Because the concentration of spectator ions can affect the concentration of dissolved gases as well as local pH, it is very difficult to say exactly what the environment of cerium cations is during drying steps. For dry syntheses, this is very little control exercised in reproducibly heating cerium oxide precursors under the same synthesis gas, and the effect of combustion products is not clear, such as those formed from removing ion exchange resins. Whether the water produced during combustion interacts with growing cerium oxide nanoparticles and what this effect is has not been clearly established. As such, reproducibility between different reports on cerium oxide synthesis is difficulty due to the strong dependence on subtleties of the synthesis conditions. Furthermore, the actual nucleation and growth of cerium oxide nanoparticles either from solution or by dry methods remains very unclear and only qualitative trends in the final oxidation state and lattice parameters can be drawn.

1.6 Cerium Oxidation State

As the oxidation state of cerium is commonly discussed in papers discussing the activity of cerium oxide, it is important to clarify the methods used to determine the oxidation of cerium in cerium oxide, the current level of understanding of these techniques, and what consensus has been reached on nomenclature.

Commonly x-ray photoelectron spectroscopy (XPS) is used for determining the oxidation state of cerium cations in the cerium oxide lattice. Furthermore, the Ce 3d edge is most commonly used for analysis, and is broken into two regions; Ce $3d_{3/2}$ and Ce $3d_{5/2}$. However, care must be taken with such studies; reduction can also occur if Ar-ion bombardment is used,[141,142] but it is possible to reduce cerium oxide under x-ray irradiation, though no significant loss is seen for the first ten minutes.[15] Work looking at the effects of varying how the XPS spectrum of cerium is fit using the standard convention for peak assignments has shown that regardless of the method of fitting, ultimately only two species can be seen in the CeO_2 photoelectron spectrum, the +3 and +4 cations,[143] viz., no intermediate oxidation states or species, such as $Ce(OH)_x$. Though deconvolution of the cerium 3d edge was understood as early as the mid-1970s, deconvolution of the Ce 3d edge was inconsistent so there are occasionally papers which use incorrect deconvolution. Theoretical work published by Kotani, et al.[144] and Burroughs, et al.,[145] are the seminal papers for understanding the deconvolution of the Ce 3d transitions; these papers clarified the structure of the Ce 3d absorption edge by solving the Schrodinger wave equation for a cerium cation and showing, based on oxidation state, which f orbitals were accessible for shake-up transitions. Consensus exists now in the literature on both the nature of the Ce 3d edge and the naming of these transitions.[146,147] For the Ce^{+3} cation, only one shake up peak is observed for the 3/2 (u-type) and 5/2 (v-type) transitions, corresponding to excitation of the $3d^{10}4f^{1}$ ground state to the $3d^{9}4f^{2}V^{n-1}$ (v^{0},u^{0}) and $3d^{9}4f^{1}V^{n}$ (v',u') final states, where V is the valence band. Furthermore, for the Ce^{+4} cation, there are two shake up transitions observed corresponding to excitations from the $3d^{10}4f^{0}$ to the $3d^{9}4f^{2}V^{n-2}$ (v,u), $3d^{9}4f^{1}V^{n-1}$ (v'',u''), and $3d^{9}4f^{0}V^{n}$ (v''',u''') final

states.[148] Figure 1.13 shows the correct peak deconvolution and labeling of the different transitions. The accepted percentage of Ce^{+3} cations is given as[140]

$$A_{Ce^{+3}} = A_{v_0} + A_{v'} + A_{u_0} + A_{u'}$$

$$A_{Ce^{+4}} = A_v + A_{v''} + A_{v'''} + A_u + A_{u''} + A_{u'''}$$

$$\%\, Ce^{+3} = \frac{A_{Ce^{+3}}}{A_{Ce^{+3}} + A_{Ce^{+4}}}$$

Where A_i refers to the area of the particular transition. Accepted values for peak positions are shown in Table 1.1,[149] as well as full width at half-max (FWHM) from the literature, to serve as a guide for reasonable values for the different transitions. It should be noted that there are no accepted ranges for the FWHM values and that there is some variation from the binding energies reported for the transitions, so the values reported are only a guide, though variations in other papers can be found.[6,49,150-152] When the angle between the sample and the detector is varied for CeO_2 films sputtered onto a platinum substrate, no change in the Ce^{+3} concentration is found, suggesting that for the (111) cerium oxide films, the concentration of Ce^{+3} in the bulk versus the surface is the same within the detection depth of XPS. However, when heated under vacuum or exposed to a strongly reducing environment, a substantial increase in Ce^{+3} concentration is seen for decreasing sampling depth, indicating that the increase of Ce^{+3} in bulk cerium oxide under these conditions is localized to the surface only.[148]

Unlike the Ce 3d components, assignments of the O 1s components have not reached a consensus in the literature.[150] Authors have commonly assigned peaks at 531 and 529 eV to oxygen atoms associated with Ce^{+3} and Ce^{+4},[14,153] respectively, and a further assignment is made to the peak at 533 eV to the $Ce(OH)_x$ groups due to its onset upon water exposure to cerium oxide,[152,154] whereby the oxidation state of the cerium

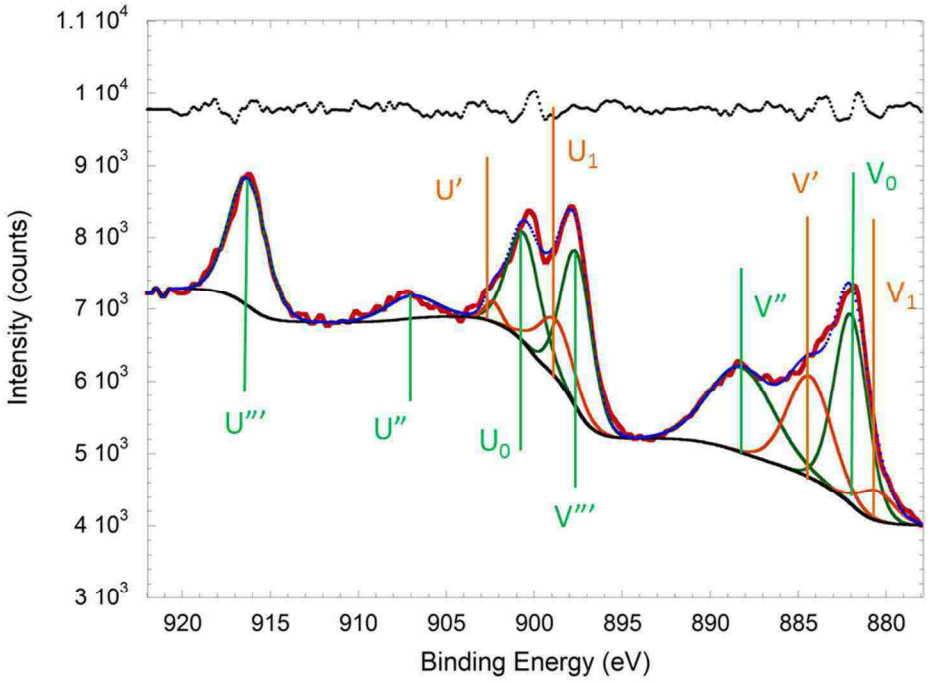

Figure 1.13 Ce 3d XPS spectrum for a 4.83 nm cerium oxide nanoparticle. The correct peak assignments are illustrated, with Ce^{+4} transitions in green and Ce^{+3} transitions in orange. The raw data is in red, the total fit in blue, and the residual fit shown in black above the spectrum.

Table 1.1 Accepted values for peak position and full width at half max (FWHM) for the different transitions in the XPS spectrum of cerium.[149]

	Ce^{+3}				Ce^{+4}					
	V_0	**V'**	**U_0**	**U'**	**V**	**V''**	**V'''**	**U**	**U''**	**U'''**
Binding Energy (eV)	882.3	884.8	901.0	903.5	880.1	888.8	898.2	898.8	907.4	916.7
FWHM (eV)	2.1	3.5	2.7	3.4	2.0	5.0	2.4	2.9	4.4	2.7

bound to the hydroxyls remains ambiguous. Other groups have simply assigned a peak at 529 eV to lattice oxygen and the other peak at 531 eV to non-lattice oxygen.[34,49,151,155] Comparison to the O 1s spectrum for Ce_2O_3 shows a similar peak at circa 531 eV,[14] and there is also an increase in the ratio of the 531 eV to the 529 eV transition as cerium oxide is heated under vacuum;[156] both observations could be used to justify the assignment to

Ce^{+3}-O^{-2} sites , but as non-lattice oxygen would be expected to associate with the surface prevalent Ce^{+3} sites, the shifts for the Ce_2O_3 and CeO_2 O 1s are not exactly the same, and the loss of oxygen is expected to be associated with a loss in lattice oxygen, there is an ambiguity in this assignment. Grazing incidence XPS has been used to justify the assignment of this transition to non-lattice species,[155] but as the increase in Ce^{+3} is associated with surface sites, this again makes the assignment of the peak ambiguous. Investigators justifying either assignment have primarily relied on the increase in surface Ce^{+3} sites as evidence for correct assignments. As cerium oxide nanoparticles become smaller, there is an increase in the fraction of Ce^{+3} sites as well as an increase in the intensity of the transition at 531 eV. While this would be justification for assigning the transition at 531 eV to Ce^{+3}-O^{-2} sites, this increase is also associated with an increase in the number of non-lattice or surface oxygen atoms due to the increasing surface to volume ratio, also justifying the assignment of the transition at 531 eV to non-lattice oxygen. As such, it is not possible to definitely state which assignment is correct. Complicating this analysis is the onset of photoemission from other oxygen species, such as hydroxides, phosphates, and carbonates, which lie in a similar range,[157] which is not always included in these studies.

X-ray absorption spectroscopy (XAS) has also been used in evaluating the oxidation of cerium. The near-edge region of the XAS spectrum (XANES) of the L_{III} edge of cerium contains four peaks, shown in Figure 1.14. The first peak, A, at circa 5.74 corresponds to a Ce^{+4} atom, which corresponds to an excitation of a 2p electron to the 5d shell with no electron in the 4f electron. A second peak, B, at circa 5.735 eV corresponds to another Ce^{+4} species, which also corresponds to an excitation of a 2p electron to the 5d shell, but in this case there is an electron in the 4f orbital due to excitation from the oxygen 2p shell. The onset of a shoulder, C, at circa 5.727 eV corresponds to a Ce^{+3} site, and a small peak, D, at circa 5.72 eV corresponds to a pre-edge feature due to the dipole forbidden $2p_{3/2} \rightarrow 4f$ transition.[140,158,159] Examination of the XANES region has mostly been used qualitatively, though some groups have attempted peak deconvolution.[140] As XAS is a bulk technique, combined with XPS analysis it provides a way to determine the difference between surface composition (XPS) and bulk composition (XAS). However, due to the qualitative nature of the XANES analysis, we cannot gain any understanding of the differences between bulk and surface composition.

As stated earlier, the decrease in the number of Ce^{+4} surface sites and the subsequent increase in Ce^{+3} surface sites with decreasing particle size[12,13,15] acts as an impetus for decreased surface tension and therefore larger lattice constants.[123] Moreover, as the nanoparticle size is decreased there is an increase in the proportion of Ce^{+3} sites when lattice expansion is seen. However, no XPS data has been published to date on the effect of Ce^{+3} concentration for lattice contraction, which would help elucidate the role of Ce^{+3} in expanding the nanoparticle lattice.

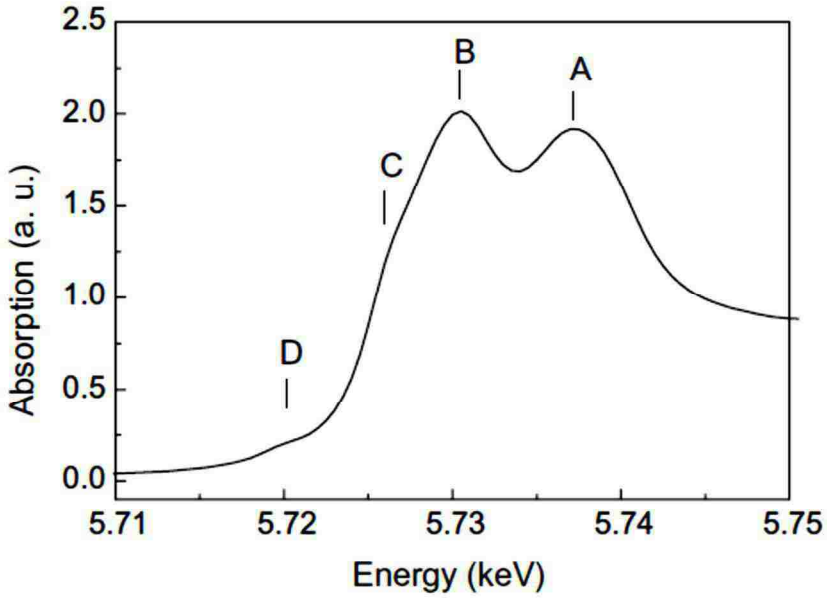

Figure 1.14 Cerium XANES spectrum from an XAS measurement.[140]

Shown in Figure 1.15, high resolution TEM paired with electron energy loss spectroscopy (EELS) of the Ce $M_{4,5}$ transition to determine the oxidation state of cerium as a function of particle size.[160] For 4 nm particles minimal Ce^{+4} was found on the surface, but for larger particles, such as 30 nm crystals, appreciable concentrations of Ce^{+4} was found on the surface, specifically on the faces of the crystals. However, Ce^{+3} surface concentration was highest near crystal edges, directly verifying paired XPS-XRD claims that as particle size decreases the surface concentration of Ce^{+3} increases. The depth of the Ce^{+3} shell on these materials, using STEM-EELS, was determined to be 1-2 atomic layers for the {111} planes but as deep as 6 atomic planes for the {200} planes. These results also verified theoretical and positron annihilation studies suggesting that Ce^{+3} sites cluster, and even went as far to show that they preferentially cluster on the edges and corners of cerium oxide and that most of the Ce^{+3} is indeed formed at the surface.

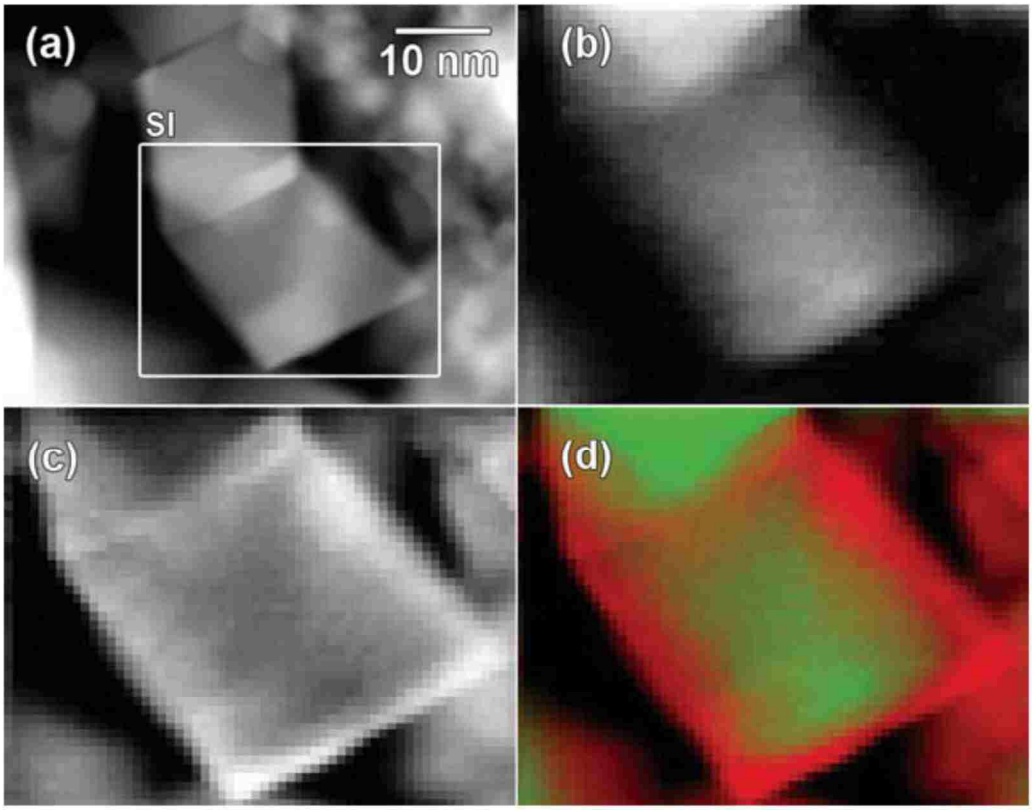

Figure 1.15 Low magnification surface reduction mapping of CeO_2 nanoparticles.[160] (a) HAADF-STEM survey image showing the scanned particles, (b) Ce^{+4} map, (c) Ce^{+3} map, (d) color map with Ce^{+3} (red) and Ce^{+4} (green).

It should be noted that the above generalizations apply only to tetrahedral or octahedral shaped particles, and while many attempts have been made to increase the number of surface Ce^{+3} sites by changing the morphology of the synthesized cerium oxide, it is difficult to find studies which directly compare Ce^{+3} surface concentration between different particle morphologies. Nanorods for instance, with surface concentrations of up to 23 at% Ce^{+3} have been report,[3] have a Ce^{+3} concentration which is not much higher than as seen with bulk cerium oxide, and from their work it cannot be determined if the increase in catalytic activity of the nanorods over cerium oxide powders is due to the increase Ce^{+3} surface concentration or due to an increase in the number of known catalytically active faces. When cerium oxides of comparable characteristic lengths, such as nanotube diameter of cube length, are compared, it can be qualitatively seen that there is more Ce^{+3} contribution in the nanorod spectra versus cubes and spheres,[91,102,161] so there is at least indirect proof of Hua and coworkers' claim found elsewhere in the literature, and positron annihilation spectroscopy has gone further to also show that the Ce^{+3} sites typically agglomerate.[3] While a separate Ce_2O_3 phase would also be consistent with these results, there are no Ce_2O_3 phases visible in any TEM images[3,91,102] or XRD spectra.[161] Revoy and coworkers[162] have claimed that cerium oxide nanocubes do not show an increase in surface Ce^{+3} concentration, but that the observed increase in Ce^{+3} concentration is an artifact of auto-reduction under XPS irradiation, and that instead smaller cerium oxide cubes are easier to reduce but under atmospheric conditions have the same surface oxidation state as larger cubes, which would explain why cubes and spheres are occasionally reported as having the same surface concentration of Ce^{+3}.[91]

1.7 Common Reactions and Applications

Cerium oxide has been used as a catalyst and as a catalyst promoter. Both these uses are attributed to cerium oxide's ability to reversibly dissociate diatomic oxygen[163] even in the presence of CO,[164] specifically the formation of superoxide species – O_2^- and O_2^{-2} – which are generally characterized using electron paramagnetic resonance, Raman, and FTIR spectroscopies.[165] An excellent review of cerium oxide's uses as an automotive catalyst was summarized in a 1996 review by Trovarelli, but focuses more on the use of cerium oxide and metals supported on cerium oxide for the elimination of SO_x, NO_x, and other automotive specific reactions.[166] Presented here is a simple list of the most common uses of cerium oxide in catalysis in an effort to give a more complete picture of the capabilities and versatility of the material. Much of the reactivity of cerium oxide is attributed to the surface Ce^{+3} sites,[167] hence the desire for smaller cerium nanoparticles, but bulk cerium oxide has also been used to catalyze several reactions.

1.7.1 Use as an Electrode

Cerium oxide has also been used as a fuel cell electrode on account of the lability of surface oxygen,[126] and due to its ionic conductivity at room temperature has been proposed as an alternative to ytrria-stabilized zirconia (YSZ) since YSZ requires much higher operating temperatures to achieve good electrical conductivity.[67,168] Generally Ni-doped YSZ has been used for SOFC stacks, but for intermediate temperature SOFCs, it has become common practice to replace YSZ with pure and doped cerium oxides.[169] Lower operating temperatures for solid oxide fuel cells (SOFCs) would imply high Nernst voltages and allow the use of cheaper electrodes and construction materials,[169] so the interest in cerium oxide as an SOFC electrode is of true commercial interest. An

SEM image of cerium oxide nanoparticles impregnated into a Ni-YSZ SOFC after exposure to H_2S is shown in Figure 1.16.

Excellent work by Ai, et al.,[170] showed the effect of adding cerium oxide and gadolinium doped cerium oxide (GDC) nanoparticle to platinum counter electrodes prior to application to a YSZ barrier layer. When cerium oxide and GDC are incorporated into platinum electrodes at only 6 wt.% incorporation, the over-potential of the electrodes decreases substantially and reproducibly from a maximum of -0.55 V (Pt) to -0.32 V (CeO_2) and -0.15 V (GDC) at a current density of 0.30 A/cm^{-2}. Moreover, impedance spectroscopy shows nearly an order of magnitude decrease in the resistance to oxygen transport for platinum when CeO_2 and GDC are incorporated into the electrode layer at 800 °C. However, the activation energy, E_a, for oxygen dissociation and diffusion on cerium oxide was determined to be 251 kJ/mol for CeO_2 versus 182 kJ/mol for GDC, suggesting that pure cerium oxide is not the best option for this system. Addition of cerium oxide nanoparticles to SOFCs has also been shown to improve sulfur tolerance.[171]

In reality pure cerium oxide not only suffers from decreased conductivity versus doped cerium oxide, but also suffers from poor mechanical stability under anode conditions, as the material quickly becomes sub-stoichiometric, driving the need for modifications which impart better conductivity and mechanical stability.[172] To overcome this problem, the addition of dopants has been used,[173-175] such as zirconium, yttrium, gadolinium, samarium, [176] and praseodymium,[177] and the choice of dopants is aimed at decreasing the dissociation energy of the dopant and the associated oxygen vancancy.[178]

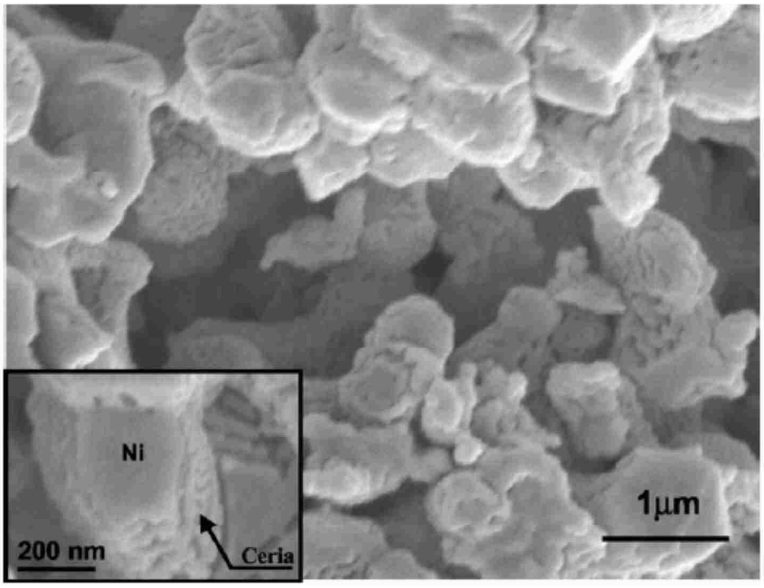

Figure 1.16 Cerium oxide nanoparticles impregnated into a Ni-YSZ SOFC after exposure to H_2S.[171]

Gadolinium has been shown to be better at increasing the ionic conductivity of cerium oxide than samarium and yttrium at similar dopant concentration; furthermore, when 10 mol% gadolinium is added to the cerium oxide lattice, the dissociation energy of gadolinium-oxygen vacancy pairs is only 0.13 eV at 400 °C.[169] At 20 % gadolinium doping, the electrical conductivity decreases, suggesting that there is an optimal gadolinium doping concentration. Praseodymium doped electrodes have also shown increased conductivity over pure cerium oxide, which is comparable to gadolinium,[179] and like gadolinium doped cerium oxide, praseodymium doped cerium oxide shows an increase in electrical conductivity at very low oxygen partial pressures ($< 10^{-16}$ atm), which is desirable for anode applications.[180] Furthermore, conductivity measurements conducted with analysis of impedance spectra show that the ionic conductivity is not affected by the thickness of the cerium film measured but rather its surface area, showing that the improved conductivity is due to oxygen transport across the surface and not with bulk transport.[179] When decorated with platinum, praseodymium doped cerium oxide electrodes also show improved promotion of the oxygen reduction reaction (ORR) and better inhibition of Pt-OH species.[177] Finally, samarium doping has been shown to have total conductivities one to two orders of magnitude better than pure cerium oxide.[181] In general, the addition of rare earths to cerium oxide is desirable as not only do these dopants increase the conductivity, but also increase the thermal conductivity making these materials more compatible with the Fe-Cr alloys used in the stack assembly. Moreover, because the rare earth doped cerium oxide have higher electrode compatibility than YSZ,[176] and conductivity of YSZ is not as good as the conductivity of comparably doped gadolinium-cerium oxide and samarium-cerium oxide,[182] yttria stabilized cerium

oxide (YSC) has also been developed. From SEM images, it is clear that less sintering occurs when yttria is incorporated into cerium oxide.[183] A wealth of trinary and quaternary mixtures of metal cations have been attempted as well to improve the conductivity over a range of temperatures, with a few of the more thorough papers cited here,[184-187] but are outside the scope of this review; the reader is encouraged to follow the review by Steele.

For low temperature, polymer membrane direct methanol fuel cells (DMFCs), the decomposition of methanol by platinum is believed to be improved by oxygen donation from the cerium lattice to platinum.[188] While the oxidation of methanol and ethanol can be performed using pure CeO_2 electrodes, their performance is 10 times less than that of electrodes decorated with platinum.[163] Furthermore, because of its ability to convert CO to CO_2, cerium oxide has also been used as an electrode for direct methanol fuel cells to eliminate CO produced during methanol oxidation, which can poison the platinum-ruthenium catalyst.[189] Pt and Pt/Au supported on cerium oxide have been used as oxidation catalysts in DMFCs. Relative to platinum, platinum particles dispersed over gold particles with a 1:2 ratio of Pt:Au have shown better oxidation current than Pt particles supported on CeO_2, with this improvement being attributed to morphology changes in the platinum itself and not due an alloy of gold and platinum, with the pure gold electrodes showing no activity at all,[190] which may be attributed to the poor electrical conductivity of cerium oxide.[55]

1.7.2 CO and NO Oxidation

Common in the literature is the use of cerium oxide for the catalytic conversion of CO to CO_2 with air, specifically in the use as a three-way automotive catalyst.[18,191]

While gold nanoparticles supported on CeO_2 are capable of performing this reaction,[8] cerium itself is also capable of CO oxidation. When cerium oxide spheres are used to catalyze CO oxidation, generally smaller particles are more catalytically active than larger particles, with rods showing the best activity.[82] Cerium oxide nanorods have been reported to have a higher activity for CO oxidation than cerium oxide nanoparticles because it has a higher proportion of oxygen vacancy clusters, as shown by TEM, and is attributed to the increased exposure of {100} and {110} planes for the higher oxygen vacancy nanorods, whereas the lower oxygen vacancy nanorods predominantly expose the {100} and {110} planes.[3,18,94] However, cerium oxide polyhedra synthesized using a hydrogen-mediated thermal plasma treatment have also shown improved performance over spherical nanoparticles as well, also due to the increase in the number of {200} and {220} planes.[81] This has been verified independently by Wang, et al.,[49] who compared the catalytic activity of cerium oxide powders, cubes, and nanorods, and found the nanofibers to demonstrate the best CO conversion at lower temperature. Wang and coworkers found that their structures were predominantly Ce^{+4}, and that like Liu and coworkers, the {100} faces were more exposed on the cubes and the nanorods exposed more of the {110} and {100} faces. Wang also investigated the effects of 10% cation doping of samarium and gadolinium on both the structure and catalyst activity of their nanostructures, and while the dopants only increased the lattice parameter of the cubic lattice and had little effect on the catalytic activity of cerium , the light-off temperature for the CO oxidation reaction over the nanofiber was found to be 605 K versus 644 K for the cerium oxide nanocube, and 623 K and 650 K for the samarium and gadolinium doped cubes, respectively. , Wang used the lack of Sm_2O_3 and Gd_2O_3 Raman lattice

modes as evidence that the samarium and gadolinium were incorporated into the lattice and did not form a separate phase. While the gadolinium doped nanocubes showed a higher concentration of oxygen vacancies, it showed worse performance than pure cerium oxide; conversely, the samarium doped nanocubes, which had more oxygen vacancies than pure cerium oxide but less than gadolinium doped cerium, showed the best performance. The samarium doped nanocubes, which had more oxygen vacancies than pure cerium oxide but less than gadolinium doped cerium, showed the best performance while the gadolinium doped nanocubes showed worse performance than pure cerium oxide despite having a higher concentration of oxygen vacancies. The authors questioned the relevance of the number of oxygen vacancies and instead they proposed that it is only one of many factors that affect the performance of cerium oxide as a CO oxidation catalyst. This is also illustrated by the performance of the nanocubes versus the nanorods; while the nanocubes have {100} exposed faces with better access to bulk oxygen vacancies, their performance is worse than that of nanorods.

Cerium oxide has been used as a support for gold nanoparticles in the conversion of CO to CO_2. When supported on different polymorphs of cerium oxide, the shape of the support cerium oxide has been shown to a strong role in determining the oxidation state for the support gold atoms, as determined by XPS; for rods gold is found only in the +1 and +3 oxidation state, with cubes having a preponderance of +0 oxidation states, and polyhedra having some +0 gold but mostly +1 and +3 oxidation states, with +1 being favored over the +3 oxidation state for all supported gold particles.[8] As the average gold nanoparticle size was between 2-5 nm, it is reasonable to assume that the shift in oxidation state of gold is due to nanoparticle-support interactions, as the particles are near

the Debye length. In studies of Au nanoparticles supported on spherical cerium oxide nanoparticles, samples annealed at temperatures between 150 °C and 400 °C showed substantially higher Ce^{+3} concentration over regular cerium oxide – 12.9% versus 0.5% at 150 °C and 77.7% versus 84.8 % - but showed similar Ce^{+3} concentration beneath 150 °C and at 500 °C.[24] From H_2-TPR, this same study showed that no hydrogen is absorbed onto Au NPs supported on gold cubes, and rods showing larger hydrogen uptake and stronger absorption than polyhedron cerium oxide.

Supported rhodium nanoparticles on cerium oxide can be used as an NO reduction catalyst, and it can be paired with CO oxidation to produce N_2 and CO_2, creating a three way catalyst.[19] TPR studies have shown a strong desorption at circa 1150 °C, but the performance of the supported rhodium is improved when zirconium oxide is incorporated into the cerium oxide. When manganese is incorporated into cerium, low temperature conversion (90 °C) of NO without CO can obtained, particularly when the manganese constitutes 40 % of the metal cations in the nanoparticles; this work was performed with $CeMnO_x$ nanoparticles supported on carbon nanotubes, and shows substantial improvement in low temperature conversion over the bulk metal oxide analogous.[192]

1.7.3 Peroxide Decomposition and Radical Scavenging

Because of the reversibility of its oxidation state, cerium oxide has also found use as a free radical scavenger and peroxide decomposer, specifically cerium cations and cerium oxide nanopowders. Due to the detrimental effects of peroxide and free radical formation inside hydrogen fuel cells, several papers in the fuel cell literature has appeared demonstrating the improved performance of fuel cells when cerium oxide is incorporated into the catalyst layer or into the membrane itself.[193] Both cerium cations[194] as well as

cerium oxide powders[1] have been used. Generally only up to 2 wt.% cerium or cerium oxide incorporation into the membrane or catalyst layer is used. The incorporation of both the cations and commercially available powders has proven beneficial in reducing membrane degradation. While cerium oxide is only a moderate peroxide decomposer, the Ce^{+4} sites which are responsible for peroxide decomposition are paired with Ce^{+3} sites which can facilitate radical scavenging. The mechanism for cerium cation decomposition of peroxide,

$$Ce^{+4} + H_2O_2 \xrightarrow{K_1} Ce^{+3} + HOO\cdot + H^+$$

$$Ce^{+4} + HOO\cdot \xrightarrow{K_2} + Ce^{+3} + O_2 + H^+$$

$$Ce^{+3} + HOO\cdot + H^+ \xrightarrow{K_{-1}} Ce^{+4} + H_2O_2$$

This mechanism was originally proposed by Baer and Stein, but using kinetic isotope effects using ^{144}Ce, Sigler and Masters were able to first verify the presence of the reverse reaction.[195] EPR studies have shown that only the peroxy-radical is present, that is to say, there are no hydrogen or hydroxyl radicals.[196] Rough values for k_1 and k_2/k_{-1} have been determined using ESR measurements, and while the value for k_2 cannot be determined directly from the measurement, the value for k_{-1} has been considered small, suggesting that k_2 is much less than k_1.[197] It should be noted that these results are only under highly acidic conditions, pH of 1.5 or less, and is only in reference to the free cation, not the oxide. The radical trap, 5,5-dimethylpyrroline-N-oxide (DMPO), was incorporated into hydrogen fuel cells during normal operation and the ESR signal was measured over time.[198] The onset of the OH·-radical was seen when no cerium was present, but when cerium cations were incorporated, a clear onset of peroxy-radical was observed. However, this analysis is complicated by the possible onset of peroxy-radical

formation by hydroxyl radical reaction with platinum.[199] So far, there have been no reports of the mechanism of peroxide decomposition over cerium oxide, but Karakoti has stated that it would not be unreasonable to make parallels between the homogenous and heterogeneous decomposition of peroxide with cerium.[13]

Under alkaline conditions, the cerium(III) cation decomposes peroxide, but not catalytically, and forms cerium oxide by the following mechanism,[88]

$$Ce^{+3} + H_2O_2 + 2OH^- \rightarrow CeO_2(OH)_2 + 2H^+$$

$$CeO_2(OH)_2 \rightarrow CeO_2 + \frac{1}{2}O_2 + H_2O$$

However, Karakoti and coworkers have shown that actually sub-stoichiometric cerium oxide is found when the above reaction is carried out, with a higher preponderance of Ce^{+3} in the cerium oxide, the concentration of which depends strongly on pH and has a complicated interaction with the water present.[13] The review presented by Karakoti gives a much better perspective on the use of cerium cations and cerium oxide nanoparticles with regards to biological applications, and the reader is encouraged to follow their references for a more in depth study, as well as the review by Ivanov.[15] Unfortunately the size dependence of Ce^{+3} concentration on particle size, and how changing this composition by varying particle size affects the activity and selectivity of cerium oxide has not been reported in the literature. As many mechanisms involving cerium oxide rely on the interplay of Ce^{+3} and Ce^{+4} on the surface, having surface cerium cations with an oxidation state fixed by the particle radius and not the environment could complicate the analysis.

As cerium oxide is capable of decomposing hydrogen peroxide, as well as serving as a solid electrode, the reverse two-electron transfer to oxygen to form peroxide has also

been investigated, with both supported cerium oxide[200] and cerium oxide supported palladium catalysts investigated.[201] While theoretical work has suggested that elevated temperatures could increase the generation of hydrogen peroxide from superoxide species on the surface of cerium oxide,[165] the few reports of synthesis of peroxide from cerium oxide have all required electrochemistry to promote the formation of hydrogen peroxide. For carbon supported cerium oxide, sub-stoichiometric cerium oxide was found for low loadings (4 wt.%) of cerium oxide and was shown to give better performance than pure CeO_2 which was found for high loadings (12 wt.%), though the best results obtained with the 4 wt.% sample were comparable to the peroxide generation from Vulcan carbon.[200] Using a supported palladium catalyst, hydrogen peroxide generation was larger for cerium oxide supported palladium than for alumina, iron (III) oxide, titania, and carbon with the same weight loadings of palladium; moreover, when gold was incorporated into the system, an increase in hydrogen peroxide generation was seen for all supports other than cerium oxide, for which a loss in activity was seen suggesting that the synergy between gold and palladium is not seen for cerium oxide.[201]

Supported gold, palladium and gold-palladium nanoparticles have been used in the synthesis of hydrogen peroxide from H_2 and O_2 in an effort to provide an alternative to the current anthraquinone process,[201] with palladium nanoparticles showing better activity over Au and Au-Pd catalysts even when the catalyst was reused. Ntainjua, et al., tested the effects of various supports on the activity of palladium nanoparticles, extending their study to Fe_2O_3, Al_2O_3, TiO_2, and carbon, and showed that cerium oxide is the best promoter for the palladium nanoparticles. However, this was not true for Au-Pd

nanoparticles, for which carbon was best at promoting the formation of hydrogen peroxide, particularly when the carbon received an acid treatment prior to use.[202]

1.7.4 Water Gas Shift (WGS) Reaction

The water gas shift reaction is given as

$$CO + H_2O \leftrightarrows CO_2 + H_2 \qquad \Delta H = -40\ kJ/mol$$

In an attempt to simplify the current use of a two-step system, specifically the high temperature shift (350-500 °C) over Fe_2O_3/Cr_2O_3 followed by the low temperature shift (200-250 °C) over $Cu/ZnO/Al_2O_3$, the use of a simplified Pt/CeO_2 catalyst has been proposed.[23,203] Of great importance is the complete conversion of CO to CO_2 to prevent poisoning of downstream systems using the H_2 generated by this reaction. When using platinum supported on cerium oxide, the reaction macroscopically obeys the following rate expression,[22]

$$r = \frac{k_1 k_2 P_{CO} P_{H_2O}}{k_1 P_{CO} + k_2 P_{H_2O}}$$

Where k_1 has an activation barrier of 19.2 kJ/mole and k_2 has an activation barrier of 30.2 kJ/mole.[25] Atomistically, dissociation of water onto the surface is believed to be catalyzed by defect Ce^{+3} surface sites,[23] and begin the process of forming formate intermediates on the surface. However, the addition of platinum to the surface of cerium oxide does affect the surface properties of cerium oxide; when platinum is added to the surface of spherical cerium oxide nanoparticles, an increase in the Ce^{+3} surface concentration is seen for annealing between 200 °C and 400 °C – 2.0 % versus 0.5 % at 200 °C and 23.8 % versus 15.2 % at 400 ° - with comparable surface Ce^{+3} concentration seen outside this range.[24] It should be noted, however, that the change in the Ce^{+3} concentration is not necessarily related to the catalytic activity – Pt/CeO_2 materials

showing high oxygen storage capacity show the least conversion, whereas materials with lower oxygen storage capacity show better conversion,[31] which does not directly correlate to Ce^{+3} concentration.

To better understand the WGS reaction, several studies have been conducted using both excesses of water and CO, as well as intermediate concentrations. When CO is dosed onto a Pt/CeO_2 WGS, more CO is consumed than comparable Pt/TiO_2 and Pt/ZrO_2, and on a subsequent dose of H_2O, both CO_2 and hydrogen are formed in quantities substantially larger than the other two platinum-support pairings. These separate dosing were used to break up the WGS into its two intermediate reactions, and investigate the effectiveness of each platinum-support pairing in catalyzing the WGS shift reaction. By comparing the products formed by the different pulses, the authors were able to conclude that when platinum is supported on cerium oxide, the reaction proceed through a associative mechanism, whereby formate is formed as an intermediate, and not by a classical redox reaction or the associated mechanism paired with a redox reaction, but were unable to rule out the use of carbonates in promoting this reaction,[203] which they attributed to also causing catalyst deactivation as well as CO_2 poisoning.[204] The bound formate species was determined to be bidentate, as evidenced by an asymmetric O-C-O bending mode at 1585 cm^{-1} measured using in situ DRIFTS measurements, and decreased sharply with increasing temperature and consequentially CO conversion.[22] From isotopic labeling studies, it was shown that for the cerium oxide supported platinum WGS catalyst, it is the decomposition of the formate species which is the rate limiting step.[205] Subsequent work by others would show that when pure cerium is used, it is through reaction of the CO to form carbonates and water to form hydroxyl

groups, that the water gas shift reaction can be catalyzed by CeO_2.[40] The formation of formate species during steam reforming of ethanol is also seen for supported rhodium nanoparticles,[206] making this a common pathway for dehydrogenation and oxidation of carbon when supported catalysts are used. This comes as no surprise, as other metal oxides such as MnO_x,[23] ZrO_2,[29] MgO,[41] and ZnO,[207] also show the onset of formate species during the WGS reaction.

Cerium oxide nanorods investigated by Han, et al.,[208] showed that during the WGS reaction the lattice parameter begins to increase in response to the conversion of CO, and was attributed to the onset of oxygen vacancies. The authors speculate that morphologies of cerium oxide which increase the surface area will be more catalytically active due to the need to form oxygen vacancies for the WGS reaction, the former being supported by the work of Zhou, et al., who showed that oxygen vacancy strongly correlates with the surface area of cerium oxide.[209]

For supported platinum nanoparticles, addition of 20 % ZrO_2 to cerium oxide has been shown to increase the turn over frequency of cerium oxide for the WGS reaction regardless of temperature, while 50 % CeO_2-ZrO_2 supports exceed the turn over numbers for 20% ZrO_2 incorporation only at higher temperatures.[204] While these studies did show the stability of the Pt/CeO_2 catalyst, both in terms of turn over frequency and platinum dispersion, they did not report the stability of Pt particles on the mixed cerium-zirconium oxides. In addition to zirconium oxide, calcium was incorporated into cerium via co-precipitation, for improved oxygen mobility, with 50 % calcium incorporation (1:1 Ce:Ca) showing the best catalytic performance.[210] In this study, the authors acquired IR measurements of the Pt/CeO_2 catalyst in site, and showed the onset of a formate feature

centered at circa 2850 cm^{-1}, verifying, at least partly, the involvement of the formate pathway in the WGS for platinum supported on cerium oxide.

Similarly, the use of cerium oxide for methanol conversion to hydrogen, has also been investigated,

$$CH_3OH + \frac{1}{2}O_2 \rightarrow CO_2 + 2H_2 \quad \Delta H_{STP} = -154.9\ kJ/mol$$

As with traditional water gas shift, methanol dissociates at the boundary between platinum nanoparticles and the cerium oxide surface, which such subsequently releases water and hydrogen to form formate, before releasing from the surface as CO_2; the surface is rehydroxylated by gas phase water, and the catalytic cycle repeats.[211] As with most work in this field, in situ DRIFTS was used to verify the formation of formate species on the surface, but other studies used isotopic labeling to show that methanol dissociation is the rate limiting step, and not the water assisted formate conversion as seen for the WGS reaction.[42,212,213] For cerium oxide nanoparticles which are not decorated with precious metals, nanorods show much better conversion of methanol than nanocubes,[214] which follows the trends observed for with CO oxidation.

1.8 Effects of Dopants

While many groups have tried to introduce dopants into the bulk of cerium oxide to improve catalytic activity,[188] conductivity,[168] and even stability,[19,183] many of the reported dopants have ultimately been shown to migrate to the surface of cerium oxide during nucleation. In general, the fluorite lattice of cerium oxide is preserved for dopant concentrations up to 40 %.When XPS spectra were taken of the doped materials, generally a loss in surface Ce^{+3} concentration was seen. In general, electrical

conductivity is improved when dopant concentration is 20 % of the total cation concentration, and the cation is comparable in ionic radius for Ce^{+3}.[168]

1.8.1 Lanthanide Doping

For Lanthanide doping, a lattice increase is seen for lanthanum through europium, with the lattice increase decreasing with an increase in the atomic number of the dopant; for gadolinium, no increase in the lattice constant is seen, but for higher atomic number lanthanides a decrease in the lattice constant is seen with an increase in the atomic number of the dopant.[168,178]

10 % lanthanum has been added to the cerium oxide lattice to improve conversion during the WGS reaction, and on its own shows worse performance than a commercially available copper catalyst, but at temperatures above 200 °C, supported 5 at% Cu on $Ce_{0.9}La_{0.1}O_x$ shows better conversion – nearing 100 % - than the commercial catalyst, and 5 at% Ni on $Ce_{0.9}La_{0.1}O_x$ shows better conversion above 250 °C.[25] Therefore lanthanum cation doping improves cerium oxide performance as a catalyst promoter, but not as a catalyst. Morphologies similar to pure cerium oxide can be obtained using lanthanides, as can be seen in Figure 1.17 for praseodymium, gadolinium, and samarium doped cerium oxide nanoparticles.

Praseodymium is a dopant which has recently found attention due to its ability to improve the conductivity of cerium oxide at high oxygen partial pressures.[215] Loss of surface area and increase in the lattice constant are seen for increasing praseodymium incorporation into cerium oxide, and a cubic CeO_2 lattice has been observed as high as

(a)

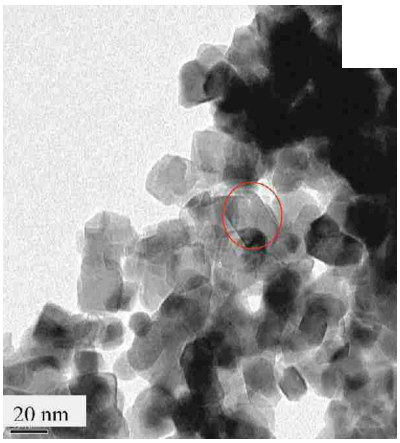

(b)

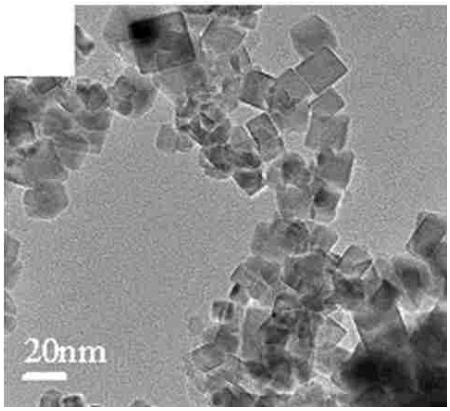

(c)

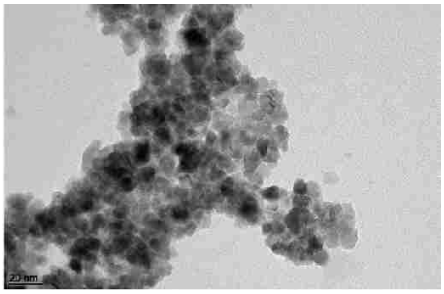

Figure 1.17 Morphologies of lanthanide doped cerium oxides; (a) praseodymium (20 at%),[216] (b) samarium (10 at%),[49] and (c) gadolinium (20 at%).[217]

83 % praseodymium cation incorporation.[218] When praseodymium is incorporated into cerium oxide, Bishop and coworkers have proposed that an intermediate band who energy depends on the partial pressure of oxygen forms between the valence and conducting bands of cerium oxide, providing more accessible energy level for electrons and thus improving the electrical conductivity of the doped material.[215] From their experiments, Bishop determined that at low oxygen partial pressures, the electrical conductivity is driven by oxygen vacancies within the cerium oxide, but at high oxygen partial pressure, the praseodymium small polarons begin to dictate the electrical conductivity, explaining the higher conductivity at higher partial pressures over pure cerium oxide. With regards to the oxygen partial pressure, it was shown in work by Chen and Tuller that as the oxygen partial pressure is increased, the number of oxygen vacancies increase both with temperature and oxygen partial pressure.[219] Due to both CeO_2 and PrO_2 sharing the same space group, $F_{m\text{-}3m}$, and both Pr^{+3}/Ce^{+3} and Pr^{+4}/Ce^{+4} cations having nearly the same ionic radii, 1.13 Å and 0.95 Å,[177,220] respectively, it is reasonable to assume *a prior* that substitution of cerium by praseodymium is random within the entire particle, so that incorporation of small amounts of praseodymium bulk lattice should not preferentially substitute catalytically active Ce^{+3} sites. But attempts have been made to determine the location of these dopants.[48,221] Of the reports on the structure of these mixed metal oxides, x-ray diffraction (XRD) evidence shows a consistent fluorite lattice, the same as that of pure cubic cerium oxide, for praseodymium doping levels up to 20%;[222,223] however, because cerium oxide and praseodymium oxide have both the same space group and have lattice constants that vary less than 10%, it is difficult to show by XRD if two separate cubic phases exist. For praseodymium

concentrations about 20%, it is possible see the onset of a clear second phase, [222,223] but it is not known if this second phase can be attributed to phase separation due to the higher praseodymium concentration or better resolution of a second phase which was not visible at lower praseodymium concentration. Raman spectroscopy has been used to determine the concentration of praseodymium as a function of laser depth,[48] and while the results are consistent with a core-shell structure, complications due to the inherent complexities of diffuse spectroscopy make this technique far from direct evidence of praseodymium surface enrichment.

Incorporation of gadolinium into the cerium oxide lattice has been shown to improve the oxygen ion-conductivity and improved thermal stability over bulk cerium oxide without loss of the fluorite structure,[49,174] and due to this increased conductivity and thermal stability, has been investigated as an electrode material in solid oxide fuel cells.[224,225] When gadolinium is used a dopant, two lattice parameters are seen when viewed using HRTEM; the bulk lattice parameter and the lattice parameter of the enriched surface, the latter being larger than the former.[175] However, most studies rely on x-ray diffraction measurements to determine lattice expansion and only report one lattice parameter for the bulk material. The lattice parameter is larger is gadolinium doped cerium oxide, and the difference in lattice expansion becomes larger as the non-stoichiometry of the material is increased.[190] At 26 at% Ce:Gd, the improvement in conductivity at grain boundaries is an order of magnitude better than bulk cerium oxide, as determined by impedance spectroscopy, but no increase in overall conductivity is seen.[62] Lack of Ce^{+3} in the surface of mixed $Ce_{0.8}Gd_{0.2}O_2$, as seen by XPS discounts Ce^{+3} involvement in electrical conductivity, at least at the surface; therefore, the increased

electrical conductivity has been attributed to defect association and dopant segregation, which has been supported by theoretical calculations.[175] When sub-stoichiometry of $Ce_{0.9}Gd_{0.1}O_{2-x}$ is plotted as a function of the partial pressure of oxygen, it was demonstrated that the value of x for both cerium oxide and gadolinium doped cerium oxide approach 0.16 as the partial pressure of oxygen approaches vacuum (10^{-23} atm), but as the partial pressure is increased, the value of x is nearly twice as much for the doped cerium oxide versus the pure cerium oxide.[190] Furthermore, in comparing the degree of sub-stoichiometry between porous and non-porous $Ce_{0.9}Gd_{0.1}O_{2-x}$, it was shown that the loss scaled with the surface area of the material and indicated that most of the oxygen loss from the material is mostly from the surface, with bulk only contributing mildly to the oxygen loss.[225] Hybrid Monte Carlo – Molecular Dynamics (MC-MD) simulations of mixed cerium-gadolinium slabs showed that the lowest energy configurations were found when gadolinium cations migrated to the first cation layer of the surface, but complete enrichment, viz., the formation of a pure gadolinium oxide layer was not seen, so that final structure was a surface enriched structure with comparably more oxygen vacancies near the surface than in the bulk.[174] Concerning the oxygen vacancies, unlike cerium oxide doped with 10 %-Sc_2O_3 which forms dimers and trimers, gadolinium induced vacancies only form dimers up to 10 % Gd_2O_3 ($[2Gd'_{Ce} - V_{\ddot{O}}]$ pairs), explaining the material's comparatively higher ionic conductivity.[178] At 900 °C, gadolinium shows high oxygen non-stoichiometry than samarium at the same cationic dopant for very low oxygen partial pressures, but like samarium, is comparable to cerium when the partial pressure of oxygen 10^{-15} atm and has less oxygen vacancies than samarium doped cerium oxide for oxygen at higher oxygen partial pressures; similar trends are seen at lower

temperatures as well.[172] Moreover, the electrostatic repulsion of these defect sites results in a larger lattice constant over undoped cerium oxide.[224]

Europium has been doped into the cerium oxide lattice to improve the red emission of cerium oxide nanoparticle in biomedical applications as a boilable and in bioassays, as well as increase the number of oxygen vacancies with increasing doping.[226] The doping levels of europium were between 5 and 30 %, but the cerium oxide cubic lattice was preserved regardless of doping level. Europium doping shows no effect on the crystal structure of cerium, but does result in a linear increase in lattice parameter with increasing europium doping. This trend, however, is offset by heating; upon higher annealing temperatures for the same europium doping, a decrease in lattice parameter was observed. For europium doping, Ce^{+3} concentration decreased for both increased doping and increased annealing temperature; europium was only found in the +3 oxidation state, and shifted towards lower binding energy for higher europium doping.[226] From O 1s deconvolution, for low europium doping only oxygen corresponding to CeO_2 was found, but for increasing doping a shouldering developed corresponding to Eu_2O_3, circa 529.6 eV, which also become more prominent for increased annealing temperature. This would suggest, at least indirectly, that like the earlier lanthanides, europium does not actually incorporate into the cerium oxide.

Finally, samarium doping has been used to improve the oxygen conductivity versus bulk cerium oxide, but the observed lattice constant was larger than bulk cerium oxide,[49] and increases for higher samarium doping.[227] Unlike pure cerium oxide, for 20 % samarium doping, the lattice parameter decreases for decreasing particle sizes.[181] However, other than isolated reports on the effect of samarium on the electrical

conductivity[169,185,227-230] and hardness,[231,232] there exist few reports on the behavior of this dopant.

1.8.2 Other Metal Cation Doping

Incorporation of non-lanthanide metals can be used to produce morphologies similar to those of pure cerium oxide, especially when doping of up to 10 at% are used, shown in Figure 1.18. Titanium has been used as a dopant in cerium oxide electrodes for DMFCs to improve oxygen donation to supported platinum nanoparticles.[188] Furthermore, from the observation of dosing CO and H_2O separately, Azzam, et al., concluded that the incorporation of TiO_2 into CeO_2 changed the mechanism of the WGS from a purely associative mechanism to a mixture of associative and redox mechanisms. The incorporation of 50 % TiO_2 into CeO_2 has been shown to double the turnover frequency of the WGS reaction versus undoped CeO_2.[136] While there have been reports from observing the kinetics of the WGS reaction over $Ti_{0.5}Ce_{0.5}O_2$ that the material must be at some level a solid solution,[204] for cubic cerium oxide, titanium cations were shown to migrate to the surface of $Ce_xTi_{1-x}O_2$ using molecular mechanics, even when a homogenous, amorphous particle is used as a starting point.[99]

Manganese doping has been used to improve the activity of CeO_2 towards the wet oxidation of organic pollutants.[151,233,234] Addition of manganese oxide shows an decrease in the surface area over cerium oxide,[192] especially for increasing cation concentration of manganese.[235] When the amount of manganese dopant exceeds 20 % of the total cations, the onset of a Mn_3O_4 phase is observed in the XRD for large (>30 nm) particles, and is seen immediately when 20 % gadolinium doping is used, though when

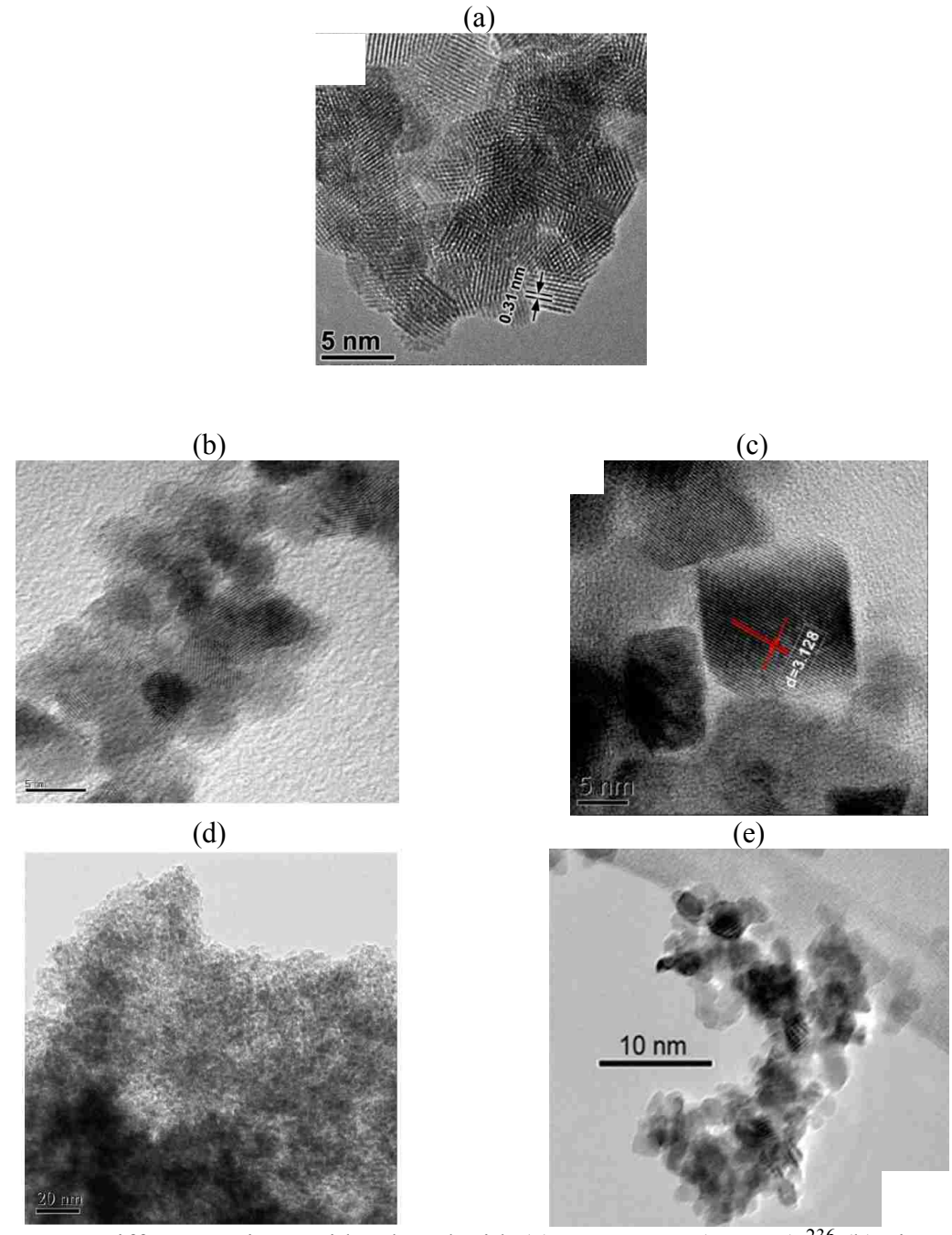

Figure 1.18 Different cerium oxides doped with (a) manganese (10 at%),[236] (b) zirconia (25 at%), (c) iron (10 at%)[237], (d) nickel (10 at%),[4] and (e) calcium (10 at%),[210] showing that the addition of different cations can still be used to obtain morphologies similar to pure cerium oxide.

synthesized using the citric acid method, a single phase is seen in the XRD up to 50 % cation incorporation until reduction in hydrogen.[233] Manganese oxide (MnO_x) and copper oxide (CuO) have been added to CeO_2-ZrO_2 (76% CeO_2) at 5 % of the total metal oxide to greatly improve the catalytic activity of the mixed oxide for aqueous decomposition of organics, with the authors implying from TPR data that these materials form a homogenous metal oxide.[238] Compared to the binary mixture, the ternary metal oxide shows improved oxygen storage capacity,[234,236] which may explain this improved performance. For the simple binary mixture, $Ce_{1-x}Mn_xO_{2-y}$, the lack of change in lattice parameter of cerium oxide and the onset of a separate manganese oxide phase for relatively low manganese doping has been argued to be evidence that a true mixed metal oxide phase is formed.[233] When Co_3O_4 is added to pure and manganese-mixed cerium oxide for preferential oxidation of CO, carbon dioxide contributes to the deactivation of the cerium-manganese oxide, and while the authors stated that improvement of preferential oxidation of CO for the mixed oxide was seen over the pure cerium oxide, the authors provided no baseline data for comparing activity of lifetime.[239] While manganese improves the electrical and ionic conductivity of cerium oxide, the improvement is substantially larger when phase separation occurs, when a Mn_3O_4 phase is created.[240] Similarly, the conversion of NO over mixed manganese-cerium oxides improves with increased manganese cation concentration,[235] the largest improvement is seen in regions where a separate manganese oxide phase is expected to form. The improvement in cerium oxide by the incorporation of manganese is generally due to the formation of a supported manganese oxide phase, and not due to a metal oxide mixture.

Zirconium has been used to improve the performance of cerium oxide as a three-away automotive catalyst,[191] as zirconium is believed to increase the thermal stability of cerium oxide,[19] as well as improve its conversion for the aqueous decomposition of organics, such as acetic acid,[238] and oxidation of simple alkanes[241] and alcohols.[29,167] Zirconium has been reported to increase the surface area of cerium oxide when doped at levels of 20 %,[204,241] 25 %,[29] and even up to 50 %,[159] but other reports at 50 % doping show that both the pure and mixed cerium oxides have comparable surface areas,[238] so ambiguity above 40 % doping remains a problem. Increasing zirconia loading also has the impact of increasing the pore volume,[242] though both pure and zirconium-doped cerium oxide both have less than 0.1 mL/g of pore volume. Much debate remains for the phase diagram of cerium-zirconium oxide due to the presence of metastable phases,[191] so what follows is the most current consensus of cerium oxide-zirconia phase separation. Unlike $Ce_xPr_{1-x}O_2$ materials, $Ce_xZr_{1-x}O_2$ have three polymorphs – a metastable tetragonal phase formed for x between 0.2 and 0.8 ($P4_{2/nmc}$), a cubic phase for x larger than 0.8 (F_{m3m}) which can be transformed to the tetragonal form at high temperatures, and a monoclinic which is formed for x less than 0.2 ($P2_{1/c}$).[20,191] Interestingly, early reports have claimed that for x=0.2, cerium-zirconium oxide forms a solid solution of homogenous composition;[238] however, even zirconium has been shown to surface segregate in the cubic form, possibly due to the disparity in the Ce^{+4} and Zr^{+4} cationic radius, which are 0.97 Å and 0.84 Å, respectively.[242] Incorporation of zirconia into cerium oxide has been shown to improve the electrical conductivity of cerium oxide by increasing the number of oxygen vacancies through grain boundaries between CeO_2 and ZrO_2 phases, though zirconia is not the best dopant to achieve this end.[168] Pure cerium

has been reported as being 11% selective for the conversion of isobutane to isobutene from 573 to 673 K regardless of the surface area, using oxygen as the oxidizing agent; however, this comes at a very low conversion of 0.13 % at 585 K to 3 % at 629 K for 6 m^2/g CeO_2 and between 9 % at 584 K to 12 % at 629 K for 22 m^2/g CeO_2.[241] This selectivity goes up for the incorporation of 20 % ZrO_2, and with an order of magnitude improvement in the conversion of isobutane; for 4.5 m^2/g $Ce_{0.8}Zr_{0.2}O_2$ the conversion ranges from 0.8 at 629 K to 2.8 at 680 K, and for 29 m^2/g $Ce_{0.8}Zr_{0.2}O_2$ the conversion goes from 5.1 % at 566 K to 11.5 % at 632 K. This activity is generally associated with the increased oxygen uptake of the mixed oxide due to increase in oxygen vacancies,[29] and regardless of composition a large increase in the oxygen and hydrogen uptake has been observed with mixed cerium and zirconium oxides,[241] especially when the materials are mixed in nearly equal molar quantities.[20] Computer simulations of these materials offer an explanation for this increased activity as well; the oxygen vacancies generated by zirconia preferentially migrate towards the stable (110) and (111) surfaces of cerium oxide, as well as decreases the barrier for Ce^{+4}/Ce^{+3} conversion.[243] For aqueous conversion of organics, pure cerium shows 9 % conversion of organics, which increases to 27 % when ZrO_2 is added to cerium oxide; this increases to 90 % when CuO and MnO_x are added to the mixed cerium oxide-zirconia mixture.[238] It is claimed by de Leitenburg, et al., that the increase in activity of the mixed cerium-zirconium oxide is due to increased oxygen mobility.

Finally, there are other cations which have also been incorporated into the cerium oxide lattice both as trace elements and large constituents, though there is very little in the literature about these dopants. In these cases, the fluorite structure of cerium oxide

preserved upon addition of the dopant, unless otherwise stated. In all cases, the dopant has been added in an attempt to improve the catalytic activity of the cerium oxide. When alkali cations are incorporated into platinum containing cerium oxide using aqueous cation exchange for a WGS shift reaction, the onset of multiple peaks in the TCD signal of the absorbed formate species observed, attributed due to the interaction of the Pt nanoparticles with the surface alkali cations; this interaction is believed to weaken the C-H bond in the formate species and increase the catalytic activity of the WGS catalyst, but incorporation of alkali cations also destabilizes carbonate species, decreasing the rate reaction, so an optimization of alkali loading to balance these competing effects is needed, with the authors showing that a low level of alkali, not high loading, is ideal.[26] Calcium has been precipitated into cerium oxide to improve oxygen mobility, while preserving the cubic lattice structure, with a larger lattice constant that pure cerium oxide that increases with increasing calcium doping.[181] While an isolated report has indicated that there is calcium enrichment at grain boundaries,[16,244] there is no direct evidence of calcium enrichment in the surface of these mixed oxides. Incorporation of calcium into the cerium lattice preserves the cubic lattice structure while increasing the lattice constant.[57] Calcium also introduces calcium reflections into the XRD pattern, which cannot be attributed to a separate CaO phase due to the lack of the intense CaO (111) and (200) reflections in the diffraction pattern.[210] Moreover, for loadings of less than 10 % calcium, surface area increases slightly, but at 25 % and above, a substantial loss approximately 30 % in surface area is seen for synthesis at 400 °C and 700 °C. Rhenium (III) oxide has been added to cerium oxide in an attempt to increase the electrical conductivity of cerium oxide for SOFC applications, but the large varaition in reports of

the lattice parameter for constant composition samples has been attributed to a heterogeneous distribution of rhenium cations in the lattice.[169] Calcium has also been shown to give two orders of magnitude increase in the electrical conductivity over pure cerium oxide, which is comparable to the improvement seen with strontium, with only rare-earth dopants showing larger increases in the electrical conductivity.[168] However, while there is an increase in the number of oxygen vacancies, these vacancies have been shown to be tightly bound to the divalent calcium cation using impedance spectroscopy.[245] SiO_2 is another common material found in cerium oxide, though its presence is usually due to impurities in the starting materials and is a contaminant more than a dopant; moreover, SiO_2 is known to migrate to grain boundaries in cerium oxide and decrease the conductivity of the material.[169]

1.9 Conclusions

1.9.1 Comments on Physical Properties

A survey of the literature shows that the physical properties of cerium oxide are, for the most part, very well understood. The most common spectroscopic techniques for analyzing cerium oxide, such as IR and UV-vis, were well worked out in the literature by the late 1990s, with both theoretical and experimental approaches used and validating one another. Some confusion still remains about the lattice parameter as a function of particle size, and in isolated reports it is understandable how such confusion can occur, but a survey of the literature reveals that syntheses rich in carbon ligands generally show lattice contraction while syntheses rich in nitrates and oxygen show lattice expansion. Although there remains a very rich discussion on the electrical properties and oxygen sub-stoichiometry of cerium oxide, there still remain gaps in the understanding of how

oxygen sub-stoichiometry varies for smaller nanoparticles. Is the relationship still a power law with respect to oxygen partial pressure? Does the pre-factor change? There is also little known about how bulk conductivity changes with regards to particle size. Is the conductivity the same regardless of particle size? Is the conductivity only dependent on oxygen sub-stoichiometry, or also on particle size, as the two parameters can be related? Future studies would be beneficial in understanding this dependence, and higher resolution impedance spectroscopy could better help in distinguishing between bulk and surface conductivity and how these vary with regard to sub-stoichiometry.

Finally, there is still a great deal of debate over the role of synthesis over the final oxidation state of cerium oxide, much of which has been complicated due to over simplification of the synthesis procedure. The large sensitivity of cerium oxide to adventitious oxygen requires that great care be taken in the preparation of cerium oxide, particularly if reproducibility is desired. Moreover, there remains a fundamental limit in the understanding of the synthesis of cerium oxide. The loss of solvent by precipitation methods can result in very complicated interactions of cerium cations with spectator ions and dissolved gases which may never be understood. For dry synthesis methods, mass transport effects such as the availability of air or the diffusion of combustion products create a situation similar to precipitation methods in that the initial moments of cerium oxide formation are difficult to measure or describe.

1.9.2 Comments on catalytic activity

While cerium oxide does have the ability to change its oxidation state readily at moderate temperatures using adventitious oxygen, the reality is that cerium oxide use as a catalytic material in this regard is not nearly as good as its performance as catalyst

promoter. That is to say, while cerium oxide can change its oxidation state to promote reactions such as the water gas shift reaction or steam reforming, the catalytic activity is enhanced by the addition of other catalytic metals such as platinum, which already catalyze these reaction, and the lability in oxidation state instead makes cerium oxide a better catalyst promoter rather than a catalyst itself. Nonetheless, cerium oxide's labile oxidation state makes it ideal for a variety of reactions, with its performance typically increasing for decreasing particle size. However, there remains a large gap in the literature concerning the selectivity of cerium oxide as a catalyst and how selectivity changes as a function of particle size. Reactions such as NO and CO oxidation generally lack issues with selectivity. However, reactions such as free radical scavenging, which can result in increased free radical concentration if the radical scavenging step becomes rate limiting, would benefit greatly from selectivity studies.

1.9.3 Comments on effects of dopants

While there have been many reports on the incorporation of metal cations into the cerium oxide lattice, subsequent reports aimed at verifying their inclusion have shown that a core-shell structure or surface enrichment occurs. Of all the reports determining the location and distribution of cation doping, at least for binary mixtures with cerium oxide, none have shown that a mixed metal oxide is formed. The most likely explanation for this observation is found in the Pourbaix diagram of cerium; precipitation of cerium oxide from a cerium solution occurs at modest pH and, for most of the elements studied, occurs before nucleation of other cations. This segregation, however, seems to be beneficial to cerium oxide in terms of electrical conductivity and as a catalytic support. Grain boundaries account for most of the labile oxygen found in mixed meta-cerium

oxide systems, and the increase of segregation between the metal-oxide and cerium oxide would increase the number of boundaries.

1.9 The Need for Better Understanding of Cerium Oxide in Fuel Cells

There are three common mechanisms of fuel cell failure.[246] First, chemical degradation resulting from membrane attack by free radicals generated during fuel cell operation. Second, mechanical degradation caused by cyclic or fatigue stresses incurred during operation, such as humidity or thermal fluctuations. Third, shorting which can result from over-compression of the membrane electrode assembly or topological irregularities of the different components of the fuel cell. Of these three means of failure, the latter two are mechanical failures which can only be addressed by improved process controls and better materials. The first mechanism, however, is due to chemical failure of the membrane and presents an opportunity for applying chemistry and chemical engineering principles to determine a solution.

During the oxygen reduction reaction (ORR), whereby oxygen is converted to water, hydrogen peroxide is formed and its decomposition into free radicals is believed to be one of the principle causes of fuel cell failure.[247] Through electron spin resonance (ESR) made on fuel cells which have had 5,5-dimethylpyrroline-*N*-oxide (DMPO, spin trap) incorporated into the membrane,[198] it has been verified that in a fuel cell without stabilizers this decomposition of peroxide follows a homolytic decomposition over platinum, shown below

$$H_2O_2 \overset{Pt}{\rightleftharpoons} 2HO^{\cdot}$$

When hydroxyl radicals interact with the proton exchange membrane, hydrogen radicals are formed that attack C-F bonds while sulfonic radicals are also generated that

subsequently decompose into SO_3 and flouroradicals.[199,246] The decomposition of sulfonic acid sites and C-F bonds ultimately leads to chain scission within the membrane, shown below.[246,248,249]

$$R_f CF_2 CF_2 CO_2 H + \cdot OH \rightarrow R_f CF_2 CF_2 \cdot + H_2 O + CO_2$$

$$R_f CF_2 CF_2 \cdot + \cdot OH \rightarrow R_f CF_2 CF_2 OH \rightarrow R_f CF_2 COF + HF$$

$$R_f CF_2 COF + H_2 O \rightarrow R_F CF_2 CO_2 H + HF$$

Ultimately the radical decomposition of the proton exchange membrane results in the emission of fluorine from the exhaust streams of the fuel cell, as well as membrane thinning which causes loss in open circuit voltage and an increase in hydrogen crossover. The thinning of the membrane further acts to increase hydrogen peroxide generation.[250] Factors that accelerate the onset of hydrogen peroxide and subsequently free radical attack of the membrane include low humidity, high temperature, and electrochemical load, and high partial pressures of reactant gases.[251-253]

Two approaches to mitigating free radical degradation of the membrane have been proposed; the use of additives and the use of composites.[246] For example, there has been much work undertaken to reduce the presence of non-flourinated ionomers in the poly-flourosulfonic acid (PFSA) membrane to eliminate possible initiation sites for free radical decomposition, as $-CH_2-$ and $-CH_3$ are easier to cleave.[194] While modification of the proton exchange membrane with sacrificial functional groups has increased the lifetime of fuel cells substantially,[254] these measures are only temporary solutions. Eventually hydroxyl radical formation removes these functional groups and degradation of the PEM results. Ideally the use of a material which can continuously remove hydrogen peroxide and free radicals catalytically is preferred, and cerium cations incorporated through cerium salts has been shown to be effective at reducing degradation,

even though cerium cations are not the fastest cations for peroxide decomposition. It may seem that a fast peroxide decomposer would be ideal as it would eliminate hydrogen peroxide before it can react with the PEM. However, a survey of the literature shows that generally the faster an ion or metal oxide decomposes hydrogen peroxide, the more radical it creates in the process, for example in the cases of transition metals such as Fe, Mn, Cr, Ti, V, and Cu.[255-257]

When incorporated into a hydrogen fuel cell, cerium cations change the mechanism of free radical generation.[198] Instead of homolytic decomposition of peroxide, the heterolytic decomposition of peroxide into HOO· and H+ through reduction of cerium oxide occurs. The HOO· radical is far more benign than the HO· radical,[199,258] providing the fuel cell with more time to either decompose the HOO· radical via platinum or simply wash the radical out with the exhaust gas.

However, the cerium cation suffers from decreasing the ionic conductivity through the membrane by occupying sulfonic acid sites in the PFSA chain.[246] Cerium oxide provides a more viable option for hydrogen peroxide decomposition in this regard, as the cerium cations are not mobile. While cerium oxide is only a kinetically moderate peroxide decomposer, like the cerium cation it can provide the Ce^{+4} sites which are responsible for peroxide decomposition are paired with Ce^{+3} sites which can facilitate radial scavenging.

1.10 Research Goals

Due to the gaps in understanding regarding the physical properties and its potential use as a radical scavenger, this work will focus on three key unresolved issues regarding cerium oxide;

1) Resolve outstanding issues over the physical properties of pure and mixed cerium oxides
2) Understand how these physical properties can be applied to improving fuel cell performance
3) Prediction, testing, and validation of new cerium oxides for fuel cell lifetime improvement based on the physical properties of cerium oxide

In particular, this work will begin with developing a fundamental understanding of cerium oxide, specifically the change in selectivity and activity of cerium oxide as a function of particle size, and how the incorporation of dopants change the selectivity and activity. From this understanding, hypotheses about the behavior of cerium oxide in hydrogen fuel cells will be tested to determine which size of cerium oxide is optimal for fuel cell applications, how dopants change the optimal particle size, and which dopants would be attractive for improving the performance of cerium oxide.

1.11 Notes on Chapter

A majority of this chapter is from the manuscript, "Nanoscale Scale CeO_2," currently being revised.

1.12 References:

(1) Trogadas, P.; Parrondo, J.; Ramani, V. *Electrochem. Solid-State Lett.* **2008**, *11*, B113.

(2) Pan, C.; Zhang, D.; Shi, L.et al. *Eur. J. Inorg. Chem.* **2008**, 2429.

(3) Hua, G.; Zhang, L.; Fei, G.et al. *J. Mater. Chem.* **2012**, *22*, 6851.

(4) Xu, J.; Xue, B.; Liu, Y.-M.et al. *Appl. Catal., A* **2011**, *405*, 142.

(5) Wang, Q.; Li, G.; Zhao, B.et al. *J. Mol. Catal. A: Chem.* **2011**, *339*, 52.

(6) Padeste, C.; Cant, N. W.; Trimm, D. L. *Catal. Lett.* **1994**, *28*, 301.

(7) Shyu, J. Z.; Otto, K.; Watkins, W. L. H.et al. *J. Catal.* **1988**, *114*, 23.

(8) Carabineiro, S. A. C.; Silva, A. M. T.; Drazic, G.et al. *Catal. Today* **2010**, *154*, 21.

(9) Kouraichi, R.; Delgado, J. J.; Lopez-Castro, J. D.et al. *Catalysis Today*, *154*, 195.

(10) Padeste, C.; Cant, N. W.; Trimm, D. L. *Catal. Lett.* **1993**, *18*, 305.

(11) Chueh, W. C.; McDaniel, A. H.; Grass, M. E.et al. *Chem. Mater.* **2012**, *24*, 1876.

(12) Feng, Z.; Peng, W.; Koberstein, J.et al. *Surf. Sci.* **2004**, *563*.

(13) Karakoti, A.; Singh, S.; Dowding, J. M.et al. *Chem. Soc. Rev.* **2010**, *39*, 4422.

(14) Mullins, D. R.; Overbury, S. H.; Huntley, D. R. *Surf. Sci.* **1998**, *409*, 307.

(15) Ivanov, V. K.; Shcherbakov, A. B.; Usatenko, A. V. *Russ. Chem. Rev.* **2009**, *78*, 855.

(16) Mogensen, M.; Sammes, N. M.; Tompsett, G. A. *Solid State Ionics* **2000**, *129*, 63.

(17) Bevan, D. J. M. *J. Inorg. Nuc. Chem.* **1955**, *1*, 49.

(18) Liu, X.; Zhou, K.; Wang, L.et al. *J. Am. Chem. Soc.* **2009**, *131*, 3140.

(19) Rao, G. R.; Fornasiero, P.; DiMonte, R.et al. *J. Catal.* **1996**, *162*, 1.

(20) Fornasiero, P.; Balducci, G.; DiMonte, R.et al. *J. Catal.* **1996**, *164*, 173.

(21) Conesa, J. C. *Surf. Sci.* **1995**, *339*, 337.

(22) Jacobs, G.; Williams, L.; Graham, U.et al. *J. Phys. Chem. B* **2003**, *107*, 10398.

(23) Ribeiro, M. C.; Jacobs, G.; Graham, U. M.et al. *Catal. Commun.* **2010**, *11*, 1193.

(24) Jacobs, G.; Patterson, P. M.; Williams, L.et al. *Appl. Catal., A* **2004**, *262*, 177.

(25) Li, K.; Fu, Q.; Flytzani-Slephanopoulos, M. *Appl. Catal., B* **2000**, *27*, 179.

(26) Evin, H. N.; Jacobs, G.; Ruiz-Martinez, J.et al. *Catal. Lett.* **2008**, *122*, 9.

(27) Gnanamani, M. K.; Ribeiro, M. C.; Ma, W.et al. *Appl. Catal., A* **2011**, *393*, 17.

(28) Hosokawa, S.; Shimamura, K.; Inoue, M. *Mater. Res. Bull.* **2011**, *46*, 1928.

(29) de Lima, S. M.; Silva, A. M.; da Cruz, I. O.et al. *Catal. Today* **2008**, *138*, 162.

(30) Holmgren, A.; Andersson, B.; Duprez, D. *Appl. Catal., B* **1999**, *22*, 215.

(31) Holmgren, A.; Duprez, D.; Andersson, B. *J. Catal.* **1999**, *182*, 441.

(32) Terribile, D.; Llorca, J.; Boaro, M.et al. *Chem. Commun.* **1998**, 1897.

(33) Terribile, D.; Trovarelli, A.; Llorca, J.et al. *J. Catal.* **1998**, *178*, 299.

(34) Fang, C.; Zhang, D.; Shi, L.et al. *Catalysis Science & Technology* **2013**, *3*, 803.

(35) Maia, T. A.; Assaf, J. M.; Assaf, E. M. *Mater. Chem. Phys.* **2012**, *132*, 1029.

(36) Rao, G. R.; Sahu, H. R. *Proc. Indian Acad. Sci. - Chem. Sci.* **2001**, *113*, 651.

(37) Bensalem, A.; Muller, J. C.; Bozonverduraz, F. *J. Chem. Soc. - Farad. Trans.* **1992**, *88*, 153.

(38) Ivanov, V. K.; Polezhaeva, O. S.; Kopitsa, G. P.et al. *Inorg. Mater.* **2008**, *44*, 272.

(39) Zaki, M. I.; Hussein, G. A. M.; Mansour, S. A. A.et al. *Colloids Surf., A.* **1997**, *127*, 47.

(40) Agarwal, S.; Lefferts, L.; Mojet, B. L. *Chemcatchem* **2013**, *5*, 479.

(41) Shido, T.; Asakura, K.; Iwasawa, Y. *J. Catal.* **1990**, *122*, 55.

(42) Shido, T.; Iwasawa, Y. *J. Catal.* **1993**, *141*, 71.

(43) Binet, C.; Daturi, M.; Lavalley, J. C. *Catal. Today* **1999**, *50*, 207.

(44) Badri, A.; Binet, C.; Lavalley, J. C. *J. Chem. Soc. - Farad. Trans.* **1996**, *92*, 4669.

(45) Binet, C.; Badri, A.; Lavalley, J. C. *J. Phys. Chem.* **1994**, *98*, 6392.

(46) Tuller, H. L.; Nowick, A. S. *J. Phys. Chem. Solids* **1977**, *38*, 859.

(47) Tuller, H. L.; Nowick, A. S. *J. Electrochem. Soc.* **1979**, *126*, 209.

(48) Luo, M. F.; Yan, Z. L.; Jin, L. Y.et al. *J. Phys. Chem. B* **2006**, *110*, 13068.

(49) Wang, Z.; Wang, Q.; Liao, Y.et al. *Chemphyschem* **2011**, *12*, 2763.

(50) Blumenthal, R. N.; Pinz, B. A. *J. Appl. Phys.* **1967**, *38*, 2376.

(51) Naik, I. K.; Tien, T. Y. *J. Phys. Chem. Solids* **1978**, *39*, 311.

(52) Faber, J.; Seitz, M. A.; Mueller, M. H. *J. Phys. Chem. Solids* **1976**, *37*, 903.

(53) Sayle, T. X. T.; Parker, S. C.; Catlow, C. R. A. *J. Chem. Soc., Chem. Comm.* **1992**, 977.

(54) Horita, T.; Yamaji, K.; Sakai, N.et al. *Electrochem. Solid-State Lett.* **1998**, *1*, 4.

(55) Mukundan, R.; Brosha, E. L.; Brown, D. R.et al. *Electrochem. Solid-State Lett.* **1999**, *2*, 412.

(56) Panlener, R. J.; Blumenthal, R. N.; Garnier, J. E. *J. Phys. Chem. Solids* **1975**, *3611*, 1213.

(57) Garnier, J. E.; Blumenthal, R. N.; Panlener, R. J.et al. *J. Phys. Chem. Solids* **1976**, *37*, 369.

(58) Faber, J.; Seitz, M. A.; Mueller, M. H. *J. Phys. Chem. Solids* **1976**, *37*, 909.

(59) Sorensen, O. T. *J. Solid State Chem.* **1976**, *18*, 217.

(60) Braunshtein, D.; Tannhauser, D. S.; Riess, I. *J. Electrochem. Soc.* **1981**, *128*, 82.

(61) Blumenthal, R. N.; Panlener, R. J. *J. Phys. Chem. Solids* **1970**, *31*, 1190.

(62) Chiang, Y. M.; Lavik, E. B.; Blom, D. A. *Nanostruct. Mater.* **1997**, *9*, 633.

(63) Blumenthal, R. N.; Hofmaier, R. L. *J. Electrochem. Soc.* **1974**, *121*, 126.

(64) Vanherle, J.; Horita, T.; Kawada, T.et al. *J. Eur. Ceram. Soc.* **1996**, *16*, 961.

(65) Kevane, C. J.; Watson, R. D.; Holverso.El *J. Appl. Phys.* **1963**, *34*, 2083.

(66) Blumenthal, R. N.; Brugner, F. S.; Garnier, J. E. *J. Electrochem. Soc.* **1973**, *120*, 1230.

(67) Chen, H.-T.; Chang, J.-G.; Chen, H.-L.et al. *J. Comput. Chem.* **2009**, *30*, 2433.

(68) Hirano, M.; Inagaki, M. *J. Mater. Chem.* **2000**, *10*, 473.

(69) Hirano, M.; Fukuda, Y.; Iwata, H.et al. *J. Am. Ceram. Soc.* **2000**, *83*, 1287.

(70) Masui, T.; Fujiwara, K.; Peng, Y. M.et al. *J. Alloys Compd.* **1998**, *269*, 116.

(71) Martinez-Arias, A.; Fernandez-Garcia, M.; Ballesteros, V.et al. *Langmuir* **1999**, *15*, 4796.

(72) Terribile, D.; Trovarelli, A.; Llorca, J.et al. *Catal. Today* **1998**, *43*, 79.

(73) Terribile, D.; Trovarelli, A.; de Leitenburg, C.et al. *Chem. Mater.* **1997**, *9*, 2676.

(74) Laosiripojana, N.; Assabumrungrat, S. *J. Power Sources* **2006**, *158*, 1348.

(75) Dengsong, Z.; Fuhuan, N.; Hongrui, L.et al. *Powder Technol.* **2011**, *207*, 35.

(76) Valechha, D.; Lokhande, S.; Klementova, M.et al. *J. Mater. Chem.* **2011**, *21*, 3718.

(77) Peiretti, L. F.; Tiscornia, I. S.; Miro, E. E. *Chem. Eng. J.* **2013**, *223*, 507.

(78) Maddler, L.; Stark, W. J.; Pratsinis, S. E. *J. Mater. Res.* **2002**, *17*, 1356.

(79) Suzuki, M.; Kagawa, M.; Syono, Y.et al. *J. Cryst. Growth* **1991**, *112*, 621.

(80) Suzuki, M.; Kagawa, M.; Syono, Y.et al. *J. Mat. Sci.* **1992**, *27*, 679.

(81) Jie, Z.; Yaohua, Z.; Xubo, S.et al. *J. Nanopart. Res.* **2011**, *13*, 4445.

(82) Chowdhury, S.; Lin, K.-S. *Journal of Nanomaterials* **2011**.

(83) Hayes, S. A.; Yu, P.; O'Keefe, T. J.et al. *J. Electrochem. Soc.* **2002**, *149*, C623.

(84) Ivanov, V. K.; Polezhaeva, O. S.; Shaporev, A. S.et al. *Russ. J. Inorg. Chem.* **2010**, *55*, 328.

(85) Niesz, K.; Reji, C.; Neilson, J. R.et al. *Cryst. Growth Des.* **2010**, *10*, 4485.

(86) Karakoti, A. S.; Kuchibhatla, S. V. N. T.; Babu, K. S.et al. *J. Phys. Chem. C* **2007**, *111*, 17232.

(87) Yu, P.; Hayes, S. A.; O'Keefe, T. J.et al. *J. Electrochem. Soc.* **2006**, *153*, C74.

(88) Scholes, F. H.; Hughes, A. E.; Hardin, S. G.et al. *Chem. Mater.* **2007**, *19*, 2321.

(89) Niesz, K.; Morse, D. E. *Nano Today* **2010**, *5*, 99.

(90) Sayle, T. X. T.; Parker, S. C.; Catlow, C. R. A. *Surf. Sci.* **1994**, *316*, 329.

(91) Torrente-Murciano, L.; Gilbank, A.; Puertolas, B.et al. *Appl. Catal., B* **2013**, *132*, 116.

(92) Wang, Z. L.; Feng, X. D. *J. Phys. Chem. B* **2003**, *107*, 13563.

(93) Zhou, K. B.; Wang, X.; Sun, X. M.et al. *J. Catal.* **2005**, *229*, 206.

(94) Lu, X.; Li, X.; Qian, J.et al. *Powder Technol.* **2013**, *239*, 415.

(95) Arul, N. S.; Mangalaraj, D.; Kim, T. W.et al. *J. Mat. Sci. - Mat. Elec.* **2013**, *24*, 1644.

(96) Kuiry, S. C.; Patil, S. D.; Deshpande, S.et al. *J. Phys. Chem. B* **2005**, *109*, 6936.

(97) Sun, C.; Li, H.; Chen, L. *J. Phys. Chem. Solids* **2007**, *68*, 1785.

(98) Sun, C.; Sun, J.; Xiao, G.et al. *J. Phys. Chem. B* **2006**, *110*, 13445.

(99) Feng, X. D.; Sayle, D. C.; Wang, Z. L.et al. *Science* **2006**, *312*, 1504.

(100) Zhang, D.; Niu, F.; Li, H.et al. *Powder Technol.* **2011**, *207*, 35.

(101) Si, R.; Flytzani-Stephanopoulos, M. *Angew. Chem. Int. Ed.* **2008**, *47*, 2884.

(102) Mai, H. X.; Sun, L. D.; Zhang, Y. W.et al. *J. Phys. Chem. B* **2005**, *109*, 24380.

(103) Huang, P. X.; Wu, F.; Zhu, B. L.et al. *J. Phys. Chem. B* **2005**, *109*, 19169.

(104) Vantomme, A.; Yuan, Z. Y.; Du, G. H.et al. *Langmuir* **2005**, *21*, 1132.

(105) Dang, F.; Kato, K.; Imai, H.et al. *Cryst. Growth Des.* **2010**, *10*, 4537.

(106) Gu, F.; Wang, Z.; Han, D.et al. *Mater. Sci. Eng., B* **2007**, *139*, 62.

(107) Zhang, D.; Fu, H.; Shi, L.et al. *Inorg. Chem.* **2007**, *46*, 2446.

(108) Sun, C. W.; Li, H.; Zhang, H. R.et al. *Nanotechnology* **2005**, *16*, 1454.

(109) Chen, G.; Xu, C.; Song, X.et al. *Inorg. Chem.* **2008**, *47*, 723.

(110) Cui, R.; Lu, W.; Zhang, L.et al. *J. Phys. Chem. C* **2009**, *113*, 21520.

(111) Cordeiro, M. A. L.; Weng, W.; Stroppa, D. G.et al. *Chem. Mater.* **2013**, *25*, 2028.

(112) Dang, F.; Kato, K.; Imai, H.et al. *Cryst. Growth Des.* **2011**, *11*, 4129.

(113) Yang, S.; Gao, L. *J. Am. Chem. Soc.* **2006**, *128*, 9330.

(114) Wang, T.; Zhang, L.; Zhang, J.et al. *Microporous Mesoporous Mater.* **2013**, *171*, 196.

(115) Zhang, D.; Yan, T.; Shi, L.et al. *Appl. Surf. Sci.* **2009**, *255*, 5789.

(116) Zhang, D.; Pan, C.; Shi, L.et al. *Microporous Mesoporous Mater.* **2009**, *117*, 193.

(117) Zhang, D.; Pan, C.; Zhang, J.et al. *Mater. Lett.* **2008**, *62*, 3821.

(118) Zhang, D.; Yan, T.; Pan, C.et al. *Mater. Chem. Phys.* **2009**, *113*, 527.

(119) Deshpande, S.; Patil, S.; Kuchibhatla, S.et al. *Appl. Phys. Lett.* **2005**, *87*.

(120) Hailstone, R. K.; DiFrancesco, A. G.; Leong, J. G.et al. *J. Phys. Chem. C* **2009**, *113*, 15155.

(121) Tsunekawa, S.; Sivamohan, R.; Ito, S.et al. *Nanostruct. Mater.* **1999**, *11*, 141.

(122) Baranchikov, A. E.; Polezhaeva, O. S.; Ivanov, V. K.et al. *Crystengcomm* **2010**, *12*, 3531.

(123) Tsunekawa, S.; Fukuda, T.; Kasuya, A. *Surf. Sci.* **2000**, *457*, L437.

(124) Tsunekawa, S.; Sahara, R.; Kawazoe, Y.et al. *Appl. Surf. Sci.* **1999**, *152*, 53.

(125) Chen, L.; Fleming, P.; Morris, V.et al. *J. Phys. Chem. C* **2010**, *114*, 12909.

(126) Tsunekawa, S.; Ishikawa, K.; Li, Z. Q.et al. *Phys. Rev. Lett.* **2000**, *85*, 3440.

(127) Qi, W.; Huang, B.; Wang, M. *Nanoscale Research Letters* **2009**, *4*, 269.

(128) Heinemann, K.; Poppa, H. *Surf. Sci.* **1985**, *156*, 265.

(129) Giorgio, S.; Henry, C. R.; Chapon, C.et al. *J. Cryst. Growth* **1990**, *100*, 254.

(130) Jiang, Q.; Liang, L. H.; Zhao, D. S. *J. Phys. Chem. B* **2001**, *105*, 6275.

(131) Qi, W. H.; Wang, M. P.; Su, Y. C. *J. Mater. Sci. Lett.* **2002**, *21*, 877.

(132) Medasani, B.; Park, Y. H.; Vasiliev, I. *Phys. Rev. B: Condens. Matter* **2007**, *75*.

(133) Wasserma.Hj; Vermaak, J. S. *Surf. Sci.* **1970**, *22*, 164.

(134) Lamber, R.; Wetjen, S.; Jaeger, N. I. *Phys. Rev. B: Condens. Matter* **1995**, *51*, 10968.

(135) Morse, M. D. *Chem. Rev.* **1986**, *86*, 1049.

(136) Balerna, A.; Bernieri, E.; Picozzi, P.et al. *Surf. Sci.* **1985**, *156*, 206.

(137) Qi, W. H.; Wang, M. P. *J. Nanopart. Res.* **2005**, *7*, 51.

(138) Ahmad, M. I.; Bhattacharya, S. S. *Appl. Phys. Lett.* **2009**, *95*.

(139) Fukuhara, M. *Phys. Lett. A* **2003**, *313*, 427.

(140) Zhang, F.; Wang, P.; Koberstein, J.et al. *Surf. Sci.* **2004**, *563*, 74.

(141) Qiu, L. M.; Liu, F.; Zhao, L. Z.et al. *Appl. Surf. Sci.* **2006**, *252*, 4931.

(142) Holgado, J. P.; Munuera, G.; Espinos, J. P.et al. *Appl. Surf. Sci.* **2000**, *158*, 164.

(143) Holgado, J. P.; Alvarez, R.; Munuera, G. *Appl. Surf. Sci.* **2000**, *161*, 301.

(144) Kotani, A.; Jo, T.; Parlebas, J. C. *Advances in Physics* **1988**, *37*, 37.

(145) Burroughs, P.; Hamnett, A.; Orchard, A. F.et al. *J. Chem. Soc., Dalton Trans.* **1976**, 1686.

(146) Paparazzo, E. *Appl. Catal., B* **2011**, *105*, 248.

(147) Paparazzo, E. *Chem. Eng. J.* **2011**, *170*, 342.

(148) Pfau, A.; Schierbaum, K. D. *Surf. Sci.* **1994**, *321*, 71.

(149) Schierbaum, K. D. *Surf. Sci.* **1998**, *399*, 29.

(150) Wang, A. Q.; Punchaipetch, P.; Wallace, R. M.et al. *J. Vac. Sci. Technol., B* **2003**, *21*, 1169.

(151) Larachi, F.; Pierre, J.; Adnot, A.et al. *Appl. Surf. Sci.* **2002**, *195*, 236.

(152) Swiatowska, J.; Lair, V.; Pereira-Nabais, C.et al. *Appl. Surf. Sci.* **2011**, *257*, 9110.

(153) Praline, G.; Koel, B. E.; Hance, R. L.et al. *J. Electron. Spectrosc. Relat. Phenom.* **1980**, *21*, 17.

(154) Koel, B. E.; Praline, G.; Lee, H. I.et al. *J. Electron. Spectrosc. Relat. Phenom.* **1980**, *21*, 31.

(155) Palmqvist, A. E. C.; Wirde, M.; Gelius, U.et al. *Nanostruct. Mater.* **1999**, *11*, 995.

(156) Preisler, E. J.; Marsh, O. J.; Beach, R. A.et al. *J. Vac. Sci. Technol., B* **2001**, *19*, 1611.

(157) Moulder, J. F.; Stickle, W. F.; Sobol, P. E.et al. *Handbook of X-ray Photoelectron Spectroscopy*; Physical Electronics, Inc.: Eden Prairie, Minnesota, 1995.

(158) Nachimuthu, P.; Shih, W. C.; Liu, R. S.et al. *J. Solid State Chem.* **2000**, *149*, 408.

(159) Overbury, S. H.; Huntley, D. R.; Mullins, D. R.et al. *Catal. Lett.* **1998**, *51*, 133.

(160) Turner, S.; Lazar, S.; Freitag, B.et al. *Nanoscale* **2011**, *3*, 3385.

(161) Ho, C. M.; Yu, J. C.; Kwong, T.et al. *Chem. Mater.* **2005**, *17*, 4514.

(162) Reyoy, M. N.; Scott, R. W. J.; Grosvenor, A. P. *J. Phys. Chem. C* **2013**, *117*, 10095.

(163) Diaz, D. J.; Greenletch, N.; Solanki, A.et al. *Catal. Lett.* **2007**, *119*, 319.

(164) Cargnello, M.; Doan-Nguyen, V. V. T.; Gordon, T. R.et al. *Science* **2013**, *341*, 771.

(165) Zhao, Y.; Teng, B.-T.; Wen, X.-D.et al. *J. Phys. Chem. C* **2012**, *116*, 15986.

(166) Trovarelli, A. *Cat. Rev. - Sci. Eng.* **1996**, *38*, 439.

(167) de Lima, S. M.; Silva, A. M.; Graham, U. M.et al. *Appl. Catal., A* **2009**, *352*, 95.

(168) Inaba, H.; Tagawa, H. *Solid State Ionics* **1996**, *83*, 1.

(169) Steele, B. C. H. *Solid State Ionics* **2000**, *129*, 95.

(170) Ai, N.; Chen, K.; Jiang, S. P. *Solid State Ionics* **2013**, *233*, 87.

(171) Kurokawa, H.; Sholklapper, T. Z.; Jacobson, C. P.et al. *Electrochem. Solid-State Lett.* **2007**, *10*, B135.

(172) Schneider, D.; Godickemeier, M.; Gauckler, L. J. *J. Electroceram.* **1997**, *1*, 165.

(173) Tuller, H. L.; Nowick, A. S. *J. Electrochem. Soc.* **1975**, *122*, 255.

(174) Lee, H. B.; Prinz, F. B.; Cai, W. *Acta Mater.* **2010**, *58*, 2197.

(175) Huang, H.; Gur, T. M.; Saito, Y.et al. *Appl. Phys. Lett.* **2006**, *89*.

(176) Horita, T.; Sakai, N.; Yokokawa, H.et al. *J. Electroceram.* **1997**, *1*, 155.

(177) He, Q.; Mukerjee, S.; Parres-Esclapez, S.et al. *J. Appl. Electrochem.* **2011**, *41*, 891.

(178) Minervini, L.; Zacate, M. O.; Grimes, R. W. *Solid State Ionics* **1999**, *116*, 339.

(179) Chen, D.; Bishop, S. R.; Tuller, H. L. *J. Electroceram.* **2012**, *28*, 62.

(180) Navarro, L.; Marques, F.; Frade, J. *J. Electrochem. Soc.* **1997**, *144*, 267.

(181) Huang, W.; Shuk, P.; Greenblatt, M. *Solid State Ionics* **1997**, *100*, 23.

(182) VanHerle, J.; Horita, T.; Kawada, T.et al. *Solid State Ionics* **1996**, *86-8*, 1255.

(183) VanHerle, J.; Horita, T.; Kawada, T.et al. *J. Am. Ceram. Soc.* **1997**, *80*, 933.

(184) Kharton, V. V.; Figueiredo, F. M.; Navarro, L.et al. *J. Mat. Sci.* **2001**, *36*, 1105.

(185) Huang, W.; Shuk, P.; Greenblatt, M.et al. *J. Electrochem. Soc.* **2000**, *147*, 4196.

(186) Huang, W. S.; Shuk, P.; Greenblatt, M. *J. Electrochem. Soc.* **2000**, *147*, 439.

(187) Adler, S. B.; Lane, J. A.; Steele, B. C. H. *J. Electrochem. Soc.* **1996**, *143*, 3554.

(188) Karakoti, A. S.; King, J. E. S.; Vincent, A.et al. *Appl. Catal., A* **2010**, *388*, 262.

(189) Anderson, J. M.; Patel, J.; Karakoti, A. S.et al. *Electrochim. Acta* **2011**, *56*, 2541.

(190) Anderson, J.; Karakoti, A.; Diaz, D. J.et al. *J. Phys. Chem. C* **2010**, *114*, 4595.

(191) Kaspar, J.; Fornasiero, P.; Graziani, M. *Catal. Today* **1999**, *50*, 285.

(192) Wang, X.; Zheng, Y.; Lin, J. *Catal. Commun.* **2013**, *37*, 96.

(193) Pearman, B. P.; Mohajeri, N.; Brooker, R. P.et al. *J. Power Sources* **2013**, *225*, 75.

(194) Coms, F. D.; Liu, H.; Owejan, J. E. In *Proton Exchange Membrane Fuel Cells 8, Pts 1 and 2*; Fuller, T., Shinohara, K., Ramani, V., Shirvanian, P., Uchida, H.,

Cleghorn, S., Inaba, M., Mitsushima, S., Strasser, P., Nakagawa, H., Gasteiger, H. A., Zawodzinski, T., Lamy, C., Eds. 2008; Vol. 16, p 1735.

(195) Sigler, P. B.; Masters, B. J. *J. Am. Chem. Soc.* **1957**, *79*, 6353.

(196) Saito, E.; Bielski, B. H. J. *J. Am. Chem. Soc.* **1961**, *83*, 4467.

(197) Czapski, G.; Bielski, B. H. J.; Sutin, N. *J. Phys. Chem.* **1963**, *67*, 201.

(198) Danilczuk, M.; Schlick, S.; Coms, F. D. *Macromol.* **2009**, *42*, 8943.

(199) Coms, F. D. In *Proton Exchange Membrane Fuel Cells 8, Pts 1 and 2*; Fuller, T., Shinohara, K., Ramani, V., Shirvanian, P., Uchida, H., Cleghorn, S., Inaba, M., Mitsushima, S., Strasser, P., Nakagawa, H., Gasteiger, H. A., Zawodzinski, T., Lamy, C., Eds. 2008; Vol. 16, p 235.

(200) Assumpcao, M. H. M. T.; Moraes, A.; De Souza, R. F. B.et al. *Appl. Catal., A* **2012**, *411*, 1.

(201) Ntainjua, E. N.; Piccinini, M.; Pritchard, J. C.et al. *Catal. Today* **2011**, *178*, 47.

(202) Ntainjua, E. N.; Piccinini, M.; Freakley, S. J.et al. *Green Chem.* **2012**, *14*, 170.

(203) Azzam, K. G.; Babich, I. V.; Seshan, K.et al. *J. Catal.* **2007**, *251*, 153.

(204) Azzam, K. G.; Babich, I. V.; Seshan, K.et al. *J. Catal.* **2007**, *251*, 163.

(205) Jacobs, G.; Khalid, S.; Patterson, P. M.et al. *Appl. Catal., A* **2004**, *268*, 255.

(206) da Silva, A. M.; de Souza, K. R.; Jacobs, G.et al. *Appl. Catal., B* **2011**, *102*, 94.

(207) Jacobs, G.; Crawford, A.; Williams, L.et al. *Appl. Catal., A* **2004**, *267*, 27.

(208) Han, W.-Q.; Wen, W.; Hanson, J. C.et al. *J. Phys. Chem. C* **2009**, *113*, 21949.

(209) Zhou, G.; Shah, P. R.; Montini, T.et al. *Surf. Sci.* **2007**, *601*, 2512.

(210) Linganiso, L. Z.; Jacobs, G.; Azzam, K. G.et al. *Appl. Catal., A* **2011**, *394*, 105.

(211) Jacobs, G.; Davis, B. H. *Appl. Catal., A* **2005**, *285*, 43.

(212) Jacobs, G.; Crawford, A. C.; Davis, B. H. *Catal. Lett.* **2005**, *100*, 147.

(213) Shido, T.; Iwasawa, Y. *J. Catal.* **1992**, *136*, 493.

(214) Yi, N.; Si, R.; Saltsburg, H.et al. *Appl. Catal., B* **2010**, *95*, 87.

(215) Bishop, S. R.; Stefanik, T. S.; Tuller, H. L. *PCCP* **2011**, *13*, 10165.

(216) Reddy, B. M.; Bharali, P.; Saikia, P.et al. *J. Phys. Chem. C* **2008**, *112*, 11729.

(217) Chandradass, J.; Nam, B.; Kim, K. H. *Colloids Surf., A.* **2009**, *348*, 130.

(218) Logan, A. D.; Shelef, M. *J. Mater. Res.* **1994**, *9*, 468.

(219) Chen, D.; Bishop, S. R.; Tuller, H. L. *Adv. Funct. Mater.* **2013**, *23*, 2168.

(220) Shannon, R. D. *Acta Crystallographica Section A* **1976**, *32*, 751.

(221) Zhi-Ying, P.; Ji-Qing, L.; Meng-Fei, L.et al. *J. Phys. Chem. C* **2007**, *111*.

(222) Matovic, B.; Boskovic, S.; Logar, M.et al. *J. Alloys Compd.* **2010**, *505*, 235.

(223) Sharma, V.; Eberhardt, K. M.; Sharma, R.et al. *Chem. Phys. Lett.* **2010**, *495*, 280.

(224) Bishop, S. R.; Duncan, K. L.; Wachsman, E. D. *Electrochim. Acta* **2009**, *54*, 1436.

(225) Bishop, S. R.; Duncan, K. L.; Wachsman, E. D. *Acta Mater.* **2009**, *57*, 3596.

(226) Kumar, A.; Babu, S.; Karakoti, A. S.et al. *Langmuir* **2009**, *25*, 10998.

(227) Huang, W.; Shuk, P.; Greenblatt, M. *Chem. Mater.* **1997**, *9*, 2240.

(228) Shemilt, J. E.; Stanway, C. L.; Williams, H. M. *Solid State Ionics* **2000**, *134*, 111.

(229) Chueh, W. C.; Hao, Y.; Jung, W.et al. *Nature Materials* **2012**, *11*, 155.

(230) Jung, W.; Dereux, J. O.; Chueh, W. C.et al. *Energy & Environmental Science* **2012**, *5*, 8682.

(231) Shemilt, J. E.; Williams, H. M. *J. Mater. Sci. Lett.* **1999**, *18*, 1735.

(232) Shemilt, J. E.; Williams, H. M.; Edirisinghe, M. J.et al. *Scripta Mater.* **1997**, *36*, 929.

(233) Zhou, G.; Shah, P. R.; Gorte, R. J. *Catal. Lett.* **2008**, *120*, 191.

(234) Li, X.; Wang, J.; Liao, C.et al. *J. Nat. Gas Chem.* **2011**, *20*, 623.

(235) Qi, G. S.; Yang, R. T. *J. Catal.* **2003**, *217*, 434.

(236) Li, H.; Tana; Zhang, X.et al. *Catal. Commun.* **2011**, *12*, 1361.

(237) Li, L.; Li, X. *J. Phys. Chem. C* **2013**, *117*, 15383.

(238) deLeitenburg, C.; Goi, D.; Primavera, A.et al. *Appl. Catal., B* **1996**, *11*, L29.

(239) Guo, Q.; Chen, S.; Liu, Y.et al. *Chem. Eng. J.* **2010**, *165*, 846.

(240) Kang, C. Y.; Kusaba, H.; Yahiro, H.et al. *Solid State Ionics* **2006**, *177*, 1799.

(241) deLeitenburg, C.; Trovarelli, A.; Llorca, J.et al. *Appl. Catal., A* **1996**, *139*, 161.

(242) Maia, T. A.; Assaf, J. M.; Assaf, E. M. *Reac. Kin. Mech. Cat.* **2013**, *109*, 181.

(243) Balducci, G.; Kaspar, J.; Fornasiero, P.et al. *J. Phys. Chem. B* **1998**, *102*, 557.

(244) Eladham, K.; Hammou, A. *Solid State Ionics* **1983**, *9-10*, 905.

(245) Eladham, K.; Hammou, A.; Ravaine, D. *J. Phys. Chem. Solids* **1983**, *44*, 281.

(246) Gittleman, C. S.; Coms, F. D.; Lai, Y.-H.et al. In *Polymer Electrolyte Fuel Cell Degradation*; Academic Press: Boston, 2012, p 15.

(247) Prabhakaran, V.; Arges, C. G.; Ramani, V. *Proceedings of the National Academy of Sciences of the United States of America* **2012**, *109*, 1029.

(248) Kinumoto, T.; Inaba, M.; Nakayama, Y.et al. *J. Power Sources* **2006**, *158*, 1222.

(249) Curtin, D. E.; Lousenberg, R. D.; Henry, T. J.et al. *J. Power Sources* **2004**, *131*, 41.

(250) Liu, W.; Zuckerbrod, D. *J. Electrochem. Soc.* **2005**, *152*, A1165.

(251) Zhang, J.; Litteer, B. A.; Gu, W.et al. *J. Electrochem. Soc.* **2007**, *154*, B1006.

(252) Liu, H.; Zhang, J.; Coms, F.et al. *ECS Transactions* **2006**, *3*, 493.

(253) Liu, W.; Crum, M. *ECS Transactions* **2006**, *3*, 531.

(254) Zhang, H.; Shen, P. K. *Chem. Rev.* **2012**, *112*, 2780.

(255) Park, J.-N.; Shon, J. K.; Jin, M.et al. *Chem. Lett.* **2010**, *39*, 493.

(256) Wang, W. D.; Bakac, A.; Espenson, J. H. *Inorg. Chem.* **1993**, *32*, 5034.

(257) Tony, M. A.; Zhao, Y. Q.; Tayeb, A. M. *J. Environ. Sci. - China* **2009**, *21*, 101.

(258) Buxton, G. V.; Greenstock, C. L.; Helman, W. P.et al. *J. Phys. Chem. Ref. Data* **1988**, *17*, 513.

Chapter 2: Experimental Methods

2.1 Materials Synthesis

2.1.1 CeO_2 Synthesis

0.60-0.65 g of cerium (III) acetate (Strem Chemicals) was dissolved in 50 mL of deionized water (Milli-Q Water System, 18.2 mΩ*cm) by addition of sufficient nitric acid to reduce the pH to 1. Above 16 mg/mL, it was difficult to obtain nanoparticles smaller than 10 nm and the syntheses had a large carbon content and the onset of a large Ce_2O_3 phase. The dissolved cerium was then precipitated by the addition of ammonium hydroxide, which raised the pH to circa 11. A bluish precipitate was formed, centrifuged, and the supernatant fluid was decanted off, leaving a blue-purple gel. The gel was rinsed three times with deionized water to remove acetates and nitrates, then dried at 140 °C for an hour to remove water and make the material easier to handle. The dried cerium oxide gel was then heated in air at different temperatures in a furnace to produce the desired particle size. A typical yield was between 200 and 300 mg of CeO_2, with no Ce_2O_3 phase. When large batches of greater than 1000 mg were needed, such as industrial tests performed at Ballard Power Systems, several small batches were synthesized and combined and their physical and catalytic properties were measured to get an average composition and performance.

2.1.2 $Ce_{1-x}Pr_xO_2$ Synthesis

$Ce_{1-x}Pr_xO_2$ was synthesized to both determine if praseodymium preferentially segregates in mixed cerium-praseodymium oxides, and to determine the effect of mixed cerium-praseodymium oxides on fuel cell lifetime and performance. To ensure that surface segregation of praseodymium was not an artifact of praseodymium concentration

and method of synthesis, two different methods of $Ce_{1-x}Pr_xO_2$ synthesis were used with three different praseodymium concentrations. For describing the concentration of praseodymium, the atomic percentage will refer to the percentage of cations substituted by praseodymium.

For the first method, cerium(III)acetate (Strem Chemicals) and praseodymium(III)acetate (Sigma Aldrich) were dissolved in deionized water acidified to obtain a solution of approximated 0.1 M metal ions (Ce + Pr), similar to cerium oxide synthesis. To the mixture concentrated nitric acid (Fisher) was added until both the cerium oxide and praseodymium acetates were dissolved (pH = 1). Once both metal acetates were dissolved, 50 v/v% ammonium hydroxide solution (Alfa Aesar) was added to the solution while it was manually agitated until the solution turned white and opaque (pH circa 10). Compared to cerium oxide, the precipitate was less blue suggesting a higher oxidation state for cerium oxide. The solution was centrifuged, then washed with DI water to remove acetate, ammonia, and nitric acid contaminants. This process was repeated three times, at which point the precipitate began to acquire a reddish hue due to the praseodymium. Samples were then dried in an oven at 140 °C for one hour to remove moisture. The dried samples were subsequently transferred to a ceramic boat and heated under air at 400 °C for 4 hours. Similar to the ion-exchange resin method, three different Ce:Pr ratios were attempted in these studies – 85:15, 90:10, and 95:5 Ce:Pr. For comparison, a sample of pure cerium oxide was synthesized by this route as well.

For the second method, circa 6 mg of Amberlite IRC-50 ion-exchange resin (Acros Organics) was added to 20 mL of deionized water. To the mixture, excess ammonium hydroxide solution (Alfa Aesar) until the pH was measured to be 11. The

mixture was shaken for 2 hours with ammonium hydroxide solution added periodically to keep the pH at 11. Once the pH was stable at 11, the mixture was decanted and washed with deionized water until the effluent was of neutral pH. The ion-exchange resin was again submerged in 20 mL of deionized water, and cerium(III)chloride (Acros Organics) and praseodymium(III)acetate (Sigma Aldrich) was added to the mixture in the proper Ce:Pr atomic ratios. The total amount of lanthanide salts added to the resin was 37 % of the weight of the ion-exchange resin prior to dispersion into deionized water. The ion-exchange resin and lanthanide salts were stirred continuously overnight at room temperature. Next, an ammonia-ammonium carbonate buffer solution (0.1 M, pH 10) was added to the ion exchange resin to precipitate out any unexchanged lanthanide salts. The ion-exchange resin solution was then washed five times with deionized water, decanted, and dried at 140 °C until the beads no longer adhered to one another (roughly one hour). To remove the carbon, the beads were heated under ambient air at 200 °C for 2 hours, then at 300 °C for two hours, and finally at 350 °C. Three different attempted Ce:Pr ratios were attempted in these studies – 85:15, 90:10, and 95:5 Ce:Pr. Due to limited microscope time, only HRTEM data for the 85:15 and 95:5 samples were collected. For comparison of the oxidation states of cerium for pure and mixed phases, a sample of pure cerium oxide was synthesized by this route as well. To determine the effects of crystallite size, additional resin-exchange samples were annealed for different times at 350 °C to get particles smaller and larger than 5 nm. Actual Ce:Pr ratios were determined by x-ray fluorescence.

In determining the effects of praseodymium doping on selectivity and activity, two series of cerium-praseodymium oxides were synthesized; one of 5 at %

praseodymium, where at% refers to the atomic percentage of metal cations substituted, and 15 at% praseodymium. All were prepared by the solution-precipitation method used above. For comparison to pure praseodymium (IV) oxide, Pr_6O_{11} (Alfa Aesar), with an average particle diameter of 35.0 nm, was used.

As with pure cerium oxide, typical yield was between 300 and 500 mg of CeO_2, with no Ce_2O_3 phase. When large batches of greater than 1000 mg were needed, such as industrial tests performed at Ballard Power Systems, several small batches were synthesized and combined and their physical and catalytic properties were measured to get an average composition and performance.

2.1.3 $Ce_{1-x}Gd_xO_2$ Synthesis

It has already been established the gadolinium surface segregates in cerium-gadolinium oxides,[1,2] so only a co-precipitation method was used to make $Ce_{1-x}Gd_xO_2$. Two different atomic ratios of cerium to gadolinium were used to compare the effects of concentration on catalytic performance; a cerium to gadolinium ratio of 95:5 and 85:15. A 13 gram mixture of cerium(III)acetate (Sigma Aldrich) and gadolinium(III)acetate (Sigma-Aldrich) of the appropriate cerium-gadolinium atomic ratio was used as stock reagent for nanoparticle synthesis. From this stock reagent, 500-800 mg was added to 50 mL of deionized water and acidified to a pH of 1 using nitric acid to dissolve the cerium(III)acetate, resulting in a clear solution of the dissolved salts. The dissolved mixture was then precipitated by the addition of ammonium hydroxide, which raised the pH to circa 11. A white precipitate was formed, and was centrifuged. The centrifuged mixture was washed three times with deionized water, and unlike with praseodymium, the mixture did not change hue on washing. The washed precipitate was dried in an oven

at 140 °C for one hour, then heated in a furnace for an hour at different temperatures to obtain a variety of particle sizes. For higher gadolinium concentration and larger particle size, the particles had a deeper pink color, but unlike the pure cerium oxide nanoparticles, the particles did not turn a deep yellow color for smaller nanoparticles but instead took on a pale yellow color.

2.1.4 $Ce_{1-x}Zr_xO_2$ Synthesis

Two different atomic ratios of cerium to zirconium were used to compare the effects of concentration on catalytic performance; a cerium to gadolinium ratio of 95:5 and 85:15. A 13 gram mixture of cerium(III)acetate (Sigma Aldrich) and zirconium(IV)acetate hydrate (Sigma-Aldrich) of the appropriate cerium-zirconium atomic ratio was used as a stock reagent for nanoparticle synthesis. Like the cerium-gadolinium syntheses, from this stock reagent 500-800 mg was added to 50 mL of deionized water and acidified to a pH of 1 using nitric acid to dissolve the cerium(III)acetate, resulting in a clear solution of the dissolved salts. The dissolved mixture was then precipitated by the addition of ammonium hydroxide, which raised the pH to circa 11. A white precipitate was formed, and was centrifuged. The centrifuged mixture was washed three times with deionized water, which turned a very deep purple color with each subsequent washing. The washed precipitate was dried in an oven at 140 °C for one hour, then heated in a furnace for an hour at different temperatures to obtain a variety of particle sizes. Particle size and zirconium concentration had no effect on the color of the final nanoparticles; the particles were consistently a faint yellow color.

2.1.5 Ink Synthesis and Membrane Electrode Assembly (MEA) Construction

Inks were made by mixing and 2 % Nafion© solution with a TKK platinum on carbon catalyst (47.9 % wt Pt) and stirring for an hour in a scintillation vial. The platinum in the TKK occasionally caused the isopropanol in the Nafion© solution to ignite, so care had to be used in pouring the TKK into the vial with the Nafion© solution. To minimize the chance of ignition, the Nafion© solution was allowed to sit in the scintillation vial for a few minutes to displace any oxygen in the vial, and the vial was quickly capped on addition of the TKK. After stirring, glycerol was added at 50 % and the total weight of the Nafion© solution, and the mixture was stirred for another hour. Next, tert-butylammonium was added at 5 % of the total weight of the Nafion© solution, and the mixture was stirred for another hour. If pure or mixed cerium oxide were too be added to inks, they were added after the tety-butylammonium was stirred into the nafion solution at 2 % of the weight of platinum, and the mixture was stirred overnight. To build the MEAs, decals were made by painting catalyst inks onto decals and hot pressing to bind the catalyst layer to the PEM. Inks were painted onto decals by hand and the loading of platinum as well as the platinum to cerium ratio were verified using XRF; all cathode decals were circa 0.23 mg Pt/cm^2 and the anode decals were circa 0.18 mg Pt/cm^2.

All MEAs were assembled on site using commercially available Dupont XL proton exchange membranes. The XL membranes were received between two protective plastic sheets, which were removed after the membranes were cut to size. For the un-stabilized and stabilized MEAs, the XL membrane was first boiled in 1 M NaOH for two hours at 150 °C, then in deionized was for two hours at 140 °C, and left to cool in

deionized water overnight. The washed membrane was partially dried at 80 °C for 10 minutes for easier handling, then hot pressed with the decals at 120 psi/cm^2 at 212 °C for 5 minutes, then allowed to cool to room temperature in air. The pressed membranes were then boiled in 1 M sulfuric acid for two hours at 150 °C, then in deionized was for two hours at 140 °C, and left to cool in deionized water overnight.

The finished membranes were partially dried at 70 °C for 10 minutes for easier handling. In assembling the fuel cells, a SGL 25BC gas diffusion later (SGL Group) was used, and black gasket material was used to ensure a good seal between the MEA and the graphite electrodes. The cells were compressed to 50 foot-pounds of torque to ensure good compression of the gasket material without driving the GDL into the membrane.

2.2 Materials Characterization

2.2.1 X-ray diffraction (XRD)

Bragg Brentano X-ray diffraction (XRD) was performed on a Siemens D5000 using a Cu Kα source operating at 40 kV and 35 A. 2 mm anti-scatter slits were used for both the X-ray source and detector positions, and a second 0.6 nm (0.18° acceptance) slit was used immediately before the detector. Samples were measured from 10 ° to 120 ° 2θ at 0.04° step resolution. Whole profile refinements were performed using Jade 9.0 MDI, Inc. on the measured patterns with both $Cu_{K\alpha1}$ and $Cu_{K\alpha2}$ spectral wavelengths used for fitting. The lattice parameter and particle size was refined using an $F_{m\text{-}3m}$ space group with Pseudo-Voidt function was used for the peak profile. Determination of lattice parameter, microstrain, stress, and sample displacement were accomplished using a full Rietveld refinement.[3]

Scherrer broadening was used to estimate the average particle diameter from the microstrain, using the Scherrer Broadening equation used below

$$B(2\theta) = \frac{K\lambda}{Lcos(\theta)}$$

Where B(2θ) is the broadening (full width at half maximum) for the given peak at 2θ, L is the average particle diameter, K is the shape factor, and λ is the wavelength of scattered x-rays. A value of 0.94 was used for the shape factor, which is used for spherical particles. From TEM images, the assumption of spherical particles is not an unreasonable assumption. Occasionally, particle stress was measured using

$$B(2\theta) = \frac{4\varepsilon \sin(\theta)}{\cos(\theta)} = 4\varepsilon \tan(\theta)$$

Where B(2θ) is the broadening (full width at half maximum) for the given peak at 2θ and ε is the degree of strain. Generally strain was ignored for profile fitting, and when included in the analysis was not significant, which is reasonable as such small particle are unlikely to have significant strain, such as non-uniform lattice distortions, dislocations, or grain surface relaxation. Sample displacement was included in fits, using

$$\Delta 2\theta = -\frac{2s\cos(\theta)}{R}$$

Where 's' is the sample displacement and R is the goniometer radius. However, much like strain, when included the sample displacement did not significantly improve the refinement. For most samples, a pseudo-Voigt function was used in profile fitting, as neither Gaussian or Lorentzian functions could adequately for particle sizes less than 20 nm. A Gaussian distribution would have been expected for very large crystallite sizes in order to describe a thermal distribution of lattice positions due to thermal vibrations. A Lorentzian function would be expected from a log-normal distribution of particle sizes,

such as the formation of nanoparticles from solution. However, as the cerium oxide nanoparticles were formed by sintering of particles formed from precipitation, a mixture of Gaussian and Lorentzian functions is needed, with the Pseudo-Voigt function emphasizing the Gaussian contribution.

Additionally, the lattice parameter of the cubic phase was determined using the Bragg equation, below

$$d_{hkl} = \frac{n\lambda}{2\sin(\theta_{hkl})} = \frac{a}{\sqrt{h^2 + k^2 + l^2}}$$

All peak heights were fit individually, and the Rietveld refinement of the entire diffraction pattern was carried out using Jade™. Fitting of all variables for stress, strain, displacement, and lattice parameter were performed using the entire scanned 2θ range. Because of significant scattering at $2\theta < 20°$, 9 points had to be used to reliably fit the background of the diffraction spectrum. For cerium oxide, a single cubic phase was used for fitting. For mixed cerium oxide, it was not possible to reliably fit the measured XRD data using two phases, one for CeO_2 and one for the dopant metal oxide, but it was possible to discount a Ce_2O_3 phase due to the difference in space groups between CeO_2 and Ce_2O_3 (P_{-3m1}).

2.2.2 X-ray Fluorescence (XRF)

For in house measurements, X-ray fluorescence (XRF) was conducted using a Spectrace QuanX with a Rh tube source and a thin copper adsorption edge filter was used to remove lower energy X-rays from the incident beam. The Kα emission lines for cerium and the Lα for platinum were used for analysis. Samples were measured in air for 100 seconds with a filament voltage of 50 kV and filament current of 0.02 mA. Cerium

oxide (CeO_2, Nanomaterials Research Corporation) and a platinum foil Alfa Aesar (99.99%) were used for calibration of the Fundamental Parameters analysis software.

For spatially resolved XRF, the advanced photon source (APS) at Argonne National Laboratory (ANL) was used. The cerium and platinum L_α transitions were measured. Samples were 0.5 cm x 0.2 cm wide, and were cut prior to arrival at APS by freezing the samples in liquid nitrogen and cutting with a razor blade, using the cutter shown in Figure 2.1a and Figure 2.1b. In order to be quantitative between samples, the cut membranes were mounted to the goniometer through a detachable sample holder. An aluminum sample post, Figure 2.1d, was attached to the goniometer, and mounted with two plastic screws to the post were two polycarbonate plates, Figure 2.1e and Figure 2.1f. To hold the sample flat and parallel to the beam, the cut MEAs were sandwiched between the two polycarbonate plates, which were held together by two plastic screws. A composite of the total sample holder is shown in Figure 2.1c. The sample holder in place at Argonne is shown in Figure 2.2. The scan width was 100 μm so that the catalyst layer could be seen and used to align the sample, and 9 scans taken 100 μm apart to get an overall picture of cross section of the MEA. Only the cleanest line scan was reported.

2.2.3 X-ray photoelectron spectroscopy (XPS)

XPS spectra were acquired on a Kratos Axis Ultra DLD X-ray photoelectron spectrometer using a Al Kα source monochromatic operating at 150 W. The base pressure was about $2*10^{-10}$ torr, and operating pressure was circa $2*10^{-9}$ torr. Charge compensation was accomplished using low energy electrons. Standard operating conditions for good charge compensation were –3.1 V bias voltage, -1.0 V filament

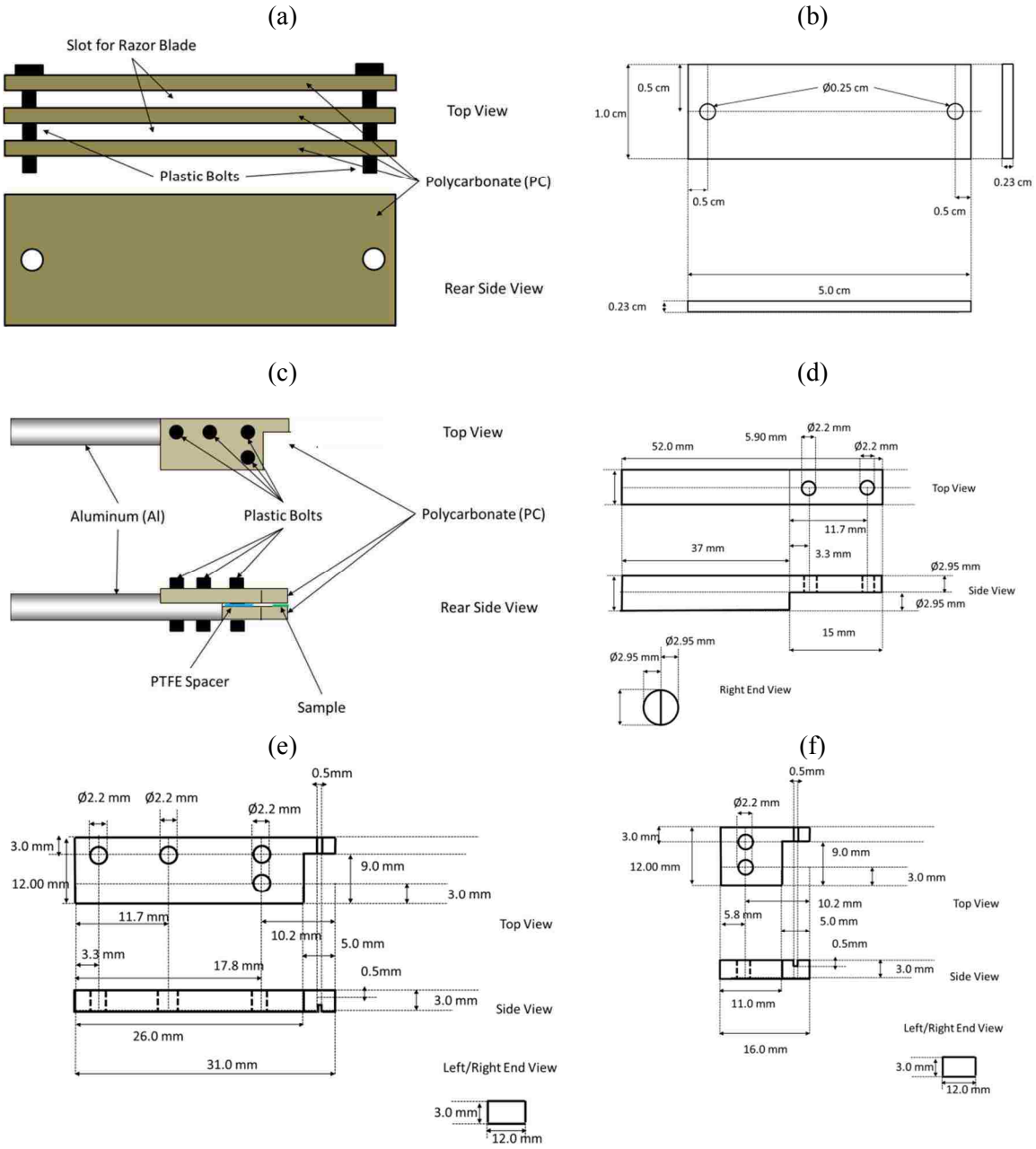

Figure 2.1 Detailed schematic of the sample holder used for spatially resolved XRF of fuel cells. (a) Schematic for sample cutter and (b) detailed design for the cutter, (c) Composite showing how the different components go together for measuring samples at Argonne, (d) aluminum rod for attachment to the goniometer, (e) to polycarbonate plate used for attaching the sample to aluminum rod, and (f) bottom polycarbonate plate for holding sample to top polycarbonate plate.

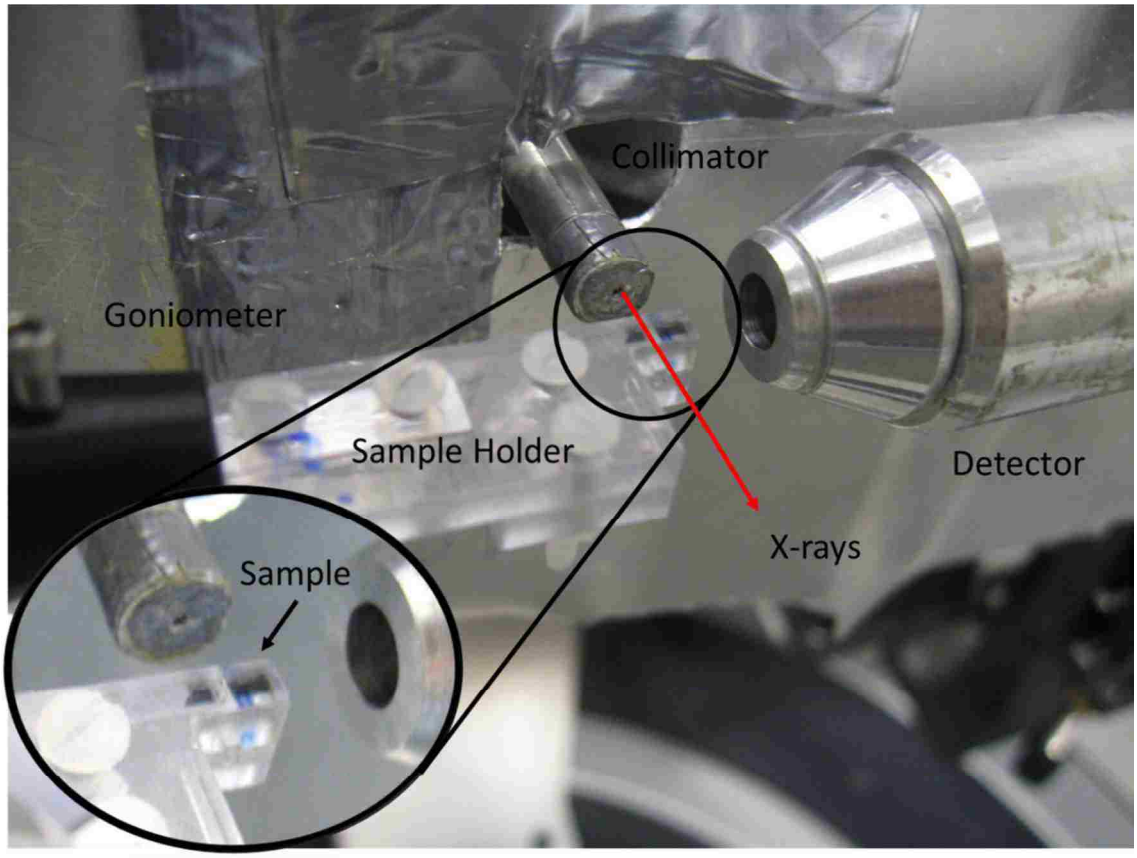

Figure 2.2 Sample positioning and alignment at APS.

voltage and a filament current of 2.1 A. Survey and high-resolution spectra were acquired at pass energies of 80 eV and 20 eV respectively. Data analysis and quantification were performed using CasaXPS software. A 70 % Gaussian/30% Lorentzian line shape was utilized in the curve-fit of spectra.

The Ce 3d edge was used to determine the ratio of Ce^{+3}/Ce^{+4}, using the methods reported in the literature and the peak assignments used by Thornton.[4] Work looking at the effects of varying how the XPS spectrum of cerium is fit using the standard convention for peak assignments has shown that regardless of the method of fitting, ultimately only two species can be seen in the CeO_2 photoelectron spectrum, the +3 and +4 cations,[5] viz., no intermediate oxidation states or species, such as $Ce(OH)_x$. For the Ce^{+3} cation, only one shake up peak is observed for the 3/2 (u-type) and 5/2 (v-type) transitions, corresponding too excitation of the $3d^{10}4f^{1}$ ground state to the $3d^{9}4f^{2}V^{n-1}$ (v^{0},u^{0}) and $3d^{9}4f^{1}V^{n}$ (v',u') final states, where V is the valence band. Furthermore, for the Ce^{+4} cation, there are two shake up transitions observed corresponding to excitations from the $3d^{10}4f^{0}$ to the $3d^{9}4f^{2}V^{n-2}$ (v,u), $3d^{9}4f^{1}V^{n-1}$ (v'',u''), and $3d^{9}4f^{0}V^{n}$ (v''',u''') final states.[6] The energy difference between the shake-up/shake-down peaks for both Ce^{+3} and Ce^{+4} were set to those of Zhang, et la.[7] To assure that the shifts in the XPS binding energy and full-width at half max (FWHM) values were reasonable, bulk cerium oxide which is predominantly Ce^{+4} was used as a benchmark, and resulted in reasonable values for the fit. For quantification of the Ce^{+3}/Ce^{+4} ratio, the following formula was used,[7]

$$Ce(III) = U_0 + U' + V_0 + V'$$

$$Ce(IV) = U + U'' + U''' + V + V'' + V'''$$

$$Ce(III)\% = \frac{Ce(III)}{Ce(III) + Ce(IV)} * 100\%$$

Quantitative determination of the oxidation state of praseodymium is not possible due to the complexities of the XPS spectrum,[8,9] so the peak binding energy of the Pr 3d edge was used to qualitatively describe the oxidation state of the surface praseodymium. Fortunately for the Pr 3d, the difference between the Pr^{+3} and Pr^{+4} binding energies can be as large as 2 eV,[10] making determination of the oxidation state possible, albeit not quantitative. The binding energies for Pr^{+3} and Pr^{+4} lie between 933-933.5 eV[11] and 935-935.5 eV,[12] respectively.

The surface composition of nanoparticles was determined by integrating the area of the Ce 3d and Pr 3d peaks in the survey scan, and taking the ratio of the areas as the atomic ratio of the two cations. Since the attenuation length for the Ce 3d and Pr 3d edges are 1.349 nm, 1.27 nm respectively, the surface penetration of the Ce 3d and Pr 3d edges are comparable, meaning that the cerium oxide and praseodymium depth information from XPS for both edges are describing the same portion of the sample, that is to say, circa 1.3 nm into the surface of the samples.

A linear background subtraction was used for quantification of C1s and O1s spectra, while a Shirley background was applied to Ce a3d and Pr 3d spectra. Sensitivity factors provided by the manufacturer were utilized. Unlike the Ce 3d components, assignments of the O 1s components has not reached a consensus in the literature.[13] For my analysis, I have assigned peaks at 531 and 529 eV to oxygen atoms associated with Ce^{+3} and Ce^{+4},[14,15] respectively, and a further assignment is made to the peak at 533 eV to

the $Ce(OH)_x$.[16,17] An additional assignment for oxygen from isopropanol (from dispersing particles for XRD analysis) at 533 eV and ethers at 535 eV was also used in oxygen peak deconvolution. The carbon 1s spectrum was deconvoluted into peaks assigned to adventitious carbon (circa 285 eV), C-H and C-C (from isopropanol, circa 286 eV), C-O (from isopropanol, circa 287 eV), carbonyls (circa 289 eV), and carbonates (circa 291 eV). For both C and O 1s peak deconvolution, the FWHM was set to 1.4 eV and

2.2.4 High Resolution Tunneling Electron Microscopy (HRTEM)

Electron microscopy was conducted on two different machines High Resolution Transmission Electron Microscopy (HRTEM) and Scanning Electron Transmission Microscopy (STEM) were performed at the University of New Mexico utilizing a JEOL 2010F operating at 200keV. Samples were crushed with pestle and mortar in 100% Ethanol and deposited on holey carbon copper grids. The Advanced Microscopy Lab (AML) at Oak Ridge National Labs provided access to their JEOL 2200FS working at 200keV for aberration-corrected stem imaging. Images were obtained simultaneously in both Bright and Dark field at a resolution of .08nm. Images were processed using DigitalMicrograph™ version 3.6.1, and line scans were plotted in KaleidaGraph™ 4.0.

2.2.5 Scanning Electron Microscopy (SEM)

A Field Emission Instruments Quanta 400F Environmental Scanning Electron Microscope was used to acquire SEM images of membranes after conditioning and accelerated stress testing. To cross-section the MEAs, they were submerged in liquid nitrogen and cold fractured using a fresh razor blade, which was pushed through the anode side of the MEA to minimize the amount of catalyst pushed into the PEM by the

edge of the blade. 5 keV incident electrons, and both backscattered (BSE) and secondary electrons (SE) were used for image formation with the clearest images shown.

For cerium mobility experiments, accelerated stress testing was performed on fuel cells prior to SEM characterization. Once AST testing was finished, cells were then dried under nitrogen at 80 °C at 0 % RH for an hour. The membrane was then frozen in liquid nitrogen and cut with a razor blade to give a clean edge; 0.5 cm wide samples were used for this analysis, and the entire length of the membrane was examined using SEM to ensure that the entire edge was clean, though the captured images only represent 100 μm of the total sample. Since mounting samples in the SEM presented a risk of damaging the sample since it had to be taped to the sample holder, one side of the cleaved membrane was characterized by SEM, and the other was measured using XRF at the Argonne National Labs' Advanced Photon Source (APS) to determine both the cerium and platinum profile.

2.2.6 Nitrogen Absorption

Nitrogen absorption using a QuantaChrome Autosorb IQ_2 was used to determine the porosity and surface area of the synthesized pure and mixed cerium oxides. Initially, 300-500 mg of sample were placed in a 4 mm bore glass absorption tube. To prepare the samples for nitrogen absorption, the samples were put under vacuum at 30 °C overnight to remove absorbed water and contaminants. The full nitrogen isotherm was used, with atmospheric pressure being 580 torr. For surface area, multipoint BET analysis was used using 11 points in a relative pressure range of 0.025 to 0.3535. The reason for multipoint BET was to determine the unitless strength of absorption, C, and verify that it was in the range of 50 to 250, wherein the BET approximation holds. The relationship between the

volume of adsorbed nitrogen, V_m, and the unitless strength of absorption, C, for multipoint BET is given in the following equation;[18]

$$\frac{1}{V\left[\frac{1}{P_r}-1\right]} = \frac{1}{V_m C} + \frac{C-1}{V_m C}(P_r)$$

Where V is the volume of nitrogen adsorbed, V_m is the monolayer volume, P_r is the reduced pressure (P/P_0), and C is the strength of adsorption. In most samples, the enthalpy of absorption was near 200. Absorption hysteresis was used to estimate the pore shapes, and desorption points from a relative pressure from 1.0 to 0.3764 were used to determine pore size distribution and pore volume using the BJH method. For all pure cerium oxides, the surface area was within 80-90 % of the expected surface as determined by the average particle diameter. However, for the mixed cerium oxides, the surface areas were 10-30 % of the surface area predicted from the average particle diameter. Regardless of composition, however, the CeO_2 showed little microporosity and Type I desorption behavior, viz., cylindrical pores. Typical values for average pore diameter and pore volume for CeO_2 were circa 16.5 Å and 0.06 mL/g, respectively.

2.3 Catalytic Characterization

2.3.1 Reactivity

To determine reactivity, a small scintillation was used as a batch reactor and the amount of oxygen evolved by peroxide decomposition was quantified using an inverted burette. Less than fifty milligrams of sample, with the mass used varied to have approximately the same amount of accessible surface area, was added to 1 mL of deionized water and stirred with a magnetic stir bar for one minute to disperse the nanoparticles. To the nanoparticle-water mixture was added 30 % w/w hydrogen

peroxide (Sigma Aldrich); the mixture was sealed in a glass vial with a port connected to an inverted burette. The amount of oxygen evolved was measured every five minutes, and the resulting oxygen volume versus time was fit to a first order exponential decay. The observed rate constant was normalized to the surface area of the catalyst used. In general, higher activity nanoparticles turned deep red for very reactive nanoparticles, deep orange for moderately reactive nanoparticles, and only slight yellowing for poorly reactive nanoparticles. Particles little or no reactivity had no color change.

2.3.2 Selectivity

To determine the selectivity, a method similar to the method used by Ramani, et al., was employed.[19] Summarized briefly, 23.5 mg of 6-carboxyfluoroscein (6CF, Sigma-Aldrich) was added to 250 mL of 1 % hydrogen peroxide. 30 mL of the 6CF-peroxide solution was added to an open beaker, and to it was added less than fifty milligrams of sample; as with the peroxide, the amount of sample added was scaled to maintain the same accessible surface area between samples. Using a multidiode UV-vis spectrometer (Hewlett Packard), the amount of loss in the 492 nm peak was used to quantify the amount of 6CF remaining in solution. Measurements were taken every five minutes for an hour, and the loss of 6CF was fit to a first order exponential decay. This rate was normalized to the nitrogen BET accessible surface area of the catalyst used. The selectivity of the reaction was defined as the normalized rate constant of oxygen production divided by the normalized rate of 6CF decomposition. However, since for large cerium oxide nanoparticles the normalized rate of 6CF decomposition was nearly zero, viz., the selectivity was infinite, the inverse selectivity (normalized rate of 6CF decomposition divided by the normalized rate of oxygen evolution) is reported. Because

6CF degrades over time due to heat and light, 6CF was only used if it was less than 3 months old. For samples which generated a large concentration of free radicals, the solution turned from green to orange, but for samples which generated very few free radicals, the 6CF solution remained green.

2.3.3 Accelerated Stress Testing (AST) of Fuel Cells

For all OCV stress testing, 50 cm^2 cells were used. Cells were conditioned by running at 80 °C and 100 % relative humidity (RH) for overnight. Beginning of life testing was carried out after conditioning at both 30 °C and 100 % RH, and 80 °C and 30 % RH. For beginning of life testing, the high frequency resistance, limiting current, power-density, and impedance spectroscopy were carried out at operating pressures and flow rates with hydrogen and air, and impedance spectroscopy, hydrogen cross over, and cyclic voltammetry were measured at 4 psi and 500 sccm gas flows with hydrogen and nitrogen. For the accelerated stress tests, hydrogen was flowed at 700 sccm and 26 psi backpressure was maintained on the anode while 1669 sccm of air with 18 psi backpressure was maintained on the cathode; the cell was held at 80 °C and the carrier gas was bubbled through a constant temperature water reservoir to give 30 % RH. The cell was allowed to operate under open circuit potential, except when tested every 24 to 72 hours to assess cell degradation. Downstream from the fuel cell, a jacketed condenser was used to remove water vapor from the exhaust gases so that the fluorine emission rate of both the anode and cathode could be measured. AST was stopped when open circuit potential dropped beneath 0.7 V, at which point impedance spectroscopy and limiting current measurements were impossible, or the cross over current looked ohmic, which was indicative of a pin-hole leak in the cell.

As a baseline, unmodified Dupont XL membrane used as received, containing both cerium cations and silica nanowires, were subjected to stress testing. Unlike the unstabilized and stabilized membranes, the control XL membranes were not boiled in sodium hydroxide or sulfuric acid; the as received membrane was pressed with decals at 80 °C for fifteen minutes, and then conditioned and tested as the other cells were.

2.3.4 Alternating Current (AC) Impedance Spectroscopy

Three different AC impedance spectrum measurements were used to characterize the performance of fuel cells using a Nyquist plot. The input sine wave was treated as a pure sine wave, and output was treated as a complex mixture of sine and cosine waves, represented as

$$S(t) = f(C,R)e^{(\theta+i\omega)t}$$

Where S(t) is the output signal, f(C,R) is a combination of the different capacitances, C, and resistances, R, found within the cell, and θ is the phase angle. High frequency impedance measurements were used to determine the high frequency resistance (HFR) of the fuel cell, which is a measure of the resistance to hydrogen transport across the proton exchange membrane. The cell was characterized under the same conditions as the AST. For these measurements, the cell was voltage was lowered to circa 0.1 V to lower the potential so that cation distributions in the cell were not due to electrostatic effects, as well as to operate the cell in a reaction-limited potential whereby hydrogen transport should be the only limitation. The measurement must be taken at constant current, so the current chosen was one which lowered the cell potential to circa 0.1 V. A 0.05 V sine wave with a frequency of 3 kHz was passed through the fuel cell, and the cell resistance was calculated from the phase change. For HFR measurements,

the phase angle of the output signal must be zero, which is difficult to do without measuring the full impedance spectrum. So when the phase angle was less than 10 ° then the calculated cell resistance was accepted as the HFR.

The next impedance spectrum was used to calculate the diffusion resistance of oxygen through the cathode catalyst layer. The cell was operated under AST conditions, with the cell held at 0.850 V and a sine wave of amplitude of 0.01 V was used. The frequency of the sine wave was varied from 100 kHz to 100 mHz with 10 points per decade of frequency changes. The resulting phase change was plotted on a Niquist plot. The cell was modeled as a combination of resistors and capacitors, with the resistance of hydrogen diffusion assumed to be very small.

The intercept of the low frequency arc with the x-axis was treated as the low frequency impedance (LFI), that is to say, the resistance to oxygen diffusion through the catalyst layer. A typical LFI spectrum is shown in Figure 2.3.

Finally, an impedance spectrum was taken of the fuel cell operated at 80 °C at 100 RH with 500 sccm flow of hydrogen on the anode at 4 psi and 500 sccm of nitrogen flow over the cathode at 4 psi after equilibration for 30 minutes. The impedance spectrum was taken in the same fashion at the LFI measurement, but at 0.2 V. No quantitative results were taken from this spectrum, but rather, it was used to qualitatively describe the permeation of the PEM. For an impermeable membrane, the capacitance of the membrane should be infinite and therefore at the sine wave is swept towards lower

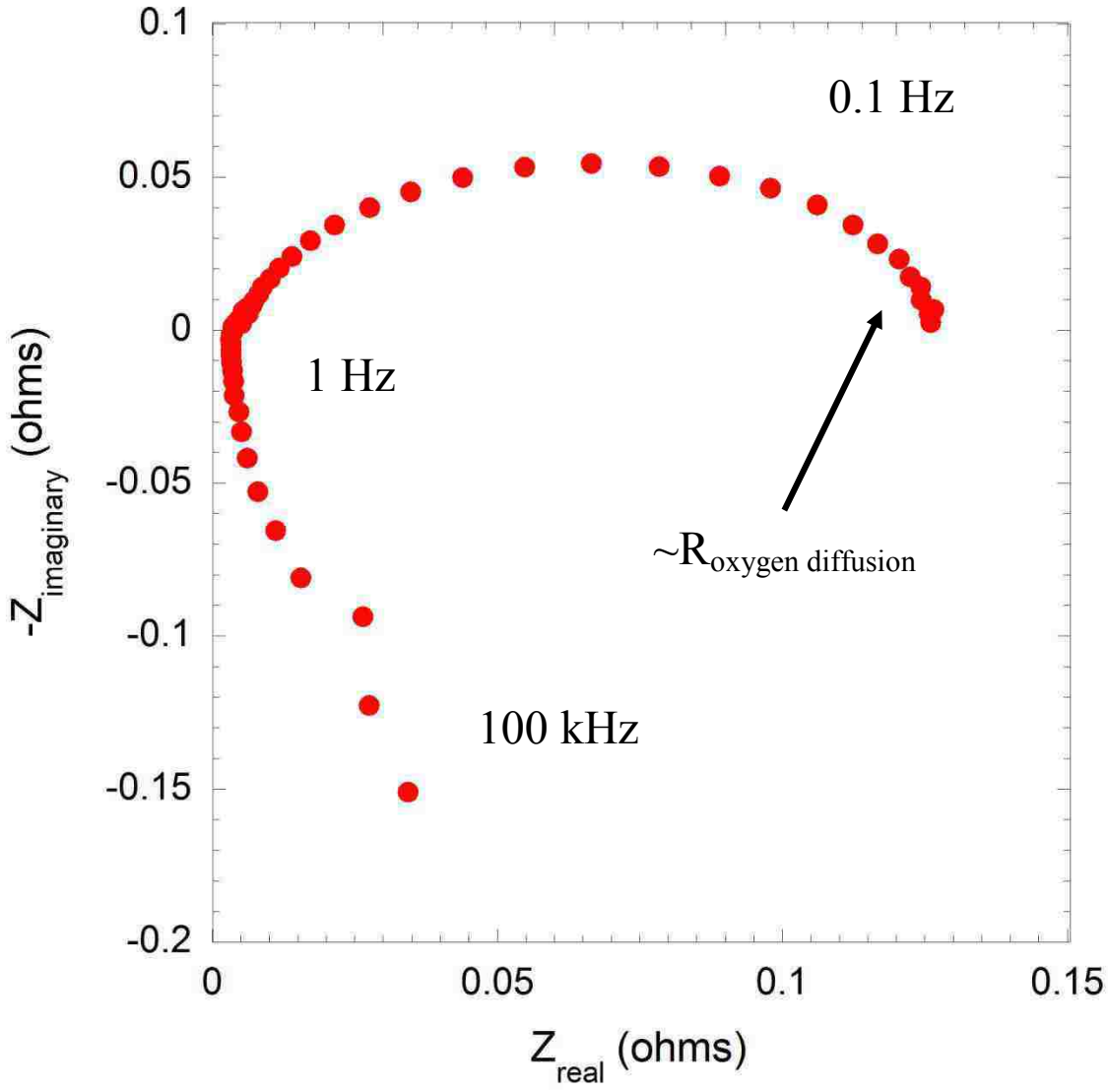

Figure 2.3 Impedance spectrum of a fuel cell under AST conditions and 0.85 V. The intercept of the low frequency arc is roughly the low frequency resistance or the resistance for oxygen transport through the cathode catalyst layer.

frequencies, the resulting Nyquist plot should show an asymptotic rise. However, for a membrane nearing failure, the Nyquist plot should begin to resemble that of the LFI plot. An overlay of two different impedance spectra as shown in Figure 2.4; the conditioned cell shows the expected asymptotic behavior, whereas the cell as it nears failure shows finite capacitance.

2.3.5 Direct Current (DC) Cell Characterization

Three DC cell characterizations were used to determine cell performance. The first was carried out under AST conditions, with the cell potential swept from 0.9 V to 0.7 V and the DC current measured. This sweep, referred to as a VIR curve, show the performance of the cell under diffusion-limited conditions, and shifts towards lower and lower current density as the cell begins to degrade.

The second two DC cell characterizations were carried out at 80 °C at 100 RH with 500 sccm flow of hydrogen on the anode at 4 psi and 500 sccm of nitrogen flow over the cathode at 4 psi after equilibration for 30 minutes. For the first characterization, referred to as a current-voltage (CV) plot, the cell potential was swept from 0.1 V to 1.0 V at a rate of 20 mV/s then back to 0.1 V three times. The first sweep was used to remove contaminants on the surface of the platinum catalyst in the anode. The second and third sweep were used to quantitatively determine the electrochemical accessibility of platinum in the anode catalyst layer. Current is negative in these curves as electrons are flowing from the cathode to the anode. The first peak at circa 0.25 V corresponds to the electrochemically accessible surface area (ECSA) of platinum on the anode side, that is to say, platinum which is at the three phase boundary of platinum, Nafion®, and carbon. This is in contrast to actual platinum surface area, which would be measured not under

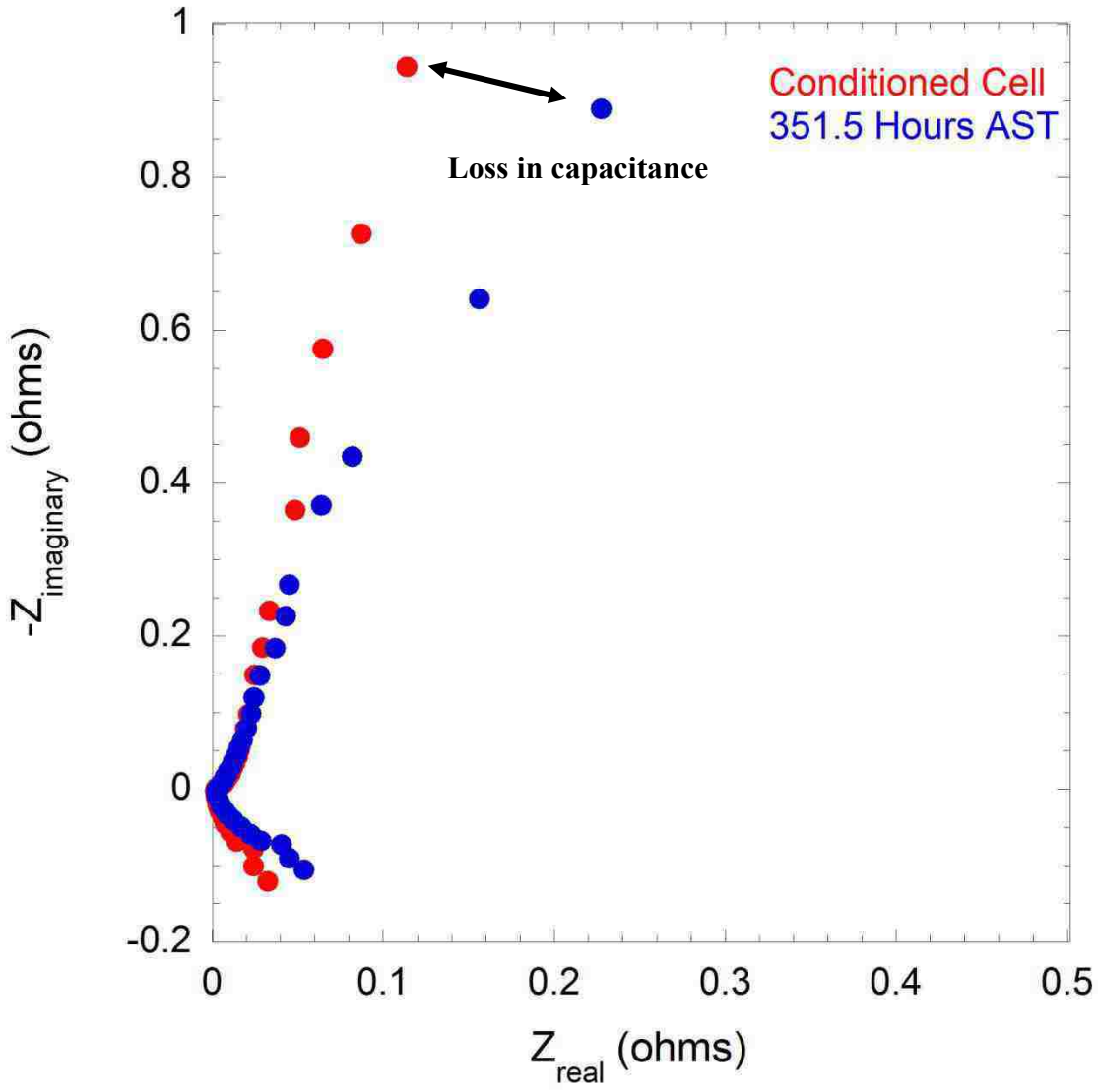

Figure 2.4 Impedance spectrum of a fuel cell at 80 C and 100 % RH, with 500 sccm flow of hydrogen in the anode and 500 sccm of nitrogen in the cathode, after 30 minutes of equilibration. The red curve is of the cell after conditioning and the blue curve is after 352 hours of accelerated stress testing.

electrochemical conditions, but instead by absorbing hydrogen gas to the platinum and measuring the volume desorbed upon heating. The area is calculated by integrating the area from 0.2 V to 0.4 V, as shown in Figure 2.5, and converting the integrated current to by converting from amperes to Coulombs, and dividing by 210 microcoulombs/cm^2. One set of peaks greater than 0.8 V is attributed to the formation of $Pt(OH)_x$ species. The hysteresis of the CV curve can be used as an estimate of the capacitance of the PEM; the larger the gap between the forward and reverse sweeps, the larger the capacitance of the PEM.

The second DC characterization was a measure of the hydrogen crossover, and like the CV curves, the current is negative as flow of electrons is from the cathode to the anode. The cell was swept from 0.1 V to 0.4 V at a rate of 2 mV/s, and a typical crossover curve is shown in figure 2.6. The use of a slow rate of sweep was used to allow sufficient time for hydrogen desorption from the anode catalyst layer. The current at 0.270 mV and 0.400 mV was used for hydrogen crossover unless there was noise in the data, at which a narrow range within the 0.270 to 0.400 mV range was used. A linear regression was fit between the currents at 0.270 mV and 0.400 mV, and the y-intercept was used to determine the hydrogen cross over and was normalized by multiplying by area of the cell.

2.4 Molecular Mechanics/Molecular Dynamics Simulations

The DL_POLY implementations was used to carry out the MM/MD simulations.[20] VMD software was used for visualization of beginning and ending structures, as well as to calculate the radial distribution function (RDF).[21] Metal-oxygen interactions were modeled using a Buckingham Potential, as well as the metal-metal

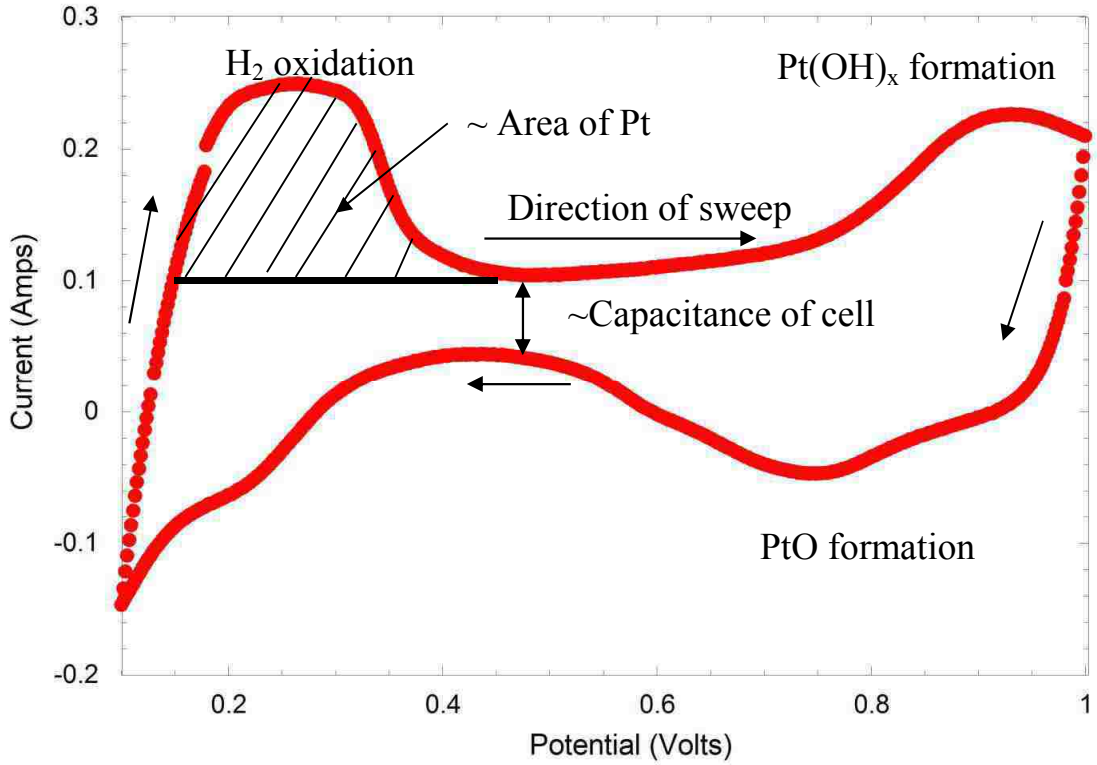

Figure 2.5 Cyclic voltammetry (CV) curve of a fuel cell at 80 C and 100 % RH, with 500 sccm flow of hydrogen in the anode and 500 sccm of nitrogen in the cathode, after 30 minutes of equilibration. The second cycle is shown.

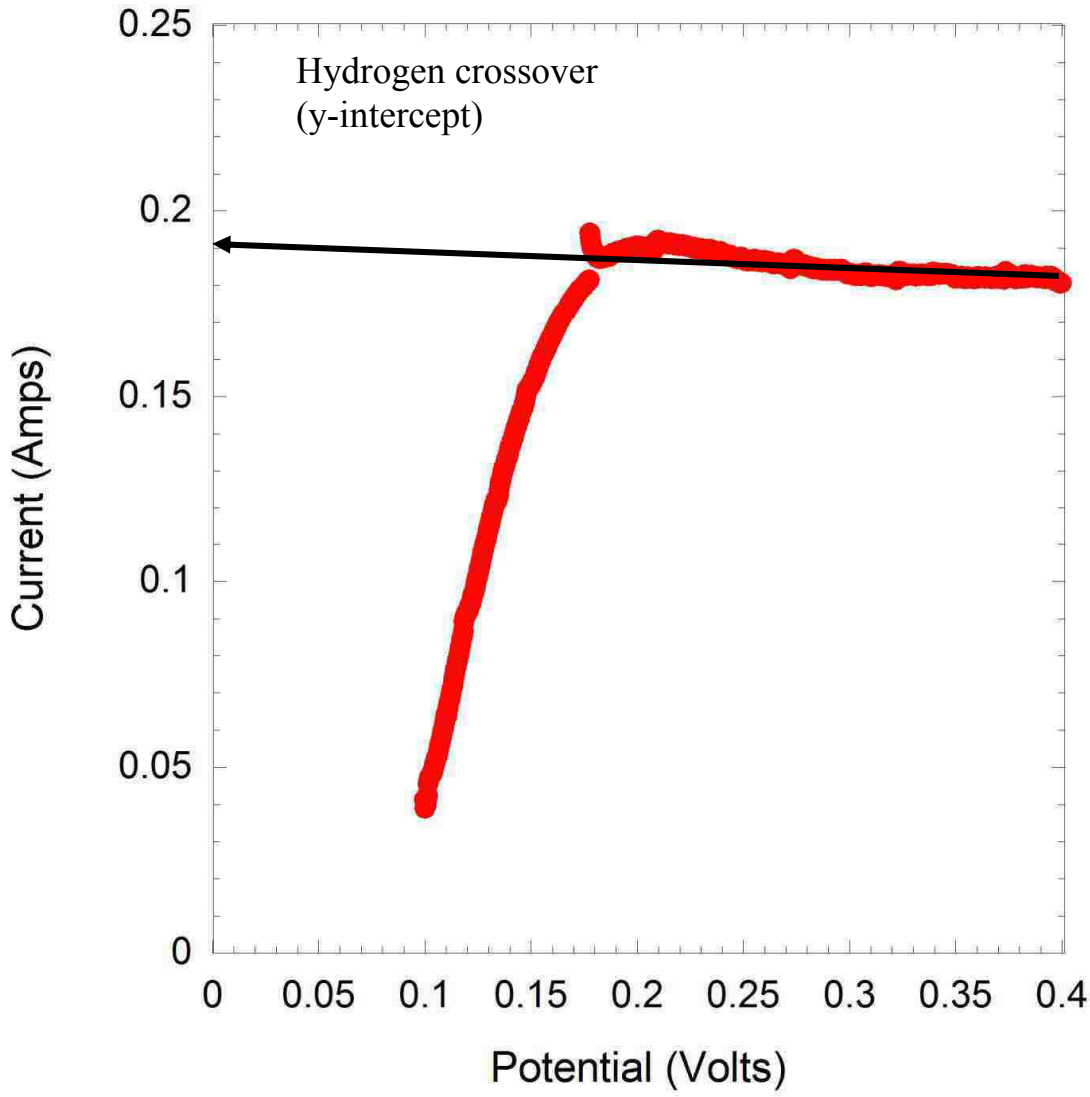

Figure 2.6 Hydrogen crossover measurement of a fuel cell at 80 C and 100 % RH, with 500 sccm flow of hydrogen in the anode and 500 sccm of nitrogen in the cathode, after 30 minutes of equilibration.

interactions. All atoms were treated as hard shell ions, with cerium and praseodymium having a +4 charge and oxygen having a -2 charge. Potentials for cerium was those used by Dao, et al.,[22] while the potentials for praseodymium were calculated by using a force balance on a praseodymium atom in a slab within a radius of 10 Å, the cutoff using in the MM simulations. The potentials are reported in table 2.1.

For a starting configuration, 4,630 cerium cations and 9,260 oxygen atoms, corresponding to a 5 nm particle, were modeled for 700 picoseconds, well past equilibration, at 7,000 K. Simulations were run with periodic boundary conditions in a 30 nm cubic box. Once the starting configuration was obtained, 692 praseodymium atoms, roughly 14.9 at% substitution, were substituted for cerium cations in five configurations. The two configurations were a CeO_2@PrO_2 and CeO_2@$CePrO_x$ structure which would represent the inverse of what was expected experimentally. Next, a $Ce_{0.85}Pr_{0.15}O_2$ mixed metal oxide, which is what would be expected for a mixed metal oxide, was run. Finally, a PrO_2@CeO_2 and $CePrO_x$@CeO_2 structure were run, which would be consistent with the HRTEM data previously reported. Structures were run for 380 picoseconds and 4000 K, well beyond the time needed for crystallization.

Table 2.1 MM Parameters for the Buckingham Potentials used in simulating cerium, praseodymium, and oxygen interactions

	$U_{(r_{ij})} = A * e^{\left(-\frac{r_{ij}}{\rho}\right)} - \frac{C}{r_{ij}^6}$		
Interaction	**A (eV)**	**ρ (nm)**	**C (eV/nm^6)**
Ce^{+4}-O^{-2}	1986.83	0.351	20.40
Pr^{+4}-O^{-2}	1948.71	0.351	20.28
O^{-2}-O^{-2}	22764.0	0.149	14.43

2.5 References

(1) Huang, H.; Gur, T. M.; Saito, Y.et al. *Appl. Phys. Lett.* **2006**, *89*.

(2) Lee, H. B.; Prinz, F. B.; Cai, W. *Acta Mater.* **2010**, *58*, 2197.

(3) Speakman, S. A. 2003.

(4) Burroughs, P.; Hamnett, A.; Orchard, A. F.et al. *J. Chem. Soc., Dalton Trans.* **1976**, 1686.

(5) Holgado, J. P.; Alvarez, R.; Munuera, G. *Appl. Surf. Sci.* **2000**, *161*, 301.

(6) Pfau, A.; Schierbaum, K. D. *Surf. Sci.* **1994**, *321*, 71.

(7) Zhang, F.; Wang, P.; Koberstein, J.et al. *Surf. Sci.* **2004**, *563*, 74.

(8) Bianconi, A.; Kotani, A.; Okada, K.et al. *Phys. Rev. B: Condens. Matter* **1988**, *38*, 3433.

(9) Hu, Z.; Kaindl, G.; Ogasawara, H.et al. *Chem. Phys. Lett.* **2000**, *325*, 241.

(10) Moulder, J. F.; Stickle, W. F.; Sobol, P. E.et al. *Handbook of X-ray Photoelectron Spectroscopy*; Physical Electronics, Inc.: Eden Prairie, Minnesota, 1995.

(11) Kondo, H.; Matsui, H.; Furuta, K.et al. *Japanese Journal of Applied Physics* **2010**, *49*.

(12) Schaefer, A.; Gevers, S.; Zielasek, V.et al. *J. Chem. Phys.* **2011**, *134*.

(13) Wang, A. Q.; Punchaipetch, P.; Wallace, R. M.et al. *J. Vac. Sci. Technol., B* **2003**, *21*, 1169.

(14) Mullins, D. R.; Overbury, S. H.; Huntley, D. R. *Surf. Sci.* **1998**, *409*, 307.

(15) Praline, G.; Koel, B. E.; Hance, R. L.et al. *J. Electron. Spectrosc. Relat. Phenom.* **1980**, *21*, 17.

(16) Swiatowska, J.; Lair, V.; Pereira-Nabais, C.et al. *Appl. Surf. Sci.* **2011**, *257*, 9110.

(17) Koel, B. E.; Praline, G.; Lee, H. I.et al. *J. Electron. Spectrosc. Relat. Phenom.* **1980**, *21*, 31.

(18) Neimark, A. V.; Sing, K. S. W.; Thommes, M. In *Handbook of Heterogeneous Catalysis*; 2nd ed.; Ertl, G., Knozinger, H., Schuth, F., Weitkamp, J., Eds.; Wiley: 2008, p 721.

(19) Prabhakaran, V.; Arges, C. G.; Ramani, V. *Proceedings of the National Academy of Sciences of the United States of America* **2012**, *109*, 1029.

(20) Todorov, I. T.; Smith, W.; Trachenko, K.et al. *J. Mater. Chem.* **2006**, *16*, 1911.

(21) Humphrey, W.; Dalke, A.; Schulten, K. *J. Mol. Graph. Model.* **1996**, *14*, 33.

(22) Das, S.; Singh, S.; Dowding, J. M.et al. *Biomaterials* **2012**, *33*, 7746.

Chapter 3: Praseodymium Enrichment of $Ce_{1-x}Pr_xO_2$ Materials

3.1 Introduction

Cerium oxide has found widespread use in the field of catalysis as a catalytically active oxide[1-3] and doped oxide,[4,5] as well as an excellent support for other catalysts[6-9] due to its ability to easily change its oxidation state through either water, free oxygen,[10] or the use of bulk oxygen.[11] In order to expand on the catalytic properties of cerium oxides, dopants such as praseodymium[12-14] and gadolinium[15] have been used to increase the electrical conductivity of cerium oxide. However, while many groups have reported on the synthesis of these mixed metal oxides, there is little known about where these dopants are incorporated into the cerium oxide lattice,[16] nor is there much known about the effect of doping on the activity and selectivity of cerium oxide.

Because many of the reactions catalyzed by cerium oxide are considered to be catalyzed by the surface Ce^{+3} sites,[17] it would be preferably that the addition of dopants to cerium oxide would not occlude or substitute these sites, but would instead increase the activity of these sites, so a dopant which is not likely to substitute surface sites would be ideal. Due to both CeO_2 and PrO_2 sharing the same space group, F_{m-3m}, and both Pr^{+3}/Ce^{+3} and Pr^{+4}/Ce^{+4} cations having nearly the same ionic radii, 1.13 Å and 0.95 Å,[18] respectively, it is reasonable to assume *a prior* that substitution of cerium by praseodymium is random so that incorporation of small amounts of praseodymium bulk lattice should have a low probability of substituting catalytically active Ce^{+3} sites. But attempts have been made to determine the location of these dopants,[16,19] and direct evidence as to the location and the chemical state of these dopants remains elusive. Of the reports on the structure of these mixed metal oxides, x-ray diffraction (XRD)

evidence shows a consistent fluorite lattice, the same as that of pure cubic cerium oxide, for praseodymium doping levels up to 20%;[20,21] because cerium oxide and praseodymium oxide have both the same space group and have lattice constants that vary less than 10%, it is impossible to show by XRD if two separate cubic phases exist. For praseodymium concentrations about 20%, it is possible see the onset of a clear second phase, [20,21] but it is not known if this second phase can be attributed to phase separation due to the higher praseodymium concentration or better resolution of a second phase which was not visible at lower praseodymium concentration. Raman spectroscopy has been used to determine the concentration of praseodymium as a function of laser depth,[16] and while the results are consistent with a core-shell structure, complications due to the inherent complexities of diffuse spectroscopy make this technique far from direct evidence of praseodymium surface enrichment. To the best of the authors' knowledge, no one has directly demonstrated whether dispersion through the bulk or preferential segregation to the surface has been demonstrated, and the effect of praseodymium incorporation has on the oxidation state of cerium and the subsequent effect on the activity and selectivity of cerium oxide. In this work, I demonstrate via high resolution tunneling electron microscopy (HRTEM) with spatially resolved EDS that praseodymium preferentially surface segregates, so that the center of the mixed oxide cerium oxide nanoparticles are predominantly cerium oxide in a fluorite crystal structure, explaining the preservation of the cubic crystal structure. Moreover, it will be shown that the praseodymium atoms are mostly on the surface of the nanoparticles, and from XPS it was shown that the dopants reduce the number of Ce^{+3} sites. As the Ce^{+3} sites are considered responsible for some of the reactions of interest for cerium oxide,[17] knowing that praseodymium removes surface

Ce^{+3} must be considering when using this dopant to promote or suppress the reactions of cerium oxide. We show that for low praseodymium dopings, viz., 5 at% Pr, improvements in activity can be seen without a loss in selectivity, but at 15 at% Pr a loss in both activity and selectivity is seen.

3.2 Results

3.2.1 XPS and XRF

Table 3.1 shows the composition of each of the nanoparticles used for HRTEM as determined by XRF, as well as the percentage of Ce^{+3} as determined by XPS, and the lattice parameter and average crystallite size as determined by XRD. From the Ce 3d XPS spectra for both the ion-exchange resin samples, Figure 3.1, and for solution-precipitation samples, Figure 3.2, the $L_{1/2}$ and $L_{3/2}$ transitions for the Ce^{+4}, at circa 883 eV and 902 eV, respectively, are far more pronounced than the analogous transitions for Ce^{+3}, and circa 882 eV and 899 eV, respectively. Moreover, when comparing the features of nano-cerium oxide and bulk cerium oxide for both methods of synthesis, the pronounced features of Ce^{+3}, specifically the shake-up transition at circa 885 eV and the main transition at 899 eV, are far more prominent than in the samples which contain praseodymium. For increasing bulk concentrations of praseodymium, there is little change see in the Ce^{+3}/Ce^{+4} ratio beyond 3 at% praseodymium. It can also be seen in Table 3.1 that a significant number of Ce^{+3} sites are no longer present in praseodymium containing cerium oxides relative to CeO_2, and that the surface cerium oxide sites of the doped nanoparticles are now predominantly Ce^{+4}.

Table 3.1 Comparison of the crystallite size and lattice constant for nanoparticles synthesized by ion exchange resin and solution-precipitation methods

Ion Exchange Resin				**Solution-Precipitation**			
Pr:Ce By XRF	**Average Crystallite size (nm)**	**Lattice Parameter (Å)**	**Percentage Ce^{+3} By XPS**	**Pr:Ce By XRF**	**Average Crystallite size (nm)**	**Lattice Parameter (Å)**	**Percentage Ce^{+3} By XPS**
15 : 85	2.90	5.4417	14%	13 : 87	5.00	5.4250	19%
15 : 85	4.61	5.4080	16%	10 : 90	4.81	5.4246	18%
15 : 85	13.34	5.4042	15%	3 : 97	4.98	5.4152	18%
12 : 88	4.84	5.4159	12%	0 : 100	4.87	5.4042	26%
11 : 89	5.00	5.4199	14%				
3 : 97	4.87	5.4068	16%				
0 : 100	4.83	5.4078	23%				

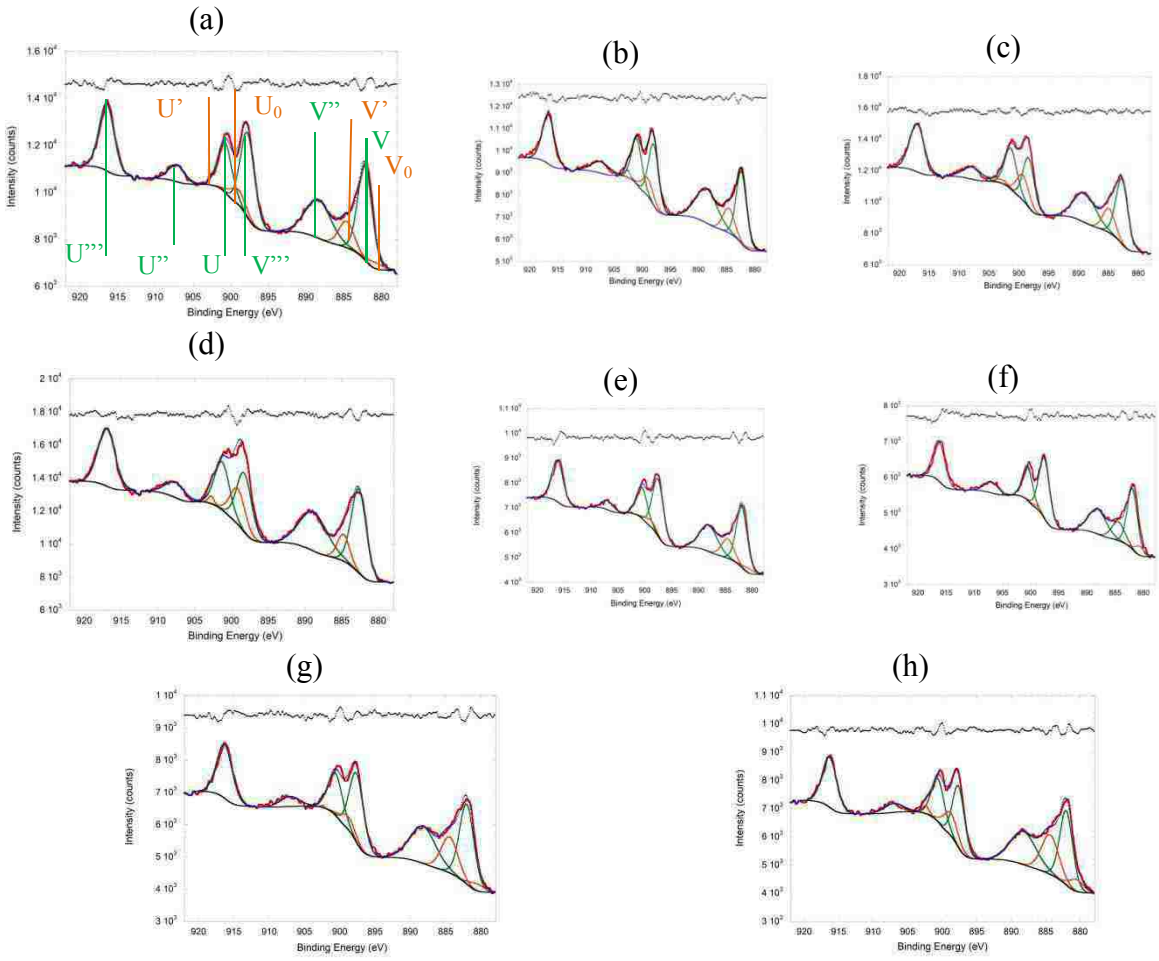

Figure 3.1 Ce 3d XPS spectra for (a) bulk CeO_2, (b) 2.9 nm 15:85 Pr:Ce $CePrO_x$, (c) 4.61 nm 15:80 Pr:Ce $CePrO_x$, (d) 13.34 nm 15:85 Pr:Ce $CePrO_x$, (e) 4.84 nm 12:88 Pr:Ce $CePrO_x$, (f) 5.00 nm 11:89 Pr:Ce $CePrO_x$, (g) 4.87 nm 3:97 Pr:Ce $CePrO_x$, and (h) 4.83 nm synthesized CeO_2, as made by an ion exchange resin. The transitions for the Ce^{+4} species are shown in green, the transitions for the Ce^{+3} species are shown in orange, data is shown in red, the fit is shown in blue, the background is shown in black beneath the data, and the residuals of the fit are shown in black above the data. For clarity, the labels for the Ce^{+3} and Ce^{+4} transitions are only labeled on the first spectra.

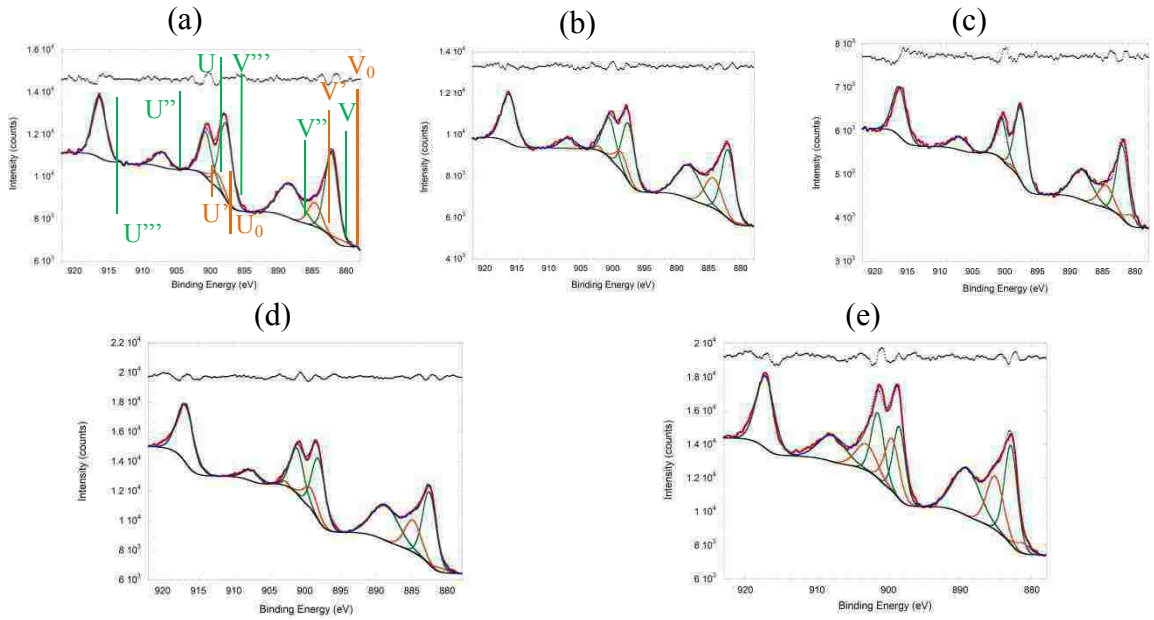

Figure 3.2 Ce 3d XPS spectra for (a) bulk CeO_2, (b) 5.00 nm 13:87 Pr:Ce $CePrO_x$, (c) 4.81 nm 10:90 Pr:Ce $CePrO_x$, (d) 4.98 nm 3:97 Pr:Ce $CePrO_x$, and (e) 4.87 nm synthesized CeO_2, as made by the solution method. The transitions for the Ce^{+4} species are shown in green, the transitions for the Ce^{+3} species are shown in orange, data is shown in red, the fit is shown in blue, the background is shown in black beneath the data, and the residuals of the fit are shown in black above the data. For clarity, the labels for the Ce^{+3} and Ce^{+4} transitions are only labeled on the first spectra.

From the Pr 3d it can be seen that most of the observed signal is from Pr^{+3} as evident by the large, prominent peak near 933.5 eV, which is to be expected.[22] For constant concentration – 15% praseodymium – but varying crystallite size, the peak of the Pr 3d transition remains constant. However, for decreasing praseodymium concentration as constant crystallite size – circa 4.9 nm – a shift from 933.8 to 933.0 can be seen, consistent with a higher proportion of Pr^{+3} sites. By integrating the area of both the Ce 3d and Pr 3d transitions in the survey scan, the cerium-praseodymium ratio was determined for the surface of the nanoparticles, viz., 1.4 nm into the surface, which is the attenuation length of the ejected electrons for both transitions.

3.2.2 XRD

For all syntheses a single CeO_2 profile (fluorite structure) phase could be seen, with the lattice parameter increasing as the amount of praseodymium is increased in agreement with the literature. From Table 3.1, the nanoparticles from the solution-precipitation method consistently show a larger lattice parameter for similar sizes, suggesting a less densely packed nanoparticle. It can also be seen that for mixed cerium-praseodymium oxide nanoparticles, and expansion of the lattice constant with increasing praseodymium content can also be seen, which is in agreement with Balaguer, et al.[22]

3.2.3 HRTEM and EDX

Figure 3.4 and Figure 3.5 show TEM images of ion-exchange resin and solution-precipitation method. Figure 3.4 shows bright field images of different particles and composition making the contrast of the crystals and the background easier to see; from these images, it can be seen that there is no amorphous phase present on the particles, and

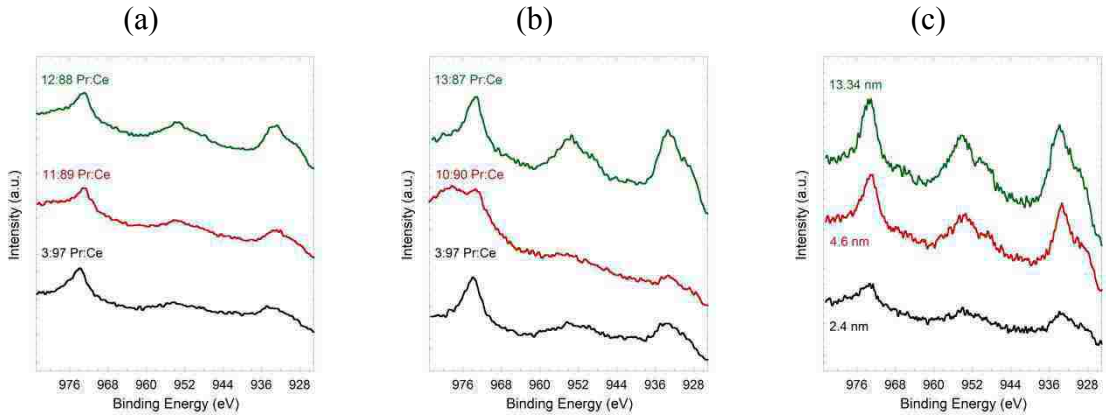

Figure 3.3 Pr 3d XPS spectra for (a) $Ce_{2-y}Pr_yO_x$ nanoparticles made by ion-exchange resin with varying compositions, (b) $Ce_{2-y}Pr_yO_x$ nanoparticles made by precipitation with varying compositions, and (c) $Ce_{0.85}Pr_{0.15}O_x$ nanoparticles made ion-exchange resin with different crystallite sizes.

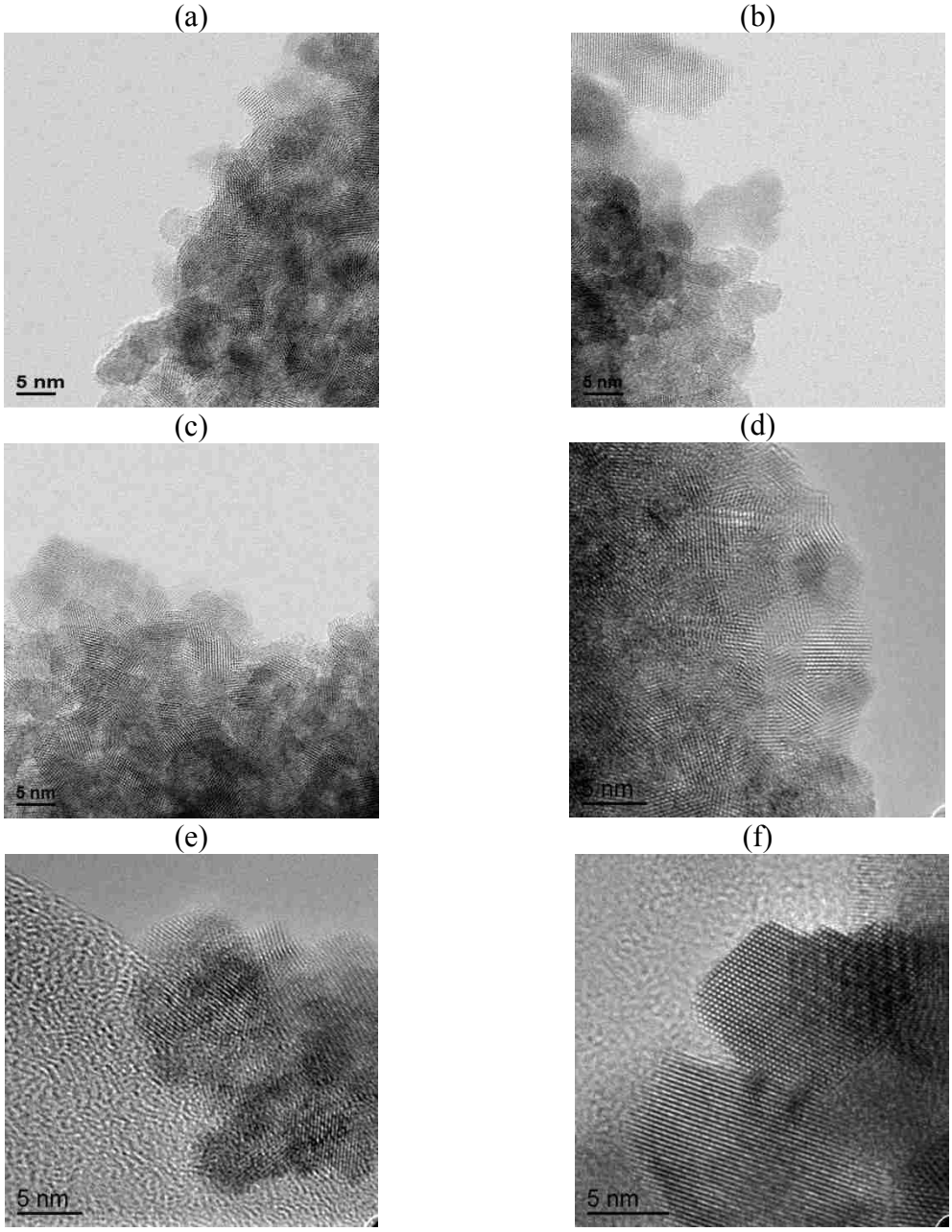

Figure 3.4 Bright field tunneling electron microscope (TEM) images for (a) 4.81 nm 10:90 Pr:Ce $CePrO_x$, (b) and 4.98 nm 3:97 Pr:Ce $CePrO_x$ made by the solution method, (c) 4.87 nm 3:97 Pr:Ce $CePrO_x$, (d) 2.90 nm 15:85 Pr:Ce $CePrO_x$, (e) 4.61 nm 15:85 Pr:Ce $CePrO_x$, and (f) 13.34 nm 15:85 Pr:Ce $CePrO_x$ made by the solution method. No particles show an amorphous surface phase.

for both large and small particles, the regular spacing of the crystal lattice can be seen to the very edge of the nanoparticles. Moreover, from these images it is evident that there is only one crystal phase present in all of the nanoparticles. Spatial resolution of cerium and praseodymium using EDX was conducted at Oakridge National Laboratory. Line scans demonstrating praseodymium and cerium intensity through the different particles are shown in Figure 3.5. Regardless of crystallite size or route of synthesis, the intensity of the praseodymium signal increases along the edges of the particles, but plateaus 2-3 nm away from the surface, whereas the cerium intensity scales with the width of the particle. Between two and six scans were made for each sample, and while the clearest images are shown here, these results are the same among all scans.

3.2.4 Molecular Mechanics/Molecular Dynamics Simulations

The theoretical lattice constant for CeO_2 were 0.578 nm versus 0.541 nm seen experimentally for bulk CeO_2,[23] and the theoretical lattice constant for PrO_2 was 0.573 nm versus 0.539 nm as seen experimentally.[16] Both of theoretical results were within 7 % of the experimental value, and correctly predicted both a cubic structure and a larger lattice spacing for CeO_2.

To prevent artifacts of starting geometries, all nanoparticles were nucleated from the same starting structure, with praseodymium substituted in for cerium cations. Figure 3.6 shows the starting and final geometries of the different starting configurations, as well as the CeO_2 starting and final configurations. No two particles produced the same final geometry, and occasionally during nucleation two distinct crystal domains would form, which would eventually coalesce. Regardless of starting position, praseodymium cations did not significantly migrate through the particle, unlike what has been seen for titanium-

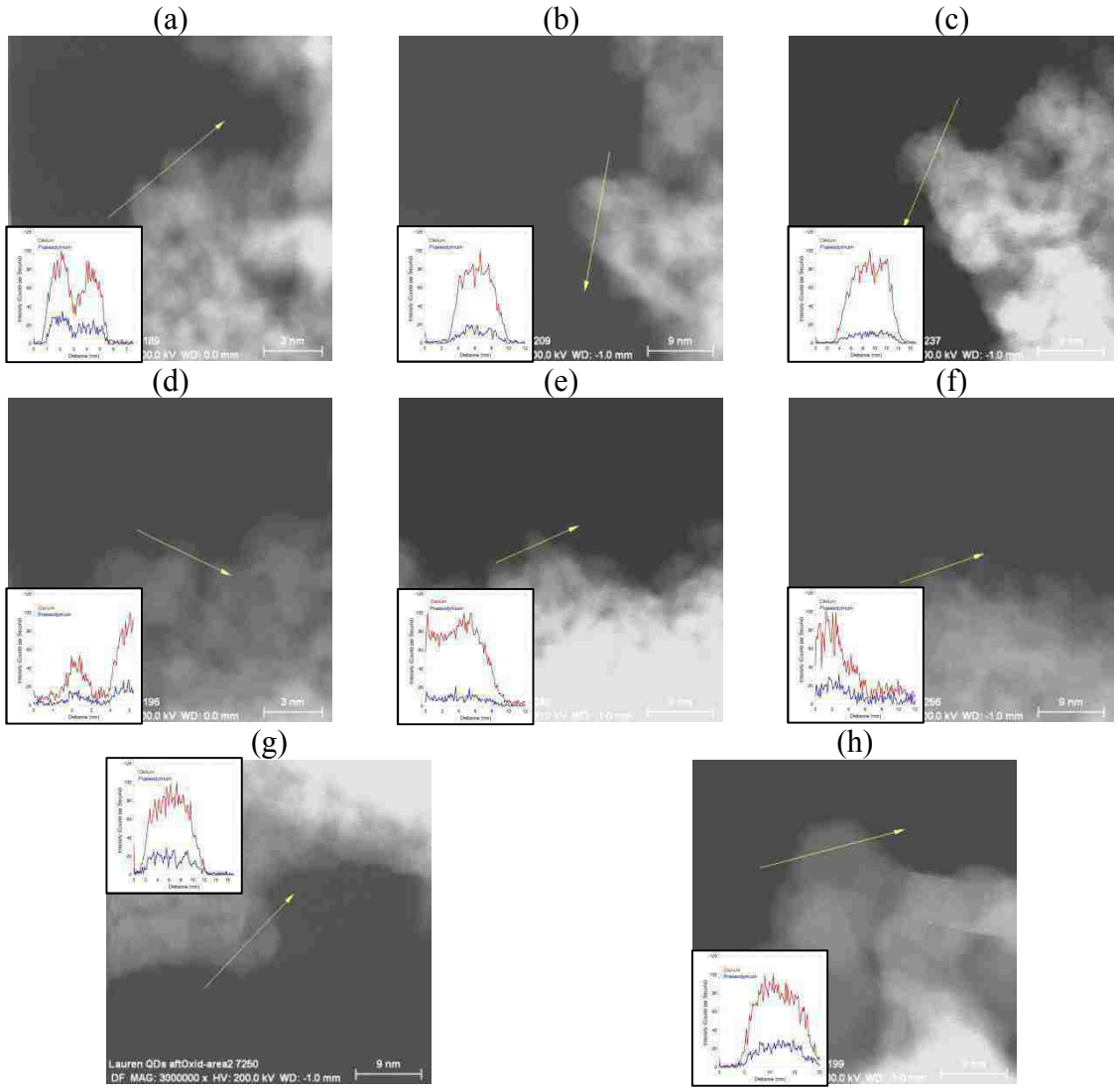

Figure 3.5 Inverted bright field tunneling electron microscope (TEM) images with inserted EDS line scans for (a) 5.00 nm 13:87 Pr:Ce $CePrO_x$, (b) 4.81 nm 10:90 Pr:Ce $CePrO_x$, (c) and 4.98 nm 3:97 Pr:Ce $CePrO_x$ made by the solution method, (d) 4.84 nm 12:88 Pr:Ce $CePrO_x$, (e) 4.87 nm 3:97 Pr:Ce $CePrO_x$, (f) 2.90 nm 15:85 Pr:Ce $CePrO_x$, (g) 4.61 nm 15:85 Pr:Ce $CePrO_x$, and (h) 13.34 nm 15:85 Pr:Ce $CePrO_x$ made by the solution method.

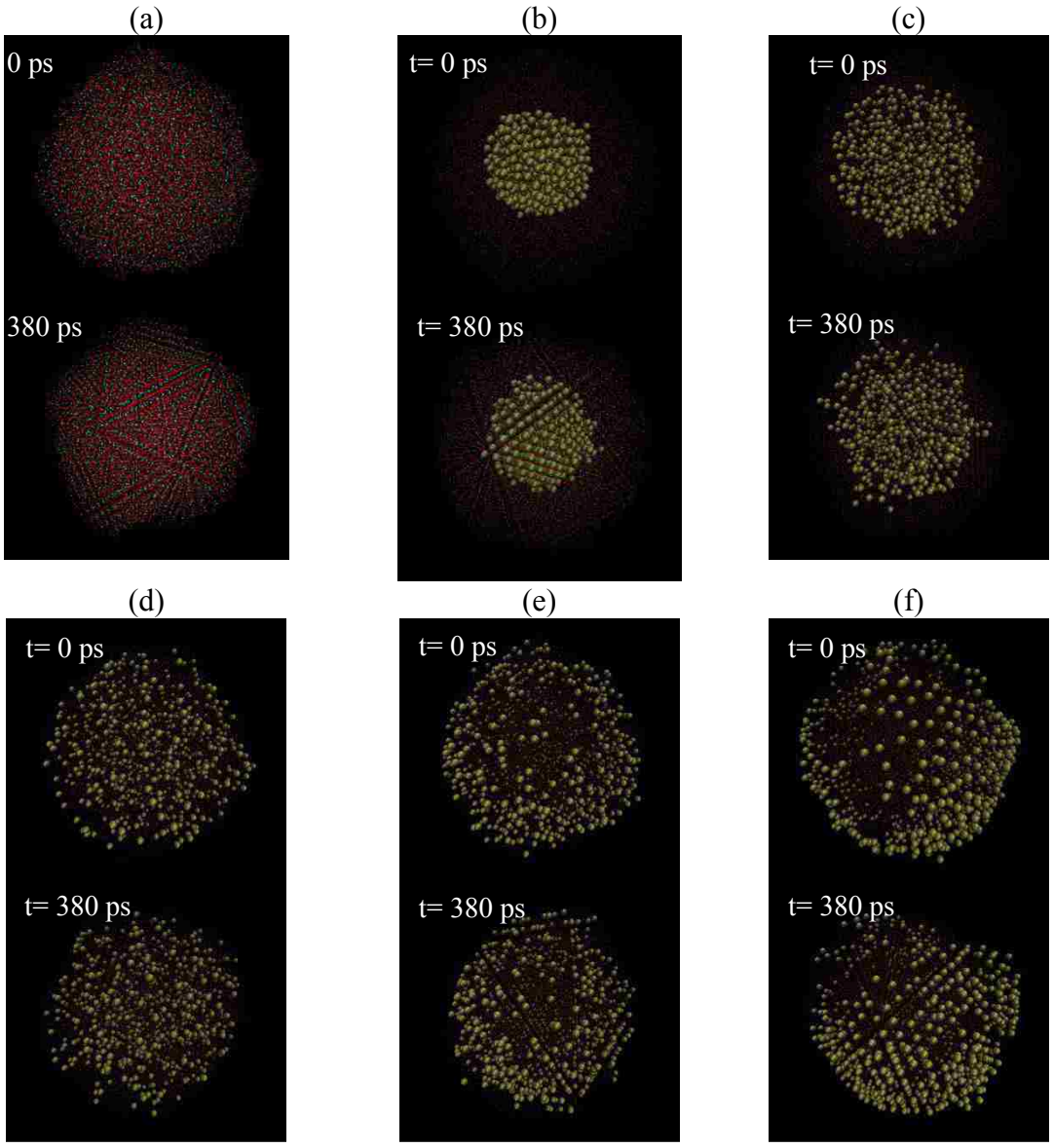

Figure 3.6 Starting (t = 0 ps) and final configurations (t = 380 ps) for (a) CeO_2, (b) CeO_2@PrO_2, (b) CeO_2@$CePrO_x$, (c) $Ce_{0.85}Pr_{0.15}O_2$, (d) $CePrO_x$@CeO_2, and (f) PrO_2@CeO_2. In all figures, red=oxygen, teal=cerium, gold=praseodymium.

cerium mixtures.[24] Therefore, there is no reason to believe that there is a Coulombic explanation for surface enrichment if cerium praseodymium oxide.

As was seen for other theoretical[22] and experimental[16] studies, a lattice expansion is seen when praseodymium is introduced homogenously throughout the cerium oxide lattice. However, as the praseodymium configuration approaches a core-shell structure, either with a cerium or praseodymium oxide core, the lattice constant approaches that of the theoretical lattice constant of pure cerium oxide. Table 3.2 shows the average number of nearest neighbors for cerium and praseodymium for the different praseodymium configurations both before and after nucleation. For pure cerium oxide, the average number of nearest neighbors is predicted to be 10.7 cerium cations; this is close to the theoretical value of 10.5, which is what would be expected if the surface cerium cations were only surrounded by 8 neighbors. As expected, the number of Pr-Pr neighbors is only larger than the number of Pr-Ce neighbors when a true core-shell structure is seen. However, it is not possible to determine by XAS the number of Pr-Pr and Pr-Ce scattering paths as the two elements only vary by Z=1. More important, conversely, is the total number of nearest neighbors. For surface enriched configurations, viz., $CePrO_x@CeO_2$ and $PrO_2@CeO_2$, the total number of Ce-Ce and Ce-Pr neighbors are 10.8 and 11.4, respectively, while for praseodymium the number of Pr-Ce and Pr-Pr neighbors are 10.0 and 9.0, respectively. While the number of cerium nearest neighbors do not significantly change, the number of praseodymium nearest neighbors does change by 10 %. Paired with XAS results, it is possible to determine the nature of the surface enriched praseodymium by the number of nearest cation neighbors.

Table 3.2 Average number of nearest neighbors for different configurations both before and after nucleation.

Structure	Average Number of Nearest Neighbors			
	Starting Configuration			
	Ce-Ce	Ce-Pr	Pr-Ce	Pr-Pr
CeO_2	10.1	N/A	N/A	N/A
CeO_2@PrO_2	9.7	0.3	1.8	9.3
CeO_2@$CePrO_x$	9.3	1.5	9.2	2.8
$Ce_{0.85}Pr_{0.15}O_2$	9.4	1.6	8.7	1.5
$CePrO_x$@CeO_2	9.6	1.2	6.7	2.4
PrO_2@CeO_2	10.8	0.6	3.3	4.5
	Final Configuration			
CeO_2	10.8	N/A	N/A	N/A
CeO_2@PrO_2	10.2	0.5	2.8	9.1
CeO_2@$CePrO_x$	9.2	1.5	8.8	2.8
$Ce_{0.85}Pr_{0.15}O_2$	9.2	1.6	8.5	1.5
$CePrO_x$@CeO_2	9.7	1.3	7.6	2.4
PrO_2@CeO_2	10.3	0.9	3.8	5.2

3.2.5 Effect on Catalytic Activity

As shown in Figure 3.7, the best reactivity is seen for 5.4 nm cerium oxide nanoparticles, which was the smallest crystallite size which could be synthesized by the precipitation method without forming a significant Ce_2O_3 phase. In seen in Figure 3.8, as the crystallite size is decreased, a substantial loss in selectivity is seen around 7 nm. However, when praseodymium is incorporated into the nanoparticle at 5 at%, the optimal reactivity is seen for circa 7 nm without any loss in selectivity, with smaller and larger crystallite sizes giving worse activity. Similarly for 15 at% incorporation, the optimal crystallite size is closer to 6 nm with a loss of activity and selectivity seen above and below this crystallite size. For the 15 at% particles, the activity and selectivity of the particles approaches that of pure praseodymium for the 22.3 nm particles, whereas the 5 at% particles, while beginning to become less selective and active for larger crystallite sizes, do not reproduce the behavior of pure praseodymium at 17.1 nm.

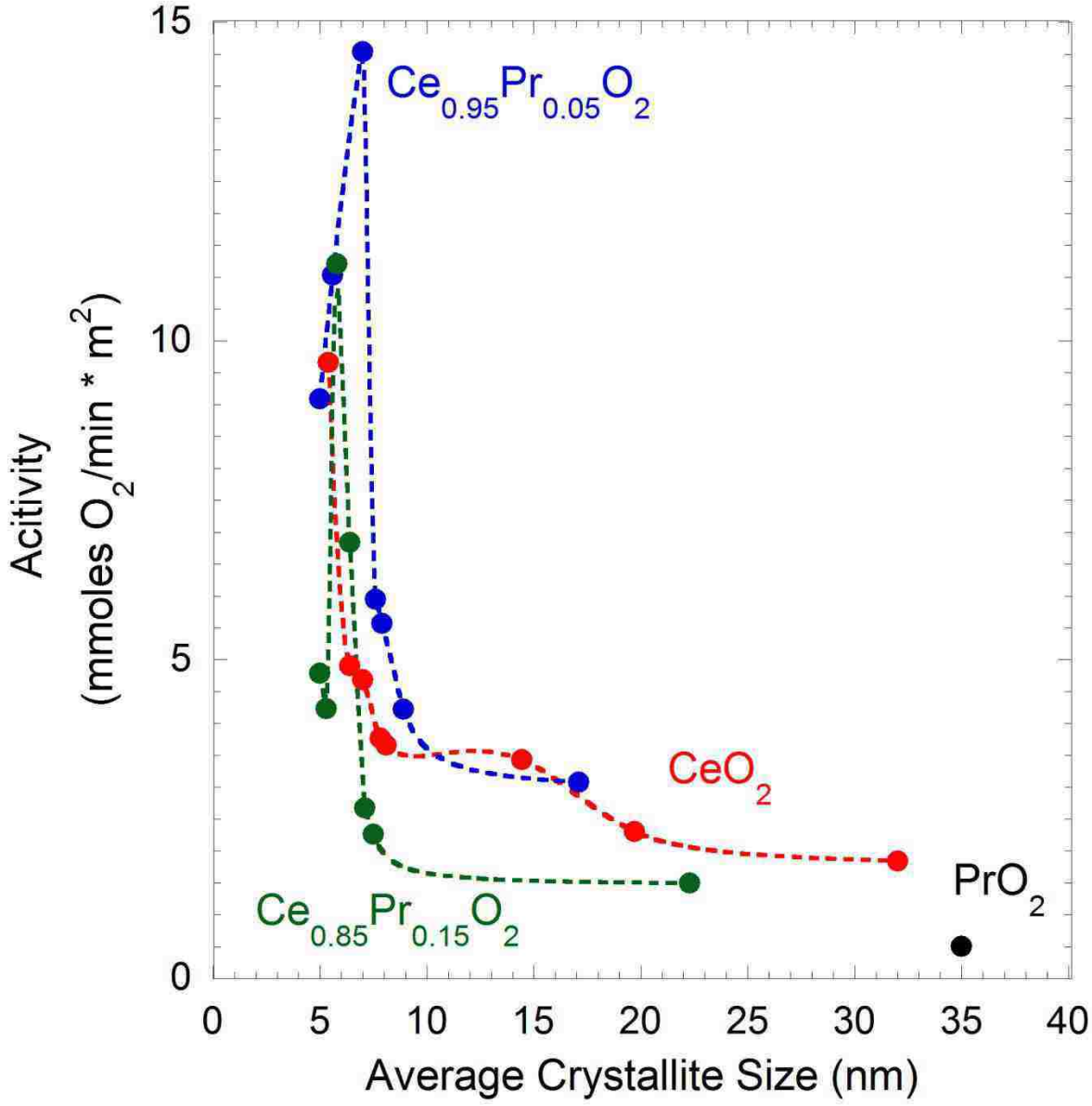

Figure 3.7 Reactivity versus crystallite size for cerium oxide (red), $Ce_{0.95}Pr_{0.05}O_2$ (blue), $Ce_{0.85}Pr_{0.15}O_2$ (green), and bulk PrO_2 (black).

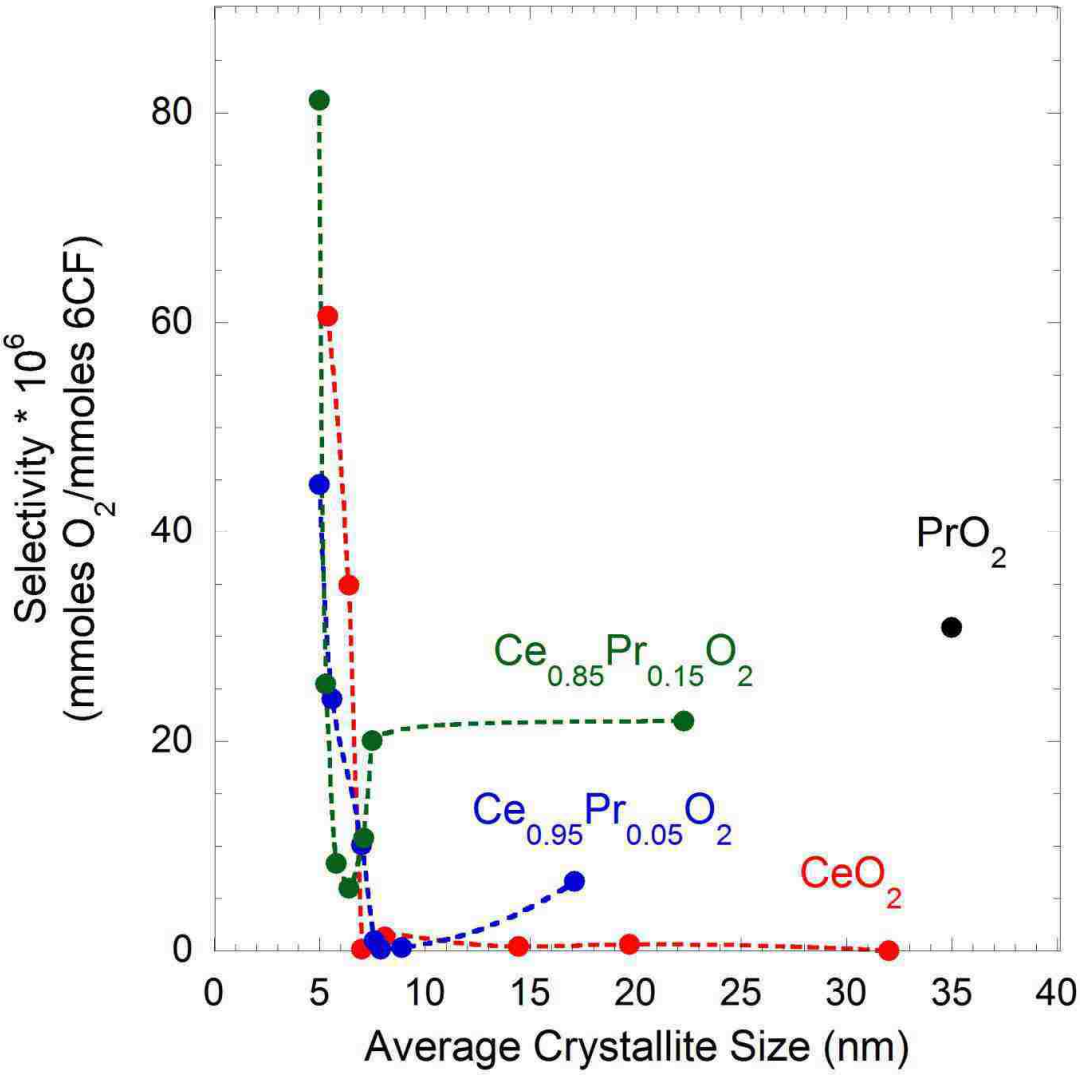

Figure 3.8 Inverse selectivity versus crystallite size for cerium oxide (red), $Ce_{0.95}Pr_{0.05}O_2$ (blue), $Ce_{0.85}Pr_{0.15}O_2$ (green), and bulk PrO_2 (black).

3.3 Discussion

3.3.1 Evidence for Single Phase Nanoparticles

It is common in the literature to treat cerium-praseodymium as a single-phase material, but no direct evidence has been presented thus far to support this claim. It is important to first establish that only $Ce_{1-x}Pr_xO_2$ nanoparticle are being observed to prevent complications of having a mixed phase system, that is to say, to ensure than amorphous or separate PrO_2 cannot account for any observations made. X-ray diffraction of all samples shows only one resolvable cubic lattice phase, precluding the presence of other crystal phases, but at CeO_2 and PrO_2 both have the same F_{m-3m} space group and similar lattice parameters, it is not possible to resolve if there are two superimposed cubic phases. However, from the HRTEM images in Figure 3.4, no amorphous phase is visible on any of the nanoparticles, precluding the possibility of another phase undetectable by XRD. Moreover, the individual lattice planes visible in the crystals are constantly spaced, suggesting that there is indeed no separate, second cubic phase. Therefore, the cerium and praseodymium are contained in the same pure, single cubic phase.

3.3.2 Effect on Praseodymium and Cerium Oxidation State for Crystallite Size and Composition

Table 3.1 summarizes the ratio of Ce^{+3} and Ce^{+4} in the pure and mixed cerium oxides. For a mixed oxide structure, substitution of cerium sites for praseodymium should be random, such that the change of substituting a Ce^{+3} or Ce^{+4} sites is equal to their concentration, and that substitution of cerium sites should not change the relative ration of Ce^{+3} and Ce^{+4} sites. However, the significant loss of Ce^{+3} sites on the addition of even small amounts of praseodymium contradicts what should be seen for bulk

incorporation of praseodymium. A core shell structure would be more consistent with these results; if Ce^{+3} sites on the surface are attributed to oxygen loss at the CeO_2 surface to reduce surface tension and increase the Ce^{+3} concentration,[25] then a shell of PrO_2 would eliminate surface termination of the CeO_2 lattice and subsequent oxygen loss, thereby explaining the decrease of Ce^{+3} sites. This would also imply that remaining Ce^{+3} sites are internal lattice defects, such as oxygen vacancies,[11] and the difference in Ce^{+3} concentration between precipitation and ion-exchange resin samples could be attributed to a different number of defect sites due to artifacts of synthesis. Building upon a core shell model, a PrO_2 shell would also be subject to lattice termination and an increase in the Pr^{+3} sites over a bulk structure. As the PrO_2 shell is increased in thickness, such as increasing the bulk praseodymium concentration, then a shift from Pr^{+3} to Pr^{+4} in the average oxidation state due to increasing PrO_2 bulk structure would be observed. From Figure 3.3, this is the case for the praseodymium concentration; for both precipitation and ion-exchange resin samples, as the bulk praseodymium concentration increases, the Pr $3d_{1/2}$ peak intensity shifts from 933.0 eV (Pr^{+3}) towards 934.0 (Pr^{+4}), and is observed regardless of crystallite size, Figure 3.3a.

3.3.3 Evidence for Surface Segregation

While the XRD and HRTEM data are in agreement with previous reports on cerium and praseodymium forming a single phase, and the expansion of the cerium oxide lattice as a function of doping is in agreement with theoretical models of bulk cerium oxides with praseodymium dopants within the bulk, the current models imply that (1) praseodymium and cerium are interchangeable within the lattice and (2) the point of substitution should be random. The first statement, (1), is reasonable as the cationic radii

of both Ce^{+3}/Pr^{+3} and Ce^{+4}/Pr^{+4}, are very similar, viz., 0.93/0.94 Å and 1.13/1.14 Å respectively.[18] However, for case (2) to be true, the bulk composition by XRF must match the composition by XPS. From the survey scan of the nanoparticles, the ratio of the Ce and Pr been shown to be substantially higher than that of the bulk. The XPS spectra of the doped cerium oxide particles is more consistent with a core-shell structure than a mixed oxide structure, but this evidence alone is not sufficiently direct to show a core-shell structure.

The strongest evidence for surface segregation comes from spatial mapping of the cerium and praseodymium using HRTEM. If the spatial concentration of cerium and praseodymium are represented as the functions Ce(x,y,z) and Pr(x,y,z) respectively, then for a given nanoparticle the predicted observed signal can be represented as an integration of all of the cerium and praseodymium atoms within the volume swept by the electron beam. Furthermore, if the concentration of cesium and praseodymium can be considered effectively constant in the regions where they are found, viz., the spatial concentration of cesium and praseodymium can be considered Heaviside functions with respect to position, then the spatial concentrations for a homogenous particle and core-shell structure for particles of radius R are given as

Homogenous Particle

(1) $$Ce(x,y,z) = \begin{cases} C, x^2 + y^2 + z^2 \leq R^2 \\ 0, x^2 + y^2 + z^2 > R^2 \end{cases}$$

(2) $$Pr(x,y,z) = \begin{cases} P, x^2 + y^2 + z^2 \leq R^2 \\ 0, x^2 + y^2 + z^2 > R^2 \end{cases}$$

Core-Shell Particle

(3) $$Ce(x,y,z) = \begin{cases} C, x^2 + y^2 + z^2 \leq R_1^2 \\ 0, x^2 + y^2 + z^2 > R_1^2 \end{cases}$$

(4) $$Pr(x,y,z) = \begin{cases} P, R_2^2 \leq x^2 + y^2 + z^2 \leq R^2 \\ 0, R_2^2 > x^2 + y^2 + z^2 \\ 0, R^2 < x^2 + y^2 + z^2 \end{cases}$$

For the core shell model, R_1 is the radius of the cerium oxide core and R_2 is the inner radius of the shell. To improve the generality of this model, R_2 does not have to

equal R_1, viz., $R \geq (R_1, R_2)$ and $R_1 \geq R_2$. For a beam of area A, the observed intensity of the praseodymium and cerium signals, I_{Pr} and I_{Ce} respectively, will be given as an integration of the cerium and praseodymium concentration along the length of the beam and averaged about the radius of the beam at some measured point (x_0, y_0). Using symmetry and placing the center of the particle at (0,0,0), the solution for the observed signals becomes

Homogenous Particle

$$I_{Ce} = \begin{cases} 2Ce \iint_A \sqrt{R^2 - x_o^2 - y_o^2}\, dA \; x_o^2 + y_o^2 \leq R^2 \\ 0, x_o^2 + y_o^2 > R^2 \end{cases} \tag{5}$$

$$I_{Pr} = \begin{cases} 2P \iint_A \sqrt{R^2 - x_o^2 - y_o^2}\, dA \; x_o^2 + y_o^2 \leq R^2 \\ 0, x_o^2 + y_o^2 > R^2 \end{cases} \tag{6}$$

Core-Shell Particle

$$I_{Ce} = \begin{cases} 2C \iint_A \sqrt{R_1^2 - x_o^2 - y_o^2}\, dA, x_o^2 + y_o^2 \leq R_1^2 \\ 0, x_o^2 + y_o^2 > R_1^2 \end{cases} \tag{7}$$

$$I_{Pr} = \begin{cases} 2P \iint_A \left(\sqrt{R^2 - x_o^2 - y_o^2} - \sqrt{R_2^2 - x_o^2 - y_o^2} \right) dA \,, x_o^2 + y_o^2 \leq R_2^2 \\ 2P \iint_A \sqrt{R^2 - x_o^2 - y_o^2}\, dA, R_2^2 \leq x_o^2 + y_o^2 \leq R^2 \\ 0, x_o^2 + y_o^2 > R^2 \end{cases} \tag{8}$$

The ratio of the intensities of the praseodymium and cerium become

Homogenous Particle

$$\frac{I_{Pr}}{I_{Ce}} = \begin{cases} \frac{P}{C}, x_o^2 + y_o^2 \leq R^2 \\ undefined, x_o^2 + y_o^2 > R^2 \end{cases} \tag{9}$$

Core-Shell Particle

$$\frac{I_{Pr}}{I_{Ce}} = \begin{cases} \infty, R_1^2 \leq x_o^2 + y_o^2 \leq R^2 \\ \frac{P}{C}\left(\frac{\iint_A \sqrt{R^2 - x_o^2 - y_o^2}}{\iint_A \sqrt{R_1^2 - x_o^2 - y_o^2} dA, x_o^2 + y_o^2}\right), R_2^2 \leq x_o^2 + y_o^2 \leq R_1^2 \\ \frac{P}{C}\left(\frac{\iint_A \left(\sqrt{R^2 - x_o^2 - y_o^2} - \sqrt{R_2^2 - x_o^2 - y_o^2}\right) dA}{\iint_A \sqrt{R_1^2 - x_o^2 - y_o^2} dA}\right), x_o^2 + y_o^2 \leq R_2^2 \\ undefined, x_o^2 + y_o^2 > R^2 \end{cases} \tag{10}$$

Therefore, for homogenously dispersed praseodymium, it is expected that while the intensity of both praseodymium and cerium signals should vary as a function proportional to the particle thickness, their relative ratio should not. For surface segregation, both the intensity of signals observed for praseodymium and cerium as well as the ratio of the two signals should vary as a function of position, with the praseodymium-cerium ratio decreasing as the particle becomes thicker. As seen in equation (12), if the cerium is not present in the surface, the ratio should be infinite at the surface, but in reality beam averaging due to finite beam thickness will make detecting a pure shell very difficult, especially for low praseodymium concentration. Regardless, for any core-shell structure the ratio of praseodymium and cerium should continue to decrease as a function of particle thickness as the observed praseodymium signal plateaus when the thickness of the particle exceeds the thickness of two surface layers of praseodymium allowing for a praseodymium free bulk phase to exist. It follows that applying this to non-spherical particles, for homogenous particles the ratio of the

praseodymium and cerium should remain particle whereas the ratio should change for surface enriched particles should vary.

From the EDS line scans in Figure 3.5, it can be seen that the cerium intensity scales with particle thickness. In particular, Figure 3.5a and Figure 3.5b show a line scan across two particles, with the cerium intensity increasing as the scan passes over both particles and coming to a minimum between the two. However, for praseodymium, it can be seen that the intensity of praseodymium increases only at the edges of the two particles, but remains constant through the bulk of the particle. This agrees with equation (8) where the intensity for praseodymium increases along the edges ($R_2^2 \leq x_o^2 + y_o^2 \leq R^2$) but remains constant throughout the bulk ($x_o^2 + y_o^2 \leq R_2^2$). Comparing the cerium intensity to the praseodymium intensity, within nanometers of the surface of the particle the ratio of praseodymium to cerium begins to decrease as the particle's thickness increases, in agreement with (10).

This strong dependence of the cerium-praseodymium ratio as a function of particle thickness is consistent with what is to be expected for a core-shell structure and not for a homogenous particle. However, due to beam averaging, viz., averaging of beam signal due to finite beam width, it is impossible to determine if the shell is a pure PrO_2 phase ($R_1=R_2$), if it is a mixed $CePrO_x$ phase ($R_1=R$), or if it is a double shell with $CePrO_x$ and PrO_2 phases ($R_2<R_1<R$). Additional work using radial distribution functions and molecular mechanics simulations must be undertaken to determine the exact nature of this shell.

3.3.4 Molecular Mechanics

Molecular mechanics simulations show that the difference between the final configurational energies, viz., the energies determined from the Buckingham-Potential, for the different configurations vary less than 0.2 kJ/mole, which is less than thermal energy at room temperature. Therefore, from enthalpic energy alone, there is no thermodynamic explanation for surface segregation and any conformation is equally favorable. If entropic effects were taken into account, the mixed metal oxide would be the most favorable conformation, as segregation minimizes entropic mixing energy. The only information which can be gleamed from the energetics as determined from MM/MD simulations is that the surface-enriched nanoparticles obtained experimentally are not the thermodynamic product of cerium-praseodymium oxide nucleation from solution, but more likely the kinetic effects.

Nonetheless, the MM/MD simulations do give very good information about the nearest neighbors for praseodymium for the different conformations. Although cerium and praseodymium cannot be resolved using x-ray absorption spectroscopy (XAS), the total number of nearest cationic neighbors (second shell) can be determined, and from Table 3.**2**, it can be seen that for $CePrO_x@CeO_2$ versus $PrO_2@CeO_2$, there are more nearest neighbors for praseodymium for the former model. If XAS measurements are made of $Ce_{1-x}Pr_xO_2$ nanoparticles of different particles sizes and concentrations, it should be possible to compare the praseodymium second shell to the number of nearest neighbors predicted by MM/MD simulations to resolve between $CePrO_x@CeO_2$ and $PrO_2@CeO_2$ for the structure of the praseodymium enriched nanoparticles.

3.3.5 Effects on Catalytic Activity

The commonly accepted mechanism for peroxide decomposition by cerium cations in solution is given as,[26]

$$Ce^{+4} + H_2O_2 \rightarrow Ce^{+3} + HOO\cdot + H^+$$

$$Ce^{+4} + HOO\cdot \rightarrow Ce^{+3} + O_2 + H^+$$

$$Ce^{+3} + HOO\cdot \rightarrow Ce^{+4} + H_2O_2$$

Because of the lability of oxygen in the bulk material, it is reasonable to assume that this mechanism could be used to describe bulk cerium oxide,[17] but for nanoparticles beneath 8 nm, an increase of Ce^{+3} sites is seen.[27-30] This is due mostly to cerium oxide nanoparticles attempting to relieve surface tension by substituting larger Ce^{+4} cations for larger Ce^{+3} cations,[17,31] explaining the increase in the lattice constant of cerium oxide nanoparticles over the bulk. However, this would imply that much of the Ce^{+3} sites on the surface of cerium oxide nanoparticles are not labile and therefore not able to participate in radical scavenging. Furthermore, due to the lack of labile Ce^{+3} sites the loss of selectivity should appear as the size of the cerium oxide particles decreased.

Furthermore, the effects of praseodymium can be explained more easily of a core-shell structure is used. As it cannot be determined from the HRTEM if the shell is pure praseodymium or a mixture of praseodymium and cerium oxide, I will use a "praseodymium shell" as a placeholder for either situation. If the material is treated as a core-shell structure, then from a simple mass balance, it can determined that the surface area of a single monolayer of praseodymium divided by the surface area of a particle for a given particle or radius R_p is given as

$$\frac{SA_{PrO_2}}{SA_{particle}} = \frac{R_p \rho_{Ce_xPr_{1-x}O_2} X_{Pr}}{3\rho_{PrO_2}} \sim R_p X_{Pr}$$

Where rho refers to density and X_{Pr} is the mass fraction of praseodymium in the nanoparticle. Since this ratio must be between 0 and 1 to make physical sense, viz., the percentage of surface coverage by praseodymium can only be as high as 100 %, this equation only serves as a guideline for describing qualitatively what happens as the particle increases in radius or the composition is changed. Two important qualitative trends can be shown from this simple analysis. First, the amount of praseodymium in the surface increases as the radius of the particle increases. Second, the rate of this increase scales with the concentration praseodymium in the material

It is expected that for large particle radii and high bulk composition thick shells of praseodymium are formed at large particle radii and high compositions, so larger particles would be expected to have behavior similar to pure praseodymium. Conversely, for small particles and low bulk praseodymium concentration, it is expected that there should be little praseodymium in the surface, and so smaller particles should approach that of pure cerium oxide. It is in the intermediate sizes that a thin praseodymium shell should be seen, and since praseodymium is a poor catalyst for peroxide decomposition, it is expected that as the bulk composition is increased and a thicker praseodymium shell is generated, that activity should decrease. From Figure 3.7, it can be seen that in the intermediate particle range for 5 at % praseodymium, that is to say, between 6 and 10 nm, strong deviation from the behavior is seen, while for small crystallite sizes activity returns to that of pure cerium oxide, and for large crystallite sizes bulk praseodymium behavior is recovered. This trend is also seen for 15 at % praseodymium, but the improvement in activity is less pronounced than the 5 at % samples and is beneath that of pure cerium oxide. However, this is to be expected if there is a thicker praseodymium

shell covering the surface. Using a mass balance and using the bulk densities of cerium oxide and PrO_2 to determine the thickness of a pure PrO_2 shell on the doped particles giving the best activity, it was found that for the 5 at% 7 nm nanoparticle the shell should be 0.12 nm and the thickness of the 15 at% 5.8 nm particle the thickness of the shell should also be 0.12 nm. So from these results, it would seem that a theoretical shell thickness of 0.12 nm for praseodymium is the best choice for activity, though the reason for the higher activity of the 5 at% over the 15 at % is probably due to a more complex effect of the particle curvature on the activity of surface sites.

Selectivity versus crystallite size is shown in Figure 3.8. Most important to note is that, regardless of sample composition, the selectivity does not follow the same trends as the activity, discounting any losses in activity strictly to an increase in activity. Rather, the decoupling of reactivity and selectivity suggests that the mechanism governing selectivity and activity being to differ in the nano regime, supporting the hypothesis that the loss in lability in Ce^{+3} surface sites would result in decreased selectivity. Also in Figure 3.8, it can be seen that for 5 at % praseodymium there is no loss in selectivity, but for 15 at % praseodymium, selectivity less is substantial and the material begins to approach the behavior of bulk PrO_2 at even intermediate crystallite sizes, which while consistent with forming a pure PrO_2 surface shell, is not direct proof. All particles, regardless of doping, lose their activity as they become smaller, but the loss in selectivity is not linear with crystallite size and is probably due to the loss of surface site oxidation state lability.

3.5 Conclusions

This work represents the first direct evidence of praseodymium phase separation in mixed cerium-praseodymium oxides. XRD and TEM were used to verify the presence of a single cubic phase with no amorphous coating. XPS showed a strong decrease in surface Ce^{+3}, and that increasing the bulk composition of praseodymium results in a shift towards the +4 oxidation state for surface praseodymium atoms, suggesting the formation of a PrO_2 shell. From EDS, it was shown that the concentration of praseodymium does not increase in proportion with cerium, demonstrating a core shell structure. Regardless of crystallite size and method of synthesis, praseodymium preferentially incorporates into or onto the surface of a cerium oxide core. However, from the current analysis it is not possible to determine of the praseodymium rich surface is pure praseodymium oxide or a mixed cerium-praseodymium. Molecular-mechanics simulations paired with extended x-ray spectroscopy fine structure (EXAFS) could be used to model the pair distribution function of praseodymium as a function of conformation and compare these results to EXAFS data, and while the MM simulations have been used to determine the thermodynamics of phase separation and number of nearest neighbors, the EXAFS measurements remain to be made. It is most likely that this core shell structure is a kinetic product and not the thermodynamic product, suggesting that a new method of synthesis must be used to obtain a true mixed structure. Until this issue is resolved, the utility of cerium-praseodymium oxides must be used knowing that praseodymium surface enrichment occurs.

This work has also shown that the addition of 5 at% praseodymium to the cerium oxide lattice shows a substantial improvement in the activity of 7 nm particles over pure

cerium oxide without a loss in selectivity. Similar behavior in the activity and selectivity of the 15 at% praseodymium samples to the 5 at % praseodymium samples was also seen, but the incorporation of 15 at% praseodymium resulted in an overall loss in activity and selectivity versus pure cerium oxide. However, by varying the concentration of praseodymium showed that, at least for these two concentrations, the ideal theoretical praseodymium shell thickness if 0.12 nm.

3.6 Notes on Chapter

Work in this chapter is taken from two manuscripts; "Surface Segregation of Praseodymium in Mixed $CePrO_x$ Materials: On the True Nature of These Mixed Oxides," currently being prepared for submission, and "Surface Segregation of Praseodymium in Mixed $CePrO_x$ Materials: The Nature of Surface Enrichment," which is awaiting x-ray absorption spectroscopy measurements at Argonne National Labs before it can be turned into another manuscript.

3.7 References

(1) Trogadas, P.; Parrondo, J.; Ramani, V. *Electrochem. Solid-State Lett.* **2008**, *11*, B113.

(2) Pan, C.; Zhang, D.; Shi, L.et al. *Eur. J. Inorg. Chem.* **2008**, 2429.

(3) Hua, G.; Zhang, L.; Fei, G.et al. *J. Mater. Chem.* **2012**, *22*, 6851.

(4) Xu, J.; Xue, B.; Liu, Y.-M.et al. *Appl. Catal., A* **2011**, *405*, 142.

(5) Wang, Q.; Li, G.; Zhao, B.et al. *J. Mol. Catal. A: Chem.* **2011**, *339*, 52.

(6) Padeste, C.; Cant, N. W.; Trimm, D. L. *Catal. Lett.* **1994**, *28*, 301.

(7) Shyu, J. Z.; Otto, K.; Watkins, W. L. H.et al. *J. Catal.* **1988**, *114*, 23.

(8) Carabineiro, S. A. C.; Silva, A. M. T.; Drazic, G.et al. *Catal. Today* **2010**, *154*, 21.

(9) Kouraichi, R.; Delgado, J. J.; Lopez-Castro, J. D.et al. *Catalysis Today*, *154*, 195.

(10) Padeste, C.; Cant, N. W.; Trimm, D. L. *Catal. Lett.* **1993**, *18*, 305.

(11) Chueh, W. C.; McDaniel, A. H.; Grass, M. E.et al. *Chem. Mater.* **2012**, *24*, 1876.

(12) Bishop, S. R.; Stefanik, T. S.; Tuller, H. L. *PCCP* **2011**, *13*, 10165.

(13) Stefanik, T. S.; Tuller, H. L. In *Solid State Ionics-2002*; Knauth, P. T. J. M. T. E. T. H. L., Ed. 2003; Vol. 756, p 163.

(14) Stefanik, T. S.; Tuller, H. L. *J. Electroceram.* **2004**, *13*, 799.

(15) Hee Sang, K.; Jong Rak, S.; Yun Chan, K.et al. *J. Alloys Compd.* **2005**, *398*.

(16) Luo, M. F.; Yan, Z. L.; Jin, L. Y.et al. *J. Phys. Chem. B* **2006**, *110*, 13068.

(17) Karakoti, A.; Singh, S.; Dowding, J. M.et al. *Chem. Soc. Rev.* **2010**, *39*, 4422.

(18) Shannon, R. D. *Acta Crystallographica Section A* **1976**, *32*, 751.

(19) Zhi-Ying, P.; Ji-Qing, L.; Meng-Fei, L.et al. *J. Phys. Chem. C* **2007**, *111*.

(20) Matovic, B.; Boskovic, S.; Logar, M.et al. *J. Alloys Compd.* **2010**, *505*, 235.

(21) Sharma, V.; Eberhardt, K. M.; Sharma, R.et al. *Chem. Phys. Lett.* **2010**, *495*, 280.

(22) Balaguer, M.; Solis, C.; Serra, J. M. *J. Phys. Chem. C* **2010**, *116*, 7975.

(23) Mogensen, M.; Sammes, N. M.; Tompsett, G. A. *Solid State Ionics* **2000**, *129*, 63.

(24) Sayle, D. C.; Feng, X.; Ding, Y.et al. *J. Am. Chem. Soc.* **2007**, *129*, 7924.

(25) Tsunekawa, S.; Fukuda, T.; Kasuya, A. *Surf. Sci.* **2000**, *457*, L437.

(26) Sigler, P. B.; Masters, B. J. *J. Am. Chem. Soc.* **1957**, *79*, 6353.

(27) Deshpande, S.; Patil, S.; Kuchibhatla, S.et al. *Appl. Phys. Lett.* **2005**, *87*.

(28) Hailstone, R. K.; DiFrancesco, A. G.; Leong, J. G.et al. *J. Phys. Chem. C* **2009**, *113*, 15155.

(29) Baranchikov, A. E.; Polezhaeva, O. S.; Ivanov, V. K.et al. *Crystengcomm* **2010**, *12*, 3531.

(30) Tsunekawa, S.; Sivamohan, R.; Ito, S.et al. *Nanostruct. Mater.* **1999**, *11*, 141.

(31) Feng, Z.; Peng, W.; Koberstein, J.et al. *Surf. Sci.* **2004**, *563*.

Chapter 4: Cerium and Cerium (IV) Oxide in Hydrogen Fuel Cells

4.1 Introduction

As the human population grows and more nations move towards industrialization, the energy needs of the world continue to grow with it, as well as the types of energy used to meet these needs.[1] But what must be understood about meeting the growing energy needs of the world is that it is not simply a matter of producing electricity, but rather producing energy which meets the needs of a variety of demands, such as industrial production, food and water production, transportation, and residential use. There are several sources of energy currently utilized to meet modern energy demands, with coal, petroleum, and natural gas being the most utilized. The US, China, and Britain have large deposits of coal available for use, but generally coal suffers from high levels of sulfur or mercury, so their use is limited in the US and Britain due to the issue of pollution. As for petroleum, while the US is the third largest producer of petroleum, it imports significantly more petroleum than it produces. Furthermore, like coal and natural gas, the inefficiency in producing energy from petroleum combustion as well as the byproduct of carbon dioxide, which is responsible for global warming, has driven governments to find greener and more efficient alternatives. In this light, renewable sources such as solar, hydroelectric, geothermal, and wind have been implemented, but suffer from limited applications, limited intervals of energy production, and difficulties in storing and moving the energy to the places where it is used.

Hydrogen fuel cells are being developed to address the issue of meeting the energy needs for transportation or energy needs requiring a mobile power source which is capable of producing a wide variety range of power output with the maximum efficiency

at lower sustained loads, but there remains much work in order to improve the lifetime of these devices for large-scale commercialization. One of the principle causes of fuel cell failure is caused by hydrogen peroxide and hydroxyl radicals that are generated during the oxygen reduction reaction (ORR), whereby oxygen is converted to water,[2] Figure 4.1. When hydroxyl radicals interact with the proton exchange membrane, hydrogen radicals are formed that attack C-F bonds while sulfonic radicals are also generated that subsequently decompose into SO_3 and flouroradicals.[3,4] Ultimately, the radical decomposition of the proton exchange membrane results in the emission of fluorine from the exhaust streams of the fuel cell, as well as membrane thinning which causes loss in open circuit voltage and an increase in hydrogen crossover. The thinning of the membrane further acts to increase hydrogen peroxide generation.[5]

While modification of the proton exchange membrane with sacrificial functional groups has increased the lifetime of fuel cells substantially,[6] these measures are only temporary solutions; eventually hydroxyl radical formation removes these functional groups and degradation of the PEM results. Ideally the use of a material that can continuously remove hydrogen peroxide and free radicals catalytically is preferred. It may seem that a fast peroxide decomposer would be ideal as it would eliminate hydrogen peroxide before it can react with the PEM. However, a survey of the literature show that generally the faster an ion or metal oxide decomposes hydrogen peroxide, the more radical it creates in the process, for example in the cases of transition metals such as Fe, Mn, Cr, Ti, V, and Cu.[7-9]

Cerium oxide provides a more viable option for hydrogen peroxide decomposition. While cerium oxide is only a kinetically moderate peroxide decomposer,

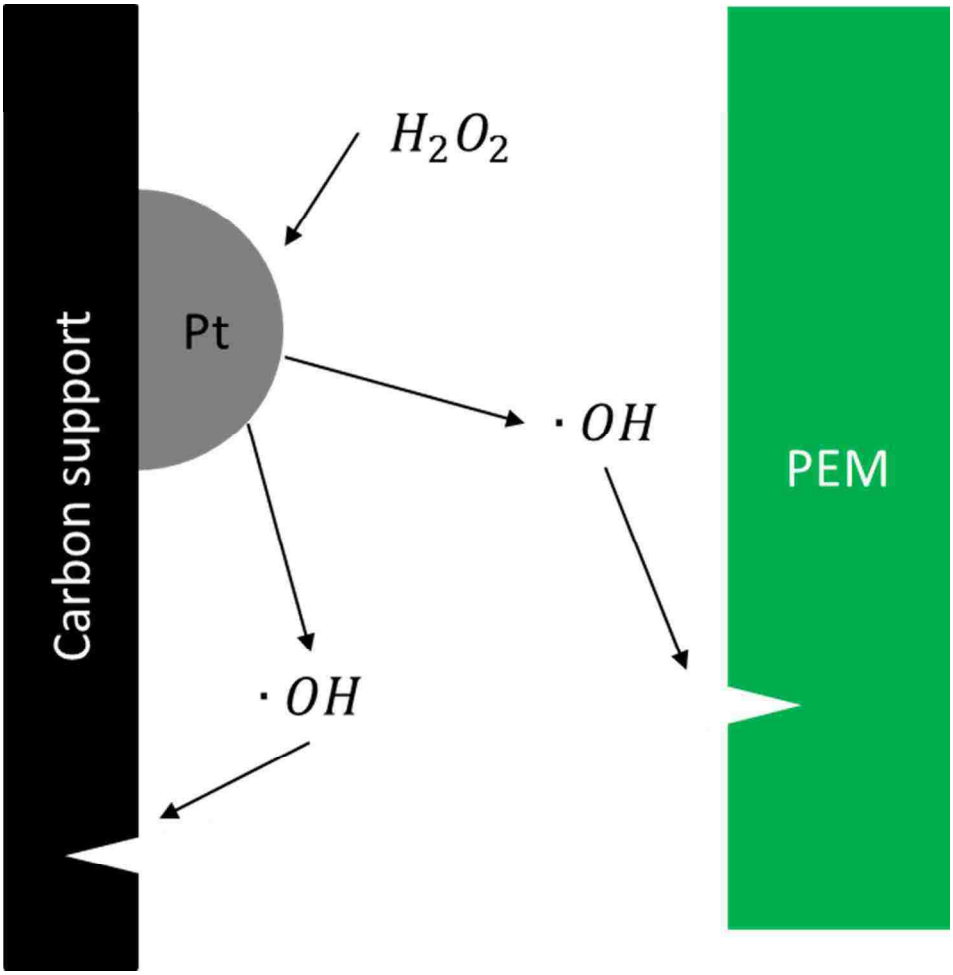

Figure 4.1 Illustration of hydrogen peroxide decomposition into hydrogen radicals in a hydrogen fuel cell, and the subsequent radical degradation of the carbon support and proton exchange membrane (PEM)

the Ce^{+4} sites which are responsible for peroxide decomposition are paired with Ce^{+3} sites which can facilitate radial scavenging. Much of this analysis is based on the mechanism for cerium catalyzed peroxide decomposition, shown below,[10] where the second mechanistic step is rate limiting.

$$(1)\quad Ce^{+4} + H_2O_2 \overset{K_1}{\rightarrow} Ce^{+3} + HOO\cdot + H^+$$

$$(2)\quad Ce^{+4} + HOO\cdot \overset{K_2}{\rightarrow} + Ce^{+3} + O_2 + H^+$$

$$(3)\quad Ce^{+3} + HOO\cdot + H^+ \overset{K_{-1}}{\longrightarrow} Ce^{+4} + H_2O_2$$

For CeO_2, it is conceivable that a balance between catalytically active Ce^{+4} sites, which initiate peroxide decomposition, and Ce^{+3} sites, which scavenge free radicals before they can diffuse away from the nanoparticle, would be optimal. Finding this optimum would represent a large step towards developing an ideal radical stabilization material for improving fuel cell lifetime, as well as understanding the catalytic properties of cerium oxide.

This work focuses on tuning the catalytic activity of cerium oxide towards hydrogen peroxide as well as controlling its selectivity by controlling the ratio of the Ce^{+3}/Ce^{+4} sites on the surface. To control the ratio of the Ce surface sizes, we synthesize cerium oxide nanoparticles of various sizes, from 5 nm to 40 nm. The activity and selectivity toward peroxide was measured as a function of particle size, and 3 different cerium oxide nanoparticles are incorporated into the cathode catalyst layer and their performance to membrane stabilization measured. Accelerated stress testing using a high fuel cell operating temperature with 30 % relative humidity of the inlet gases was used to increase degradation of the fuel cell membrane to simulate long-term operation. Open circuit voltage (OCV), hydrogen crossover, and the fluorine emission rate (FER) from

both the anode and cathode exhaust gases were used to quantify the rate of degradation of the fuel cell membrane electrode assembly (MEA) among the different types of fuel cells – those with cerium cations, those with cerium oxide, and those without cerium or cerium oxide stabilizers. Scanning electron microscopy images of the tested membranes was used to determine the extent of thinning of the anode side of the MEA versus the cathode side of the MEA as an external validation of the performance loss measured by OCV, hydrogen crossover, and FER.

4.2 Results

4.2.1 Migration of Cerium Cations in Hydrogen Fuel Cells

Figure 4.2 shows the effect of AST on the position of cerium in the membrane and catalyst over time. The pressed cell, Figure 4.2a, , represents the cerium distribution after hot pressing; as none of the components of the catalyst layers contains cerium, the presence of cerium in the catalyst layers after pressing suggests that hot pressing alone drives cerium from the XL membrane into the catalyst layer. After conditioning, Figure 4.2b it becomes apparent that regular fuel cell operating begins to deplete cerium from the proton exchange membrane (PEM), and over time more and more cerium leaves the PEM until it becomes mostly concentrated in the catalyst layers. From the ratio of cerium to platinum, it appears that there is no preference for cerium in either the anode or cathode catalyst layers after pressing, and after conditioning only migration of the cerium towards the membrane in the anode catalyst layer occurs. However, during prolonged operation, there is a migration of cerium towards the proton exchange membrane for both the anode and cathode. This may be due to migration of cerium out of the membrane, but this is not clear.

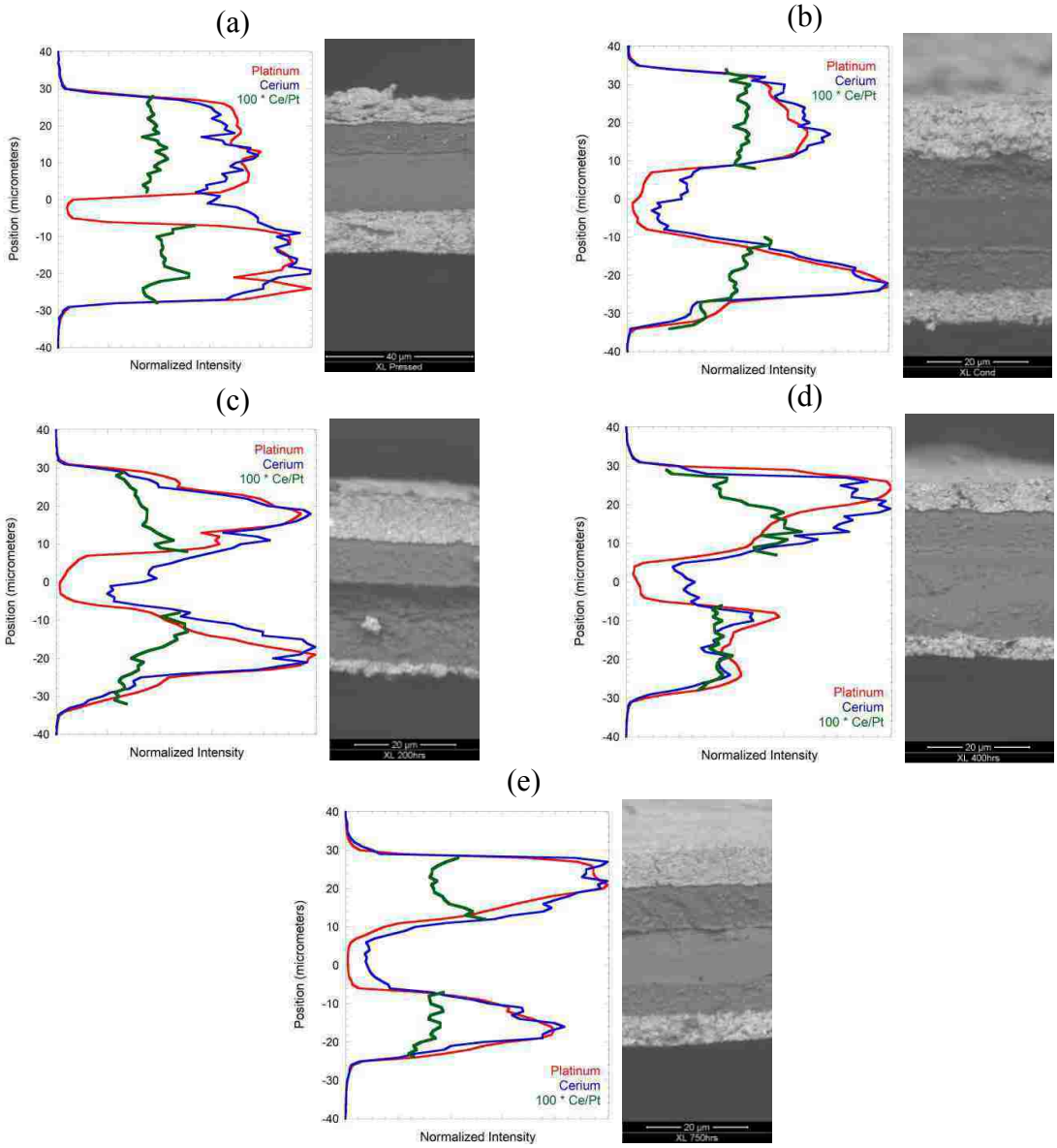

Figure 4.2 DuPont XL membranes after (a) pressing, (b) conditioning, (c) 200 hours, (d) 400 hours, and (e) 200 hours of AST. The left graph is a profile of cerium (blue), platinum (red), and the ratio cerium and platinum signals (green). To the right are back scattered SEM images of the membranes.

Figure 4.3a shows the cerium distribution when CeO_2 is incorporated into the cathode catalyst layer. Boiling the MEA in sulfuric acid removes the cerium cations from the membrane, depleting cerium from the PEM and anode catalyst layer, but the CeO_2 remains in the catalyst layer. However, during fuel cell operation, the cerium oxide begins to dissolve in the highly acidic environment,[11] and from Figure 4.3 b, it appears that the cerium cations begin to migrate across the PEM into the anode catalyst layer. After pressing, there is an increase in the Ce/Pt ratio in the anode due to cerium migration, but ultimately both the profile of the cerium cations in fuel cell with CeO_2 as well as the Ce/Pt ratio in the catalyst layers approaches that of the XL membrane with cerium cations, Figure 4.3e. The profile of cerium cations on pressing does not follow the platinum profile, but as the fuel cell continues to operate, the cerium cations begin to distribute themselves in platinum rich regions of the MEA, similar to the XL membrane. Furthermore, in the anode side there is generally an increase in the cerium to platinum ratio at the interface of the membrane-anode catalyst layer interface during operation. However, for the cathode side, while there is some increase in the cerium-platinum ratio at the membrane-cathode catalyst layer interface, it is not as pronounced and may be due to the immobility of the cerium oxide in the catalyst layer.

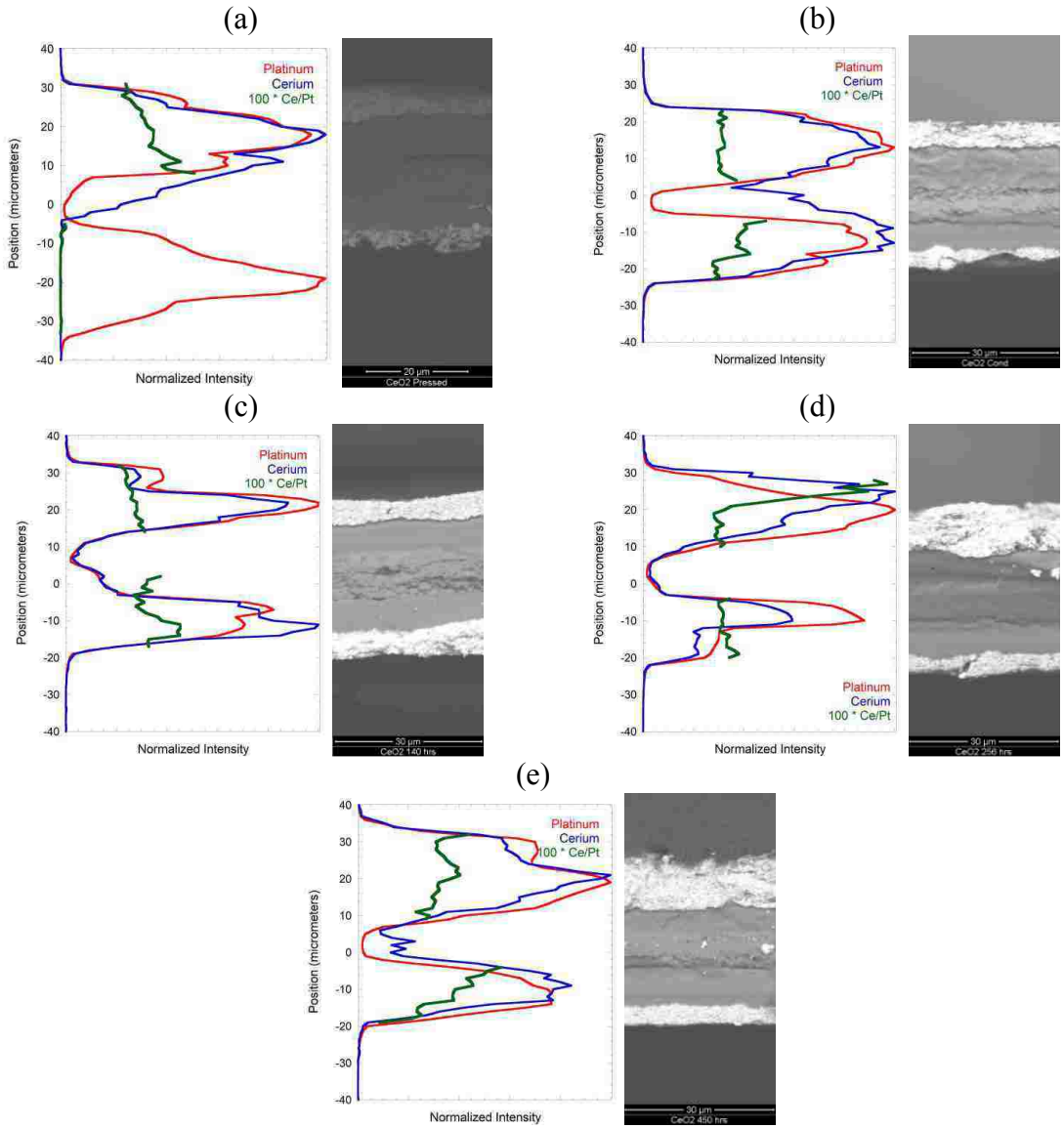

Figure 4.3 DuPont XL membranes with CeO_2 after (a) pressing, (b) conditioning, (c) 140 hours, (d) 256 hours, and (e) 450 hours of AST. The left graph is a profile of cerium (blue), platinum (red), and the ratio cerium and platinum signals (green). To the right are back scattered SEM images of the membranes

4.2.2 Selectivity and Activity of Nanoparticles as a Function Particle Size

Work studying the reactivity and activity of cerium oxide as a function of particle size has been shown earlier. Reproduced again in Figure 4.4 in a more useful format, as the average particle diameter of cerium oxide decreases, the activity increases without change in selectivity until circa 7.0 nm, at which point the selectivity becomes increasingly worse for decreasing particle size. This change in selectivity begins where surface tension effects are known to affect the surface Ce^{+3} concentration.[10,12] While the rate of peroxide decomposition increases with decreasing particle size, so does the loss in selectivity beneath 7 nm. As Figure 4.4 does not show a linear relationship, the loss in selectivity cannot be directly attributed to the increase in the rate of peroxide decomposition. To probe the effects of adding cerium oxide of different particle sizes to the cathode of a hydrogen fuel cell for improved stability, three particle sizes were selected, and are highlight in Figure 4.1; 37.7 nm (red), 7.0 nm (blue), and 5.4 nm (green).

4.2.3 X-ray Photoelectron Spectroscopy

Table 4.1 shows the results of deconvoluting the Ce 3d absorption edge for the x-ray photoelectron spectra of three cerium oxide nanoparticles used in these studies. Peak deconvolution of the synthesized particles revealed that the 37.7 nm particle is 23 % Ce^{+3}, the 37.7 nm particle is 24 % Ce^{+3}, and the 37.7 nm particle is 26 % Ce^{+3}. Therefore for decreasing particle size, there is an increase in the Ce^{+3} concentration.

4.2.4 Accelerated Stress Testing (AST)

Three types of fuel cells were tested; control DuPont XL cells (XL-control), unstabilized DuPont XL (XL-unstabilized), and DuPont XL stabilized with cerium oxide

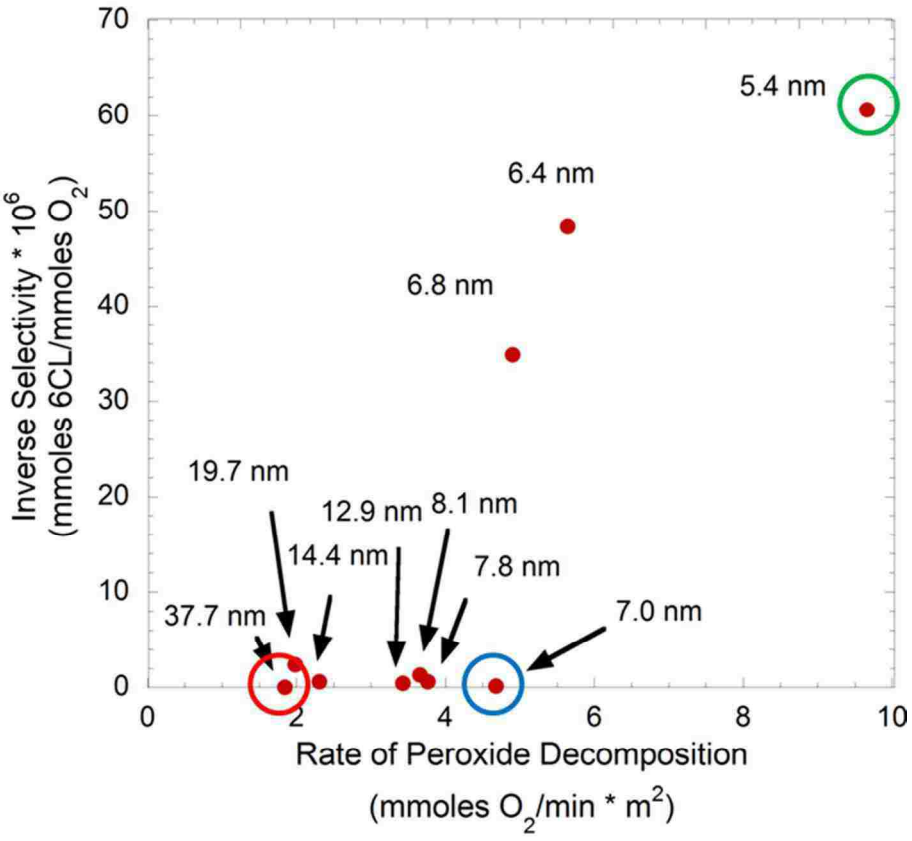

Figure 4.4 Inverse selectivity versus activity for peroxide decomposition for different particle sizes of cerium oxide. The red circle indicates the large cerium nanoparticles used for accelerated stress testing, the blue circle indicates the medium sized cerium oxide nanoparticles, and the green circle indicates the small sized cerium oxide nanoparticles.

Table 4.1 Ce 3d XPS Results

Average Particle Diameter (nm)	Area of Transition										Total Area		Composition	
	Ce^{+3}				Ce^{+4}						Ce^{+3}	Ce^{+4}	Ce^{+3}	Ce^{+4}
	V_1	V'	U_1	V'	V_0	V''	V'''	U_0	U''	U'''				
5.4	609	2740	2114	409	3802	4016	2602	2192	919	3574	5873	17105	26 %	74 %
7.0	767	3698	2722	257	5770	5495	5597	3813	3069	4476	7443	23914	24 %	76 %
37.7	644	3376	2249	361	4767	4436	3797	2993	1168	4731	6630	21892	23 %	77 %

nanoparticles. Three sizes of cerium oxide nanoparticles were used: large cerium oxide nanoparticles (37.7 nm) added to the cathode catalyst layer for stability (XL-LNPs), DuPont XL with medium cerium oxide nanoparticles (7.0 nm) added to the cathode catalyst layer for stability (XL-MNPs), and DuPont XL with small cerium oxide nanoparticles (5.4 nm) added to the cathode catalyst layer for stability (XL-SNPs). Three metrics were used to gauge the stability and performance of these cells during accelerated stress testing; the decrease in open circuit voltage (OCV), hydrogen crossover (CO), and the fluorine emission rate (FER).

Figure 4.5 shows the OCV for each cell as a function of time. The OCVs of the modified cells were consistently lower than of the unmodified cells due to damage incurred by the membrane during processing, by boiling in sodium hydroxide and sulfuric acid. The XL-unmodified cell showed excellent stability for over 600 hours, with no loss in OCV. The XL-unstabilized cells show a linear loss in voltage over time, with a loss of -0.30 mV/hr. When large cerium oxide nanoparticles are incorporated into the catalyst layer, the OCV loss drops to -0.15 mV/hr, and the loss is still linear over the lifetime of the cell. However, when medium sized cerium oxide nanoparticles are incorporated into the catalyst layer, then for the first 350 hours the loss in OCV is 0.00 mV/hr, a substantial improvement over the unstabilized cell and the same as the as received membrane. However, after 350 hours, the loss in OCV becomes significantly worse, and when fit to a linear regression, this loss is -0.5 mV/hr. When small cerium oxide nanoparticles are incorporated into the catalyst layer, some initial stabilization is seen in the first 100 hours, but the cell begins to lose OCV, and when fit to with a linear regression, this loss if -0.4 mV/hr.

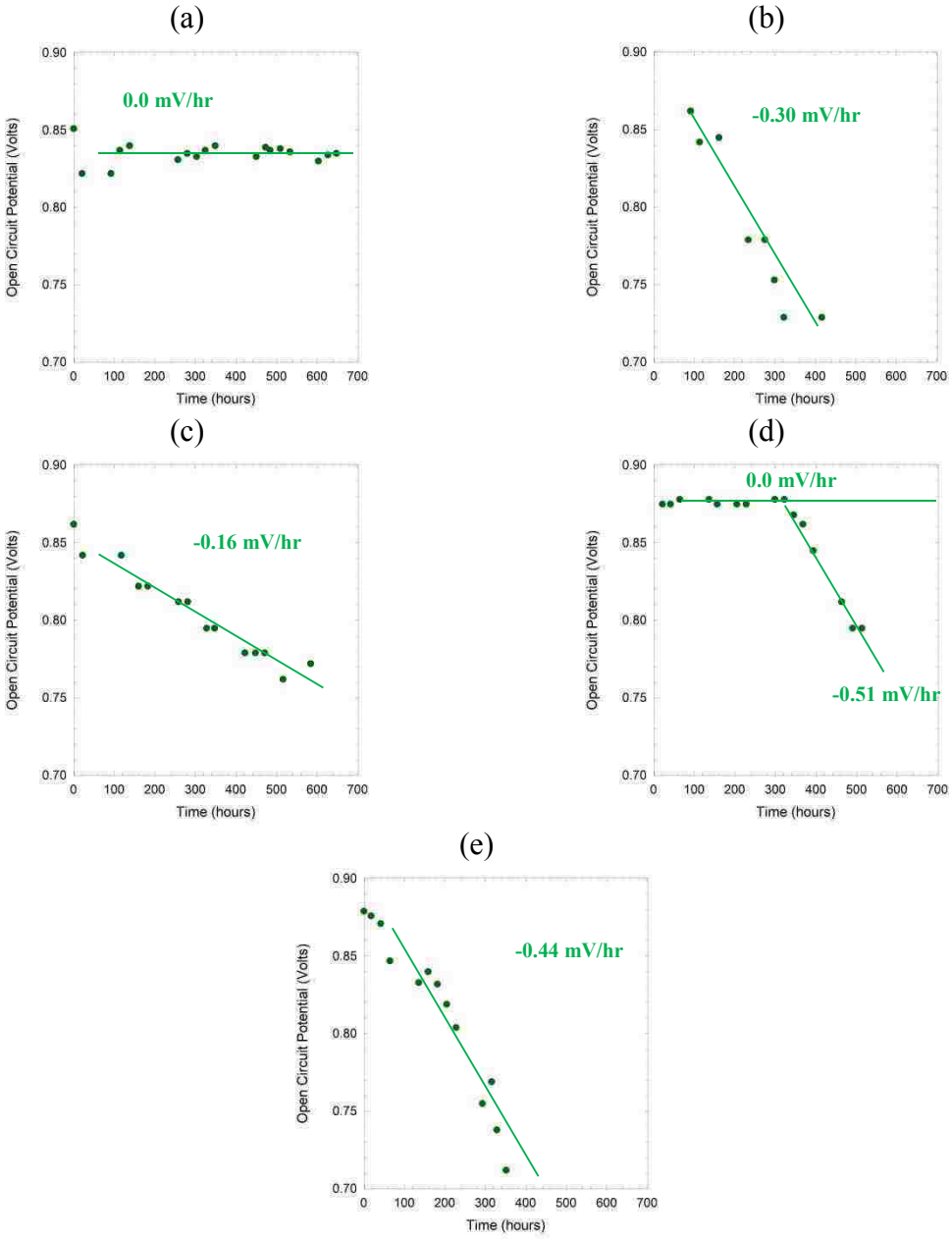

Figure 4.5 Open circuit potential (OCV) versus time for the different fuel cells: (a) XL-unmodified, (b) XL-unstabilized, (c) XL-LNPs, (d) XL-MNPs, and (e) XL-SNPs. The rate of change in the OCV is reported on each figure, and for the XL-MNPs the rate of change has been broken into two regions – before and after 350 hours.

Figure 4.6 shows the change in hydrogen cross-over (CO) for each of the different fuel cells. The control XL membrane showed no increase in hydrogen crossover during 600 hours of operation, other than subtle changes in crossover associated with slight variations in flow and pressure between measurements. For the unstabilized fuel cell, the increase in the hydrogen crossover is somewhat linear and increases at a rate of 4.4 $\mu Amps/cm^2$-hr. When large cerium oxide nanoparticles are incorporated into the catalyst layer, it shows trends similar to the unstabilized cells, but the increase in hydrogen crossover decreases to 0.9 $\mu Amps/cm^2$-hr. As with the OCV, the hydrogen cross over for the cells with medium cerium oxide nanoparticles in the catalyst layer show no loss of OCV for the first 350 hours comparable to the control XL membrane, but after this time the rate of hydrogen crossover increases, and when fit with a linear regression, increases at roughly 20 $\mu Amps/cm^2$-hr. For small cerium oxide nanoparticles, this trend with OCV is also seen; while there is some initial stabilization, the increase in hydrogen crossover increases and when fit with a linear regression, shows an increase of 16 $\mu Amps/cm^2$-hr.

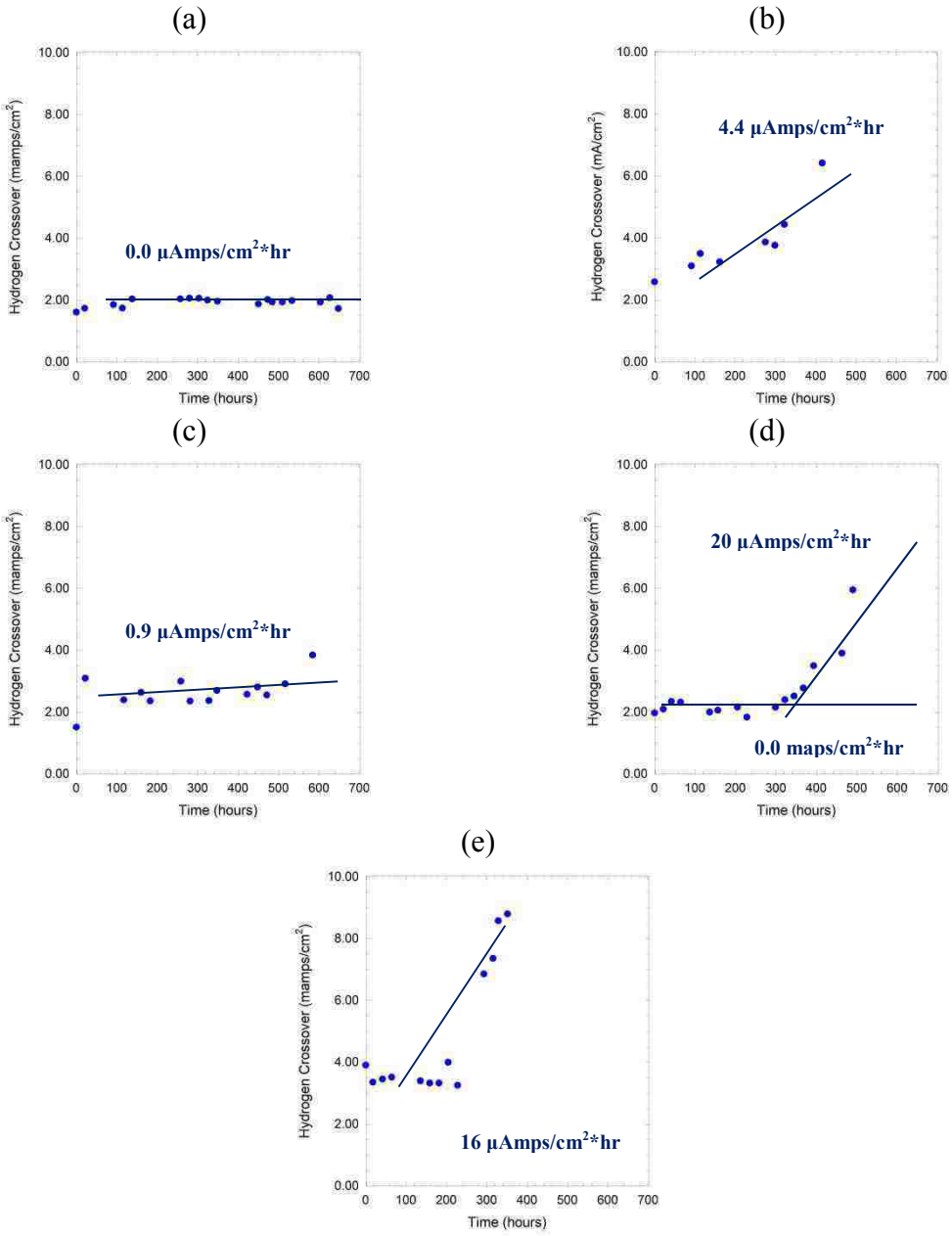

Figure 4.6 Hydrogen Cross-over (CO) versus time for the different fuel cells: (a) XL-unmodified, (b) XL-unstabilized, (c) XL-LNPs, (d) XL-MNPs, and (e) XL-SNPs. The rate of change in the CO increase is reported on each figure, and for the XL-MNPs the rate of change has been broken into two regions – before and after 350 hours.

Figure 4.7 shows the change in fluorine emission rate (FER) as a function of time. For the unmodified XL membrane, the rate of increase in the fluorine emission rate is 0.024 μg F^-/hr^2 for the cathode and 0.004 μg F^-/hr^2 for the anode. For the unstabilized cell, the fluorine emission rate increases linearly at 0.6 μg F^-/hr^2 for the cathode and 0.3 μg F^-/hr^2 for the anode, with the FER for the anode and cathode remaining comparable; not significantly increasing relative to one another. When large cerium oxide nanoparticles are incorporated into the catalyst layer, the FER decreases to 0.11 μg F^-/hr^2 for the cathode and 0.06 μg F^-/hr^2 for the anode, with the anode and cathode FER staying comparable. However, when medium and small cerium oxide nanoparticles are incorporated into the catalyst layer, this linear loss of fluorine is not observed. The medium cerium oxide nanoparticles show an FER of 0.09 μg F^-/hr^2 for the cathode and 0.04 μg F^-/hr^2 for the anode in the first 350 hours, then increasing to 0.40 μg F^-/hr^2 for the cathode and 0.25 μg F^-/hr^2 for the cathode. As with the unstabilized cell, the FER is comparable between the anode and cathode for the first 350 hours, but beyond 350 hours the FER for the cathode decouples from the FER of the anode. Similarly, when small cerium oxide nanoparticles are incorporated into the cathode catalyst layer, the FER of the cell increases, and when fit to a linear regression, this increase is 0.70 μg F^-/hr^2 for the cathode and 0.23 μg F^-/hr^2 for the anode. As with medium cerium oxide nanoparticles beyond 350 hours, the cathode and anode FER become decoupled and the cathode increases much faster than the anode.

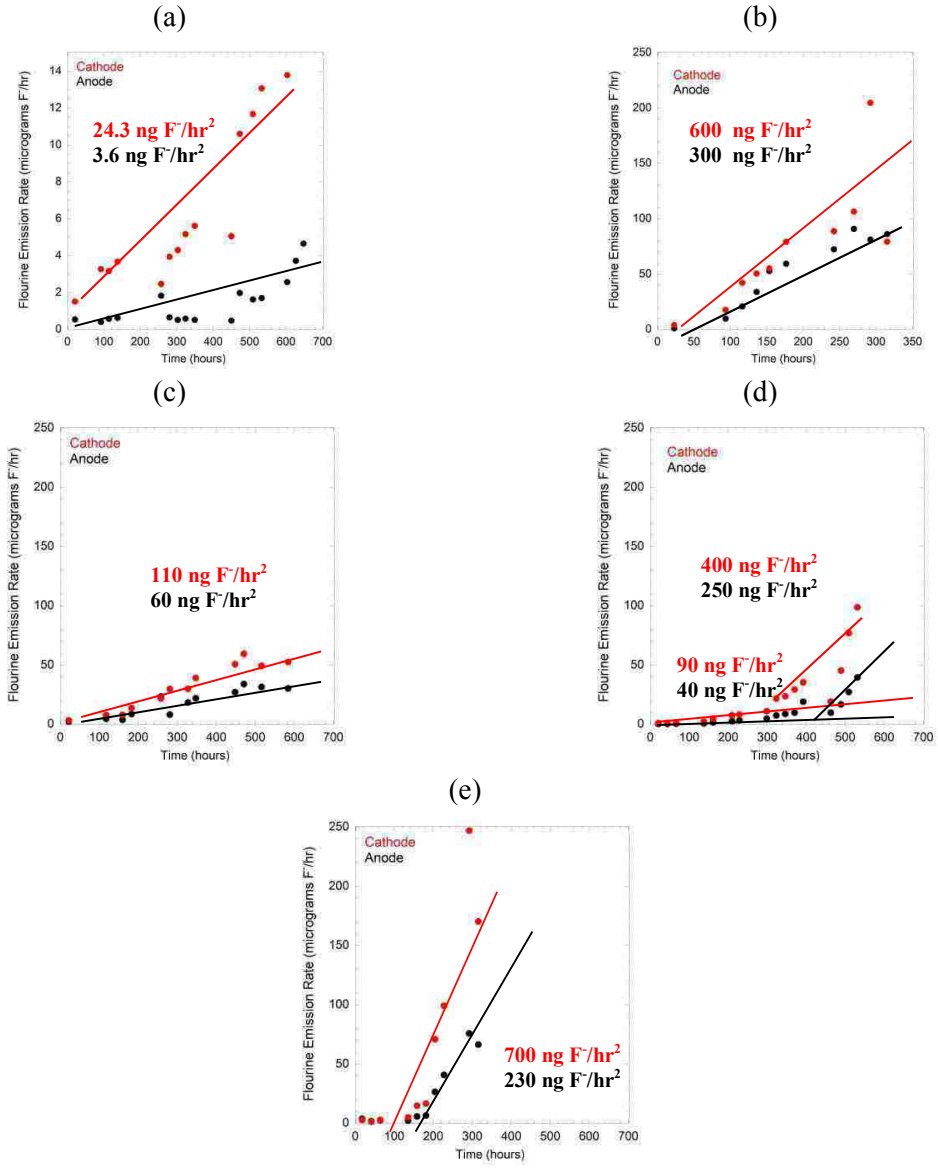

Figure 4.7 Fluorine emission rate (FER) versus time for the different fuel cells: (a) XL-unmodified, (b) XL-unstabilized, (c) XL-LNPs, (d) XL-MNPs, and (e) XL-SNPs. Here, the anode FER is the square markers, and the cathode FER are the round markers. Note that the scale for (a), XL-unmodified membrane, is a much smaller scale to show the features of the fluorine emission rate. The rate of change in the FER is reported on each figure (cathode in red, anode in black), and for the XL-MNPs the rate of change has been broken into two regions – before and after 350 hours.

4.2.5 SEM

SEM cross-sectional images of the different cells after AST testing are shown in Figure 4.8. The actual thickness of the membrane depends on the degree of hydration, so comparison of the thicknesses of the actual membranes is not as telling as the degree of thinning of the anode and cathodes relative to the extruded Teflon layer in the center of the membrane. Figure 4.8f shows an as received DuPont XL membrane; the thickness of the extruded PTFE layer, viz., the layer running through the center of the membrane, is as thick as the Nafion layers coating it, and ratio of the two Nafion layers on the outside of the PTFE is unity. The ratio of the cathode to the anode is used to determine the effect of adding dopants, as the cathode is expected to thin faster than the anode due to the onset of free radicals at the cathode and catalysts which will mitigate the effect of free radicals will increase the ratio of cathode/anode Nafion layer over time.

The unstabilized membrane shows nearly complete removal of the Nafion from the cathode side of the membrane, with thinning of the anode observed as well. However, the ratio of the cathode to the anode is 0.72 from the SEM image and will be used as the baseline for fuel cell improvement. For the cell modified with large cerium oxide, some thinning is seen on the cathode side, but the membrane sees little degradation after 600 hours, especially relative to the unstabilized cell. The ratio of the cathode to the anode after 600 hours is 0.95, showing substantial improvement over the control cell. When medium sized cerium oxide nanoparticles are mixed into the catalyst layer, the ratio of the cathode and anode is 0.67, which is worse than the control cell. However, this ratio is after 600 hours and after a large increase in fluorine emission suggesting that

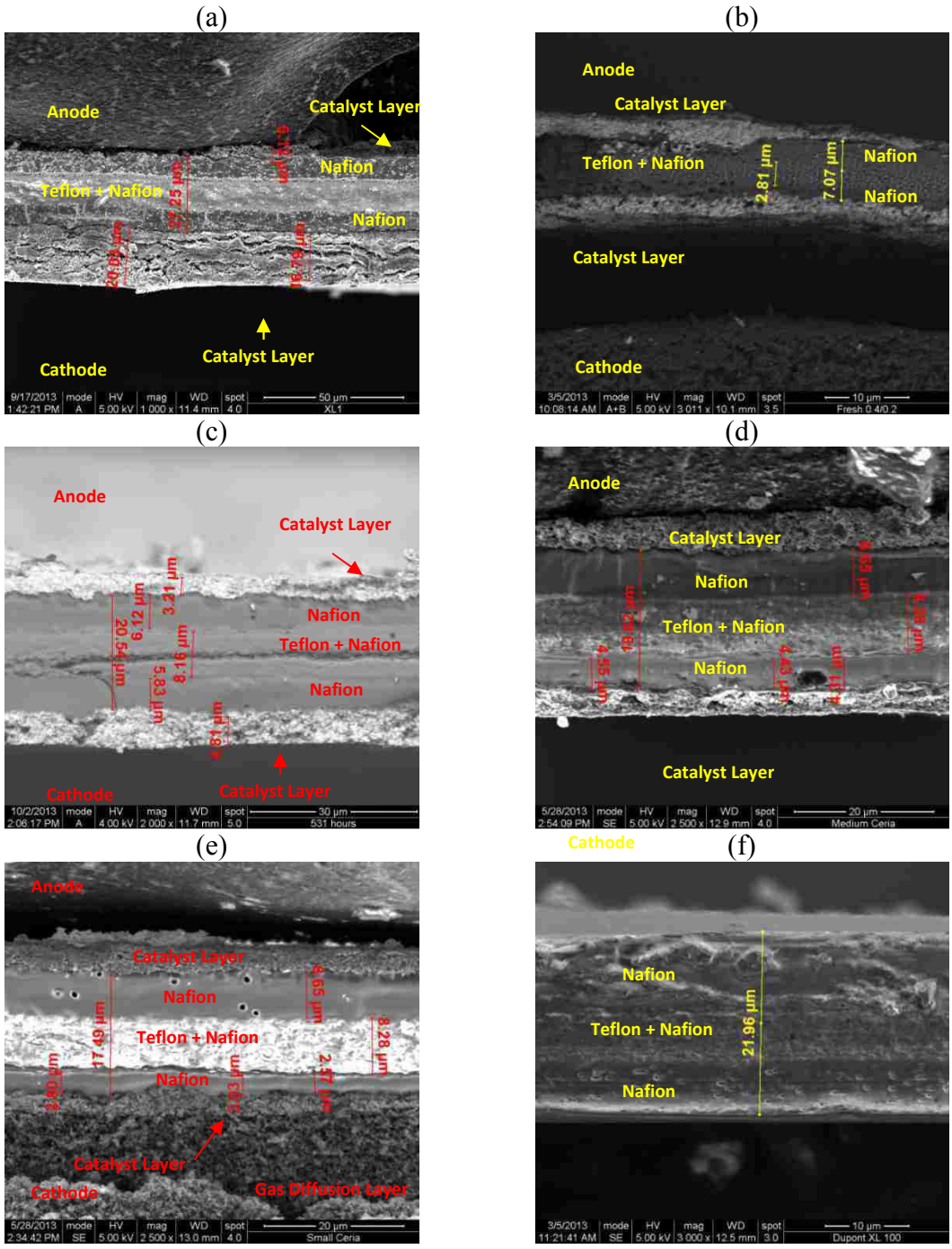

Figure 4.8 SEM images of the different fuel cells after AST; (a) XL-unmodified (700 hours), (b) XL-unstabilized (409 hours), (c) XL-LNPs (hours), (d) XL-MNPs (hours), (e) XL-SNPs (hours), and (f) a Dupont XL membrane as received.

much of this thinning occurred in the last 100 hours of operation. When small cerium oxide nanoparticles are introduced into the catalyst layer, substantially thinning of the cathode is seen; the ratio of the cathode to anode is 0.43 suggesting a substantial increase in cathode thinning over the control cell, consistent with increased free radical generation. For the unmodified XL membrane, the ratio of the cathode to the anode is 0.98, close to that of the starting material and similar to that of large cerium oxide.

4.3 Discussion

4.3.1 Migration of Cerium Cations Through Hydrogen Fuel Cells

If cerium migration during fuel cell operating were due to diffusion, the cerium profile should even across the membrane, as in Figure 4.2a, , and if the profile were due to electrostatic forces, the cerium profile would expected to be a linear rise of cerium concentration from the anode to the cathode, due to the higher number of electrons at the cathode. Moreover, as the profile of cerium more closely resembles that of the platinum profile, the migration of cerium from the PEM into the catalyst layer may be due to either interactions of cerium with the platinum or interaction of cerium with the reactions localized to the platinum, with buildup of cerium at the catalyst-membrane interface due either to cerium depletion from the membrane.

Figure 4.3a shows the cerium distribution when CeO_2 is incorporated into the cathode catalyst layer. Boiling the MEA in sulfuric acid removes the cerium cations from the membrane, depleting cerium from the PEM and anode catalyst layer, but the CeO_2 remains in the catalyst layer. However, during fuel cell operation, the cerium oxide begins to dissolve in the highly acidic environment,[11] and from Figure 4.3b, it appears that the cerium cations begin to migrate across the PEM into the anode catalyst layer.

After pressing, there is an increase in the Ce/Pt ratio in the anode due to cerium migration, but ultimately both the profile of the cerium cations in fuel cell with CeO_2 as well as the Ce/Pt ratio in the catalyst layers approaches that of the XL membrane with cerium cations, Figure 4.2e. The profile of cerium cations on pressing does not follow the platinum profile, but as the fuel cell continues to operate, the cerium cations begin to distribute themselves in platinum rich regions of the MEA, similar to the XL membrane. Furthermore, in the anode side there is generally an increase in the cerium to platinum ratio at the interface of the membrane-anode catalyst layer interface during operation. However, for the cathode side, while there is some increase in the cerium-platinum ratio at the membrane-cathode catalyst layer interface, it is not as pronounced and may be due to the immobility of the cerium oxide in the catalyst layer.

4.3.2 Effect of CeO_2 particle size on Ce^{+4} to Ce^{+3} Site Fractional Occupancies

In drawing an analogy between cerium and cerium oxide for hydrogen peroxide decomposition, the common assumption has been that surface cerium ions in cerium oxide behaves the same as cerium ions in solution, that is to say, the oxidation state for surface cerium cations is labile. For large particles, this may be a reasonable assumption; oxygen lability is sufficient so that the material should obtain equilibrium with gaseous oxygen.[10] However, the substoichiometry of bulk cerium oxide is known to depend strongly on the partial pressure of oxygen,[13-15] but for very small particles, less than 10 nm, the behavior of cerium oxide becomes dependent on both on oxygen concentration, and surface tension effects,[10,12] so that the amount of Ce^{+3} in the surface is larger than would be expected for bulk cerium oxide. This increase suggests that there is also an increase in the number of surface Ce^{+3} which are not capable of changing their oxidation

state, greatly reducing the population of Ce^{+3} cations on the surface capable participating in the radical scavenging reaction (reaction 3).

Therefore, for small particles, which have highly active Ce^{+4} sites but Ce^{+3} sites which cannot change to Ce^{+4} due to positive surface strain effects, selectivity should be poor. As particle size increases, the catalytic activity of the Ce^{+4} sites should decrease as the fraction of surface to bulk sites decrease and the catalyst will become more selective towards peroxide decomposition. Finally, as the particle becomes very large, the relative rate of peroxide decomposition should be very slow but the selectivity for peroxide decomposition very high. When cerium oxide nanoparticles are added to the catalyst layer of hydrogen fuel cells, small particles should cause a decrease in lifetime due to the increase number of free radicals generated upon peroxide decomposition, whereas moderate and large particles should improve fuel cell lifetimes, whereby the moderate particles show the largest improvement.

4.3.3 Accelerated Stress Testing

To verify this, we examine the results from the 3 different particle sizes of cerium oxide incorporated into the catalyst layer versus the unmodified fuel cell containing cerium cations and the unstabilized membrane containing no cerium oxide or cerium. Large cerium oxide nanoparticles should be slower at selectively decomposing peroxide than cerium, but should still offer some stabilization due to their ability to selectively decompose peroxide, giving improvement over the unstabilized cell. Medium cerium oxide nanoparticles should perform better than the large cerium oxide nanoparticles for selective peroxide decomposition since medium cerium oxide nanoparticles have comparable selectivity to large cerium oxide nanoparticles but demonstrate a larger rate

of peroxide decomposition, Figure 4.4. Therefore, there should be no increase in the rate of free radical generation versus large cerium oxide nanoparticles, while the medium should perform comparably to cerium due to their improved peroxide decomposition rate. Small cerium oxide nanoparticles, conversely, should increase the number of free radicals produced during normal operation and reduce the lifetime of the fuel cell due to high kinetics for reaction 1, but low rates for reaction 2 and 3, ultimately performing worse than an unstabilized cell for fuel cell lifetime improvement.

For the large cerium oxide nanoparticles, the expected results were observed; the rate of OCV loss, hydrogen cross over increase, and the rate of increase in the FER were all lower than the unstabilized cell. Moreover, the same linear changes in performance were seen with the large cerium oxide nanoparticles as were seen with the unstaiblized cell. As with the unmodified and unstabilized membranes, the fluorine emission rate for the cathode was higher than the anode, but the rates of fluorine emission generally tracked together. The rate of thinning, as estimated from the ratio of the cathode Nafion thickness to the anode Nafion thickness, is comparable to that of cerium cations, suggesting that bulk cerium oxide does indeed behavior similarly to cerium oxide cations.

However, with the small and medium cerium oxide nanoparticles, the loss in performance was substantial after the initial stabilization. Prior to 350 hours, medium cerium oxide nanoparticles gave the same performance as cerium cations, suggesting that near 7.0 nm, the behavior of cerium oxide and cerium is similar. However, while the medium cerium oxide nanoparticles exceeded the performance of the large cerium oxide nanoparticles for the first 350 hours, there was sudden dramatic loss in performance after 350 hours that followed the same loss as the small cerium oxide nanoparticles. The

fluorine emission rate prior to 350 hours is comparable to that of the cerium impregnated control cell, and as with both the unmodified and unstabilized cell, the fluorine emission rate for the cathode tracks with the anode. Beyond 350 hours, a large increase in the fluorine emission of the cathode over the fluorine emission rate of the anode is seen, though both increase. This increase in fluorine emission rate is also accompanied by increase in hydrogen cross over and loss of open circuit voltage.

As the small cerium oxide nanoparticle also saw some initial stabilization, it is possible that there is a critical loss in selectivity which causes performance loss, but nonetheless, this behavior is different than the behavior of the large nanoparticle which only saw a linear loss in performance over time with no initial stabilization. However, after less than 200 hours, a loss in performance is seen, and as with the medium cerium oxide nanoparticle beyond 350 hours, the fluorine emission rate of the cathode stops tracking the anode fluorine emission rate. As with the unstabilized cell and the other cerium oxide impregnated fuel cells in this study, the loss in open circuit voltage and increase in hydrogen cross over tends to scale with the rate of fluorine emission. The increase in the rate of free radical generation is supported also by the increase in thinning of the cathode Nafion layer on the proton exchange membrane, as seen in the SEM images of the cells after failure.

The explanation for loss in the performance of medium and small cerium oxide nanoparticles is the change in the solubility of cerium oxide with particle size. The free energy of small nanoparticles in general becomes more positive relative to the bulk due to Gibbs-Thomson effects and dissolution is more favorable. Previous work by our group[11] has shown that as the surface area of cerium oxide increases, which is expected for

smaller nanoparticles, the rate of dissolution in acidic media increases per total mass of cerium oxide nanoparticles. For the large cerium oxide nanoparticles, 30 % loss of cerium oxide mass after 600 hours was seen, which would correspond to a loss in roughly 10 % of the particle radius, that is to say, the 37.7 nm nanoparticles, if they all loss the same mass, would shift to an average particle size of 34.0 nm. From our earlier work, the performance of the 37.7 nm and 34.0 nm particles should be comparable, explaining why the particles would give a linear loss. However, for medium and small cerium nanoparticles a loss of particle radius shifts the selectivity of the particles towards more free radical generation. Therefore, when the medium and small cerium oxide nanoparticle dissolve, they become worse for the fuel cell when they go beneath an optimal particle size. For small cerium oxide nanoparticles, this optimal size seems to be at 100 hours, but for the medium cerium oxide nanoparticles, this seems to be after 350 hours. So even though the medium cerium oxide nanoparticles initially behaved in a manner consistent with our proposed mechanism – good peroxide decomposition, good selectivity – ultimately particle dissolution generates smaller, less selective particles that ultimately degrade the fuel cell. From Figure 4.8d, it can be seen that there was substantially thinning of the cathode side alone, as well as a higher fluorine emission rate, suggesting that more radicals were formed by the small cerium oxide, which is also consistent with the reaction mechanisms in reaction 1, 2, and 3.

4.4 Conclusions

From these results, it is apparent that the ultimate fate of cerium in a fuel cell is to enrich both the anode and cathode catalyst layers, with little cerium left in the PEM. Moreover, the profile of cerium cations will generally mimic that of the platinum during

sufficiently long operation, with some cerium enrichment of the catalyst layer near the proton exchange membrane for longer operation. Future work must focus on understanding the mechanism of this migration, as well as understanding why cerium cations preferentially move to areas which are rich in platinum.

This work has also shown for cerium oxide nanoparticle sizes of circa 7.0 nm, cerium oxide nanoparticles incorporated in the cathode catalyst layer and cerium cations dispersed in the membrane impart the same stabilization for fuel cells. However, due to cerium oxide dissolution, this improvement is short lived, and eventually cerium oxide particle sizes become small changing the surface cerium oxide oxidation states, so that the selectivity of the cerium oxide for free radical decomposition becomes too small and the cerium oxide generates more free radicals than it scavenges. When compared to an unstabilized cell, large cerium oxide nanoparticle have stabilizing effects, which results in a lower linear loss in performance over time. Both medium and small cerium oxide nanoparticles also show some initial stabilization, however, ultimately they have detrimental effect on the lifetime of the fuel cells during accelerated stress testing, causing an increase in hydrogen cross over, fluorine emission, and exponential loss in open circuit voltage. The loss in performance in attributed to the loss of cerium oxide due to dissolution, which increases for decreasing particle size.

4.5 Notes on Chapter

The data in this chapter have been used write two manuscripts, "Cerium Migration Through Hydrogen Fuel Cells During Accelerated Stress Testing" and "Effects of Particles Size on Lifetime Improvement for Cerium (IV) Oxide in Hydrogen Fuel Cells," both of which are being prepared for submission.

4.6 References

(1) DOE/EIA *International Energy Outlook 2011*, Department of Energy, 2011.

(2) Prabhakaran, V.; Arges, C. G.; Ramani, V. *Proceedings of the National Academy of Sciences of the United States of America* **2012**, *109*, 1029.

(3) Coms, F. D. In *Proton Exchange Membrane Fuel Cells 8, Pts 1 and 2*; Fuller, T., Shinohara, K., Ramani, V., Shirvanian, P., Uchida, H., Cleghorn, S., Inaba, M., Mitsushima, S., Strasser, P., Nakagawa, H., Gasteiger, H. A., Zawodzinski, T., Lamy, C., Eds. 2008; Vol. 16, p 235.

(4) Gittleman, C. S.; Coms, F. D.; Lai, Y.-H.et al. In *Polymer Electrolyte Fuel Cell Degradation*; Academic Press: Boston, 2012, p 15.

(5) Liu, W.; Zuckerbrod, D. *J. Electrochem. Soc.* **2005**, *152*, A1165.

(6) Zhang, H.; Shen, P. K. *Chem. Rev.* **2012**, *112*, 2780.

(7) Park, J.-N.; Shon, J. K.; Jin, M.et al. *Chem. Lett.* **2010**, *39*, 493.

(8) Wang, W. D.; Bakac, A.; Espenson, J. H. *Inorg. Chem.* **1993**, *32*, 5034.

(9) Tony, M. A.; Zhao, Y. Q.; Tayeb, A. M. *J. Environ. Sci. - China* **2009**, *21*, 101.

(10) Karakoti, A.; Singh, S.; Dowding, J. M.et al. *Chem. Soc. Rev.* **2010**, *39*, 4422.

(11) Banham, D.; Ye, S.; Cheng, T.et al. In *224th Electrochemical Society Meeting*; ECS: San Francisco, CA, 2013.

(12) Feng, Z.; Peng, W.; Koberstein, J.et al. *Surf. Sci.* **2004**, *563*.

(13) Panlener, R. J.; Blumenthal, R. N.; Garnier, J. E. *J. Phys. Chem. Solids* **1975**, *3611*, 1213.

(14) Blumenthal, R. N.; Hofmaier, R. L. *J. Electrochem. Soc.* **1974**, *121*, 126.

(15) Blumenthal, R. N.; Panlener, R. J. *J. Phys. Chem. Solids* **1970**, *31*, 1190.

Chapter 5: $Ce_{1-x}Pr_xO_2$, $Ce_{1-x}Gd_xO_2$, and $Ce_{1-x}Zr_xO_2$ Materials for Fuel Cells

5.1 Introduction

Cerium oxide provides a more viable option for hydrogen peroxide decomposition. While cerium oxide is only a moderate peroxide decomposer, the Ce^{+4} sites which are responsible for peroxide decomposition are paired with Ce^{+3} sites which can facilitate radial scavenging.[1] The effect of adding praseodymium, gadolinium, and zirconium to cerium oxide on reactivity and selectivity was investigated, and the effect of adding $Ce_{0.95}Pr_{0.05}O_2$ nanoparticles to the cathode catalyst layer of fuel cells was investigated for three different particle sizes. Praseodymium is capable of changing its oxidation state from +3 to +4, but with a 149 kJ/mole higher barrier than cerium,[2] making it a multivalent oxidation state cation, but with a higher barrier to conversion and a propensity to stay in the +3 oxidation state. Zirconium and gadolinium, however, have fixed oxidation states; zirconium is a fixed +4 oxidation state, and gadolinium is a fixed +3 oxidation state. Like praseodymium,[3,4] both gadolinium and zirconium cations preferentially surface segregate,[5,6] allowing them to alter the surface chemistry of the cerium oxide nanoparticles. These studies elucidate the effect of using multi versus single oxidation state cation dopants on the activity and selectivity of cerium oxide nanoparticles, and provide some preliminary results of how these nanoparticles perform in hydrogen fuel cells.

5.2 Results

5.2.1 Nitrogen Absorption Analysis

Figure 5.1 shows the nitrogen absorption data for the three nanoparticle sizes used in the accelerated stress tests in Chapter 3. Nitrogen absorption data in this chapter

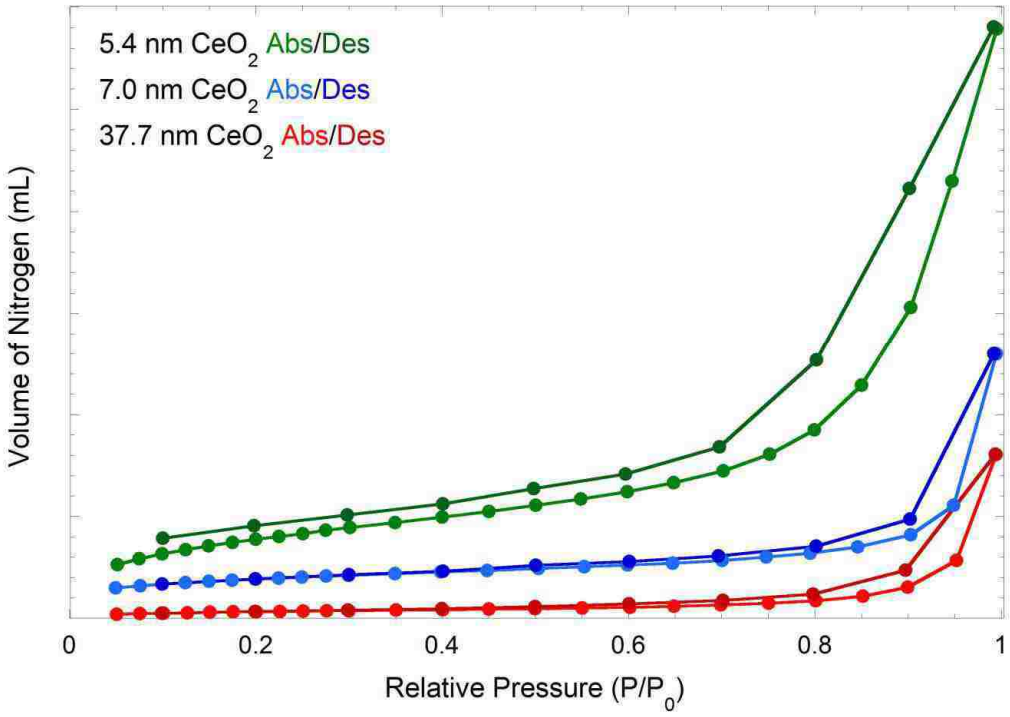

Figure 5.1 Nitrogen absorption data over the three cerium oxide particle sizes used for accelerated stress testing. The absorption data has been shifted to emphasize features in the data.

has been scaled and shifted to emphasize details in the absorption curves and so no scale is provided on the y-axis. Forty absorption and desorption points were used for all samples except for the cerium oxide nanoparticles, which due to time limitations when the measurements were taken very few absorption and desorption points could be collected.

Nonetheless, cerium oxide nanoparticles show little microporosity and mesoporosity and type H1 desorption behavior, viz., cylindrical pores, though due to the similarity in the absorption and desorption curves, it is also possible that the pores follow H3 desorption behavior, which is indicative of disordered pore structure. The surface area predicted from the multipoint BET analysis is 80 % of the surface area predicted from the average particle diameter, indicating that there is little agglomeration of the particles regardless of particle size.

Figure 5.2 and Figure 5.3 show the nitrogen absorption curves for $Ce_{0.95}Pr_{0.05}O_2$ and $Ce_{0.85}Pr_{0.15}O_2$ nanoparticles, respectively. Unlike cerium oxide, the surface areas predicted from the multipoint BET analysis are only 30 % of the surface area predicted from the average particle size, suggesting that there is substantial agglomeration of the nanoparticles, regardless of particle size. Comparing the desorption curves, both materials exhibit H3 hysteresis from disordered pore shapes. For 5 at% praseodymium incorporation, the nitrogen absorption curves are very similar to that of pure cerium oxide, suggesting that low praseodymium incorporation has little effect on the porosity. At 15 at% praseodymium incorporation, the porosity increases substantially, especially for larger particle sizes, and for increasing praseodymium incorporation and increased particle size, the hysteresis becomes more pronounced. The average pore diameter for

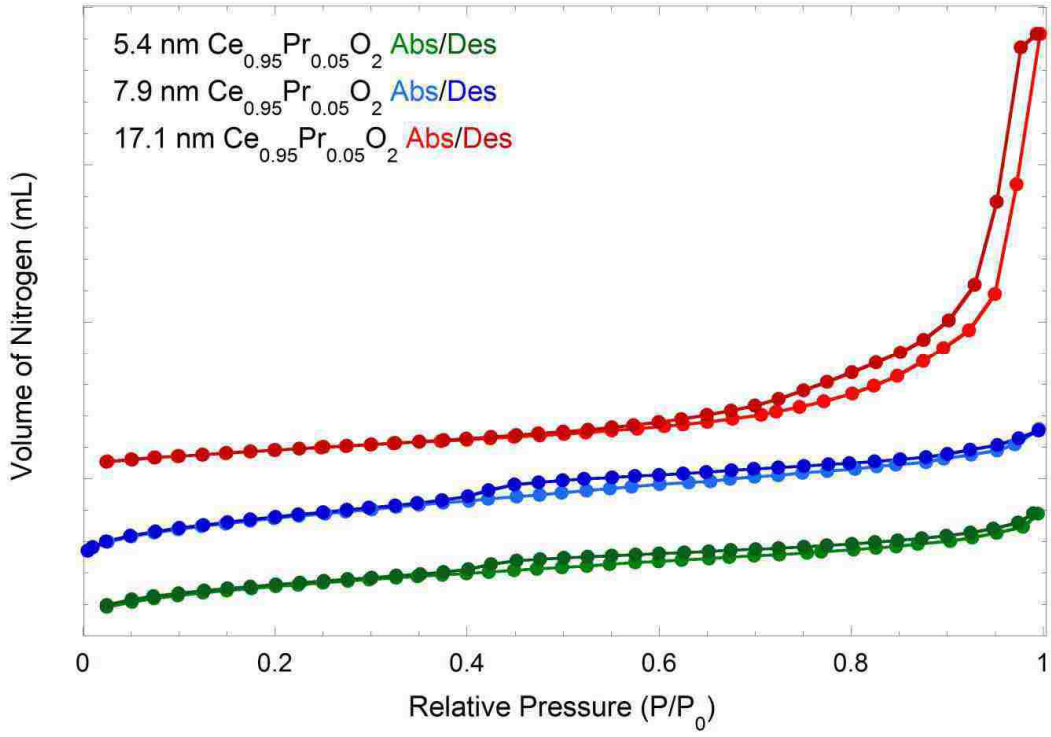

Figure 5.2 Nitrogen absorption data over the three $Ce_{0.95}Pr_{0.05}O_2$ particle sizes used for accelerated stress testing. The absorption data has been shifted to emphasize features in the data.

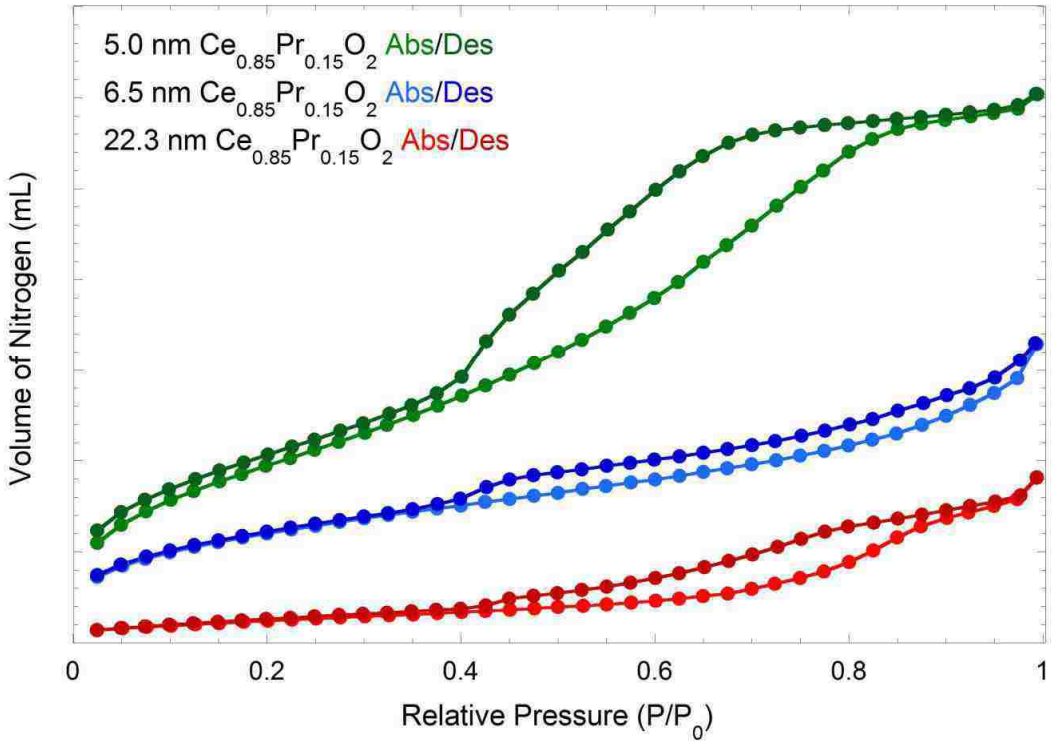

Figure 5.3 Nitrogen absorption data over three $Ce_{0.85}Pr_{0.15}O_2$ particle sizes. The absorption data has been shifted to emphasize features in the data.

both the 5 at% and 15 at% praseodymium particles were between 16.5 and 17.5 Å. For the 5 at% praseodymium nanoparticles, the pore volume was typically 0.02-0.04 mL/g, but for the 15 at% praseodymium nanoparticles, the pore volume ranged from 0.06-0.08 mL/g for small particles and decreasing down to 0.02-0.04 mL/g for large nanoparticles.

Figure 5.4 and Figure 5.5 show the nitrogen absorption curves for $Ce_{0.95}Gd_{0.05}O_2$ and $Ce_{0.85}Gd_{0.15}O_2$ nanoparticles, respectively. As expected, the surface area decreases as the average crystallite size increased, but the surface areas as measured from multi-point BET was generally 10 to 20 % of the surface area predicted from the average crystallite size regardless of doping concentration, so the particles agglomerate more than the praseodymium particles. Unlike the praseodymium nanoparticles, dopant concentration had very little effect on the pore diameter and volume and there was no correlation between pore diameter or volume or particle size. For all particle sizes and concentrations, the average pore diameter as 16.6±0.1 Å and the pore volume was between 0.02 and 0.03 mL/g. Increasing particle diameter decreases the separation of the between the absorption and desorption curves, and shifts the desorption characteristics from H2 behavior for small particles to H3 for larger particles. In other words, the smaller nanoparticles demonstrate desorption behavior consistent with a mixture of spherical and cylindrical pores, and increasing the average crystallite size shifts the desorption behavior to that of a disordered pore structure.

Figure 5.6 and Figure 5.7 show the nitrogen absorption curves for $Ce_{0.95}Zr_{0.05}O_2$ and $Ce_{0.85}Zr_{0.15}O_2$ nanoparticles, respectively. The surface area of the nanoparticles decreased with increasing crystallite diameter, but as with the gadolinium the calculated surface area is 10 to 20 % of the surface as calculated from the crystallite size.

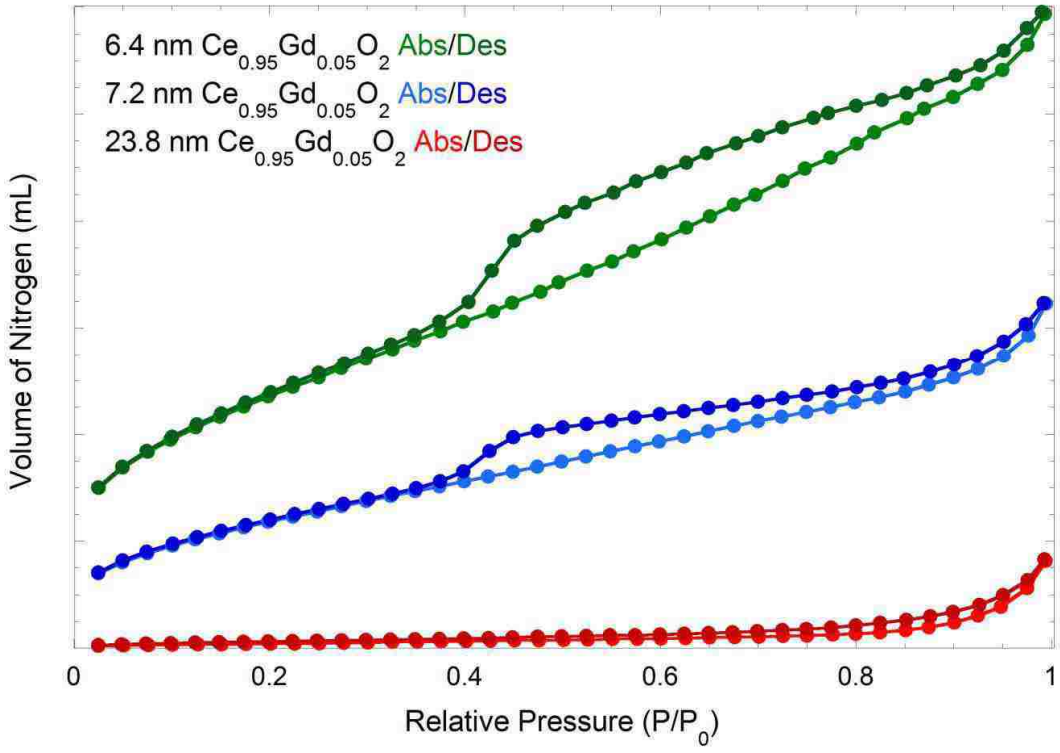

Figure 5.4 Nitrogen absorption data over three $Ce_{0.95}Gd_{0.05}O_2$ particle sizes. The absorption data has been shifted to emphasize features in the data.

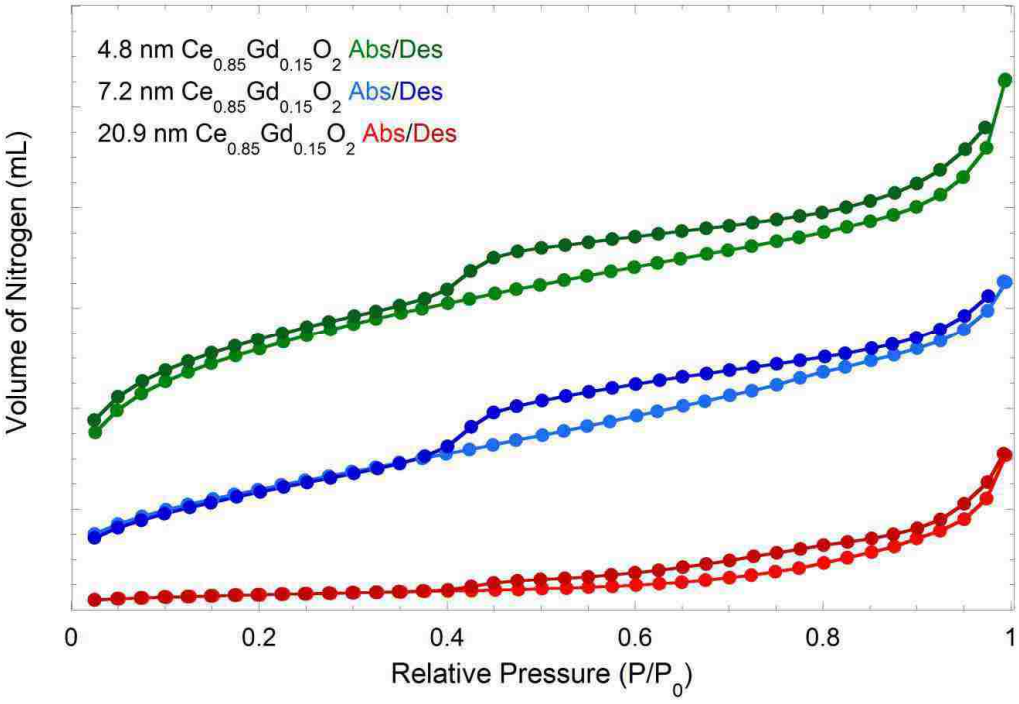

Figure 5.5 Nitrogen absorption data over three $Ce_{0.85}Gd_{0.15}O_2$ particle sizes. The absorption data has been shifted to emphasize features in the data.

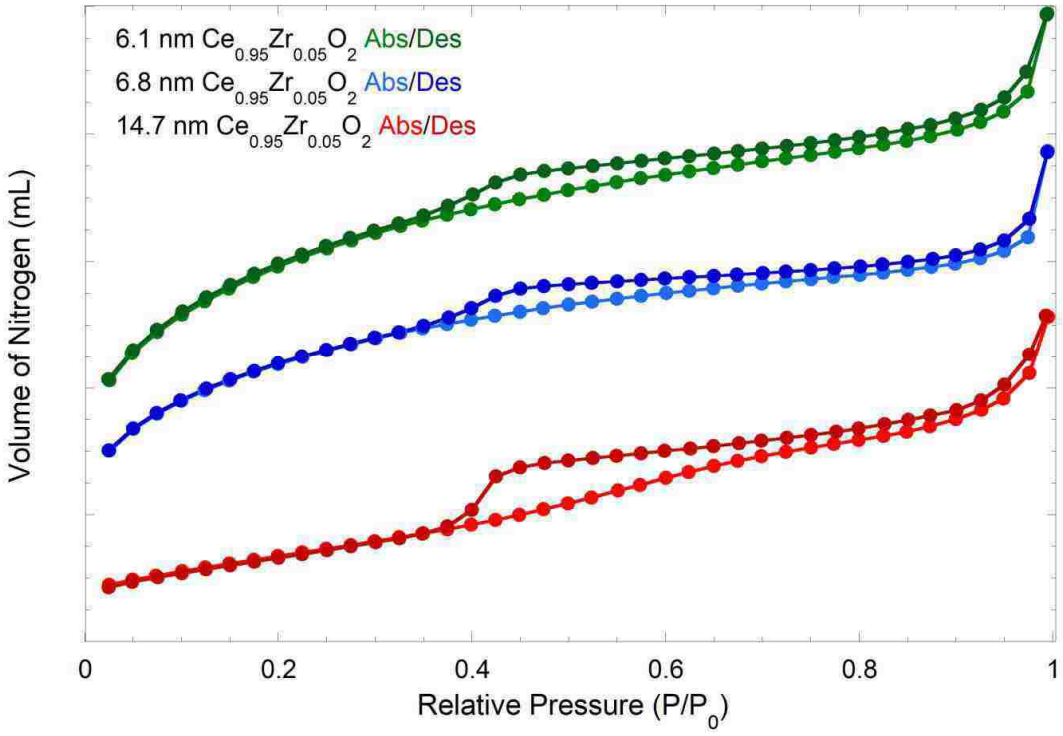

Figure 5.6 Nitrogen absorption data over three $Ce_{0.95}Zr_{0.05}O_2$ particle sizes. The absorption data has been shifted to emphasize features in the data.

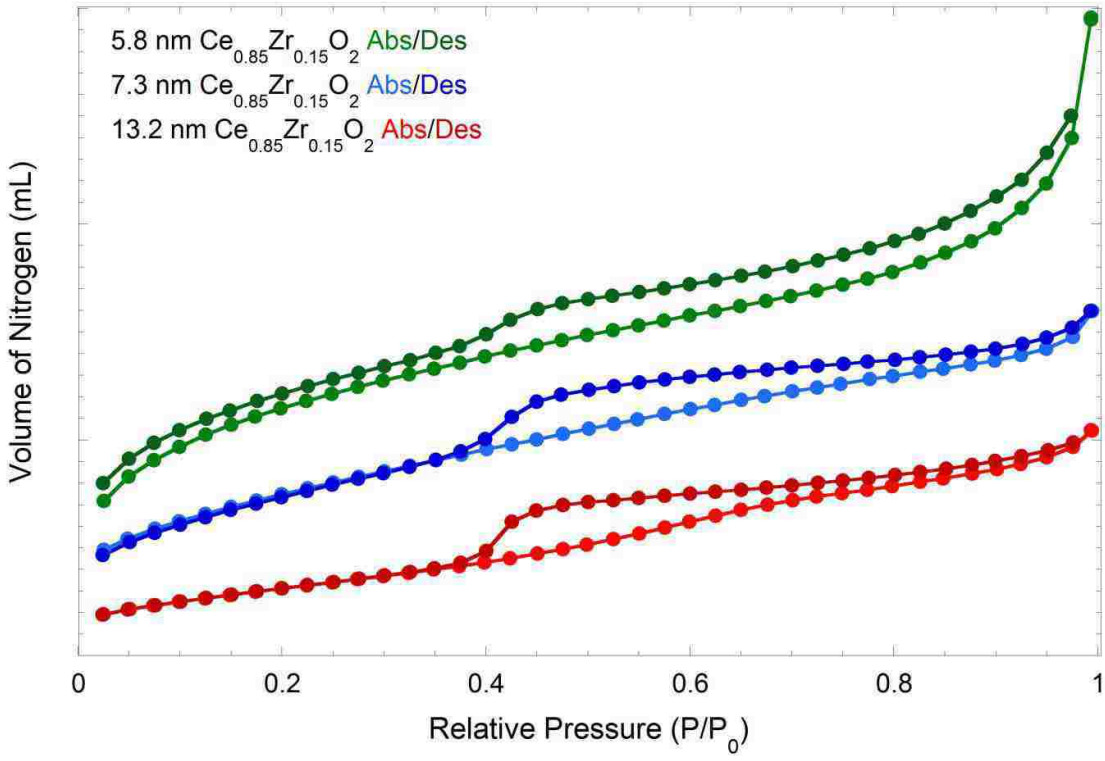

Figure 5.7 Nitrogen absorption data over three $Ce_{0.85}Zr_{0.15}O_2$ particle sizes. The absorption data has been shifted to emphasize features in the data.

Moreover, increasing zirconium concentration does not have an effect on the average pore diameter or pore volume. Like the gadolinium, the average pore diameter as 16.6±0.1 Å and the pore volume was between 0.02 and 0.03 mL/g regardless of crystallite size. However, unlike gadolinium, smaller nanoparticles demonstrate H3 desorption behavior suggesting disordered pore structures. As the average crystallite size is increased, the behavior of the nitrogen desorption shifts towards H2 behavior, suggesting a shift toward more organized pore structure consistent with cylindrical and spherical pores.

5.2.2 Selectivity and Activity of Doped Nanoparticles as a Function Particle Size

5.2.2.1 $Ce_{1-x}Pr_xO_2$

Figure 5.8 shows a plot of inverse selectivity versus reactivity, using the data for cerium oxide nanoparticles shown in Chapter 4. An ideal catalyst would be one that maximizes reactivity while minimizing inverse selectivity, viz., the particle size that gives the fastest peroxide decomposition while producing the least free radicals. Compared to pure cerium oxide, when praseodymium is incorporated into the nanoparticle at 5 at%, the optimal reactivity is seen for circa 7 nm without any loss in selectivity, with smaller and larger crystallite sizes giving worse activity. Similarly for 15 at% incorporation, the optimal crystallite size is closer to 6 nm with a loss of activity and selectivity seen above and below this crystallite size. For the 15 at% particles, the activity and selectivity of the particles approaches that of pure praseodymium for the 22.3 nm particles, whereas the 5 at% particles, while beginning to become less selective and active for larger crystallite sizes, do not reproduce the behavior of pure praseodymium at

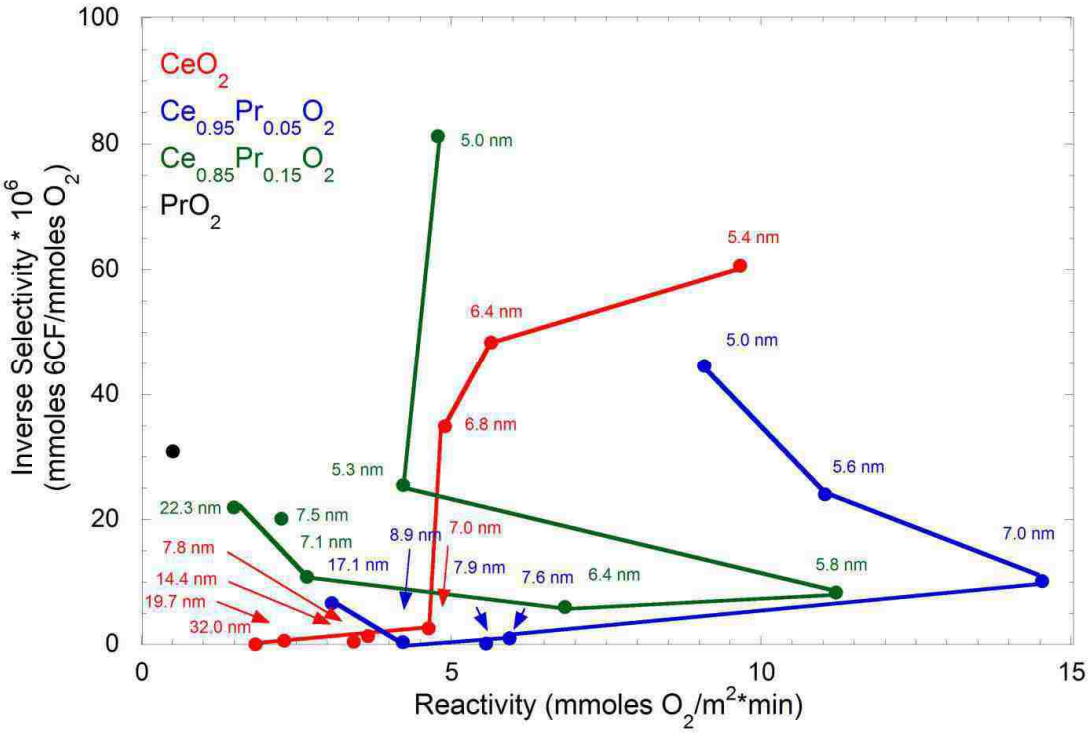

Figure 5.8 Inverse selectivity versus activity for peroxide decomposition for different particle sizes of cerium oxide (red), $Ce_{0.95}Pr_{0.05}O_2$ (blue), $Ce_{0.85}Pr_{0.15}O_2$ (green), and bulk PrO_2 (black). Particle sizes for the different cerium oxide and mixed cerium oxides are listed beside the data points.

17.1 nm. However, the 5 at% particles gives better performance over pure cerium oxide and 15 at% nanoparticles, so they were chosen for use in improving hydrogen fuel cell lifetime.

5.2.2.2 $Ce_{1-x}Gd_xO_2$

Figure 5.9 shows the effect on selectivity and activity on doping cerium oxide with gadolinium. Like praseodymium, there is an increase in the catalytic activity of the doped nanoparticles over pure cerium oxide for an intermediate particle sizes, but the selectivity is comparable to that of intermediate cerium oxide nanoparticles. Increasing gadolinium doping increases the activity of the nanoparticles, but also at the cost of decreasing the optimal particle size range for the nanoparticles – from 11.5 to 6.7 nm for 5 % gadolinium doping to 7.1 to 5.3 nm for 15 % gadolinium doping. Gadolinium doping also decreases the selectivity of the nanoparticles for very large and very small crystallite sizes over pure cerium oxide, particularly for increased gadolinium doping, suggesting that gadolinium doping is not ideal for improving cerium oxide performance in fuel cells.

5.2.2.3 $Ce_{1-x}Zr_xO_2$

Figure 5.10 shows the effect on activity and selectivity on doping cerium oxide with zirconia. Unlike both praseodymium and gadolinium, there is no loss in activity and selectivity with decreasing crystallite size. In fact, decreasing particle size and increasing zirconia content improve both activity and selectivity in these nanoparticles, and suggests that any cerium-zirconium nanoparticles beneath 7 nm would be ideal for selectively decomposing hydrogen peroxide.

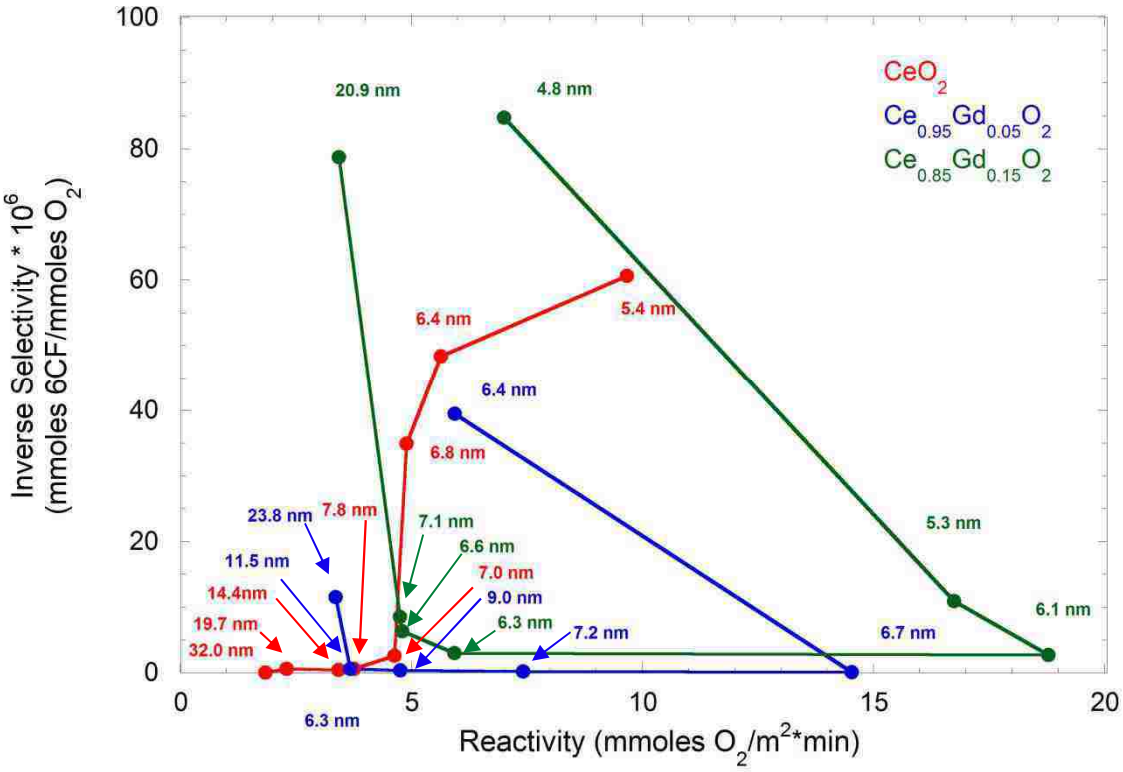

Figure 5.9 Inverse selectivity versus activity for peroxide decomposition for different particle sizes of cerium oxide (red), $Ce_{0.95}Gd_{0.05}O_2$ (blue), and $Ce_{0.85}Gd_{0.15}O_2$ (green). Particle sizes for the different cerium oxide and mixed cerium oxides are listed beside the data points.

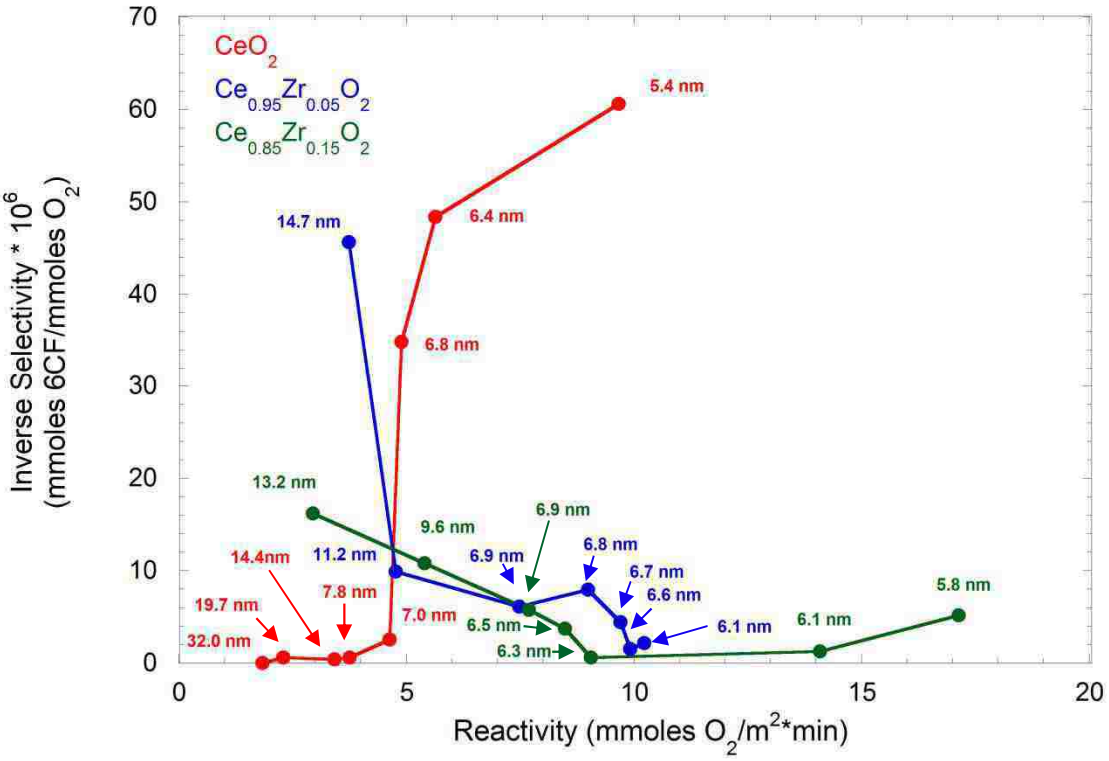

Figure 5.10 Inverse selectivity versus activity for peroxide decomposition for different particle sizes of cerium oxide (red), $Ce_{0.95}Zr_{0.05}O_2$ (blue), and $Ce_{0.85}Zr_{0.15}O_2$ (green). Particle sizes for the different cerium oxide and mixed cerium oxides are listed beside the data points.

5.2.3 Accelerated Stress Testing (AST)

Unfortunately, only the fuel cell modified with small cerium-praseodymium nanoparticles was able to run to failure. The cell modified with large cerium-praseodymium nanoparticles failed due to a pin hole generated from over pressurizing of the cell by the test stand. The cell modified with medium cerium-praseodymium nanoparticles was stopped prematurely due to the possible shutdown of Los Alamos National Labs during a Congressional impasse over the government budget, so the government could not be run to failure. Nonetheless, Figure 5.11 shows the open circuit potential versus time for different hydrogen fuel cells, with plots for unmodified and unstabilized XL membranes reproduced in figures a and b, respectively, for comparison. The early behavior of the large cerium-praseodymium nanoparticles does show an improvement in OCV loss over time versus the control cell comparable to large cerium oxide nanoparticles. When small cerium-praseodymium nanoparticles are added to the cathode catalyst layer, behavior similar to small cerium oxide nanoparticles is seen, specifically the exponential loss in OCV. However, the exponential loss in performance is not as pronounced as with small cerium oxide nanoparticles. When medium cerium-praseodymium oxide nanoparticles have nearly the same OCV decrease as the large cerium nanoparticles, and while the behavior after 450 hours begins to show a loss of performance, without operating the cell to failure it is impossible to tell if this is the start of the exponential loss seen with the small nanoparticles.

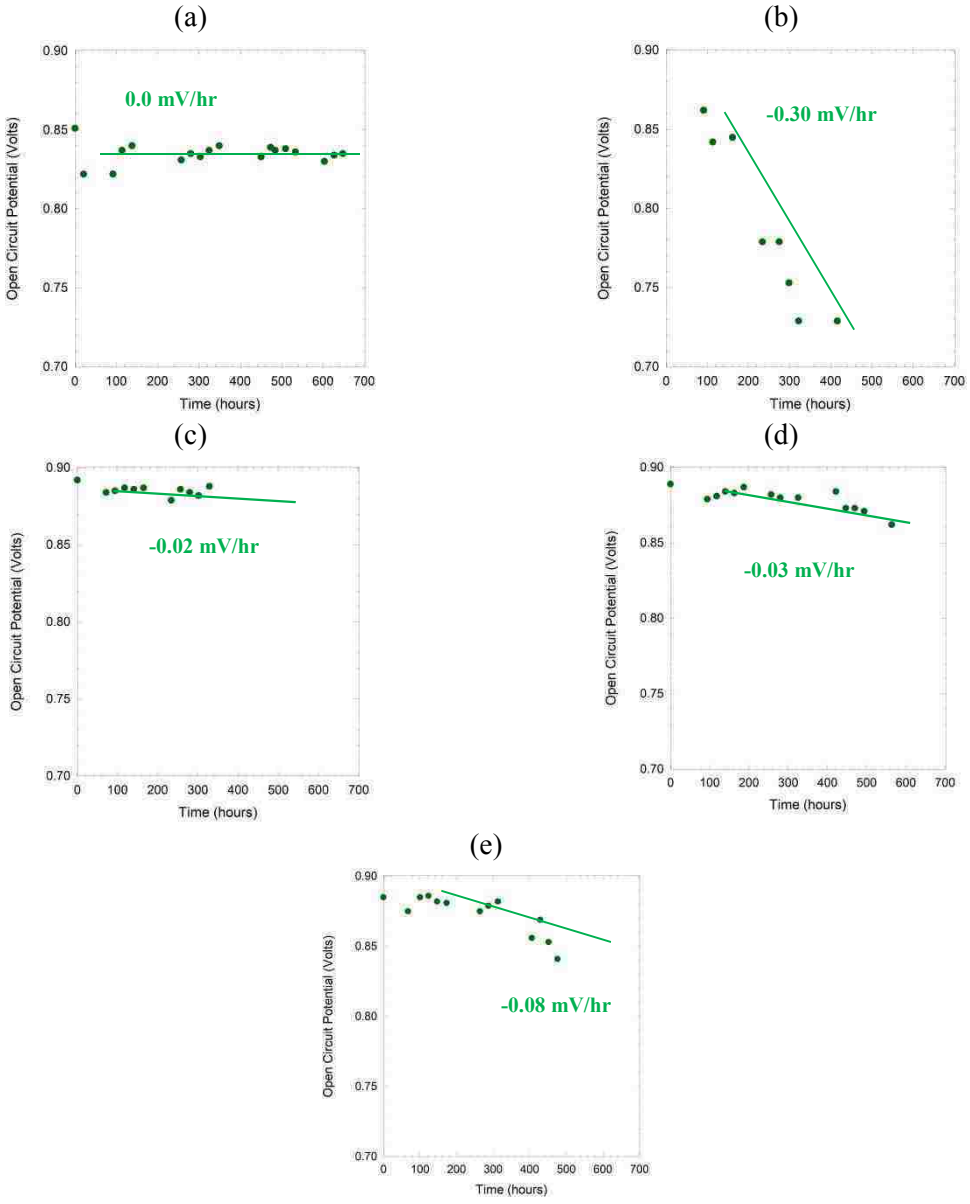

Figure 5.11 Open circuit potential (OCV) versus time for the different fuel cells: (a) XL-unmodified, (b) XL-unstabilized, (c) XL-LNPs, (d) XL-MNPs, and (e) XL-SNPs.

Figure 5.12 shows hydrogen crossover as a function of time for the modified cells, with the performance of the unmodified and unstabilized XL membranes reproduced in figures a and b, respectively, for comparison. As with OCV, the large cerium-praseodymium nanoparticles show an improvement over the unstabilized cell, and the performance is comparable to large cerium oxide nanoparticles in hydrogen fuel cells. Small cerium oxide-praseodymium nanoparticles show an exponential increase in hydrogen crossover over time, but the exponential loss is not as pronounced as with the small cerium oxide nanoparticles and the cell is able to operate for longer. Medium cerium-praseodymium oxide nanoparticles show no improvement over large nanoparticles, and as with the OCV, it is hard to tell if the loss in performance is the start of the exponential loss in performance as with the small nanoparticles.

Figure 5.13 shows the fluorine emission rate of the fuel cells for both the anode and cathode exhaust gases. As with the OCV and hydrogen crossover, the performance of the unmodified and unstabilized XL membranes reproduced in figures a and b, respectively, for comparison. The large cerium-praseodymium nanoparticles were able to reduce the fluorine emission rate for both the anode and cathode beneath that of the unstabilized fuel cell. The small cerium-praseodymium nanoparticles have a higher fluorine emission rate than the unmodified cell, but still less than that of the small cerium oxide nanoparticles explaining the improvement in lifetime over small cerium oxide nanoparticles. Medium nanoparticles show an interesting deviation from the behavior seen with the control cells and cerium oxide modified cells – the fluorine emission rate for the cathode side is less than that of the anode, and the rate of increase is less for the anode than the cathode.

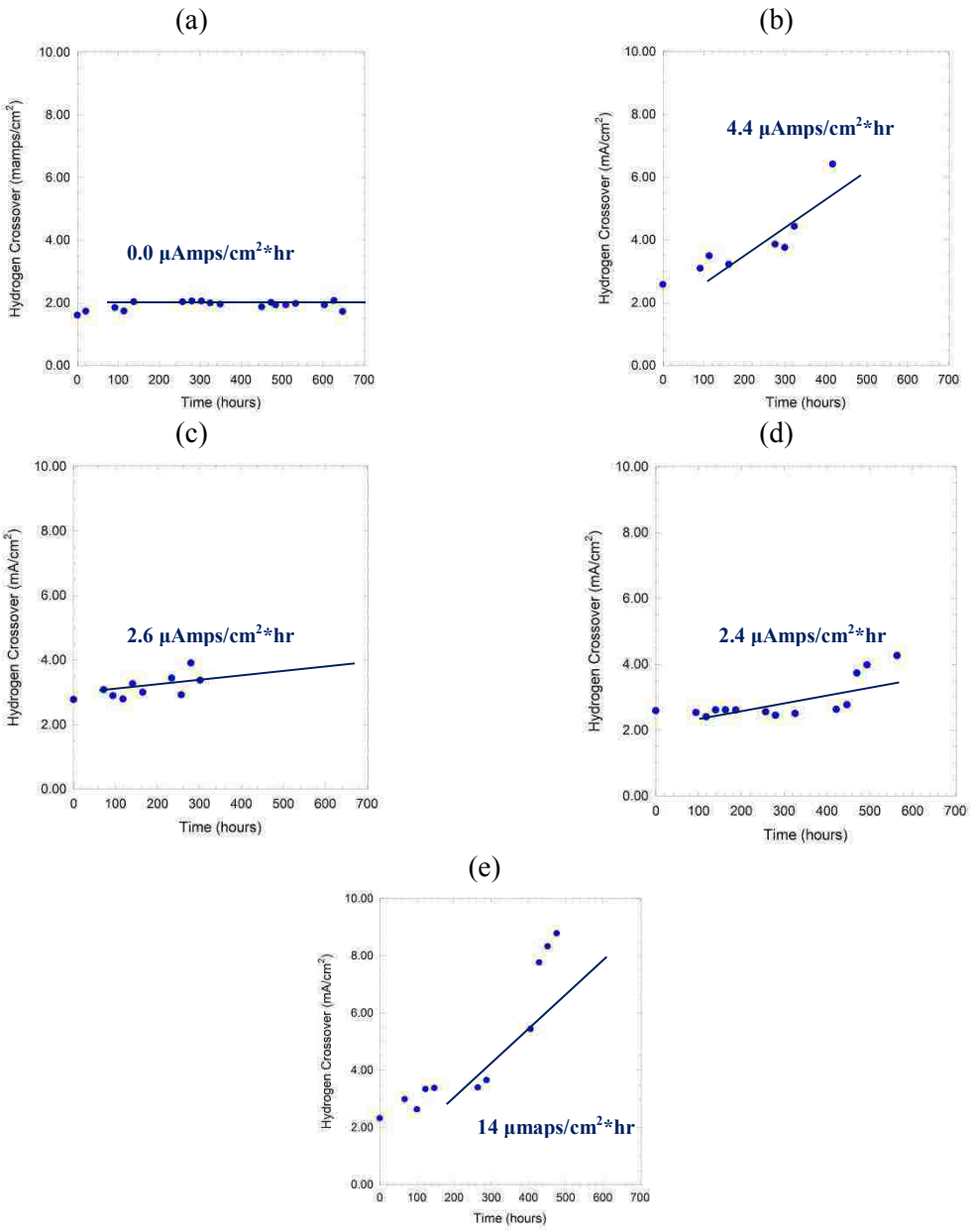

Figure 5.12 Hydrogen Cross-over (CO) versus time for the different fuel cells: (a) XL-unmodified, (b) XL-unstabilized, (c) XL-LNPs, (d) XL-MNPs, and (e) XL-SNPs. The rate of change in the CO increase is reported on each figure.

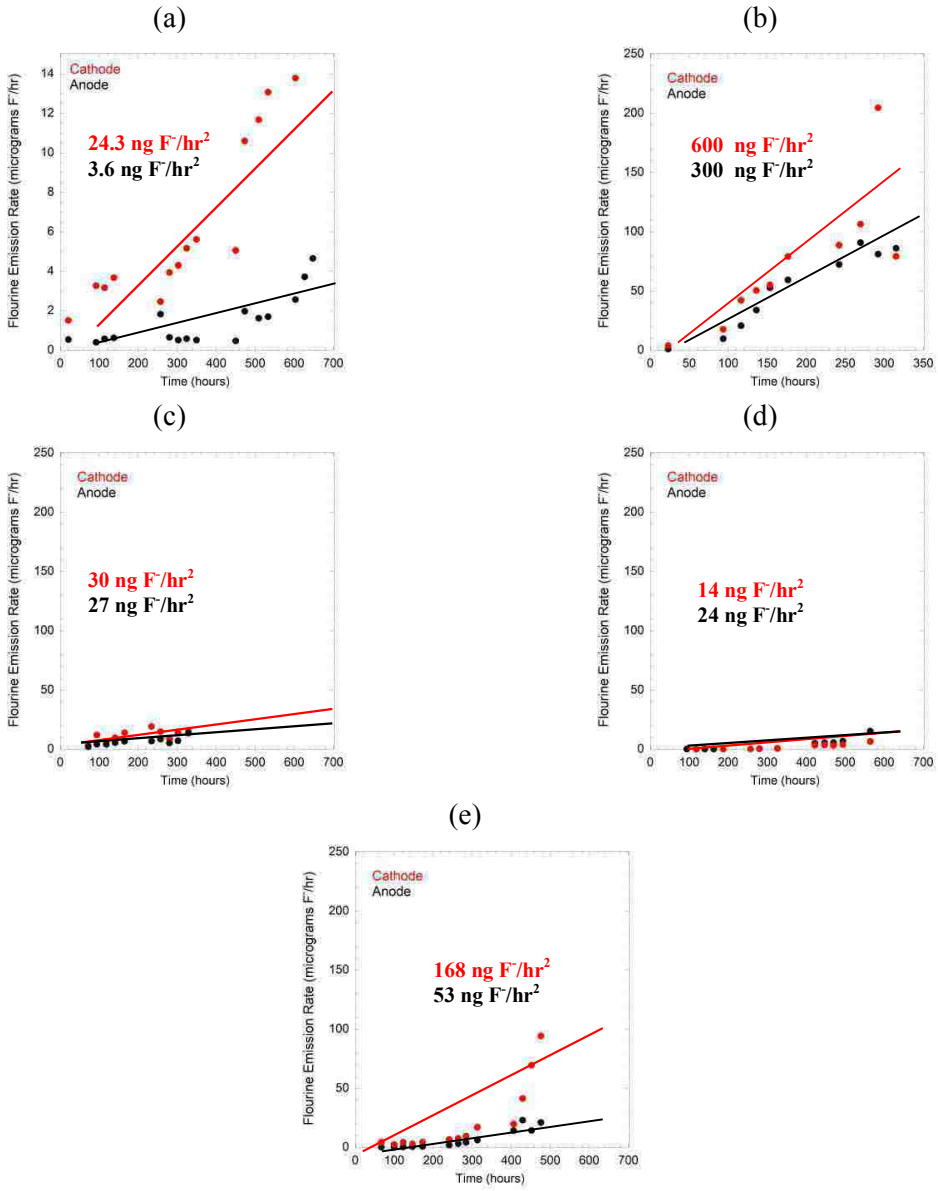

Figure 5.13 Flourine emission rate (FER) versus time for the different fuel cells: (a) XL-unmodified, (b) XL-unstabilized, (c) XL-LNPs, (d) XL-MNPs, and (e) XL-SNPs. Here, the anode FER is the square markers, and the cathode FER are the round markers. The insert in over the XL-modified membrane is of the same graph but with a smaller scale to show the features of the fluorine emission rate.

5.2.4 SEM

Figure 5.14 shows SEM images of the fuel cells after ASTM testing. The ratio of the cathode Nafion thickness to the anode Nafion thickness was used as a metric for free radical mitigation. For the unmodified XL membrane, the ratio of cathode to anode Nafion thickness is 0.95 while for the unstabilized membrane was 0.72. For the small cerium-praseodymium nanoparticles, the ratio of cathode to anode at failure was 0.71 versus 0.43 for small cerium oxide nanoparticles; while this ratio is on par with the unstabilized cell, this was after more hours of operation and represents and improvement in performance. The medium cerium-praseodymium nanoparticles actually show more thinning of the anode Nafion layer than the cathode Nafion layer, with a ratio of 1.3 after 560 hours, which is consistent with the fluorine emission rate of the anode being higher than that of the cathode. Finally, the large cerium-praseodymium particles had a cathode to anode ratio of 0.92, but because of how early this cell testing was stopped, it is hard to tell if this is an actual improvement over an unstabilized cell or the large cerium oxide nanoparticles.

5.3 Discussion

5.3.1 Performance of Doped Nanoparticles

An ideal nanoparticle catalyst is one which maximizes the rate of peroxide decomposition while being very selective to peroxide decomposition over free radical generation. However, the high acidity of the fuel cell cathode under normal operation require that both the catalyst dissolution must also be considered. Therefore, the ideal dopant not only maximizes activity and selectivity, but also increases the crystallite range on which the nanoparticles are selective and active.

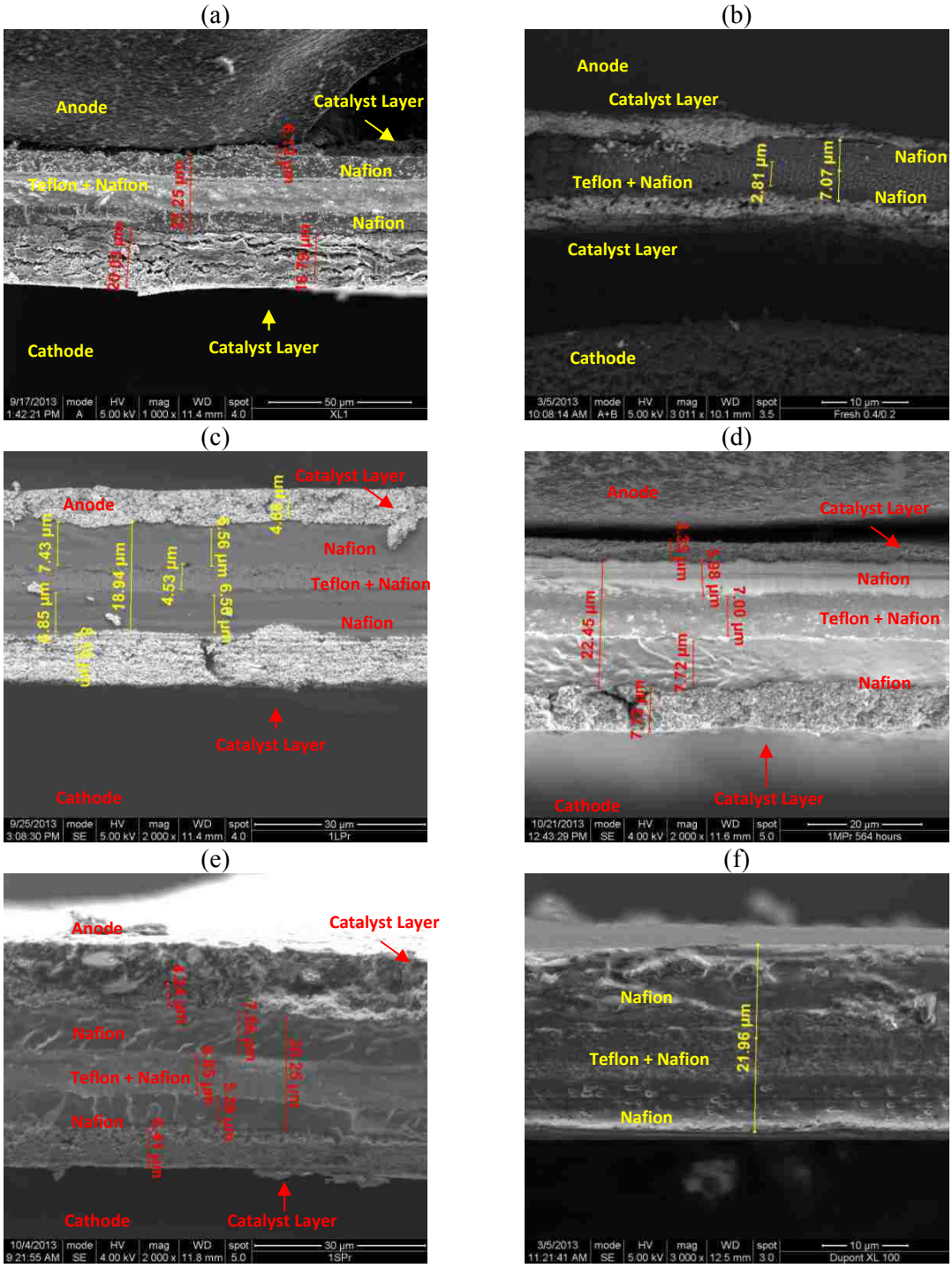

Figure 5.14 SEM images of the different fuel cells after AST; (a) XL-unmodified, (b) XL-unstabilized (409 hours), (c) XL-LNPs (hours), (d) XL-MNPs (hours), (e) XL-SNPs (hours), and (f) a Dupont XL membrane as received.

When praseodymium is added as a dopant to cerium oxide, it seems that less praseodymium doping is better than more. As the bulk concentration of praseodymium is increased, both the activity and selectivity of the nanoparticles decrease. Moreover, increasing the bulk praseodymium concentration also limits the range of crystallite sizes suitable for use in a fuel cell; the ideal crystallite range for the 5 % praseodymium nanoparticles is from 17.1 nm to 7.0 nm, versus 7.1 to 5.8 nm for the 15 % praseodymium nanoparticles. However, there remains an underlying problem with the cerium-praseodymium nanoparticles, which is the same as with cerium oxide; beneath a certain crystallite size, the cerium-praseodymium nanoparticles become very unselective towards peroxide decomposition, and as the particles are dissolving under the acidic conditions of the cathode, ultimately these particles will contribute to degradation of the fuel cell.

A similar trend is seen with gadolinium doped cerium oxide. Increasing the bulk gadolinium content in the mixed nanoparticles generally has the adverse effect of decreasing selectivity, and while the activity is better for the 15 % gadolinium nanoparticles beneath 6.4 nm, the activity of these particles is much less than the 5 % gadolinium nanoparticles on a much larger range. Furthermore, increasing the gadolinium content decreases the ideal crystallite range for the doped cerium oxide nanoparticles, so much like praseodymium, it is ideal to use less dopant to improve the performance of the doped nanoparticles. However, like cerium oxide and praseodymium-doped cerium oxide there remains an underlying problem with the cerium-praseodymium nanoparticles in that as the particles are dissolving under the

acidic conditions of the cathode, ultimately these particles will contribute to degradation of the fuel cell.

Zirconium doped cerium oxide nanoparticles are the only nanoparticles which demonstrate the ideal behavior for peroxide scavenging catalysts for hydrogen fuel cells. For both 5 % and 15 % zirconium doping, the selectivity and activity of the nanoparticles improves as the nanoparticles become smaller. While 6.8 nm and larger cerium oxide nanoparticles are more selective the zirconium doped cerium oxide nanoparticles of comparable size, at crystallite sizes smaller than 6.8 nm zirconium doped cerium oxide nanoparticles are substantially more selective and far more active. Additionally, the zirconia doped cerium oxide nanoparticles show improvement for 15 % doping versus 5 % doping, unlike praseodymium and gadolinium.

5.3.2 Accelerated Stress Testing with Praseodymium-doped Cerium oxide

Addition of large cerium-praseodymium oxide nanoparticles to fuel cells did not improve the performance of fuel cells over the improvement seen by large cerium oxide nanoparticles. Both the OCV loss and increase in hydrogen crossover are the same as the rates seen for large cerium oxide, which is consistent with the selectivity versus activity curves; while the selectivity of the large cerium-praseodymium oxide nanoparticles is worse than the large cerium nanoparticles, they have comparable rates of peroxide decomposition. This, however, is only based on the initial 300 hours of operation, and without information up to 600 hours, it is hard to tell if an improvement in performance would be seen due to the large cerium-praseodymium oxide nanoparticles dissolving to a particle size with better selectivity and activity.

As with small cerium oxide nanoparticles, as the accelerated stress testing was conducted, the performance became exponentially worse, most likely due to dissolution of the nanoparticles which results in smaller, less selective nanoparticles. Furthermore, the loss of open circuit potential and increase in hydrogen cross is not as dramatic as small cerium oxide nanoparticles, which is consistent with the improved selectivity of the cerium-praseodymium oxide nanoparticles over cerium oxide nanoparticles. So while the addition of praseodymium to cerium oxide does improve stabilization of fuel cells, the same exponential loss of performance is seen with dissolution of the nanoparticles over fuel cell operation.

However, the most interesting results are for the medium cerium-praseodymium oxide nanoparticles. The fluorine emission rate from the anode exhaust is the same as the large cerium-praseodymium oxide nanoparticles, but the fluorine emission rate for the cathode was nearly half that of the anode. This is consistent with the SEM image, which shows that there is indeed more thinning of the anode than the cathode. This would suggest that the loss in performance with the OCV and crossover may be due to thinning on the anode side, and not the cathode side. From these results, it would suggest that the medium cerium-praseodymium oxide nanoaprticles are very good as decomposing peroxide, and for the initial 450 hours there is no increase in hydrogen crossover or loss in open circuit potential. This behavior is similar to that of medium cerium oxide nanoparticles, and the increase in operating window for the cerium-praseodymium oxide nanoparticles would explain why the medium cerium-praseodymium oxide improved the lifetime of the fuel cell for longer than regular cerium oxide nanoparticles. This cell was not run to failure but stopped prematurely, so it would be interesting to see the behavior

of the fuel after 700 hours of operation, and to see if the exponential loss in performance is recovered with these nanoparticles as was seen with medium cerium oxide nanoparticles.

5.4 Conclusions

Praseodymium does have a positive impact on the performance of cerium oxide nanoparticles, increasing the lifetime of fuel cells for both medium and small nanoparticle sizes. However, as seen with the small praseodymium-doped cerium oxide nanoparticles, when the dissolution of the nanoparticles is severe enough, the nanoparticles become destructive. From the preliminary data on the large praseodymium-doped cerium oxide nanoparticles, it does appear that the improvement in performance is comparable to that of large cerium oxide nanoparticles so there is no advantage to doping large cerium oxide nanoparticles for fuel cell applications for the first 300 hours, but as the nanoparticle dissolves, the performance of the doped cerium oxide nanoparticles is predicted to be better than the undoped cerium oxide nanoparticles, so doping is advantageous when dissolution is considered, and may be an advantage when large nanoparticles are used. Medium cerium-praseodymium oxide nanoparticles show the most interesting behavior due the inverse trends seen with membrane thinning and fluorine emission. When mixed into the cathode catalyst layer, the medium cerium-praseodymium oxide nanoparticles decrease the fluorine emission rate from the cathode to beneath that of the anode, resulting of more thinning of the anode Nafion layer than the cathode Nafion layer over time. If stabilizers had been placed in the anode catalyst layer as well, it is possible that the medium cerium-praseodymium oxide nanoparticles would have shown performance comparable to unmodified XL membranes.

But of the three dopants, zirconium cations are the only dopants which demonstrate ideal behavior for fuel cell dopants; increasing selectivity and activity with decreasing particles size, with no lower limit on particle size. Future work on doped cerium oxides for hydrogen fuel cells should focus on zirconium doped cerium oxides, and see how these materials affect performance and stability.

5.5 References

(1) Karakoti, A.; Singh, S.; Dowding, J. M.et al. *Chem. Soc. Rev.* **2010**, *39*, 4422.

(2) Pourbaix, M. *Atlas of electrochemical equilibria in aqueous solutions*; Pergamon Press, 1966.

(3) Luo, M. F.; Yan, Z. L.; Jin, L. Y.et al. *J. Phys. Chem. B* **2006**, *110*, 13068.

(4) Zhi-Ying, P.; Ji-Qing, L.; Meng-Fei, L.et al. *J. Phys. Chem. C* **2007**, *111*.

(5) Huang, H.; Gur, T. M.; Saito, Y.et al. *Appl. Phys. Lett.* **2006**, *89*.

(6) Maia, T. A.; Assaf, J. M.; Assaf, E. M. *Reac. Kin. Mech. Cat.* **2013**, *109*, 181.

Chapter 6: Conclusions and Future Directions

6.1 Ceria

6.1.1 Physical Properties

The physical properties of ceria are, for the most part, very well understood. The most common spectroscopic techniques for analyzing ceria, such as IR[1-6] and UV-vis,[7-9] were well worked out in the literature by the late 1990s, with both theoretical and experimental approaches used and validating one another. Some confusion still remains about the lattice parameter as a function of particle size,[10-15] and in isolated reports it is understandable how such confusion can occur, though a survey of the literature reveals that syntheses rich in carbon ligands generally show lattice contraction while syntheses rich in nitrates and oxygen show lattice expansion. While there remains a very rich discussion on the electrical properties and oxygen sub-stoichiometry of ceria,[16] there still remain gaps in the understanding of how oxygen sub-stoichiometry varies for smaller nanoparticles. Is the relationship still a power law with respect to oxygen partial pressure? Does the pre-factor change? There is also little known about how bulk conductivity changes with regards to particle size. Is the conductivity the same regardless of particle size? Is the conductivity only dependent on oxygen sub-stoichiometry, or also on particle size, as the two parameters can be related? Future studies would be beneficial in understanding this dependence, and higher resolution impedance spectroscopy could better help in distinguishing between bulk and surface conductivity and how these vary with regard to sub-stoichiometry.

6.1.2 Comments on catalytic activity

While ceria does have the ability to changes its oxidation state readily at moderate temperatures using adventitious oxygen or water,[17,18] the reality is that ceria use as a catalytic material in this regard is not nearly as good as its performance as catalyst promoter. That is to say, while ceria can change its oxidation state to promote reactions such as the water gas shift reaction or steam reforming, this behavior is enhanced by the addition of other catalytic metals such as platinum, which already promote these reaction, and this lability in oxidation state makes ceria a better catalyst promoter rather than a catalyst itself. Moreover, the lability of oxidation state seems to decrease for decreasing particle size as surface tension effects drive more surface sites to the Ce^{+3} oxidation state.[19,20] Nonetheless, ceria's labile oxidation state makes it ideal for a variety of reactions, with its performance typically increasing for decreasing particle size. However, there remains a large gap in the literature concerning the selectivity of ceria as a catalyst and how selectivity changes as a function of particle size. Reactions such as NO and CO oxidation generally lack issues with selectivity. But reactions such as free radical scavenging, where peroxide decomposition can result in increased free radical concentration if the radical scavenging step becomes rate limiting, would benefit greatly from selectivity studies.

6.2 Ceria in Fuel Cells

Cerium impregnated Nafion membranes have been commonly used in fuel cell construction for many years, and even in this study, remain the best in terms of stability and lifetime. The use of the cerium cation as a radical scavenger is not a new idea,[20] but the understanding of its behavior in fuel cells has been lacking. Contrary to what has

been traditionally believed, cerium does not remain stationary during cell operation. On construction, the cerium cations are only in the PEM, when the cerium profile is taken across the MEA, the concentration closely resembles a step function in the PEM. However, during conditioning there is migration of cerium from the PEM into the cathode and anode catalyst layers, perhaps moving into the Nafion found in the catalyst ink. This migration does not resemble what would be expected for normal diffusion, which would be a symmetric Gaussian or Lorentzian centered within the MEA, but rather a linear drop in concentration from the cathode side of the MEA to the anode side of the MEA. In the cathode, there is an abrupt drop in cerium cation concentration moving away from the PEM, whereas the anode cerium cation concentration continues the same concentration profile seen through the MEA. Most likely this is due to the build-up as positive charges in the anode (H^+) and negative charges in the cathode (e^- or O^-). A similar trend is seen with ceria as well. Prior to conditioning, there is a large concentration of cerium in the cathode catalyst layer only, but after conditioning the profile is similar to that of the unmodified XL membrane. However, depletion of cerium from the ceria cell is much higher than that of the XL membrane.

Compared to an unstabilized membrane, large ceria nanoparticles improve the lifetime of hydrogen fuel cells. There is both an increase in overall lifetime, there is a decrease in the fluorine emission rate and a decrease in the rate of increase fluorine emission, OCV loss, and hydrogen crossover. Moreover, after 600 hours, the ratio of cathode Nafion thickness to anode Nafion thickness is higher than that of the unstabilized membrane after 400 hours. This improvement, however, is not on par with cerium stabilized membranes which show now OCV loss after 700 hours, and marginal increase

in the hydrogen crossover and fluorine emission during the same time. While 7.0 nm ceria nanoparticles give comparable performance to cerium cations for the first 350 hours, the dissolution of the nanoparticles over time results in an exponential increase in the fluorine emission rate, hydrogen cross over, and rate of OCV loss after 350 hours. Similarly, small ceria nanoparticles show an exponential increase in the fluorine emission rate, hydrogen cross over, and rate of OCV loss after 100 hours of initial stabilization. This was predicted from the selectivity versus activity curves, which shows that as ceria nanoparticles become smaller, they quickly lose selectivity and generate high concentrations of free radicals during peroxide decomposition. From these results, it is concluded that while ceria can stabilize hydrogen fuel cells, only large ceria nanoparticles should be used; medium and small ceria nanoparticles will eventually dissolve to particle sizes which are detrimental to fuel cell lifetime. Ultimately cerium cations outperform any ceria nanoparticles, and if a choice is made between cerium oxide and cerium cations for stabilizing fuel cells, cerium is the best choice.

6.3 Doped Cerias

While there have been many reports on the incorporation of metal cations into the ceria lattice, subsequent reports aimed at verifying their inclusion have shown that a core-shell structure or surface enrichment occurs. Of all the reports determining the location and distribution of cation doping, at least for binary mixtures with ceria, none have shown that a mixed metal oxide is formed. The most likely explanation for this observation is found in the Pourbaix diagram of cerium;[21] precipitation of ceria from a cerium solution occurs at modest pH and, for most of the elements studied, occurs before nucleation of other cations. This segregation, however, seems to be beneficial to ceria in

terms of electrical conductivity and as a catalytic support. Grain boundaries account for most of the labile oxygen found in mixed meta-ceria systems, and the increase of segregation between the metal-oxide and ceria would increase the number of boundaries. In terms of peroxide decomposition

In continuing to improve the understanding of ceria, the structure of cerium-praseodymium oxide was resolved to better understand its catalytic properties. This work represents the first direct evidence of praseodymium phase separation in mixed cerium-praseodymium oxides. EDS paired with high resolution TEM was used to show that the praseodymium concentration profile was more consistent with surface enrichment – either a $Ce_{1-x}Pr_xO_2$@CeO_2 or PrO_2@CeO_2 structure – but was unable to show which of the two structures was formed. XPS showed a strong decrease in surface Ce^{+3}, and that increasing the bulk composition of praseodymium results in a shift towards the +4 oxidation state for surface praseodymium atoms, suggesting the formation of a PrO_2 shell. MM simulations were used to determine the thermodynamics of phase separation, and molecular dynamics was be used to model the movement of praseodymium during cerium oxide crystallization. There was no preferential migration of praseodymium to the surface of nucleating nanoparticles regardless of starting configuration, and the configurational energies of the different conformations were not significantly different. If entropic mixing is accounted for, the mixed cerium-praseodymium oxide nanoparticles are the most favorable conformations. However, since this is not the final conformation seen experimentally, the final conformation must be a kinetic product.

In terms of the effect of structure on catalytic activity, catalytic testing has shown that the addition of 5 at% praseodymium to the ceria lattice shows a substantial

improvement in the activity of 7 nm particles over pure ceria without a loss in selectivity. Similar behavior in the activity and selectivity of the 15 at% praseodymium samples to the 5 at % praseodymium samples was also seen, but the incorporation of 15 at% praseodymium resulted in an overall loss in activity and selectivity versus pure ceria. However, by varying the concentration of praseodymium showed that, at least for these two concentrations, the ideal theoretical praseodymium shell thickness is 0.12 nm.

Praseodymium does have a positive impact on the performance of ceria nanoparticles, increasing the lifetime of fuel cells for both medium and small nanoparticle sizes. However, as seen with the small praseodymium-doped ceria nanoparticles, when the dissolution of the nanoparticles is severe enough, the nanoparticles become destructive. From the preliminary data on the large praseodymium-doped ceria nanoparticles, it does appear that the improvement in performance is comparable to that of large ceria nanoparticles so there is no advantage to doping large ceria nanoparticles for fuel cell applications for the first 300 hours, but as the nanoparticle dissolves, the performance of the doped ceria nanoparticles is predicted to be better than the undoped ceria nanoparticles, so doping is advantageous when dissolution is considered, and may be an advantage when large nanoparticles are used. Medium sized cerium-praseodymium oxide nanoparticles show the most interesting behavior due the inverse trends seen with membrane thinning and fluorine emission. When mixed into the cathode catalyst layer, the medium cerium-praseodymium oxide nanoparticles decrease the fluorine emission rate from the cathode to beneath that of the anode, resulting of more thinning of the anode Nafion layer than the cathode Nafion layer over time. If stabilizers had been placed in the anode catalyst layer as well, it is possible

that the medium cerium-praseodymium oxide nanoparticles would have shown performance comparable to unmodified XL membranes.

Finally, the change in the catalytic properties of ceria for two other dopants was investigated. Zirconium cations are the only dopants which demonstrate ideal behavior for fuel cell dopants; increasing selectivity and activity with decreasing particles size, with no lower limit on particle size. Gadolinium behaves similarly to praseodymium; there is an improvement in activity and selectivity for intermediate particle sizes, but for small nanoparticles, there is a loss in activity and selectivity. Future work on doped cerias for hydrogen fuel cells should focus on zirconium doped cerias, and see how these materials affect performance and stability.

6.4 Future Directions

The work in thesis represents a large step forward to better understanding the catalytic properties of ceria and doped ceria in the nano-regime. However, there are still many unanswered questions which, while alluded to in this work, merit further investigation.

In terms of structure, it needs to be determined if the praseodymium in doped cerium-praseodymium nanoparticles forms a pure PrO_2 phase or a mixed $Ce_xPr_{1-x}O_2@CeO_2$phase. While EDS measurements did show the surface enhancement of the doped nanoparticles did occur, it cannot be determined from EDS what the enhanced surface is composed of. The MM/MD simulations have only shown that the different configurations of cerium-praseodymium oxide nanoparticles do not have a strong configurational preference for surface enhancement, and qualitatively accounting for entropic mixing would suggest that the mixed $Ce_xPr_{1-x}O_2@CeO_2$nanoparticles are

predicted to thermodynamically exist. As the final structure of the cerium-praseodymium oxide nanoparticles is that of a surface enriched material, the only information which can be currently gleamed from these simulations is that the final structure is not the thermodynamic product but more likely the kinetic product. However, MM/MD paired with x-ray absorption spectroscopy can provide much more information. EXAFS will help provide a more complete picture of this material, and provide direct evidence of the nature of the Ce-Pr interactions. By correlating the structure of CePrOx with catalytic performance, we will be able to develop more catalytically active CePrOx catalysts by engineering core-shell structures resulting in a strained and more catalytically active CeO_2 shell, something which has not previously been attempted.

Argonne National Labs, specifically the Advanced Photon Source (APS), is the only x-ray source in the US capable of providing x-rays of sufficient energy for exciting the K-edge of praseodymium. If a proposal were written and accepted, then work at APS will involve looking at the K edges of praseodymium. Studies would focus on determining the number of nearest neighbors for praseodymium for particles of different crystallite sizes and bulk concentration. The K edges of cerium and praseodymium vary by circa 1500 eV (40443 eV versus 41991 eV for Ce and Pr, respectively, for a k-space of roughly 8.8 $Å^{-1}$), which would be sufficient for first and second shell fitting of praseodymium. The measurements would be done in air, and because of the x-ray absorption cross section of praseodymium at 42 keV, transmission measurements would be used. The number of nearest neighbors (2^{nd} shell) would be measured for different particle sizes and compositions, and the results would be compared to MM/MD simulations to see which configuration matches best. From this, the actual structure of

the enhanced nanoparticles – $Ce_xPr_{1-x}O_2@CeO_2$ or $PrO_2@CeO_2$ – could be determined. At the time this thesis was published, such time had been applied for with a high score, but time was not granted due to beam demand and a third proposal has been submitted in hoped of getting time in the Spring of 2014.

Finally, the utility of $Ce_xPr_{1-x}O_2$ in hydrogen fuel cells has been discounted by this work due to its similar behavior to pure ceria, viz., the loss of selectivity upon decreasing particle size, which is likely to occur during normal operating due to the high acidity of the cathode. A similar conclusion was drawn concerning the catalytic behavior of $Ce_xGd_{1-x}O_2$ as well. However, $Ce_xZr_{1-x}O_2$ stand in sharp contrast; the improvement in both activity and selectivity for cerium-zirconium nanoparticles for decreasing particle size suggests that even if dissolution occurs, these nanoparticles will continue to improve fuel cell lifetime during accelerated stress testing. This hypothesis needs to be verified through accelerated stress testing of fuel cells with incorporation of cerium-zirconium oxide into the cathode catalyst layer. If the results are shown to be comparable to cerium-impregnated membranes, they may show a major trend toward improving fuel cells by other means. The AST testing should also be paired with XRF mapping of the cations through the fuel cell during operation to determine the fate of the zirconium ion during fuel cell operation to see if migrates through the fuel cell during operation.

6.5 References

(1) Jacobs, G.; Williams, L.; Graham, U.et al. *J. Phys. Chem. B* **2003**, *107*, 10398.

(2) Holmgren, A.; Andersson, B.; Duprez, D. *Appl. Catal., B* **1999**, *22*, 215.

(3) Shido, T.; Asakura, K.; Iwasawa, Y. *J. Catal.* **1990**, *122*, 55.

(4) Shido, T.; Iwasawa, Y. *J. Catal.* **1993**, *141*, 71.

(5) Badri, A.; Binet, C.; Lavalley, J. C. *J. Chem. Soc. - Farad. Trans.* **1996**, *92*, 4669.

(6) Binet, C.; Daturi, M.; Lavalley, J. C. *Catal. Today* **1999**, *50*, 207.

(7) Maia, T. A.; Assaf, J. M.; Assaf, E. M. *Mater. Chem. Phys.* **2012**, *132*, 1029.

(8) Rao, G. R.; Sahu, H. R. *Proc. Indian Acad. Sci. - Chem. Sci.* **2001**, *113*, 651.

(9) Bensalem, A.; Muller, J. C.; Bozonverduraz, F. *J. Chem. Soc. - Farad. Trans.* **1992**, *88*, 153.

(10) Deshpande, S.; Patil, S.; Kuchibhatla, S.et al. *Appl. Phys. Lett.* **2005**, *87*.

(11) Hailstone, R. K.; DiFrancesco, A. G.; Leong, J. G.et al. *J. Phys. Chem. C* **2009**, *113*, 15155.

(12) Tsunekawa, S.; Sivamohan, R.; Ito, S.et al. *Nanostruct. Mater.* **1999**, *11*, 141.

(13) Baranchikov, A. E.; Polezhaeva, O. S.; Ivanov, V. K.et al. *Crystengcomm* **2010**, *12*, 3531.

(14) Chen, L.; Fleming, P.; Morris, V.et al. *J. Phys. Chem. C* **2010**, *114*, 12909.

(15) Tsunekawa, S.; Ishikawa, K.; Li, Z. Q.et al. *Phys. Rev. Lett.* **2000**, *85*, 3440.

(16) Mogensen, M.; Sammes, N. M.; Tompsett, G. A. *Solid State Ionics* **2000**, *129*, 63.

(17) Padeste, C.; Cant, N. W.; Trimm, D. L. *Catal. Lett.* **1993**, *18*, 305.

(18) Chueh, W. C.; McDaniel, A. H.; Grass, M. E.et al. *Chem. Mater.* **2012**, *24*, 1876.

(19) Feng, Z.; Peng, W.; Koberstein, J.et al. *Surf. Sci.* **2004**, *563*.

(20) Karakoti, A.; Singh, S.; Dowding, J. M.et al. *Chem. Soc. Rev.* **2010**, *39*, 4422.

(21) Hayes, S. A.; Yu, P.; O'Keefe, T. J.et al. *J. Electrochem. Soc.* **2002**, *149*, C623.